Peter Schaaf
Editor

SPRINGER SERIES IN MATERIALS SCIENCE 139

Laser Processing of Materials

Fundamentals, Applications and Developments

Springer Series in
MATERIALS SCIENCE 139

Springer Series in
MATERIALS SCIENCE

Editors: R. Hull C. Jagadish R.M. Osgood, Jr. J. Parisi Z. Wang H. Warlimont

The Springer Series in Materials Science covers the complete spectrum of materials physics, including fundamental principles, physical properties, materials theory and design. Recognizing the increasing importance of materials science in future device technologies, the book titles in this series reflect the state-of-the-art in understanding and controlling the structure and properties of all important classes of materials.

Please view available titles in *Springer Series in Materials Science*
on series homepage http://www.springer.com/series/856

Peter Schaaf
Editor

Laser Processing of Materials

Fundamentals, Applications and Developments

With 110 Figures

Springer

Editor

Professor Dr. Peter Schaaf
TU Ilmenau, Institut für Werkstofftechnik
und Institut für Mikro- und Nanotechnologien
Gustav-Kirchhoff-Str. 5, 98693 Ilmenau, Germany
E-mail: peter.schaaf@tu-ilmenau.de

Series Editors:

Professor Robert Hull
University of Virginia
Dept. of Materials Science and Engineering
Thornton Hall
Charlottesville, VA 22903-2442, USA

Professor Chennupati Jagadish
Australian National University
Research School of Physics and Engineering
J4-22, Carver Building
Canberra ACT 0200, Australia

Professor R. M. Osgood, Jr.
Microelectronics Science Laboratory
Department of Electrical Engineering
Columbia University
Seeley W. Mudd Building
New York, NY 10027, USA

Professor Jürgen Parisi
Universität Oldenburg, Fachbereich Physik
Abt. Energie- und Halbleiterforschung
Carl-von-Ossietzky-Straße 9–11
26129 Oldenburg, Germany

Dr. Zhiming Wang
University of Arkansas
Department of Physics
835 W. Dicknson St.
Fayetteville, AR 72701, USA

Professor Hans Warlimont
DSL Dresden Material-Innovation GmbH
Pirnaer Landstr. 176
01257 Dresden, Germany

Springer Series in Materials Science ISSN 0933-033X
ISBN 978-3-642-13280-3 e-ISBN 978-3-642-13281-0
DOI 10.1007/978-3-642-13281-0
Springer Heidelberg Dordrecht London New York

Library of Congress Control Number: 2010931835

© Springer-Verlag Berlin Heidelberg 2010
This work is subject to copyright. All rights are reserved, whether the whole or part of the material is concerned, specifically the rights of translation, reprinting, reuse of illustrations, recitation, broadcasting, reproduction on microfilm or in any other way, and storage in data banks. Duplication of this publication or parts thereof is permitted only under the provisions of the German Copyright Law of September 9, 1965, in its current version, and permission for use must always be obtained from Springer. Violations are liable to prosecution under the German Copyright Law.
The use of general descriptive names, registered names, trademarks, etc. in this publication does not imply, even in the absence of a specific statement, that such names are exempt from the relevant protective laws and regulations and therefore free for general use.

Cover design: eStudio Calamar Steinen

Printed on acid-free paper

Springer is part of Springer Science+Business Media (www.springer.com)

Preface

The most recent and most promising developments in laser materials processing are described on an graduate/scientist level. The book emphasizes the practical applications in modern materials and material applications.

Laser Materials Processing has made tremendous progress and is now at the forefront of industrial and medical applications. The book describes these recent advances in smart and nanoscaled materials going well beyond the traditional cutting and welding applications. As no analytical methods are described, the examples are really going into the details of what nowadays is possible by employing lasers for sophisticated materials processing, giving rise to achievements not possible by conventional materials processing.

All contributing authors have year long practical experience in laser materials processing and are working in the field at the forefront of the research and technological applications.

The help of the Springer team in the creation of this book is gratefully acknowledged.

Ilmenau
May 2010

Peter Schaaf

Contents

1 Introduction 1
Peter Schaaf
References 3

2 Basics of Lasers and Laser Optics 5
Michelle Shinn
2.1 Introduction 5
2.2 Optical Processes 5
2.3 Time Dependence 8
2.3.1 Q-Switching 8
2.3.2 Mode-Locking 9
2.3.3 Ultrashort Pulse Generation 9
2.3.4 Harmonic Generation 9
2.4 Free-Electron Lasers 10
2.5 Laser Optics 12
2.5.1 Optical Propagation 13
2.5.2 Sizing Optical Elements and Other Tricks of the Trade 14
2.5.3 Fiber Optics 14
2.5.4 Managing Diffraction 15
2.5.5 The Aspheric Lens Beamshaper 15
2.5.6 Holographic Optical Elements 16
2.5.7 Laser Damage 17
2.5.8 Optical Modeling Software 19
2.6 Conclusions 19
References 19

3 Fundamentals of Laser-Material Interactions 21
Ettore Carpene, Daniel Höche, and Peter Schaaf
3.1 Basic Considerations 21
3.2 Laser 22
3.3 Heat in Solids: Electronic and Lattice Dynamics 23

3.4 Laser-Material Interactions 27
3.4.1 Single Photon and Multi-Photon Processes 27
3.4.2 Laser Reflection and Absorption 28
3.4.3 Temperature Profiles 31
3.5 Phenomena Occurring on the Target Surface 35
3.5.1 Vaporization 35
3.5.2 Recondensation 36
3.5.3 Plasma Formation 37
3.5.4 Laser Supported Absorption Waves 39
3.6 Material Transport Phenomena 42
3.7 Conclusions 44
References 44

4 Laser–Plasma Interactions 49
Ion N. Mihailescu and Jörg Hermann
4.1 Introduction 49
4.2 Fundamentals of Laser–Plasma Interaction 50
4.3 Processes in Nanosecond Laser–Plasma Interactions 55
4.3.1 Laser-Induced Gas Breakdown 55
4.3.2 Plasma Shielding During Laser Material Processing 59
4.3.3 Laser-Supported Absorption Waves 63
4.3.4 Plasma Shutter for Optical Limitation 66
4.4 Plasma Interactions with Femtosecond Laser Pulses 69
4.4.1 Laser Beam Filamentation 69
4.4.2 Generation of XUV Radiation by Laser Plasma 75
4.4.3 Plasma Mirror 80
4.5 Conclusion 83
References 84

5 Laser Ablation and Thin Film Deposition 89
Christof W. Schneider and Thomas Lippert
5.1 Pulsed Laser Ablation 89
5.2 Lasers Used for Laser Ablation 91
5.3 Initial Ablation Processes and Plume Formation 92
5.3.1 Femtosecond Laser Irradiation 93
5.3.2 Nanosecond Laser Irradiation 93
5.4 Plume Expansion 94
5.4.1 Plume Expansion in Vacuum 94
5.4.2 Plume Expansion into a Background Gas 94
5.4.3 Imaging 95
5.4.4 Kinetic Energy of Plume Species 97
5.4.5 Thin Film Growth 98

5.5 Laser Ablation of Polymers 104
5.5.1 Ablation Mechanism 105
5.5.2 Polymer Film Ablation 106
5.5.3 Film Pattern Transfer 107
5.6 Conclusions 109
References 109

6 Processing with Ultrashort Laser Pulses 113
Jürgen Reif
6.1 Introduction and General Considerations 113
6.2 Laser-Material Coupling 114
6.2.1 Nonlinear Absorption 115
6.2.2 Hot Electron Generation 116
6.2.3 Incubation 116
6.2.4 Resolution Below the Diffraction Limit 117
6.3 Dissipation Dynamics 118
6.3.1 Dissipation Channels 118
6.3.2 Transient Material Modification 118
6.4 Desorption/Ablation 120
6.4.1 Concept 120
6.4.2 Applications 120
6.5 3-D Bulk Modifications, Waveguide Writing 122
6.5.1 Bulk Structuring, Waveguide Writing 123
6.5.2 Multiphoton Polymerization 123
6.6 Phase Transformation, Laser Annealing 124
6.7 Medical Applications 124
6.8 Nanostructures and Nanoparticles 124
6.9 Conclusions 126
References 126

7 Creating Nanostructures with Lasers 131
Paolo M. Ossi and Maria Dinescu
7.1 Introduction 132
7.2 Fundamentals 133
7.2.1 Plasma–Gas Interaction at Increasing Gas Pressure in ns PLD: Experiments and Modeling 133
7.2.2 Nanoparticle Synthesis 140
7.2.3 Controlled Deposition of 2D Nanoparticle Arrays: Self-Organization, Surface Topography, and Optical Properties 143
7.3 NP Formation in Femtosecond PLD: Experimental Results and Mechanisms 146
7.4 Applications 151
7.4.1 Direct Writing 152
7.4.2 Laser LIGA 152

7.4.3 Laser Etching 153
7.4.4 Pulsed Laser Deposition 154
7.4.5 Matrix-Assisted Pulsed Laser Evaporation (MAPLE) 160
7.4.6 Laser-Assisted Chemical Vapor Deposition (LA-CVD) 161
7.4.7 Lasers for MEMS (Micro-Electro-Mechanical Systems) 163
7.5 Concluding Remarks 163
References 165

8 Laser Micromachining 169
Jürgen Ihlemann
8.1 Basic Considerations 169
8.2 Processing Limits 169
8.3 Materials and Processes 171
8.3.1 Polymers 171
8.3.2 Glass 173
8.3.3 Ceramics 173
8.3.4 Metals 174
8.3.5 Layer Ablation 175
8.3.6 Indirect Ablation 176
8.4 Hole Drilling 178
8.5 Patterning of Thin Films 179
8.5.1 Dielectric Masks 179
8.5.2 Diffractive Optical Elements 180
8.6 Fabrication of Micro Optics and Micro Fluidics 181
8.6.1 Gratings 181
8.6.2 Micro Lenses 182
8.6.3 Micro Fluidics 183
8.7 Conclusions 184
References 185

9 Laser Processing Architecture for Improved Material Processing 189
Frank E. Livingston and Henry Helvajian
9.1 Laser Machining and Materials Processing 190
9.1.1 Introduction 190
9.1.2 Materials, Thermodynamic Properties, and Light/Matter Interaction 192
9.1.3 Photolytic Control: Conventional Approaches and Future Trends 193
9.1.4 Process Control 194
9.2 Laser Genotype Pulse Modulation Technique 196
9.2.1 Concept 196
9.2.2 Experimental Setup and Design 198
9.2.3 Performance Tests and Diagnostics 204

9.3 Selected Applications ... 211
9.3.1 Photosensitive Glass Ceramics: A Candidate Protean Material Class ... 211
9.3.2 Nanostructured Perovskite Thin-Films ... 215
9.4 Summary and Perspective ... 219
9.4.1 Laser Genotype Process Integration ... 219
9.4.2 Pulse Script Database: A Public Domain Catalog for Materials Processing ... 221
References ... 222

Index ... 225

Contributors

Ettore Carpene CNR-IFN, Dipartimento di Fisica, Politecnico di Milano, Piazza Leonardo da Vinci 32, 20133 Milano, Italy, ettore.carpene@fisi.polimi.it

Maria Dinescu Institute of Atomic Physics, National Institute for Lasers, Plasma and Radiation Physics, 409 Atomistilor Street, PO Box MG-16 Magurele, 077125 Bucharest, Romania, dinescum@ifin.nipne.ro

Henry Helvajian Micro/Nanotechnology Department, Space Materials Laboratory, The Aerospace Corporation, P.O. Box 92957, Los Angeles, CA 90009, USA, henry.helvajian@aero.org

Jörg Hermann Laboratoire Lasers, Plasmas et Procédés Photoniques, LP3 UMR 6182 CNRS - Université Aix-Marseille II, Campus de Luminy, Case 917, 13288 Marseille Cedex 9, France, hermann@lp3.univ-mrs.fr

Daniel Höche II. Institute of Physics/Atomic- and Nuclear Physics, University of Göttingen, Friedrich Hund Platz 1, 37077 Göttingen, Germany, dhoeche@uni-goettingen.de

Jürgen Ihlemann Laser-Laboratorium Göttingen e.V., Hans-Adolf-Krebs-Weg 1, 37077 Göttingen, Germany, juergen.ihlemann@llg-ev.de

Thomas Lippert Materials Group, General Energy Research Department, Paul Scherrer Institut, 5232 Villigen PSI, Switzerland, thomas.lippert@psi.ch

Frank E. Livingston Micro/Nanotechnology Department, Space Materials Laboratory, The Aerospace Corporation, P.O. Box 92957, Los Angeles, CA 90009, USA, Frank.E.Livingston@aero.org

Ion N. Mihailescu "Laser-Surface-Plasma Interactions" Laboratory, Lasers Department, National Institute for Lasers, Plasma and Radiation Physics, PO Box MG-54, 77125, Bucharest-Magurele, Romania, ion.mihailescu@inflpr.ro

Paolo M. Ossi Dipartimento di Energia, Politecnico di Milano, Via Ponzio 34/3, 20133 Milano, Italy, paolo.ossi@polimi.it

Jürgen Reif Lehrstuhl Experimentalphysik II/Materials Science, Brandenburgische Technische Universität Cottbus, Universitätsstrasse 1, 03046 Cottbus, Germany, reif@tu-cottbus.de

Peter Schaaf Department of Materials for Electronics, Institute of Materials Engineering and Institute of Micro- and Nanotechnologies, IMN MacroNano, Ilmenau University of Technology, POB 10 05 65, 98684 Ilmenau, Germany, peter.schaaf@tu-ilmenau.de

Christof W. Schneider Materials Group, General Energy Research Department, Paul Scherrer Institut, 5232 Villigen PSI, Switzerland, christof.schneider@psi.ch

Michelle Shinn Free Electron Laser Division, Thomas Jefferson National Accelerator Facility, Newport News, VA 23606, USA, shinn@jlab.org

Chapter 1
Introduction

Peter Schaaf

In recent years, laser based technologies became important or even dominant in industrial applications such as welding or cutting. Further possibilities of processing, innovation, and advancement of laser material treatments are still in progress and very challenging. Laser-based analysis [1], spectroscopy [2], or metrology [3] are well known and established methods. For this field of research, a number of reviews, books, and other literature were published in order to give detailed descriptions of laser based physics [4]. The very broad field of laser materials processing [5, 6] is still very fast developing.

The primary goal of this book is to give a detailed insight into current research topics of this part of laser technology, especially in the field of laser processing of materials in high-tech applications.

The basics of lasers and laser optics, the fundamentals of laser material interactions, and their application for demanding applications are described. The first part of the book gives an introduction to the physics of lasers and laser optics, laser radiation interaction with materials and the effects occurring as a result of such irradiations. Chapter 2 will explain the basics of lasers, its spatial and temporal shaping, and of course the optical transport. New requirements and demands of light sources, their possibilities, and the status quo of laser based research will be instructed. In Chap. 3, a detailed description of laser-material interaction is given. Basics of electromagnetic wave propagation, absorption, etc., will be discussed. Different interaction time regimes will be explained according to the actual state of theory. Effects like vaporization, transfer of heat, and material will be considered as a result of irradiation. Then Chap. 4 deals with the interaction of laser light with plasmas. Fundamentals of plasma physics and their relationship to laser radiation will be explained. Laser induced breakdown will be given the main attention. Plasma

P. Schaaf
Ilmenau University of Technology, Institute of Materials Engineering and Institute of Micro- and Nanotechnologies MacroNano, Department of Materials for Electronics, POB 100565, 98684 Ilmenau, Germany
e-mail: peter.schaaf@tu-ilmenau.de

effects will be related to different time regimes and an insight into their applications for technology is given.

The next part of the book will give an overview about current research topics and the state-of-the-art in materials processing. Achievements in nanostructuring or in film depositing will be shown, including current trends and developments of methods. Further, future applications and their importance for medicine, biotechnology and nanotechnology will be discussed.

A huge field of interest is Pulsed Laser Deposition and its possibilities [7]. Chapter 5 gives an insight into the method and its involved physics. Basics of ablation will be discussed and the resulting plasma plume expansion into different ambients, too. Energy balances will be related to thin film growth and their properties. The growth behavior gets widely discussed for different materials like metals or polymers. In Chap. 6, a detailed instruction into processing with ultrashort laser pulses is given. Actual developments in this field are, for example, treatment of transparent materials [8]. On the femtosecond timescale, nonlinear and non-thermal effects determine the processing. This offers new possibilities in research and for industrial applications.

Typically, surface structuring is one of the most famous application fields in laser based technology. Chapter 7 shows the scope of creating nanostructures by means of laser irradiation. Nanoparticle generation and its limitations will be explained and related to selforganizing processes. Typical examples for structuring of glass are discussed in [9, 10]. Established techniques like direct writing (nice example [11]) or laser etching will be discussed extensively.

Laser microprocessing will be discussed in Chap. 8. In the literature, this subject has been widely discussed [12, 13]. The miniaturization in every kind of application field is still in progress. Here, a discussion of laser treatment of several materials will be given. Process limits in microstructuring of, for example, glasses and ceramics will be explained. A nice example for structuring polymers is shown in [14]. Another area of interest is the micro optic. In [15, 16], the developments in this technique are explained. Further, classical applications like drilling will be reviewed in relation to scaling and efficiency.

For the improvement of several laser based methods, sometimes, new beam parameters are necessary. Chapter 9 tries to depict the trends and the aim of shaping laser radiation. In recent works [17, 18], tailoring of laser pulses in spatial and temporal distribution is shown. The chapter discusses the problem of modulation and of controlling the process. At last, first applications will be shown, followed by future ideas.

Altogether, the book contains the state-of-the art in laser materials microprocessing. The authors of the chapters are specialists in their fields and have tried to explain the achievements in their subject on an up-to-date scientific level. Therefore, the book can be assumed to be a reference work for advanced laser materials processing for a long time.

Acknowledgements All contributors are gratefully acknowledged for their cooperative efforts in setting up an interesting book, covering latest topics of their research. Also, the Springer team is acknowledged for their help in finalising the book in an attractive manner.

References

1. A. Miziolek, V. Palleschi, I. Schechter, *Laser Induced Breakdown Spectroscopy.* (Cambridge University Press, Cambridge, 2006)
2. A. Corney, *Atomic and Laser Spectroscopy.* (Oxford University Press, USA, 2006)
3. D. Williams, J. Briers, *Optical Methods in Engineering Metrology.* (Chapman & Hall, London, 1993)
4. Y. Shen, *The Principles of Nonlinear Optics*. (Wiley-Interscience, New York, 1984)
5. M. Von Allmen, A. Blatter, *Laser-Beam Interactions with Materials: Physical Principles and Applications.* (Springer, New York, 1995)
6. D. Bäuerle, *Laser Processing and Chemistry.* (Springer, Berlin, 2000)
7. R. Eason, *Pulsed Laser Deposition of Thin Films: Applications-led Growth of Functional Materials.* (Wiley-Interscience, Chichester, 2007)
8. R.R. Gattass, E. Mazur, Nat. Photon. **2**(4), 219 (2008)
9. R. Taylor, C. Hnatovsky, E. Simova, Laser Photon. Rev. **2** (2008)
10. H. Niino, Y. Kawaguchi, T. Sato, A. Narazaki, T. Gumpenberger, R. Kurosaki, J. Laser Micro/Nanoeng. **1**(1), 39 (2006)
11. W. Yang, P.G. Kazansky, Y.P. Svirko, Nat. Photon. **2**(2), 99 (2008)
12. A. Gillner, Laser Techn. J. **4**(1), 21 (2007)
13. A. Gillner, Laser Techn. J. **5**(1) (2008)
14. C. Aguilar, Y. Lu, S. Mao, S. Chen, Biomaterials **26**(36), 7642 (2005)
15. M. Aeschlimann, M. Bauer, D. Bayer, T. Brixner, F. de Abajo, W. Pfeiffer, M. Rohmer, C. Spindler, F. Steeb, Nature **446**(7133), 301 (2007)
16. E. Mcleod, C.B. Arnold, Nat. Nanotechnol. **3**(7), 413 (2008)
17. F. Livingston, L. Steffeney, H. Helvajian, Appl. Surf. Sci. **253**(19), 8015 (2007)
18. S. Bielawski, C. Evain, T. Hara, M. Hosaka, M. Katoh, S. Kimura, A. Mochihashi, M. Shimada, C. Szwaj, T. Takahashi, Nat. Phys. **4**(5), 390 (2008)

Chapter 2
Basics of Lasers and Laser Optics

Michelle Shinn

Abstract The purpose of this chapter is to introduce the entering professional or graduate student to the basics of laser physics and optics. I start with the various types of lasers, some rather exotic, and the ever-increasing span of wavelengths that has resulted since the laser's invention in 1960. I then discuss typical techniques as well as the "rules of thumb" used to transport and manipulate the laser output so it can be used for materials processing. The chapter concludes with a discussion of laser damage, as these physical processes limit the ability to transport and manipulate high intensity beams.

2.1 Introduction

When this book is published, the laser will be just months from the 50th anniversary of its first demonstration on May 16, 1960. That first laser operated in millisecond long bursts at 694 nm [1]. Since then, lasers have operated with wavelengths spanning mm to angstroms, and were found to occur naturally in the atmospheres of Mars and other planets [2]. In this section, we touch briefly on the optical arrangement that makes laser action possible, then discuss how this enables lasers to span such an enormous spectral range. While some spectral ranges may seem less amenable to use in a laser processing application than others, one never knows what future opportunities might yet arise.

2.2 Optical Processes

Quantum mechanics has been quite successful in explaining the absorption and emission of light in atomic systems, no matter what state of matter they find themselves in. Bound states exist due to the behavior of electrons moving in the central

M. Shinn
Free Electron Laser Division, Thomas Jefferson National Accelerator Facility,
Newport News, VA, USA
e-mail: shinn@jlab.org

potential of the nucleus, *modulo* perturbations due to the bonding of atoms to one another, as in the case of liquids and solids [3–5]. Electrons transitioning between states do so through several processes, namely through stimulated absorption from one state to a more energetic state, followed by spontaneous emission, and, as will be explained shortly, stimulated emission from this higher state to the same, or another, lower state. Absorption and spontaneous emission occur around us all the time, because these are processes that occur in systems in thermal equilibrium, e.g., the emission of photons from an incandescent light. Stimulated emission requires that more electrons be in the upper, or excited state than the state they will transition to. This is known as population inversion. Population inversion requires energy in excess of that provided by thermal equilibrium, e.g., a laser diode pumping an energy level in a laser crystal. It is the EM field from the photons whose energy matches the transition energy of the excited electrons in the vicinity that stimulates them to emit coherently. As the field propagates through the excited ensemble of electrons, the field grows exponentially stronger. For laser action to occur, the gain per pass through the system must be greater than the loss. The population inversion process has been diagrammed in many publications, the reader is referred to Figs. 1.21, 1.27, and 1.28 in [3].

In many cases, particularly in systems where the gain for each pass through the medium is low, mirrors are used. One mirror is as completely reflective as practical, with the value R_{HR}, the other is a partially transmissive (typical reflectivities are in the range 70–99%), with the value R_{OC} and is known as the outcoupler. This is the configuration one generally conjurs up when thinking of a laser; and this configuration is shown in Fig. 2.1.

The threshold condition for laser oscillation occurs when the gain per unit length g for each pass just equals the loss (absorption, scattering, etc.) per unit length α:

$$R_{HR} R_{OC} = \exp(g - \alpha)2l = 1 \tag{2.1}$$

Where l is the length of the gain region. Different arrangements of these mirrors are used to create a resonant EM field that selects and provides positive feedback to the stimulating field. On the early passes through the gain medium, the number of photons increases exponentially, as expressed in (2.1). This is called the small signal regime. However, the stimulating field increases the stimulated emission rate to the point that the upper level population becomes depleted at exactly the excitation rate. At this point, the gain and loss become equivalent, and the gain is said to be saturated and in most cases is equal to the transmission of the outcoupling mirror. A discussion of optical resonators is given in [3, 5, 6].

Fig. 2.1 The laser resonator configuration

A pumped gain medium without mirrors still undergoes stimulated and spontaneous emission. Without further intervention, such a system would emit in all directions, at a rate sufficient to bring the populations in the lower and upper states to equilibrium. But, if one unidirectionally introduces light in resonance with the energy difference, stimulated emission amplifies the light as it traverses the medium. The pumped gain medium is termed a laser amplifier. For decades, systems composed of the exciting laser oscillator pumping the laser amplifiers have been used to achieve output powers unachievable using just an oscillator. Systems as small as erbium doped fiber amplifers (EDFA) are used in fiber optic communications systems to extend the distance between repeater stations [7, 8]. On the other end of the scale, the National Ignition Facility (NIF) starts with an injected energy of 0.75 nJ and amplifies it to over 1 MJ [9].

However, in systems with sufficient gain, it is possible to obtain laser emission without the use of an optical cavity. This phenomena, termed self-amplified stimulated emission (SASE) makes lasers possible at wavelengths where laser resonators can not easily be constructed, such as the soft X-ray spectral region (sub 5 nm). Table-top realizations of such systems were demonstrated in 1994 by J.J. Rocca and a coworkers [12], who demonstrated lasing at 46.9 nm by creating a long capillary discharge in Ne gas. A schematic of this system is shown in Fig. 2.2.

The region termed the laser channel in the figure contains a region of highly excited Ar ions in a highly inverted population. Spontaneous emission from the region near the switch is amplified by the confined region of the discharge, and amplified as they traverse it. Using the same principles, but with a different gas, the same group has produced a laser emitting at 13.9 nm.

Other techniques for achieving laser emission in the soft X-ray region include laser ablation and high harmonic generation (HHG) in gases. These are discussed in more detail in Chap. 4. While one might consider such wavelengths irrelevant for laser processing applications, consider the fact that the shorter the wavelength, the smaller the spot at focus, and, as discussed in later chapters, processing need

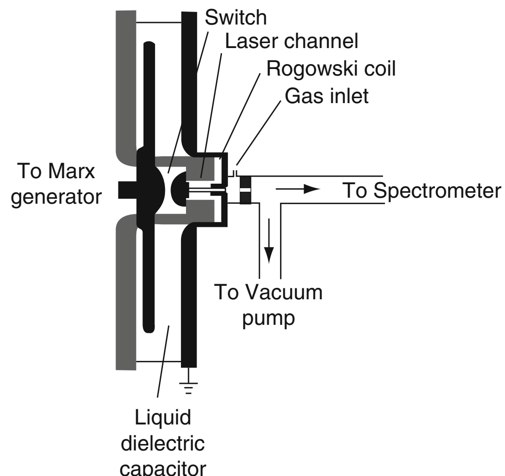

Fig. 2.2 Schematic diagram of the capillary discharge setup used to obtain saturated amplification of the 46.9 nm line of Ne-like Ar from Rocca et al. [10–12]

not be ablative, it can also be physicochemical. Thus, these soft X-ray lasers open possibilities for lithography and even ablative processes [13].

2.3 Time Dependence

So far we have concentrated on the interplay of the three electronic processes, absorption, spontaneous emission, and stimulated emission, to explain the lasing process, without regard to the time dependence of the laser output. So long as there is a population inversion that provides sufficient gain to overcome losses laser action will occur. But it is possible to introduce a time dependence on the laser output, and this greatly expands laser's increasingly important role in both the sciences and technology, so they deserve a brief mention. More lengthy (and excellent) discussions are found in [3, 6].

2.3.1 Q-Switching

In atomic systems where the lifetime of the upper state (the inverse of the spontaneous emission rate) is relatively long, of order 100 μs or more, it is then possible to let the population build by suppressing stimulated emission until the population saturates. At that time, the suppressant is removed and stimulated emission begins. Since the upper state population is so much larger than it would have been otherwise, the rate is much higher and a larger percentage of the population suddenly transitions to the lower state. The output, rather than being continuous, becomes a brief burst, the duration of the burst being dependent on the technology used to create, then remove the stimulated emission suppressant. Resonant cavities have a quality factor Q rigorously defined as the ratio of energy stored to power dissipated per unit angular frequency. However, we will take the more common approach of defining the laser cavity Q as the ratio of the mirror reflectivities:

$$Q = \frac{R_{\mathrm{HR}}}{R_{\mathrm{OC}}} \approx \frac{1}{R_{\mathrm{OC}}} \tag{2.2}$$

Since the reflectivity of the HR mirror is so close to 1, the approximation to unity is quite good. So, the cavity Q typically ranges from 3 to 100. When the suppressor is active, the Q is essentially infinite. The device that changes the cavity is called a Q switch, and the phenomena, once called *giant pulsing*, is now called Q-switching. A schematic representation of the phenomena is shown in Fig. 26.1 from [3].

Typically, the pulselength of Q-switched pulses is of the order 10 ns. As much of the upper level population is depleted in a very short time, peak power can be several orders of magnitude greater than the average power.

2.3.2 Mode-Locking

In any laser system in a resonator configuration, as opposed to one that operates via SASE, there are a number of longitudinal modes, analogous to the tones on a plucked string, that satisfy the round trip condition. As the resonator length is short, relative to the distance traveled by light in a second, a great number of closely-spaced longitudinal modes exist in a laser resonator. Mode selection occurs to some extent by the spectral width, and hence the frequency span over which there is sufficient gain. If one sets the cavity length of the resonator very accurately (to within microns) of that required to support the longitudinal mode so it precisely fulfills the requirement that:

$$f = \frac{c}{2L} \tag{2.3}$$

Then this one mode predominates. The resonator, instead of producing a cw (time independent) output, produces a continuous train of short pulses. Pulse widths ranging from a few ps to 100 ps have been demonstrated, with repetition rates ranging from 10's of MHz to GHz. While these lasers have generally been used in scientific applications, there are material processing applications as well.

2.3.3 Ultrashort Pulse Generation

The quest to understand the details of electronic excitation and de-excitation has driven the laser technology for producing ultrashort (less than 1 ps) pulse lengths. This is due to the fact that the timescales for these processes can be as short as some 10's of femtoseconds. In order to create laser pulses of such short duration, modulation of the cavity population is sometimes done using mode-locking. In addition, ultrashort pulses can only be generated by materials that have a sufficiently wide spectral (and thus frequency) bandwidth. This is because the time-bandwidth product satisfies the equation:

$$\Delta\tau\Delta\nu = \text{const} \tag{2.4}$$

The value for the constant depends on the lineshape, for most ultrafast solid state lasers it is 0.33. The original technique for producing ultrashort pulses, colliding pulse amplification (CPA) has been largely replaced by Kerr lens mode-locking (KLM), and the reader should consult [14] for more information.

2.3.4 Harmonic Generation

When short (fs-ns) laser pulses are focused sufficiently to create high intensities (typically $>10^8$ W/cm^2) in materials, the electric field strengths (in V/m) become so great that nonlinearities in material properties emerge. Chief among them is the

index of refraction, n. Thought a constant of the material, and a manifestation its bonding, at high intensity, nonlinear terms become evident. One that is exploited is that of harmonic generation, where light of some frequency (expressed as ω) is focused into a material and some of this light is converted to higher frequencies, either 2ω or 3ω, depending on the material. These can then be focused into other materials to generate 4ω, 5ω, etc., although the efficiency drops rapidly, so typically only these harmonics are generated. While these nonlinearities can be created in the appropriate gases, liquids, or solids, from a practical, and sustainable point of view, solids are preferable and the norm. A good review of the processes and applications may be found in [6].

2.4 Free-Electron Lasers

So far we have discussed lasers based on bound electron systems. It is possible to have laser action using an ensemble of free electrons. At first blush, elementary quantum mechanics would lead one to think that since a free electron has a continuous set of energy levels to choose from, there is no upper or lower energy level to transition between. As we will see below, it is possible to create such a pair of states. What is notionally correct, based on elementary quantum theory is that one can set the transition energy over an enormous range. Laser action has been demonstrated at millimeter wavelengths to as short as 6.5 nm (at this time), with plans to operate at a scientific user facility at 0.15 nm in the next couple of years. Since these lasers use free electrons, they are called free-electron lasers (FEL).

The first FEL was operated at 3.4 μm in 1976 [15]. A recent review of FELs is found in [16]. A schematic view of an FEL, using superconducting linear accelerator technology to achieve high average power, is shown in Fig. 2.3.

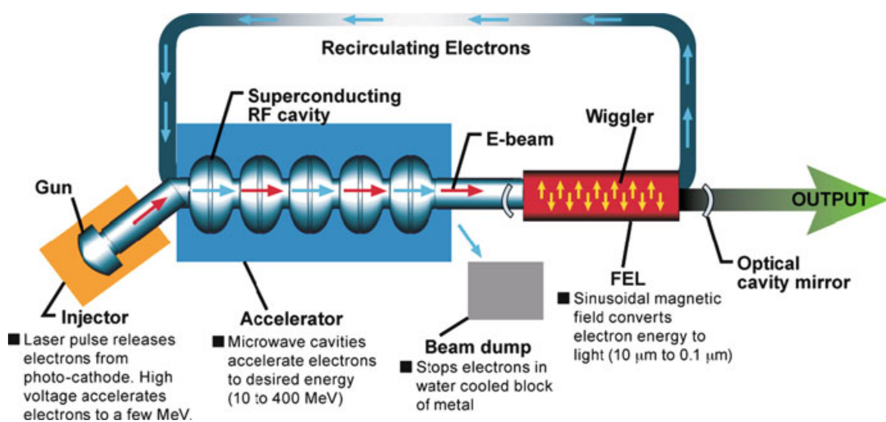

Fig. 2.3 Schematic diagram of a free-electron lasers (FEL) (courtesy Jefferson Lab)

As shown in the figure, bunches of free electrons (the charge per bunch is in the range of 10's of pC to about a nC) are accelerated to relativistic speeds and enter a structure known as a "wiggler", a periodically-spaced arrangement of magnets. As the electron's trajectory oscillates, they radiate through the well-known phenomenon of synchrotron radiation [17]. This radiation interacts with the magnetic field of the wiggler to form a ponderomotive wave, which appears at rest with respect to the electrons. The electrons bunch in the troughs of this wave, and form energy levels. There is a natural population inversion, as the electrons have a lot of kinetic energy. The photons that are present from spontaneous emission serve as the seed for stimulating emission from the electrons. Each bunch is separated by one wavelength from the adjacent bunch, so the light adds coherently.

As described, this arrangement has gain. In most cases, the gain is low for each pass through the wiggler, so mirrors are used to form a resonator, as shown in Fig. 2.3. This raises the stimulating field, or thinking in terms of photons, the flux, which increases the gain. However, the gain enhancement only occurs if the photons produced by a previous electron bunch arrive in time to stimulate a fresh electron bunch in the wiggler. Thus, the optical cavity length must be precisely set, to within a few microns, so the following equation is satisfied:

$$L = \frac{nc}{2f} \tag{2.5}$$

Where f is the electron bunch frequency, and $n = 1, 2, 3, \ldots$ to allow for longer cavity lengths that are also in synchronism [18].

With the enhancement provided by the resonant cavity, small signal gains of the order of 10's to over 100% per pass can be achieved with short wigglers of a couple of meters length, or less. With a superconducting radiofrequency (SRF) linac, it is possible to continuously produce fresh bunches of electrons, so the output power can be quite high. At the Thomas Jefferson National Accelerator Facility, we have produced over 14 kW of average power at 1.61 μm, and kilowatt levels of power through the near-IR to mid-IR spectral range [18]. A schematic depiction of this machine is shown in Fig. 2.4. These machines are always big, typically many 10's of meters in length, so they tend to be installed as part of multiuser facilities. At present, there are over a dozen of such facilities around the world. Given the wavelength flexibility of FELs, there has been a growing trend to build them to produce X-rays. The proper electron bunch parameters and the use of longer wigglers allow the gain through the wiggler to reach many orders of magnitude, typically 10^3–10^7. In these cases, lasing of the SASE type occurs. This is how the 6.5 nm laser was produced [19].

With high repetition rates (MHz), ultrashort pulse lengths, and tunable wavelength output, FELs are being used in science and technology to answer questions in the fields of medicine, materials research, and as a tool for materials processing. It is not clear whether stand alone facilities for materials processing will be built solely for materials processing, but clearly it has the ability to map out a parameter space in order to optimize a process [20, 21].

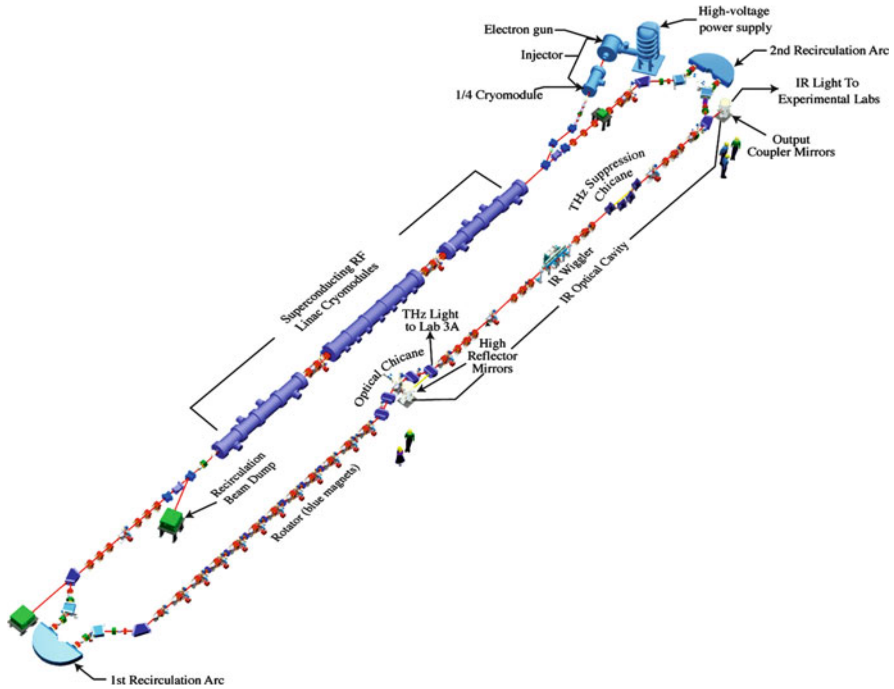

Fig. 2.4 Schematic layout of the FEL at the Thomas Jefferson National Accelerator Facility (USA)

2.5 Laser Optics

A laser without optics to transport and condition the beam to meet the goals of the experiment or process is like having an automobile engine without the transmission and tires necessary to use it; it may deliver impressive performance, but not be too useful. The light emitted from the laser naturally has a divergence set by the radius of the source, the properties of the outcoupler mirror, and the wavelength. Left to freely propagate to the plane of interest, the irradiance (in W/cm^2) or fluence (in J/cm^2) will probably not be sufficient. Hence, the user must place intervening optics to correct for the divergence and any pathlength requirements imposed by the space available, then condition the beam to achieve the desired beam conditions at the surface being irradiated, as diagramed in Fig. 2.6. This section discusses the basic optics required to achieve simple beam propagation and conditioning, subsequent sections treat more recent and complicated means for beam conditioning. This has been well-covered elsewhere, so in my treatment, I will tend to emphasize the tricks of the trade (Fig. 2.5).

Fig. 2.5 Generic diagram of a laser and its optical system

2.5.1 Optical Propagation

When thinking about how to design an optical transport system or to optimize one you have acquired, there are two ways to come to an answer; using geometrical optics, or by using physical optics. Geometrical optics treats light as traveling in rays and as these rays propagate, they are manipulated by optical elements such as lenses in precise ways, and from a starting point, known as the object, one propagates to an image, which can be either at a particular point or plane in space. Geometrical optics works well when thinking how to first set up an optical system as it directly addresses the spacing of optical elements. It does not handle the very real (and obvious when using a laser source) ramifications of the wave nature of light, such as diffraction and interference. To properly treat these cases, one moves into physical optics, which treats light as being composed of electromagnetic waves. The mathematical treatment of light propagation is more complicated than that employed for geometrical optics, but it has great validity when considering the size of optical elements, and on the diameter of the final image, as I will discuss later.

While there are a number of formulae relating to geometrical optics, only a few are needed for most applications. For an optical system with a net focal length f, a distance from the source to the focal plane o (object distance), and a distance from the focal plane to the target i (image distance)

$$\frac{1}{f} = \frac{1}{o} + \frac{1}{i} \tag{2.6}$$

There is a sign convention for focal lengths and the object and images distances. These are covered in detail in elementary physics and optics textbooks [22–24]. These references also explain and have examples on how to solve for the image position when using a combination of lenses and mirrors. Or, one can use optical modeling software, which will be discussed later in this chapter.

The laser manufacturer typically specifies the output diameter, which we will define as 2ω, where ω is the beam radius measured at the $1/e^2$ point (in either irradiance or fluence) as well as the divergence θ. It is important to note whether the divergence is the full angle or half-angle, there is no standard. This is the source point in the calculations done either analytically, or by using optical modeling software. From this information, one can calculate the beam diameter at the first optical element, and on through the system. This brings us to an important consequence of physical optics, the size of the optical elements.

2.5.2 Sizing Optical Elements and Other Tricks of the Trade

A premise of physical optics is that the waves traveling away from the source are smoothly-varying functions in both space and time. Hence, if the beam is "too big" when it intercepts an optical element, the wavefront will be truncated (clipped is the vernacular term). While the effects of this truncation are subtle while the beam is relatively large in extent, when brought to a focus, one will see intensity fringes within and surrounding the central spot. It is surprising just how little of the clear aperture of the optic can be filled before these effects become apparent. As discussed in detail in [3], to be assured of minimum fringing it is best to have the clear aperture of the optic be about four times the beam radius. This "4ω" criterion will transmit 99.96% of the incident power and have about 1.1% of the power in the fringes when brought to focus. As tempting as it might be to let the beam fill more of the aperture (especially when trying to save money), consider what happens if you use a $\pi\omega$ criterion. While the transmission remains high, 99%, now 17% of the power has been moved into the diffraction fringes. This can be a serious problem if you are trying to remove material in the smallest area, as the diffraction ripple causes uneven ablation and prevents the laser from focusing to the smallest spot, as "Airy rings" around the central lobe can also induce ablation. Another factor impacting final image quality is the orientation of lenses in the beam path. One learns in an optics class that the "principle of reversibility" states that rays of light will trace the same path through an optic independent of direction. However, with optics made to some wavefront tolerance (e.g., $\lambda/10$), there is a difference. In general, it is best to place the curved surface of the optic toward the beam path, if the beam is collimated (object at infinity). An exception to this rule is when a high power; especially high peak power laser beam is incident on a concave surface. The concave surface forms a virtual image before it, and the intensity can become high enough that you get breakdown of the air at the focal point. If that focal point happens to lie on or within another optical element, you can damage that element.

Finally, always check the optics you buy, at least for focal length. Vendors state a precision in their specs, but production parts are checked at the level of a percent or so, and parts with 5% error can easily pass inspection. If one is tightly tolerancing their optical beam train, some care to confirm the optical elements meet specifications will ensure that the desired performance is obtained.

2.5.3 Fiber Optics

No discussion of laser transmission is complete without at least a passing reference to fiber optics. As the name implies, rather than propagating a laser through free space, the beam is propagated down a thin (about 5 μm to 1 mm) fiber, usually made of fused silica glass. The size of the fiber is chosen for the application – a bundle of fibers will carry more power than a single fiber, but the divergence of the output will suffer due to the fact that without some effort, the individual

beams are not coherently locked in phase to one another. For cw laser systems in the kW class, transmission with fiber optics is the norm, particularly in industrial installations, as there are fewer surfaces to become contaminated or misaligned. For pulsed systems, particularly when the pulselength is in the 100's of femtoseconds and shorter, fiber optics need to be carefully chosen or avoided entirely. The dimensionally-constrained environment in the fiber raises the electric field (and hence, the intensity) within it, and short pulses can easily push this field to the damage limit (see the following section on this phenomena). For femtosecond pulses, the fiber's dispersion (index variation with wavelength) can result in undesirable pulse lengthening. For more detail, the reader should consult [25].

2.5.4 Managing Diffraction

The previous discussion on the deleterious role that aperturing of laser beams has on beam properties might lead one to believe that diffraction is to be avoided at all cost. However, diffraction can be tailored to shape the beam's intensity profile to enhance the processing effectiveness. Consider the fact that the low order transverse mode output of a laser usually results in a Gaussian output. If the laser is multimode, the output is at least smoothly-varying, with the maximum intensity at the center. In most cases, this is not the most efficient beam profile to ablatively remove material, because the wings of the beam profile do not deposit enough power into the material to heat it to vaporization. At best, it has wasted power, at worst, it creates a heat-affected zone around the region being processed. The best way to avoid this is to reshape the beam profile from a gaussian to a flat-top, where the power is constant with respect to the beam radius to a certain diameter, then falls quickly to zero. There are several ways to obtain this profile, one is with aspheric lenses, the other way is with holographic optical elements (HOE) sometimes called diffractive optical elements (DOE). We will examine both.

2.5.5 The Aspheric Lens Beamshaper

A common arrangement of two spherical optical elements, planoconvex and planoconcave lenses, can be arranged to form a Galilean telescope. This arrangement is shown in Fig. 2.6. The Galilean telescope takes a collimated beam (object distance at infinity) and either expands or condenses it by an amount equal to the ratio of the focal distances.

However, this leaves the beam's intensity profile unchanged, a Gaussian profile remains Gaussian. If one uses aspheric lenses, the telescope becomes a beam shaper as well, either expanding or condensing the beam and converting the Gaussian profile to a flat top. First published by B. Frieden in 1965 [26], it was little noticed until

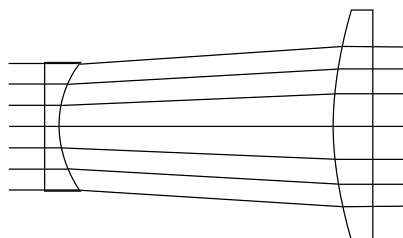

Fig. 2.6 A Galilean telescope. Collimated light entering from the *left* leaves the telescope on the *right* magnified by the ratio of the focal lengths

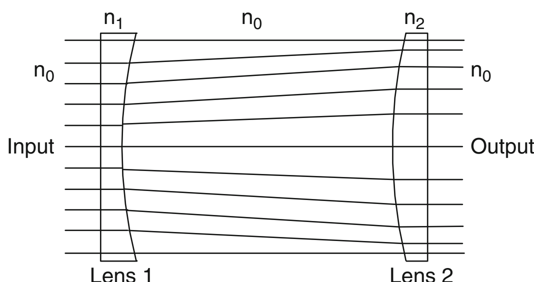

Fig. 2.7 Design of a two-element beam shaper (from [28])

the early years of this century [27] and can now be purchased from several optics manufacturers in the USA and Europe.

These designs (Fig. 2.7) require careful alignment of the beam shaper with respect to the input beam, e.g., about 100 rad angular and $<50\,\mu$m in linear misalignment, necessitating the use of lasers able to deliver a very stable input – these include fiber lasers and laser diode-pumped laser systems.

2.5.6 Holographic Optical Elements

Another way to shape a beam so as to give the user a far larger set of patterns to choose from is to use (or have fabricated) a HOE. As the name implies, these elements are computer designed for a particular laser wavelength and set of beam parameters, then holographically patterned. An advantage of a HOE over a beam shaper is the relatively small size; an HOE usually looks like a rather thin substrate with a characteristic spectrum of colors when a light source is viewed in reflection. A disadvantage (partially shared by the beam shaper) is the sensitivity to beam parameters and angle.

Having covered how to shape and transmit a laser's output to the target, we now turn to the final optics used to adjust the irradiance to the desired value. Since the irradiance through the transport must be low enough to not damage the transport optics, it is the final optics that have the task to bring the irradiance to the desired high value. The choice of the final optics is dictated by the geometry of the processing site. Two geometries are common, as shown in Fig. 2.8, either a moving beam or a moving target.

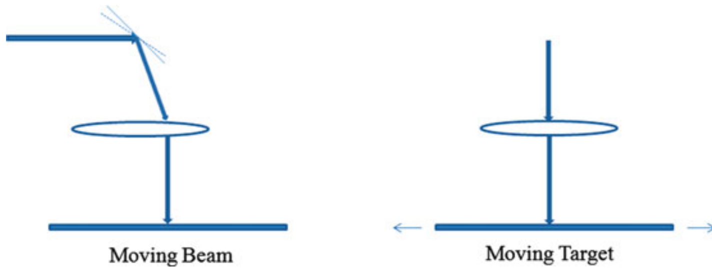

Fig. 2.8 Two common laser processing target geometries

In the moving beam geometry, the f-theta lens is used. This optical system produces a focus at the target plane even though the angle of incidence of the beam is changing. In the case of the moving target, the lens system may be as simple as a planoconvex lens, or as complicated as the lenses used in UV lithography, which may number as many as 20 elements. These lenses are now augmented with a fluid placed between the lens and the target – the nonunity index of refraction effectively makes the wavelength shorter by 30–40%, thus creating a tighter focus.

2.5.7 Laser Damage

Since this text treats the latest aspects of laser material processing, it is given that lasers, used properly, will damage and ablate material. But what about those cases when apparently transparent media, the optical elements the beam traverses, suddenly fails? What are the causes? Since it was first observed in the 1960s, laser damage, the irreversible change in the optical properties (be they reflectance, transmission, etc.) has been studied, and over the years both measurements and models have advanced our understanding of the mechanisms that cause it. An annual conference devoted to the topic has been held in Boulder, Colorado, since 1969 and the proceedings of these conferences are available [29,30]. There is a good summary on the subject in [5]. The underlying mechanisms for laser damage depend on whether the source is pulsed or cw (or quasi-cw) and whether the duration of the pulse is less than about 10 ps or not. In general, laser damage occurs because either an absorbing defect raised its temperature above the melting point, or a flaw, be it a pit, scratch, embedded nodule of the coating or polishing material results in a local increase of the E-field intensity to the level that a few free electrons are accelerated to the point that they impact and free other electrons. The free electron population increases to a level that the region becomes absorbing enough to melt and/or vaporize the immediate defect and its surroundings. This is known as the electron avalanche process. Ultrashort pulses cause laser damage in a slightly different manner. The E-field is sufficiently high that multiphoton absorption occurs, promoting electrons to the conduction band so they are free to move and collisionally promote other electrons to

the conduction band. This impact ionization continues until the population is high enough that the material becomes absorbing and damages as the material vaporizes. Note the subtle difference—longer pulses require some free electrons, which may or may not be present at the location the laser strikes, whereas ultrashort pulses al-ways make them. Consequently, while long pulse damage is stochastic in nature, ultrashort laser damage is deterministic. Moving from general comments about damage mechanisms to more specific comments on how to prevent damage, doing all that one can to minimize the introduction of contaminants on optical surfaces will raise the damage threshold of a given optical element. Handling should be done with gloved hands and speaking should be kept to a minimum (or, wear a face mask). If the surfaces are observed to be contaminated, one can attempt to remove the contaminant with "canned air" or with a solvent like isopropal alcohol or acetone and lens tissue. A thorough discussion of cleaning techniques and their efficacy is in [31]. Depending on the irradiance (if the laser output is cw or quasi-cw) or fluence (if pulsed), surface quality is important. Surface quality is still generally defined by "scratch-dig" values, these have an advantage for the optics fabrication shop, but at best are semiquantitative. Generally, a scratch-dig value of 20-10 is sufficient for cw lasers, while 10-5 is necessary for ns pulsed lasers. Of course, in any optical transport system the optics will be coated, and one can increase the damage threshold by choosing the type of coating deposition technique that works best for the time structure of the laser system. For long-pulsed (>few ns duration), electron beam deposited films are best, for cw or quasi-cw lasers, ion beam deposited films perform better. Having touched on the "why" laser damage occurs, we turn now to the how to design an optical system that would not damage. Over time experimenters desired to have a standard for determining laser-induced damage thresholds (LIDT) values, the testing procedures are given in ISO 11254. A recent summary of current LIDT values was recently published [32], Tables 2.1 and 2.2 summarize the values presented in this paper.

LIDT values are different for other substrates. An excellent discussion and data are presented in [5].

Table 2.1 CW laser-induced damage thresholds for high reflectors as a function of spot size and wavelength [31]

	30–50 μm	100 μm	>5 mm
0.55 μm	>1 MW/cm^2	>500 kW/cm^2	25 kW/cm^2
1–2 μm	50–200 MW/cm^2	10 MW/cm^2	75 kW/cm^2

Table 2.2 Pulsed laser-induced damage thresholds for different coating applications as a function of pulse duration at 1,064 nm for IBS films on fused silica substrates [31]

	1 ps	10 ps	10 ns
AR	–	–	>18 J/cm^2
Brewster angle polarizer	–	–	>20 J/cm^2
HR	>2.5 J/cm^2	>8.5 J/cm^2	>20 J/cm^2

2.5.8 Optical Modeling Software

Throughout this chapter, we have relied on relatively straightforward examples that are amenable to analytical solutions. For actual laser and transport system design, this is more often than not too simplistic or too tedious to contemplate. The coherence of laser sources is actually an asset when it comes to calculations, but also drives the designer to eschew the typical ray-tracing design packages, in favor of software designed for physical optics (see Sect. 2.6) which properly treat diffraction from the edges of optical elements or other physical apertures. Of the various software packages available, three that I typically use are Paraxia™ [33], GLAD™ [34], and OPC [35]. The first two software packages are commercial products while the last is offered for free, noncommercial use. Paraxia has the advantage of an easy, graphical interface, and the ability to "drop and drag" optical and free space elements into place. It does not have a way to incorporate gain regions. The other two software packages use scripting languages to construct the optical system, although one of my students has been developing a "user friendly" graphical front end to OPC, known as the Jefferson Lab Interactive Front End (JLIFE) which is under development [36]. GLAD, an acronym for General Laser Analysis and Design, has commands that incorporate atmospheric and optical aberrations, OPC, an acronym for Optical Propagation Code, both allow gain regions; the former can simulate the gain from solid state or gas lasers, the latter is particularly good at treating free-electron laser gain. For examples of the Paraxia or GLAD interfaces, consult the software creator's websites shown in [33, 34].

2.6 Conclusions

In this chapter, I have attempted to acquaint the reader with both conventional and emerging laser sources. Fiber lasers and laser diodes create robust and easy-to-use sources in the near infrared, while FELs offer the opportunity to exploit material properties with power at wavelengths where conventional sources are not available. In the chapters that follow, the applications of lasers are discussed in more detail.

Acknowledgements I wish to acknowledge my colleagues at the Jefferson Lab FEL User Facility, in particular, its first and current Associate Directors, Fred Dylla and George Neil, respectively, for offering me the opportunity to work with them. I would also like to thank Jorge Rocca for his review and comments on the soft X-ray laser section.

References

1. T. Maiman, Nature **187**(4736), 493 (1960)
2. D. Smith, H. Frey, J. Carvin, H. Zwally, F. Lemoine, D. Rowlands, J. Abshire, R. Afzal, X. Sun, M. Zuber, J. Geophys. Res. **106**(E10), 23, 689—23, 722 (2001)
3. A.E. Siegman, Lasers, *University Science Books*. (Mill Valley, CA, 1986)

4. E. Condon, G. Shortley, *The Theory of Atomic Spectra.* (Cambridge University Press, Cambridge, 1935)
5. W. Koechner, *Solid-State Laser Engineering.* (Springer, Berlin, 2006)
6. H. Kogelnik, T. Li, Appl. Opt. **5**(10), 1550 (1966)
7. R. Mears, L. Reekie, I. Jauncey, D. Payne, Electron. Lett. **23**(19), 1026 (1987)
8. K. Nakagawa, S. Nishi, K. Aida, E. Yoneda, Lightwave Technol. J. **9**(2), 198 (1991)
9. C.A. Haynam et al., National Ignition Facility laser performance status. App.Opt. **46**, 3276–3303 (2007)
10. J. Rocca, V. Shlyaptsev, F. Tomasel, O. Cortazar, D. Hartshorn, J. Chilla, Phys. Rev. Lett. **73**, 2192 (1994)
11. J. Rocca, D. Clark, J. Chilla, V. Shlyaptsev, Phys. Rev. Lett. **77**(8), 1476 (1996)
12. B. Benware, C. Macchietto, C. Moreno, J. Rocca, Phys. Rev. Lett. **81**(26), 5804 (1998)
13. G. Vaschenko, A.G. Etxarri, C.S. Menoni, J.J. Rocca, O. Hemberg, S. Bloom, W. Chao, E.H. Anderson, D.T. Attwood, Y. Lu, B. Parkinson, Opt. Lett. **31**(24), 3615 (2006)
14. J. Diels, W. Rudolph, *Ultrashort Laser Pulse Phenomena*, 2nd edn. (Academic, San Diego, 1996)
15. D. Deacon, L. Elias, J. Madey, G. Ramian, H. Schwettman, T. Smith, Phys. Rev. Lett. **38**(16), 892 (1977)
16. S.V. Benson, *Tunable Free-Electron Lasers.* Tunable Lasers Handbook, (Academic, New York, 1995)
17. H. Wiedermann, *Synchrotron Radiation.* (Springer, Heidelberg, 2002)
18. G. Neil, C. Behre, S. Benson, M. Bevins, G. Biallas, J. Boyce, J. Coleman, L. Dillon-Townes, D. Douglas, H. Dylla, Nucl. Inst. Methods Phys. Res. A **557**(1), 9 (2006)
19. S. Schreiber, B. Faatz, K. Honkavaara, in *Operation of FLASH at 6.5nm wavelength*, Proceedings of the EPAC08 Conference, Genoa, Italy (2008)
20. M. Shinn, *Experience and plans of the JLab FEL facility as a user facility*, Proceedings of the FEL07 Conference, Novosibirsk, Russia (2007)
21. S.V. Benson, D. Douglas, G.R. Neil, M.D. Shinn, *The Jefferson Laboratory FEL Program – Producing the World's First 4th Generation Light Source*, to be published in J. Physics Conference Series
22. D. Halliday, R. Resnick, J. Walker, *Fundamentals Of Physics*, 7th edn. Wiley, New York (2004)
23. E. Hecht, *Optics*, 4th edn. (Addison Wesley, Reading, 2001)
24. W. Smith, *Modern Optical Engineering: The Design of Optical Systems*. (McGraw-Hill Professional, New York, 2007)
25. J. Crisp, B. Elliott, *Introduction to Fiber Optics*, 3rd edn. (Newnes, London, 2005)
26. B. Frieden, Appl. Opt. **4**(11), 1400 (1965)
27. F. Dickey, S. Holswade, *Laser Beam Shaping: Theory and Techniques*. (Marcel Dekker, New York, 2000)
28. S. Zhang, G. Neil, M. Shinn, Opt. Express **11**(16), 1942 (2003)
29. Laser-Induced Damage in Optical Materials: Collected Papers, 1969–1998 (Special Collection) Proceedings of SPIE Volume: CD08 (1999)
30. Laser-Induced Damage in Optical Materials: Collected Papers, 1999–2003 (Special Collection) Proceedings of SPIE Volume: CDP32 (2004)
31. J.M. Bennett, Proc. SPIE **5273**, 195–206 (2004)
32. G.W. DeBell Proc. SPIE **5991**, 599116 (2005)
33. For information on Paraxia see http://www.sciopt.com
34. For information on GLAD see http://www.aor.com/
35. For information on OPC see lpno.tnw.utwente.nl/project.php?projectid=21&submenu=16
36. A. Watson, M. Shinn, The jefferson lab interactive front end (JLIFE) to the optical propagation code, Jefferson Lab Technical Note, available from the authors. (2009)

Chapter 3
Fundamentals of Laser-Material Interactions

Ettore Carpene, Daniel Höche, and Peter Schaaf

Abstract The following chapter illustrates the basic physical processes occurring during laser-material interaction. It considers fundamentals of electrodynamics in relation to electron–phonon interaction, electromagnetic wave propagation and phase transformations that take place. The theory explains the influence of interaction times and their consequences on heat and material transport.

3.1 Basic Considerations

Laser-material interactions are very complex and only in some simple cases, the laser may be merely seen as a heat source. The numerous facets of laser-material coupling have been the focus of physical research immediately after the first operating laser was built [1–8]. Absorption, heating, melting, evaporation, recoil pressure, piston effect, plasma formation, laser-supported absorption waves (LSAW), Marangoni convection, and Kelvin-Helmholtz instabilities are among the intricate aspects of the laser-material interaction, and they all should be taken into account in order to understand in details the effects of laser processing on the irradiated substrate.

In this chapter, we give a short overview on some of the main features of common types of lasers (Sect. 3.2), sketch the basic electron–electron and electron-lattice dynamics related to laser-material coupling (Sect. 3.3), discuss the fundamental aspects of laser-material interaction (Sect. 3.4.1) with connection to the thermophysical properties of the substrate (Sect. 3.4.2), and show the results of numerical simulations on some common materials (Sect. 3.4.3). In Sect. 3.5, we give an overview of the phenomena occurring at the sample surface during energetic pulsed laser processing: in particular evaporation (Sect. 3.5.1), recondensation (Sect. 3.5.2), plasma formation (Sect. 3.5.3), and LSAW (Sect. 3.5.4) will be outlined. We will conclude sketching some basic aspects of material transport processes (Sect. 3.6).

E. Carpene (✉)
CNR-IFN, Dipartimento di Fisica, Politecnico di Milano, piazza Leonardo da Vinci 32, 20133 Milano, Italy
e-mail: ettore.carpene@fisi.polimi.it

3.2 Laser

It took many years since the publication of the basic theoretical principles of the stimulated emission of radiation by Einstein in 1917 [9] until the first radiating laser was built by Maiman in 1960 [10]. With the development of powerful lasers, also their applications in material treatments rapidly developed [11–16]. Today, an uncountable number of lasers are used in industrial production processes, especially for the treatment of metals.

A laser (**LASER** = **L**ight **A**mplification by **S**timulated **E**mission of **R**adiation) is a device that emits light (i.e., electromagnetic radiation) through the process of stimulated emission. The basic principles of a laser are described in [17–20]. One can classify lasers into the following types, according to the lasing medium:

1. Gas lasers (e.g., CO_2, excimer)
2. Liquid lasers (organic liquid dye)
3. Solid state lasers (e.g., Nd-YAG, Ti:sapphire, fibre laser)
4. Semiconductor laser (e.g., quantum cascade lasers, diode laser)
5. Free electron laser (FEL)

A laser can radiate either in continuous wave (cw) mode or in pulsed mode. The first operating laser was a Ruby laser [10], i.e., a solid state laser. Here, the population inversion was produced by optical pumping. Semiconductor lasers are using a voltage/current to invert the state occupancy, while in gas laser the inversion is obtained by gas discharge. In particular, the excimer laser (excimer=excited dimer) is a pulsed, high pressure gas laser, using a noble gas – halogen mixture [21]. FELs use relativistic electrons as lasing medium and they provide the widest spectral tunability (form far IR to deep UV or soft X-rays). The main properties of laser radiation are the high brightness (i.e., power emitted per unit surface area per unit solid angle), high monochromaticity (i.e., extremely narrow bandwidth), minimal divergence, and high spatial and temporal coherence [3, 22]. These are the reasons for the high focussability of laser radiation, which leads to the production of large irradiances (up to 10^{21} W/cm^2), enough to evaporate any material or even to start a nuclear fusion reaction [17]. The temporal structure of pulsed lasers depends on the specific lasing process, but it can range from milliseconds to femtosecond with the mode-locking technique. The spatial energy distribution in the laser beam is mainly depending on the geometry of the laser resonator, on the mirrors and on the extraction optics [23, 24]. Best focussability is given at low transversal electromagnetic radiation modes (TEM00, i.e., Gaussian), whereas for surface treatments a top-hat profile is preferred in order to achieve a homogeneous treatment. The most important lasers for material treatments are the CO_2 laser, the Nd:YAG laser, and the excimer laser. Recently, also diode lasers are attracting great interest [25]. For laser processing of metals, the beam wavelength is relatively important as long as light is absorbed. For dielectric materials, on the other hand, considerable absorption takes place only if the photon energy overcomes the optical/mobility gap.

The typical wavelengths λ of various laser types are summarized in Table 3.1 [26].

Table 3.1 Wavelengths for selected laser types [26]

Lasing medium	Laser type	Wavelength
Solid-state	Ruby	694 nm
	Nd:YAG	1,064 nm
	Ti:Sapphire	650–1,100 nm
Gas	CO_2	10.4 μm
	Excimer	193 nm (Ar–F)
		248 nm (Kr–F)
		308 nm (Xe–Cl)
		351 nm (Xe–F)
Semiconductor	GaN	0.4 μm
	Quantum cascade	mid-far IR
Free electron		far IR to vacuum UV

For laser processing of solid substrates, the typical power of the laser beam is ranging up to 100 MW with pulse durations τ_{pulse} of 10–100 ns and repetition rates up to 1 kHz [20, 26, 27].

3.3 Heat in Solids: Electronic and Lattice Dynamics

To understand the effect of the laser beam on the irradiated material, the electronic and lattice dynamics must be taken into account. In order to induce any effect on the substrate, the laser light must be absorbed and the absorption process can be thought as an energy source inside the material. However, although driven by the incident light beam, the source can develop its own dynamics depending on the specific electronics and lattice responses of the material. The description of the absorption phenomena is based on Maxwell's equations and on their solution for time-varying electric and magnetic fields. The optical properties of solids are accessible with conventional optical methods using light in the infrared, visible, and ultraviolet spectral range. In this section, we summarize the basic electronic and lattice dynamics of solids, emphasizing their typical time scales and their consequences on the laser-material interaction.

For typical laser wavelengths (from near infrared to near ultraviolet), photons are absorbed by electrons through inter- and intra-band electronic transitions. Therefore, the laser beam induces a non-equilibrium electronic distribution that thermalizes via electron–electron and electron–phonon interactions. The electron–electron thermalization can be rather complex depending on the specific electronic structure of the irradiated sample: for semiconductors and insulators, the laser photons can promote electrons from the valence band to the conduction band, across the optical/mobility gap, creating electron-hole pairs. Subsequently, electronic recombination reestablishes the equilibrium condition on a time scale that can be as long as nanoseconds, depending on the material properties [28].

For metals, the situation can be very different. Electron scattering events can take place within a few femtoseconds, thus electronic thermalization can be extremely fast. The simplest approach is provided by the Drude model [29], where the electron scattering time τ_D can be deduced from the electrical conductivity σ_{el} as:

$$\sigma_{el} = Ne^2\tau_D/m \tag{3.1}$$

Here, N is the conduction electron density, e is the electron charge, and m is the electron mass. Typical values of τ_D are a few femtoseconds, representing the time scale of electron scattering events. Drude model simply provides the electron scattering time even under equilibrium conditions, with no insight on the specific mechanism. Since the laser photons induce a non-equilibrium electronic distribution, more sophisticated approaches must be employed. The lifetime τ_{ee} of excited electron is due to electron–electron collisions and is described by the Fermi liquid theory [30] as:

$$\tau_{ee} = \tau_0 \left(\frac{\varepsilon_F}{\varepsilon - \varepsilon_F} \right)^2 \tag{3.2}$$

where τ_0 is of the order of a femtosecond, ε_F is the Fermi energy, and $\varepsilon - \varepsilon_F$ is the excited electron energy as referred to the Fermi level. Notice that with laser photons in the visible-UV range and with a typical Fermi energy of 10 eV, $\tau_{ee} \sim 1 - 10$ fs and it rapidly increases as the electron energy relaxes towards the Fermi level. This lifetime dependence has been thoroughly investigated and confirmed by several time-resolved photoemission experiments using femtosecond lasers (see for instance [31, 32]). Due to the ultrafast character of electron–electron interaction, these processes can only be revealed with laser pulses which duration compares with τ_{ee}, i.e., Ti:sapphire lasers operating in mode-locking condition. For longer laser pulses, the electron–electron thermalization occurs *within* the pulse duration and the electron dynamics substantially follows the time evolution of the laser pulse.

Electrons, however, do not only scatter among each other, but they can also interact with the lattice through electron–phonon scattering processes. The theory of electron-lattice scattering has been developed since the 1960s, especially with the discovery of superconductivity. The basic features of the interaction have been outlined in the fundamental work of Eliashberg (see [33]). A simplified approach, directly related to laser interaction with solid has been proposed by P. B. Allen [34], and is based on the rate of change of the electron and phonon distributions due to collisions. Allen derived an expression for the energy transfer between the photo-excited electrons and the lattice that allows to evaluate the variation of the electronic temperature T_e as a simple rate equation:

$$\partial T_e/\partial t = (T_L - T_e)/\tau_{ep} \tag{3.3}$$

(T_L is the lattice temperature) where the electron–phonon coupling time τ_{ep} depends on the electronic temperature, a coupling constant λ_p ($\sim$ 0.5, see [35]) characteristic of the material and the Debye frequency ω_D of the irradiated solid as:

$$\tau_{ep} = (2\pi k_B T_e)/(3\hbar\lambda_p\omega_D^2) \tag{3.4}$$

For $T_e \sim 10^3$ K and using typical values of the Debye frequency for metals ($\hbar\omega_D$ of a few tens of meV), $\tau_{ep} \sim 0.1-1$ ps. Thus, the energy transfer from the electronic bath to the lattice occurs on the picosecond time scale and is roughly two orders of magnitude slower than the electron–electron scattering time.

From these considerations, it is clear that electrons and lattice can develop distinct dynamics upon laser irradiation, and the time evolution of the energy (or temperature) of the electron gas and the lattice can be described by two separate, but coupled heat transport equations:

$$C_e \frac{\partial T_e}{\partial t} = \nabla(k_e \nabla T_e) - H(T_e, T_L) + S(t) \tag{3.5}$$

$$C_L \frac{\partial T_L}{\partial t} = H(T_e, T_L) \tag{3.6}$$

Here, C_e and C_L are the electronic and lattice specific heat (J m^{-3} K^{-1}), respectively, $S(t)$ represents the absorbed laser power per unit volume (W m^{-3}), $H(T_e, T_L)$ is the rate of energy transfer between electrons and lattice (W m^{-3}), and $\nabla(k_e \nabla T_e)$ is the diffusive electronic heat transfer. These coupled differential equations represent the celebrated two-temperature model (TTM) developed by Anisimov et al. in 1975 [36]. In the last 30 years, several authors have investigated theoretically and experimentally various aspects on the TTM, including the detailed electronic [37–45] and spin [46] scattering mechanisms.

Under proper experimental conditions (see [38,47]), the energy transfer between electrons and lattice can be simplified as:

$$H(T_e, T_L) = g_{ep}(T_L - T_e) \tag{3.7}$$

where the quantity $g_{ep} = C_e/\tau_{ep}$ represents an alternative way (but equivalent to the approach proposed by Allen) to describe the electron–phonon coupling.

It should be noted that (3.5) and (3.6) are useful as long as the laser pulse duration τ_{pulse} is comparable to the typical time constants of electron–electron and electron–phonon couplings. If $\tau_{pulse} \gg \tau_{ee}, \tau_{ep}$, then electrons and lattice thermalize within the pulse duration and their dynamics substantially coincide (thus $T_e = T_L = T$). To illustrate this effect, (3.5) and (3.6) have been solved numerically (details on the numerical simulation of the temperature profiles will be discussed in Sect. 3.4.3) using the thermal and optical parameters of copper as a benchmark. The temporal profiles of the source term $S(t)$ has been assumed gaussian and the laser fluence has been chosen for each pulse duration in order to produce a maximum electronic temperature rise $\Delta T < 100$ K. For copper, $C_e = \gamma T_e$, with $\gamma = 10^{-4}$ J/cm^{3}K^2 [48], $C_L = 3.4$ J/cm^{3}K [48], $k_e = 4$ W/(cm K) [49] and $g_{ep} = 10^{10}$ W/cm^3 K [49], corresponding to an electron–phonon coupling time $\tau_{ep} \sim 0.3$ ps. The results are reported in Fig. 3.1.

For $\tau_{pulse} = 50$ fs, electrons and lattice are essentially decoupled: the electronic temperature rise is determined by the laser pulse and its subsequent relaxation is completed on a time scale comparable to a few τ_{ep}. The lattice temperature, on the

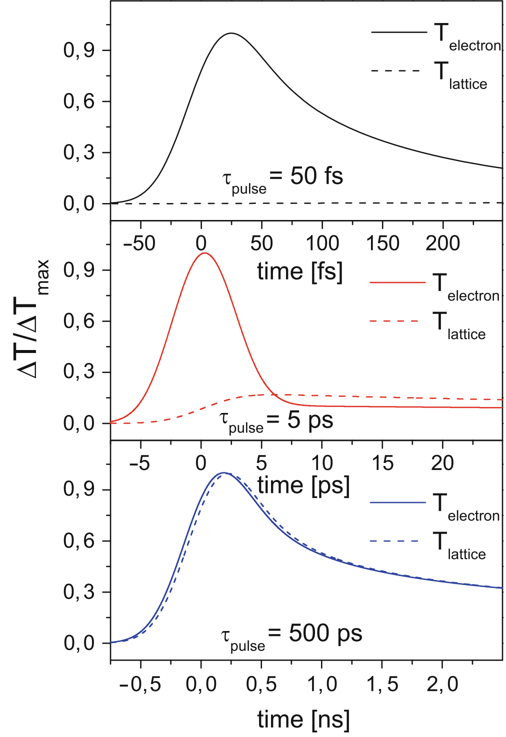

Fig. 3.1 Electronic and lattice temperature profiles (simulations obtained with the TTM) in cupper irradiated by laser pulses of different durations (ranging from 50 fs to 500 ps). With 50 fs pulses, electrons and lattice are completely decoupled and the lattice is substantially unaffected by the laser beam. With 500 ps pulses, electron and lattice follow almost identical temperature evolutions

other hand, shows a negligible change since the lattice cannot respond on a time scale as short as the pulse duration. When $\tau_{\text{pulse}} = 5\,\text{ps}$, the electronic temperature closely resemble the time evolution of the laser pulse (i.e., gaussian profile) since its intrinsic dynamics is much faster than τ_{pulse}. Besides, energy is transferred to the lattice within the pulse duration and T_{L} clearly rises. If the laser pulse duration is further increased to $\tau_{\text{pulse}} = 500\,\text{ps}$, electronic and lattice dynamics are essentially similar since the rate of energy exchange between them is much shorter than τ_{pulse} and they evolve as if they were in local thermal equilibrium condition.

In this last case, the TTM becomes redundant, and (3.5) and (3.6) can be simplified. In fact, by substituting (3.6) in (3.5) one obtains:

$$(C_{\text{e}} + C_{\text{L}})\frac{\partial T}{\partial t} = \nabla(k_{\text{e}}\nabla T) + S(t) \tag{3.8}$$

Considering that the electronic specific heat is usually much smaller than the lattice one [29, 48], the term C_{e} can be neglected and the standard heat transport equation is obtained:

$$C_{\text{L}}\frac{\partial T}{\partial t} = \nabla(k_{\text{e}}\nabla T) + S(t) \tag{3.9}$$

The main features and the most important consequences of this equation will be described in detail in the next sections.

3.4 Laser-Material Interactions

The laser is usually seen as a very special and intense heat source and only its thermal effects are to be considered. Nevertheless, in recent years also laser induced chemical reactions, where photons with high enough energy may directly induce chemical reactions, play a considerable role [1, 7].

Even if the laser processing is performed in the presence of a reactive atmospheric environment (e.g., nitrogen or methane for laser-induced nitriding and carburizing, respectively), photon energy in the near UV spectral range is too small to directly interact with the surrounding gas with typical ionization energy of tens of eV (e.g., $E_{\text{ioniz}} = 15.6\,\text{eV}$ for nitrogen [50]). Moreover, the intensity of the laser irradiation normally used in laser processing of matter is too small to induce a gas breakdown, which needs a threshold irradiance of $I_{\text{break}} \approx 10^{10}\,\text{W/cm}^2$ [1, 51]. Thus, the laser irradiation will hit the substrate surface unhindered, without absorption in the surrounding gas.

3.4.1 Single Photon and Multi-Photon Processes

The processes taking place when the laser radiation hits a material depend on the amount of deposited laser energy. This energy and its spatial and temporal distribution determine what kind of material modification will occurs [52]. The main laser-solid interaction process is the excitation of electrons from their equilibrium states to some excited states by absorption of photons [53]. These typical single photon processes are well-known in a wide field of physics and have been discussed extensively [54, 55]. Other possible excitations involve multiphoton electronic transitions. At a constant laser fluence, a shorter laser-material interaction time favors multiphoton excitation processes, because the probability of nonlinear absorption increases strongly with a growing laser intensity.

A general expression for the n-photon transition probability W is given by the following equation:

$$W = s^n I^n \tag{3.10}$$

where I describes the laser intensity and s the cross section of the single-photon process. Due to their strong nonlinear character, multiphoton processes are in general rather complex and will not be considered in the next sections. Further information are available in the work of Linde et al. [53].

3.4.2 Laser Reflection and Absorption

As already mentioned in previous chapters, laser light in the near IR-near UV spectral region normally interacts only with the electrons of a material, because ions are too heavy to follow the high frequency fields [56]. The optical properties of metals are determined by the free (valence) electrons, because the inner electrons only weakly interact with the applied electric field. These free electrons are accelerated in the electrical field and gain energy. Due to the periodic change of the field vector, the oscillating electrons also re-radiate energy, which causes the high reflectivity of metals. The interactions of laser radiation with matter are significantly simplified if the pulse duration is long compared to the typical elementary scattering times (picoseconds), and the classical Drude theory [57] can be used.

Describing the laser radiation by a propagating electric field plane wave:

$$\mathbf{E}(\mathbf{r}, t) = \mathbf{E_0} \exp\{\, \mathrm{i}\,(\mathbf{kr} - \omega t)\,\} \tag{3.11}$$

with frequency $\omega = 2\pi c/\lambda$, wavevector $\mathbf{k}$, space coordinate $\mathbf{r}$, time t, and field amplitude $\mathbf{E}_0$, one can treat the solid as a combination of harmonic oscillators (Lorentz model), resulting in the equation of motion for electrons:

$$m\ddot{\mathbf{r}} + m\gamma_{\mathrm{D}}\dot{\mathbf{r}} + m\omega_0^2\mathbf{r} = -e\mathbf{E}_{\mathrm{loc}}(\mathbf{r}, t) \tag{3.12}$$

with electron mass m, attenuation $\gamma_{\mathrm{D}} = 1/\tau_{\mathrm{D}}$, eigenfrequency ω_0 and the local field strength $\mathbf{E}_{\mathrm{loc}}$.

Here the finite mass of the atoms and the weak magnetic forces have been neglected. The attenuation constant γ_{D} includes the interaction of the electrons with lattice phonons and vacancies, by which energy is transferred within picoseconds to the whole solid [8]. The fraction of absorbed radiation is determined by the optical properties of the sample. The locally acting electric field $\mathbf{E}_{\mathrm{int}} = \langle \mathbf{E}_{\mathrm{loc}} \rangle$ is the response of the material to the external field and is determined by the dielectric tensor ε via:

$$\mathbf{E}_0 = \varepsilon \cdot \mathbf{E}_{\mathrm{int}} \tag{3.13}$$

For isotropic materials, the dielectric tensor reduces to a complex constant and in the framework of the Drude model for metal, considering that free electrons have no retention force, i.e., $\omega_0 = 0$, the dielectric index $\varepsilon = \varepsilon_1 + \mathrm{i}\,\varepsilon_2$ is given by:

$$\varepsilon_1 = n^2 - \kappa^2 = 1 - \frac{\omega_{\mathrm{p}}^2 \tau_{\mathrm{D}}^2}{1 + \omega^2 \tau_{\mathrm{D}}^2} \tag{3.14}$$

$$\varepsilon_2 = 2n\kappa = \frac{\omega_{\mathrm{p}}^2 \tau_{\mathrm{D}}}{\omega(1 + \omega^2 \tau_{\mathrm{D}}^2)}, \tag{3.15}$$

with n and κ being the so-called refractive index and the extinction coefficient. As already discussed, τ_{D} is the mean time between two electronic collisions. The plasma frequency ω_{p} depends on density of free electrons N:

$$\omega_p = \sqrt{\frac{Ne^2}{m\varepsilon_0}} \tag{3.16}$$

(here, ε_0 is the vacuum dielectric constant). The reflectivity R_0 and the absorption coefficient α, or the optical absorption length $d_{opt} = 1/\alpha$ (at normal incidence), may be obtained via n and κ by:

$$R_0 = \frac{(n-1)^2 + \kappa^2}{(n+1)^2 + \kappa^2} \tag{3.17}$$

$$\alpha = \frac{2\omega\kappa}{c} = \frac{4\pi\kappa}{\lambda} \tag{3.18}$$

Simultaneously, the plasma frequency ω_p is connected to the electrical conductivity of the metal σ_{el}:

$$\sigma_{el} = \frac{Ne^2\tau_D}{m} = \omega_p^2\tau_D\varepsilon_0 \tag{3.19}$$

and is usually in the UV regime.

For optical wavelengths $\omega \ll 1/\tau_D$ (IR spectral range), the reflectivity R_0 and the absorption coefficient α can be estimated using the electrical resistivity $\rho_{el} = 1/\sigma_{el}$ (Hagen-Rubens-equation [56, 58]):

$$R_0 = 1 - 2\sqrt{2\omega\varepsilon_0\rho_{el}} \tag{3.20}$$

$$\alpha = \sqrt{\frac{2\omega}{c^2\varepsilon_0\rho_{el}}} \tag{3.21}$$

resulting in $R_0 \approx 90 - 99\%$, and $\alpha^{-1} \approx 10$ nm for metals and radiation below the plasma frequency [56]. The absorption coefficient increases with decreasing wavelength and is proportional to the resistivity ρ_{el} [59], while above the plasma frequency the reflectivity drops drastically (UV-transparency of metals) [60]. The values of R_0 and α, or alternatively n and κ, are available in the literature for many pure solids and for a number of compounds in a wide range of laser wavelengths [50, 61].

The absorption at surfaces not only depends on the wavelength of the laser radiation, but also on other factors such as incident angle, surface roughness, and temperature of the solid. For example, the roughening of the surface (roughness $R_a > \lambda$) enhances the absorption by multiple reflections [59]. For most metals, the absorption increases with increasing surface temperature. A dramatic increase of the absorption is found for most metals at the melting point [56]. Also for high enough laser intensities (10^5–10^6 W/cm^2), anomalous absorption by nonlinear processes can enhance the energy transfer [19, 62].

As stated by (3.9), the absorbed energy is spatially distributed by heat conduction. For laser with pulse duration up to tens of nanoseconds, the thermal diffusion length z_{th} never exceeds a few µm (for metals $z_{th} = \sqrt{\tau_{pulse}k_e/C_L} < 1$ µm, where

k_e/C_L is the so-called thermal diffusivity). Assuming a laser spot size much larger than the thermal diffusion length z_{th} (that is a rather common situation in standard laser processing), one can use the one-dimensional heat diffusion equation, and (3.9) can be further simplified. For the isotropic case with temperature dependent material properties, this can be written as:

$$C_L(T)\frac{\partial T(z,t)}{\partial t} = \frac{\partial}{\partial z}\left[k_e(T)\frac{\partial T(z,t)}{\partial z}\right] + S(z,t), \tag{3.22}$$

where $T(z,t)$ is the temperature at depth z at time t; $\zeta = \frac{k_e(T)}{C_L}$, where $k_e(T)$ is the heat conductivity, $C_L(T)$ is the specific heat and $S(z,t)$ is the absorbed or released energy per unit time and unit volume.

Here, $S(z,t)$ incorporates the laser heat sources, i.e., the absorbed laser energy $I_{abs}(z,t)$, as well as internal heat sinks $\Delta U(z,t)$ due to phase transformation:

$$S(z,t) = I_{abs}(z,t) + \Delta U(z,t) \tag{3.23}$$

The absorbed laser energy can be evaluated using the laser *irradiance* $I(t)$ (i.e., energy per unit area and unit time), the reflectivity R_0 and the absorption coefficient α:

$$I_{abs} = I(t)\alpha(1 - R_0)\exp(-\alpha z)\,. \tag{3.24}$$

that is a direct consequence of Beer's law:

$$\frac{\partial I(t,z)}{\partial z} = -\alpha I(t,z). \tag{3.25}$$

The temporal shape of the laser beam can be modeled according to the laser specification, but it is customary to use a Gaussian profile:

$$I(t) = (\phi/\sigma\sqrt{2\pi}) \cdot \exp(-(t-t_0)^2/2\sigma^2). \tag{3.26}$$

where ϕ is the laser *fluence* (i.e., energy per unit area) and $\tau_{pulse} = 2\sigma\sqrt{\ln 2}$ (i.e., the FWFM of the gaussian profile).

When a phase transformation occurs (e.g., melting, evaporation, or solidification) at a given temperature T_{phase}, the corresponding latent heat L_{phase} is a heat sink that must be taken into account. A convenient approach is to re-define heat in the proximity of the phase transition temperature in such a way that uniquely describes the state of the material as a function of the temperature [28]:

$$dH(T) = \begin{cases} C_L dT & \text{if } T < T_{phase}; \\ C_L dT + L_{phase} & \text{if } T \geq T_{phase}. \end{cases} \tag{3.27}$$

When the material changes phase, the extra heat sink L_{heat} is "automatically" included in the heat equation.

If the temperature overcomes the melting point, significant evaporation might start, and this must be carefully included into the calculation, because evaporation not only removes heat but also matter. Above the melting temperature, the liquified matter evaporates according to the following evaporation flux j_{ev} [8, 63]:

$$j_{ev} = \rho \frac{\partial z_{ev}}{\partial t} = \frac{p_D(T)}{\sqrt{(2\pi k_B T/M_a)}} \tag{3.28}$$

where $p_D(T)$ is the vapor pressure of the material at temperature T, M_a is the atomic mass, and ρ is the material density. Boiling is neglected, since the high recoil pressure and the plasma pressure, as we will see later, are increasing the boiling temperature.

The vapor pressure p_D can be described by the Clausius-Clapeyron equation:

$$p_D(T) = p_0 \exp\left[-\frac{\Lambda_b}{R}\left(\frac{1}{T} - \frac{1}{T_b}\right)\right] \tag{3.29}$$

with p_0 being the initial pressure (before evaporation starts), Λ_b the molar latent heat of boiling, T_b the boiling temperature, and R the gas constant. Then, the heat flux U_{ev} removed by the evaporation process is given by

$$U_{ev} = j_{ev}\Lambda_b(T)/M = \rho \frac{\partial z_{ev}}{\partial t} \cdot \Lambda_b(T)/M. \tag{3.30}$$

(M is the molar mass). Since the sample surface is a discontinuity, it requires a boundary condition for the heat diffusion, and it can be included as follows:

$$k_e(T) \left.\frac{\partial T}{\partial z}\right|_{\text{surface}} = U_{ev} = \left.\left(\frac{\Lambda_b p_0}{\sqrt{2\pi RTM}} \exp\left[\frac{\Lambda_b}{R}\left(\frac{1}{T_b} - \frac{1}{T}\right)\right]\right)\right|_{\text{surface}}. \tag{3.31}$$

As it will be shown in the next sections, during the laser irradiation, an enormous pressure ($\sim 10^2$ bar) is acting on the target surface. According to 3.29, the boiling point is shifted to a higher temperature and the liquid can be heated above T_b, making the condition described in (3.27) unnecessary for the liquid–vapor phase transition.

In most general cases, the thermal and optical parameters appearing in (3.22)–(3.31) are temperature-dependent and the only way to solve the heat transport equation is numerically, as it will be illustrated in the following section with some specific examples.

3.4.3 Temperature Profiles

In this section, we will outline how numerical calculations of the laser induced temperature rise can be performed by the method of finite differences. Due to the fast

and local supply of energy from the laser source, the irradiated sample can melt and even evaporate. The latter is normally connected to the formation of a plasma above the surface. The dependence of temperature, melt depth and evaporation rate on time, depth, and laser fluence will be calculated. Material transport and convection in the melt are neglected at this stage.

In the finite differences approach, time t and space z are divided into discrete points $t^i = i \cdot \Delta t$ and $z_n = n \cdot \Delta z$. Thus, the sample is sliced into thin layers z_n ($n = 0 \dots N$) of equal distance Δz and the time steps are Δt. The partial time derivative of the temperature can be expressed by the finite difference (forward differentiation) representation:

$$\frac{\partial T}{\partial t} = \frac{T_n^{i+1} - T_n^i}{\Delta t}, \tag{3.32}$$

where T_n^i is the temperature at the time $t^i = i \cdot \Delta t$ in the layer $z_n = n \cdot \Delta z$. The calculation starts at $i = 0$ with $T_n^0 = 300\,\mathrm{K}$ (ambient temperature) for all n. The second derivative in space can also be expressed by a finite difference as:

$$\frac{\partial^2 T}{\partial z^2} = \frac{T_{n-1} - 2T_n + T_{n+1}}{(\Delta z)^2} \tag{3.33}$$

therefore, (3.22) can be re-written as

$$T_n^{i+1} = T_n^i + \Delta t \cdot \left[\frac{k_\mathrm{e}(T_n^i)}{C_\mathrm{L}(T_n^i)} \cdot \frac{(T_{n-1}^i - 2T_n^i + T_{n+1}^i)}{(\Delta z)^2} + \frac{S_n^i}{C_\mathrm{L}(T_n^i)} \right] \tag{3.34}$$

which is called the "forward time centered" space scheme. The source term S_n^i is simply re-written from (3.24)–(3.26) in terms of discrete time and depth.

Also the boundary condition of (3.31) is included in the surface layer ($n = 1$):

$$k_\mathrm{e}(T) \frac{\partial T}{\partial z}\bigg|_{\mathrm{surface}} = k_\mathrm{e}(T_2^i) \frac{T_2^i - T_1^i}{\Delta z} = \frac{\Lambda_\mathrm{b} p_0}{\sqrt{2\pi R T_1^i M}} \exp\left[\frac{\Lambda_\mathrm{b}}{R}\left(\frac{1}{T_\mathrm{b}} - \frac{1}{T_1^i}\right)\right]. \tag{3.35}$$

Melting and solidification are implemented in the computation via (3.27) by checking for every given layer n at any given time i when the melting point T_m is reached, i.e., $T_n^{i+1} \geq T_\mathrm{m} \geq T_n^i$. If the amount of heat $\Delta H = C_\mathrm{L}(T_n^i)(T_n^{i+1} - T_\mathrm{m}) \leq L_\mathrm{m}$, the layer n starts to melt, the new temperature is held to $T_n^{i+1} = T_\mathrm{m}$ and the fraction $\Delta H / L_\mathrm{m}$ of the slab is molten. On the other hand, if $\Delta H = C_\mathrm{L}(T_n^i)(T_n^{i+1} - T_\mathrm{m}) > L_\mathrm{m}$ the whole slab is molten and the extra heat $\Delta H - L_\mathrm{m} = C_\mathrm{L}(T_n^i)(T_n^{i+1} - T_\mathrm{m})$ determines the temperature T_n^{i+1} of the melt. The solidification process is computed in a similar way.

The heat equation in finite differences becomes an algebraic equation that can be solved with respect to T_n^{i+1}: the temperature is calculated iteratively for each layer at each time step. The values of Δz and Δt are not arbitrarily chosen, but they must satisfy the Neumann criterion [64]:

$$\Delta t < \Delta z^2 \left[\frac{C_L(T)}{2k_e(T)} \right]_{\text{minimum}}, \tag{3.36}$$

in order to obtain convergent, physical solutions. All these details can be implemented into a program running on a standard PC which calculates the temperature profile, the molten depth, and the evaporation rate [65–69].

The simulations presented below refer to a XeCl excimer laser source ($\lambda = 308$ nm, $\tau_{\text{pulse}} = 55$ ns).

Table 3.2 reports the thermal and optical parameters of Fe, Al, and Si used in the thermal calculations, while Fig. 3.2 shows the temperature dependence of the thermal conductivity $k_e(T)$ and the molar specific heat $c_p(T)$ for pure iron, aluminum, and silicon. Figure 3.3 reports the time evolution of the surface temperature profiles T_1^i and the melting depths of the iron and the aluminum targets irradiated at a laser fluence $\phi = 4$ J/cm^2. Considering the typical thermal parameters of the investigated materials, the values of $\Delta z \sim 10$ nm and $\Delta t \sim 1$ ps have been used.

Although it is known that the optical reflectivity R_0 of metals decreases with increasing temperature [28], due to the lack of experimental data, it is assumed

Table 3.2 Thermal and optical parameters of iron, aluminum and silicon used in the heat equation (data from [50])

	Fe	Al	Si
M [g/mole]	56	27	28
ρ [g/cm^3]	7.86	2.7	2.33
L_m [kJ/mole]	15	10.5	49.8
L_{ev} [kJ/mole]	350	296	420
T_m [K]	1,810	933.5	1,685
T_b [K]	3,023	2,740	2,628
R_0 ($\lambda = 308$ nm)	0.53	0.5[(a)]	0.6
α [cm^{-1}] ($\lambda = 308$ nm)	1×10^6	1.5×10^6	1.5×10^6

[(a)] Measured.

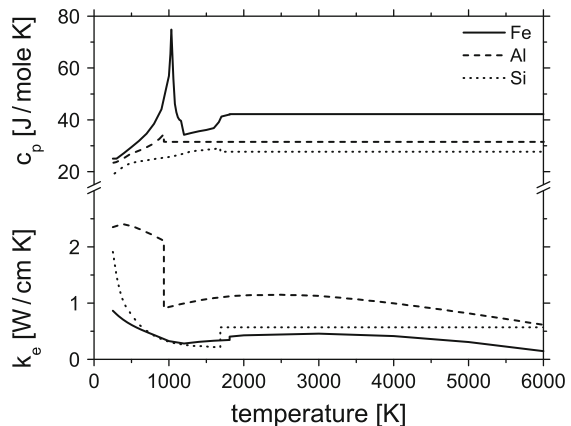

Fig. 3.2 Temperature dependence of the molar specific heat (*top*) and the thermal conductivity (*bottom*) of iron (*solid line*), aluminum (*dashed line*) and silicon (*dotted line*). Data from [70]

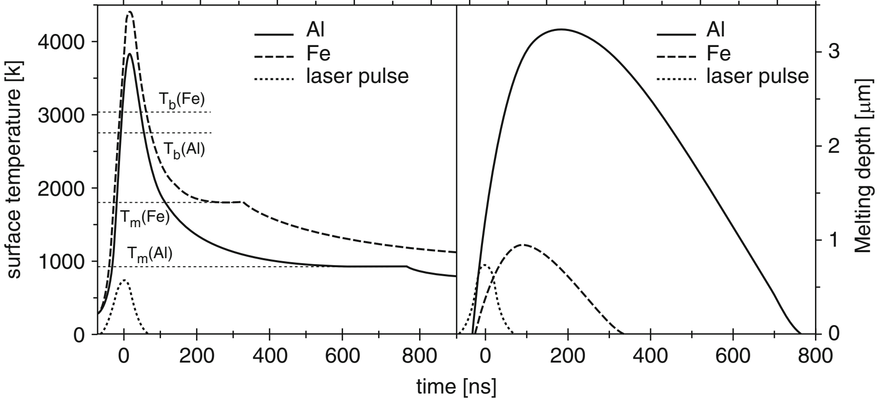

Fig. 3.3 Time evolution of the surface temperature profiles (*left*) and the melting depths (*right*) of the iron and the aluminum substrates irradiated at 4 J/cm^2. The melting and the boiling points of each element are indicated

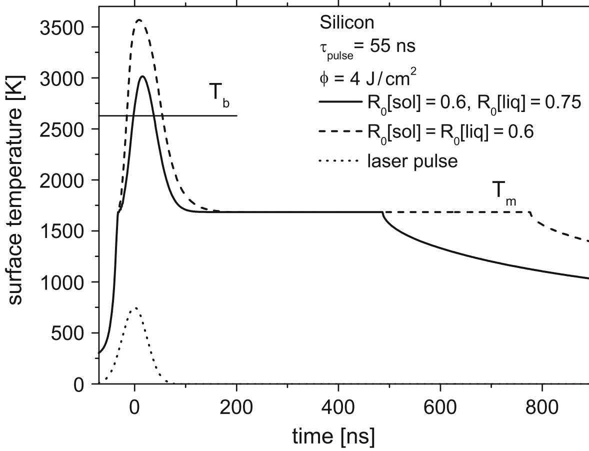

Fig. 3.4 Comparison between the Si surface temperature profiles obtained using temperature-dependent (*solid line*) and temperature-independent (*dashed line*) reflectivities

temperature-independent. In the case of the silicon substrate, the reflectivity of the solid is about 20% lower than the liquid (for near UV wavelength, $R_0(T < T_m) \simeq 0.6$ and $R_0(T \geq T_m) \simeq 0.75$ [61, 71, 72]) and different temperature profiles are obtained if the temperature dependence of R_0 is taken into account, as illustrated in Fig. 3.4. In particular, when the melting point is reached, the higher reflectivity of the liquid phase reduces the absorbed laser energy, leading to a decrease of the maximum surface temperature and of the melting time.

Powerful laser beams not only affect the intrinsic optical properties but also the surface topography (shape, roughness) of the irradiated material, which influences the beam-solid coupling. Surface corrugations are almost always related to melting

or evaporation. In particular, melting of a surface by a laser beam typically leaves its trace in form of ripples or corrugations. The patterns are often unrelated to the beam profile and they appear even if the beam is perfectly smooth [8].

3.5 Phenomena Occurring on the Target Surface

Although the temporal evolution of the temperature profiles and the related phase transformations *inside* the irradiated substrates have been described, important phenomena take place also *on* the surface of the target, as illustrated in the following sections.

3.5.1 Vaporization

According to the heat transport equation, the laser beam can be absorbed by the substrate causing melting and vaporization. In the case of strong evaporation, typically at fluences of several J/cm^2 with nanosecond pulse duration, the more proper boundary condition at the target surface would be to include also the velocity v_{ev} of the evaporation front. Using (3.28), we can write [61]:

$$v_{\mathrm{ev}} = \frac{j_{\mathrm{ev}}}{\rho} = \frac{p_{\mathrm{D}}(T)}{\rho\sqrt{(2\pi k_{\mathrm{B}} T / M_{\mathrm{a}})}} \tag{3.37}$$

In the reference frame attached to the liquid–vapor interface moving with velocity v_{ev}, the left-hand-side of the heat equation, (3.22), should be written as:

$$C_{\mathrm{L}}(T)\frac{\partial T(z,t)}{\partial t} \to C_{\mathrm{L}}(T)\left(\frac{\partial T(z,t)}{\partial t} - v_{\mathrm{ev}}\frac{\partial T(z,t)}{\partial z}\right). \tag{3.38}$$

Both cases of stationary and non-stationary evaporations can be treated with proper approximations [61], but the correct treatment should consider: (a) the hydrodynamic motion of the evaporated material, (b) the decrease of the vapor temperature due to its expansion, and (c) the backward flux of the evaporated species. The vaporized atoms/molecules leave the substrate at temperature T_{s} with half-Maxwellian non-equilibrium velocity distribution (the velocity is initially in the direction normal to the target surface). Due to the collisions with other atoms/molecules, the vapor propagates with hydrodynamic speed v_{v} and the velocity distribution becomes Maxwellian (i.e., in thermodynamical equilibrium) [73]. The transformation from non-equilibrium to equilibrium distributions takes place in a thin layer of few mean free paths called *Knudsen layer*, as sketched in Fig. 3.5.

The detailed mathematical analysis of the transformation was performed by Anisimov [74] with a proper definition of the velocity distribution and using the conservation of mass, momentum, and energy across the Knudsen layer. The results show that the temperature T_{v} of the vapor beyond the Knudsen layer is lower than T_{s},

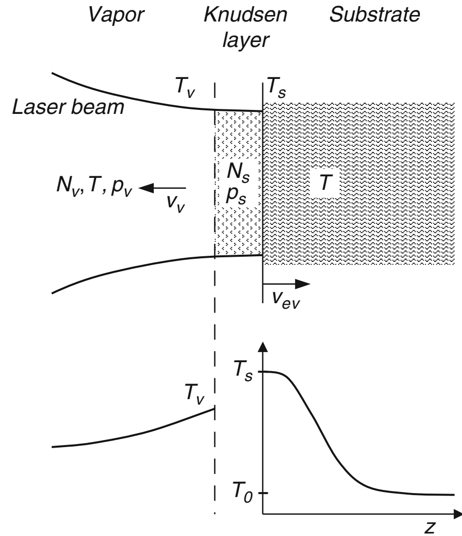

Fig. 3.5 Irradiation geometry (*top*) and temperature profiles within the target and the ambient medium (*bottom*): effect of the Knudsen layer

due to the partial transformation of thermal energy into kinetic energy of the expanding vapor plume. Besides, the number density of the vaporized species and the vapor pressure behind the Knudsen layer (subscript "*v*", i.e., vapor) can be related to the same values within the layer (subscript "*s*", i.e., surface) as follows:

$$\begin{aligned} T_\mathrm{v} &= T_\mathrm{s}(1 - 0.33\ \Pi); \\ N_\mathrm{v} &= N_\mathrm{s}(T_\mathrm{s})/(1 + 2.2\ \Pi); \\ p_\mathrm{v} &= N_\mathrm{v} k_\mathrm{B} T_\mathrm{v} = p_\mathrm{s}(T_\mathrm{s}) \frac{1 - 0.33\ \Pi}{1 + 2.2\ \Pi}, \end{aligned} \tag{3.39}$$

where the *Mach number* Π determines the expansion velocity v_v of the species beyond the Knudsen layer: in general $v_\mathrm{v} = \Pi c_\mathrm{s}$, where c_s is the speed of sound. For a vapor expanding in vacuum, $\Pi = 1$ [73], but if the laser irradiation takes place in a gaseous medium, Π (with $0 < \Pi < 1$) must be calculated theoretically or measured experimentally [61].

3.5.2 Recondensation

Using (3.39) and considering the vapor as an ideal gas, it can be verified that the vapor beyond the Knudsen layer is strongly supersaturated. In fact:

$$N_\mathrm{v} = N_\mathrm{s}(T_\mathrm{s})/(1 + 2.2\ \Pi) > N_\mathrm{s}(T_\mathrm{v}) = p_\mathrm{s}(T_\mathrm{v})/k_\mathrm{B} T_\mathrm{v}$$

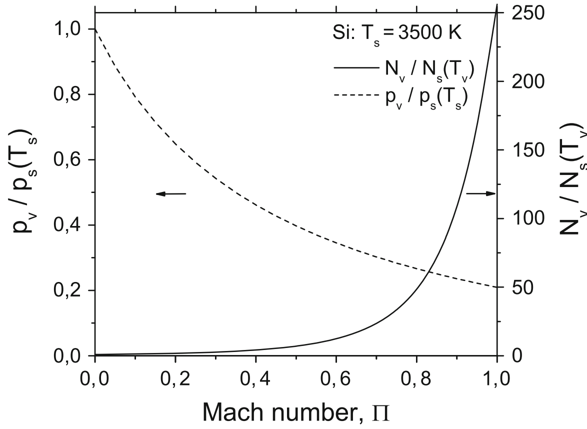

Fig. 3.6 Ratios of the vapor pressures within and beyond the Knudsen layer (*dashed line*) and the densities of the vaporized species obtained from the Anisimov analysis and from Clausius-Clapeyron equation (*solid line*) as a function of the Mach number for a silicon surface at 3,500 K

An example is reported in Fig. 3.6. The ratios $N_v/N_s(T_v)$ and $p_v/p_s(T_s)$ for a silicon target at $T_s = 3{,}500$ K are plotted as a function of the Mach number Π.

The supersaturation is always present ($N_v/N_s(T_v) > 1$), and it is much stronger for high values of Π (i.e., for low ambient pressures). Therefore, the recondensation of the evaporated species may start beyond the Knudsen layer. Besides, in the presence of a reactive atmosphere, the chemical reaction between the vapor and the ambient gas might lead to the formation and the subsequent condensation of chemical compounds. The pressure acting on the target surface is the pressure inside the Knudsen layer, that is the saturated vapor pressure p_s at the temperature T_s, given by the Clausius-Clapeyron equation (3.29). For silicon at $T_s = 3{,}500$ K, we have $p_s(T_s) \simeq 10^2$ bar. The dramatic effect of the surface temperature on the saturated vapor pressure is illustrated in Fig. 3.7: the surface temperature profiles of the silicon target already shown in Fig. 3.4 have been used to compute the vapor pressure vs. time according to the Clausius-Clapeyron equation.

A moderate increment of the surface temperature from 3,000 to 3,500 K leads to the enormous increase of the vapor pressure from 10 bar to almost 160 bar for a time interval comparable to the pulse duration ($\tau_{pulse} = 55$ ns).

3.5.3 *Plasma Formation*

When the laser irradiance is high enough ($\geq 10^9$ W/cm^2), the vapor or the ambient gas can become ionized, and properly described as a *plasma*. Within a gas at temperature T_g, the collisions between thermal electrons and vaporized species produce a certain degree of ionization given by the Saha equation [61]. The ionized

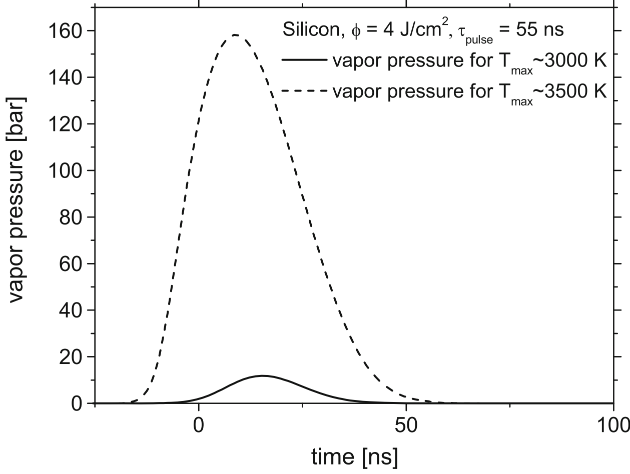

Fig. 3.7 Influence of the Si surface temperature on the saturated vapor pressure (the temperature profiles shown in Fig. 3.4 have been used to calculate the vapor pressures)

gas strongly absorbs the laser radiation and expands within the laser beam channel, thus shielding the substrate from the laser light. The propagating plasma is generally termed LSAW. If the LSAW moves with subsonic velocity with respect to the ambient medium, it is called laser-supported combustion wave (LSCW). As the laser intensity increases, the LSAW can exceed the sound speed becoming a laser-supported detonation wave (LSDW). The typical irradiance necessary to ionize a gas with a free propagating laser (i.e., without any target) is of the order of $10^9 - 10^{11}$ W/cm^2, but it can decrease by several orders of magnitude in front of a solid or liquid target [28, 61]. The theories of LSC and LSD waves have been developed in the Seventies [6, 75–77] obtaining quantitative evaluations of the propagation velocity of the wave front and the pressure behind it. In the case of LSC wave, the laser-light is absorbed within the plasma and dissipated in the ambient medium via heat conduction and thermal radiation. The energy balance can be written as [77]:

$$k^{\text{eff}} \Delta T / d = d(\alpha_{\text{p}} I_0 - J^{\text{loss}}), \tag{3.40}$$

where k^{eff} is an effective thermal conductivity, α_{p} is the absorption coefficient of the plasma, ΔT is the temperature jump across the LSC wave, d is the thickness of the wave front, I_0 is the laser irradiance, and J^{loss} is the volumetric energy loss [J/cm^3 s] of the plasma, due to radiation/conduction. Using the heat transport equation, we obtain [77]:

$$C_{\text{gas}} \frac{\partial T}{\partial t} = C_{\text{gas}} v_{\text{LSC}} \frac{\Delta T}{\Delta x} = v_{\text{LSC}} C_{\text{gas}} \frac{\Delta T}{d} = k^{\text{eff}} \frac{\Delta T}{d^2} \tag{3.41}$$

where C_{gas} is the specific heat of the hot gas, while v_{LSC} is the velocity of the wave front. Using (3.40) in (3.41) to eliminate d, the LSCW front velocity becomes [77]:

$$v_{LSC} = \frac{k^{eff}}{C_{gas}} \sqrt{\frac{\alpha_p I_0 - J^{loss}}{k^{eff} \Delta T}}. \tag{3.42}$$

For intense laser beams ($I_0 \gg J^{loss}/\alpha_p$), we have $v_{LSC} \propto I_0^{1/2}$ and typical values of $10 - 100$ m/s [28]. On the other hand, if $I_0 \approx J^{loss}/\alpha_p$, we have $v_{LSC} \approx 0$ and the LSCW becomes a stationary wave called *plasmatron* [78, 79]. If the velocity of the propagating wave exceeds the sound velocity of the medium, a supersonic LSD wave is produced. Treating such a wave as a hydrodynamic discontinuity, and using the conservation of mass, momentum and energy, its velocity can be estimated as [75]:

$$v_{LSD} = [2(\gamma^2 - 1) I_0/\rho_0]^{1/3} \propto I_0^{1/3}, \tag{3.43}$$

where γ is the adiabatic coefficient and ρ_0 is the mass density of the ambient gas. The gas pressure behind the wave is [75]:

$$p_{LSD} = \frac{\rho_0 \, v_{LSD}^2}{\gamma + 1} \propto I_0^{2/3}. \tag{3.44}$$

Even at moderate laser irradiance $I_0 \approx 10^8$ W/cm^2 and considering air in standard conditions ($\rho_0 \approx 1.3$ kg/m^3 and $\gamma \approx 7/5$) as a medium, we obtain $v_{LSD} \approx 10^4$ m/s and $p_{LSD} \approx 5 \times 10^2$ bar.

It is clear that in both cases of pure vaporization or plasma formation, the pressure acting on the target surface is of the order of 10^2 bar, and the melt can be heated well above the boiling point. Such high pressures acting on the surface might give rise to strong hydrodynamic motion (convection, piston effect) of the molten layer.

3.5.4 Laser Supported Absorption Waves

The vapor formed by intense laser irradiation plays an important role in laser material treatment. The range of irradiances where evaporation is achieved stretches from some 10^3 W/cm^2 to the highest realized irradiances of 10^{21} W/cm^2 [5, 80, 81]. It is clear that many physically distinct regimes are found in this enormous energy range. At relatively low irradiances (below 10^6 W/cm^2), the vapor is tenuous and essentially transparent, but with increasing irradiance it becomes supersaturated. Between roughly 10^7 and 10^{10} W/cm^2 and depending on the wavelength, the vapor becomes partially ionized and absorbs a substantial fraction of the laser energy. On the other hand, radiation re-emitted from the vapor plasma may heat the solid very efficiently [8].

If the vapor becomes ionized and absorbs part or all of the incident irradiation, the energy is converted into internal energy of the plasma, radiated away as

thermal radiation or consumed in hydrodynamic motion. This plasma forms close to the evaporating surface, and the temperature and degree of ionization depend on the incident irradiance. If an absorbing gas plasma has formed, an interesting effect is observed. The plasma expands from the surface and moves towards the incoming laser beam. Such a propagating plasma is called LSAW. LSA waves are generally divided into several regimes: Laser Supported Combustion (LSC), Laser Supported Detonation (LSD), and Laser Supported Radiation (LSR). All these and the related phenomena are extensively described theoretically in the literature [6, 8, 73, 75, 76, 82–87], but experimental results are rarely found. The two most important regimes are divided according to the propagation velocity of the plasma front, i.e., if the latter is subsonic or supersonic with respect to the gas. The weakly absorbing subsonic variation is called LSCW. The absorbing plasma heats and compresses the surrounding gas by expansion and thermal radiation until this hot and compressed gas itself becomes an absorbing plasma. Under these condition, the absorption front is moving towards the laser beam, because the metal surface is blocking its propagation in the opposite direction. For this case, a stationary plasma above the surface is formed. A similar behavior is valid for the LSD wave, except that there the plasma front is moving with supersonic velocity and the laser radiation if fully absorbed in the plasma front. The theory of LSC and LSD waves was formulated by Raizer [6], who calculated the plasma surface pressure (plasma pressure acting at the surface) caused by the LSD waves to be:

$$p_s^{\mathrm{LSD}} = \frac{[2(\gamma^2-1)]^{2/3}}{\gamma+1}\left[\frac{\gamma+1}{2\gamma}\right]^{\frac{2\gamma}{\gamma-1}} \rho_0^{1/3} I_0^{2/3} \tag{3.45}$$

and the velocity of the LSD wave v_w^{LSD} to be:

$$v_w^{\mathrm{LSD}} = \left[2(\gamma^2-1)\frac{I_0}{\rho_0}\right]^{1/3}. \tag{3.46}$$

For the LSC wave [82, 83, 88] the surface pressure is:

$$p_s^{\mathrm{LSC}} = \left[1-\frac{2W}{\gamma_0-1}\right]\left[\frac{\gamma_0+1}{2}\right]^{1/3}\left[\frac{(\gamma-1)(\gamma+1)}{(\gamma+W)(\gamma_0-1-2W)}\right]^{2/3} \rho_0^{1/3} I_0^{2/3}, \tag{3.47}$$

with W being a dimensionless particle velocity, $W = 0.009 \cdot I_0^{2/3}$ for I_0 in $\mathrm{MW/cm^2}$. The wave velocity is:

$$v_w^{\mathrm{LSC}} = (W+1)\left[\frac{2(\gamma-1)(\gamma_0-1)}{(\gamma_0+1)(\gamma+W)(\gamma_0-1-2W)} \cdot \frac{I_0}{\rho}\right]^{1/3} \tag{3.48}$$

where $\gamma_0 = 1.4$ and $\gamma = 1.2$ are the adiabatic exponents for the surrounding gas and the metal vapor, respectively.

For the irradiation with 4 J/cm^2, i.e., for an irradiance of 7.27×10^7 W/cm^2, taken as constant for 55 ns, a LSC pressure of $p_s^{LSC} = 48$ MPa is derived. This is in agreement with experimental results given by Schutte [89].

Reilly et al. [90] developed a model for the temporal behavior of the plasma pressure in a LSC wave. They estimated the time when the rarefaction fans from the sides and the top reaches the surface and thus lower the plasma surface pressure. For the modeling of the temporal behavior of the plasma pressure acting at the surface, Reilly et al. used a two-dimensional model [90], which takes into account the expansion of the plasma at its lateral borders. During expansion, zones with lowered pressures are formed, and they move inwards with the sound velocity c_S inside the plasma. The time τ_{2D}, which is needed by the lateral rarefaction fans to reach the center is given by:

$$\tau_{2D} = \frac{r_p}{c_S}, \quad (3.49)$$

where r_p is the radius of the laser spot (here assumed circular) and the sound velocity c_S is given by:

$$c_S^{LSC} = \left(\frac{\gamma\, p_s^{LSC}}{\rho_0}\right)^{1/2} \left[\frac{W+1}{W}\,\frac{\gamma_0 - 1}{\gamma_0 + 1}\right]^{1/2}. \quad (3.50)$$

A second rarefaction wave is starting when the laser pulse ends at time τ_p and the shock wave is no longer heated by the laser beam, but is still expanding and cooling. The rarefaction then needs the time τ_z:

$$\tau_z = \tau_p + v_w^{LSC} \tau_p / c_S^{LSC} \quad (3.51)$$

to reach the metal surface. In conclusion, the development of the plasma pressure $p_S(t)$ in time, acting at the surface, is characterized by the three times τ_p, τ_z, and τ_{2D}. If we assume a LSC wave, different cases have to be regarded, depending on the order of these times. For the present case with the values of $I = 72$ MW/cm^2, $\rho_0 = 1.25$ g/cm^3, $\gamma = 1.2$, and $\gamma_0 = 1.4$ a sound velocity of $c_S = 7{,}551$ m/s is obtained[1]. Taking the width of the laser spot as $r_p = 2$ mm, we obtain $\tau_{2D} = 265$ ns and from (3.51) follows $\tau_z = 113$ ns. Therefore, the times order as $\tau_p \leq \tau_z \leq \tau_{2D}$ and according to Reilly [90] the following behavior of the plasma surface pressure at the center of the laser spot is obtained:

$$t \leq \tau_z : p(t) = p_P \quad (3.52)$$

$$\tau_z \leq t \leq \tau_{2D} : p(t) = p_P \left(\frac{t}{\tau_z}\right)^{-2/3} \quad (3.53)$$

$$\tau_{2D} \leq t : p(t) = p(\tau_{2D}) \left(\frac{t}{\tau_{2D}}\right)^{-6/5}. \quad (3.54)$$

[1] Here, a constant laser irradiance over the 55 ns pulse duration is assumed.

It is important to note that the high pressures induced by the plasma waves is acting for times much longer than the laser pulse duration and also larger than the time the surface remains liquid.

3.6 Material Transport Phenomena

At laser molten metal surfaces, many mechanisms contribute to material transport phenomena, such as convection, evaporation, and hydrodynamic motions caused by temperature and pressure gradients [1, 8, 73, 91]. The pressures are produced by the evaporation itself (recoil pressure) or by the LSAW as discussed before. The most important mechanisms for lateral material transport in the liquid state are connected to the temperature dependence of the surface tension $\sigma(T)$ and the piston mechanism [1, 4]. Variations of the surface tension may arise from temperature gradients across the surface of the molten material. If this is due to an inhomogeneous laser intensity profile, this is called thermocapillary effect. An approximation of the radial component of this effect is given by Baeuerle [1],

$$v_{\text{lat}} \approx \frac{d_{\text{liq}} \Delta T}{\eta_{\text{v}} d_p} \cdot \frac{\mathrm{d}\sigma}{\mathrm{d}T}, \tag{3.55}$$

where d_{liq} again is the melting depth, ΔT the lateral temperature difference, η_{v} the dynamic viscosity of the material, d_{p} the diameter of the laser spot and $\mathrm{d}\sigma/\mathrm{d}T$ the temperature dependence of the surface tension. An upper limit for the velocity v_{lat} as calculated with the values $\mathrm{d}\sigma/\mathrm{d}T = -5 \times 10^{-4}$ N/(m K), $d_{\text{p}} = 2$ mm, $d_{\text{liq}} = 1$ µm, $\eta_v = 6.9 \times 10^{-3}$ Pa·s and $\Delta T = 4,700$ K, yields $v_{\text{lat}} \approx 0.2$ m/s.

There are two other main mechanisms of material removal in the beam interaction zone: (a) melt ejection by the vaporization-induced recoil pressure and plasma pressure and (b) melt evaporation (high power or short pulses) [92]. At moderate temperatures above the melting temperature, the vaporization recoil and plasma pressure are the primary factors for the material transport out of the laser beam interaction zone under the regime of hydrodynamic flow. At higher surface temperature (higher fluences), the melt removal due to evaporation exceeds the hydrodynamic mechanism. The mechanisms of the propagation of the evaporation front were considered in detail by Anisimov and Khokhlov [73].

The vapor particles escaping from a hot surface have a Maxwellian velocity distribution corresponding to the surface temperature, but their velocity vectors all point away from the surface. This anisotropic distribution is brought to equilibrium within a few mean-free paths by atomic collisions (Knudsen layer) [86, 93–96]. Some of them are also scattered back to the surface and are then contributing to the recoil pressure [92], which is in the order of the saturated vapor pressure [73]. Beyond this Knudsen layer, the vapor reaches a new internal equilibrium with homogeneous velocity distribution, but with a different temperature. Poprawe [86] made

a detailed calculation of the recoil pressure p_r. For the irradiation with 4 J/cm^2, for example, we achieved $p_r = 2.9 \times 10^7$ Pa, when using his parameterizations.

As just discussed, a high plasma pressure and the recoil pressure are acting at the liquid surface inside the laser spot of length a and width b. This pressure difference to the ambient pressure Δp is acting as a piston and moves material from the center through the sides out of the melt pool. This causes a lowering of the surface by the piston.

The problem was treated by von Allmen [4, 8] and also by Luft et al. [97] for pulsed laser drilling. They assumed a non-viscous and incompressible melt and the pressure distribution was approximated by a " top hat" profile with pressure $p_0 + \Delta p$ inside the laser spot of radius r_p and ambient pressure p_0 outside. Then, the radial velocity of the melt extraction follows from the volume work:

$$v_{\text{lat}} = \sqrt{\frac{2\Delta p}{\rho}} \tag{3.56}$$

where ρ is the density of the liquid ($\rho = 7$ g/cm^3) and Δp is the pressure difference which is given by the sum of plasma pressure and recoil pressure $\Delta p = p_p + p_r$. With $p_r = 2.9 \times 10^7$ Pa and $p_p = 4.8 \times 10^7$ Pa, this yields $v_{\text{lat}} = 148$ m/s, which has to be compared to a lateral velocity $v_r \approx 0.2$ m/s, induced by the Marangoni convection [1]). Thus, the piston mechanism should be the dominant mechanism for the lateral material transport.

The liquid escapes through the perimeter of the melt pool and if the two streams of melt extraction and new laser melting are in a stationary state, i.e., u is describing the velocity of the lowering piston, by assuming a rectangular laser spot with dimensions $a \times b$ and the pressure being constant inside the laser spot, we obtain:

$$\dot{V}_{\text{lat}} = \dot{V}_{\text{pist}} \Leftrightarrow 2(a+b)\, d_{\text{liq}}\, \rho\, v_{\text{lat}} = a\, b\, \rho\, u. \tag{3.57}$$

The thickness of the melt d_{liq} was estimated [8] to be:

$$d_{\text{liq}} = \frac{k}{u} \ln\left(\frac{T_b}{T_m}\right), \tag{3.58}$$

so that for the velocity of the piston movement u follows:

$$u = \sqrt{\frac{2(a+b)\, k\, \ln(T_b/T_m)}{a \cdot b}} \cdot \left(\frac{2\Delta p}{\rho}\right)^{1/4}. \tag{3.59}$$

Since the numerical simulation for the melting depth d_{liq} has been performed, it is much more accurate to use this for the calculation of the piston effect. From (3.57), we can extract the following expression for the total piston movement or surface lowering Δz^{pist} during the laser pulse:

$$\Delta z^{\text{pist}} = \int_0^{t_{\text{liq}}} \frac{2 \cdot (a+b) \cdot d_{\text{liq}}(t)}{a \cdot b} \cdot \sqrt{\frac{2\Delta p}{\rho}}\, \mathrm{d}t. \tag{3.60}$$

For example by using $\rho = 7\,\text{g/cm}^3$, area $A = a \times b = 2 \times 3\,\text{mm}^2$ and a pressure difference $\Delta p = (4.8 + 2.9) \times 10^7\,\text{Pa}$, we calculate for $\phi = 4\,\text{J/cm}^2$ with the simulation given above a piston effect of $\Delta z^{\text{pist}} = 12(4)\,\text{nm/pulse}$.

Also turbulences or bifurcations may play an important role for a fast material transport. During carburizing of iron by irradiation with a CO_2 laser in propane, carburized layers of about $d \approx 10\,\mu\text{m}$ have been found, where the thickness and homogeneity of these layers could not be explained with diffusion in the liquid state alone [98]. Also during the nitrification of Ti by irradiation with an ns excimer laser in nitrogen atmosphere, a significant influence of turbulences for the transport of the nitrogen is expected [99, 100]. These turbulences in the liquid surface may evolve from pressure gradients, produced by local changes in the plasma density or the temperature [101]. The number of turns of a turbulence during irradiation is approximated [101, 102] via the lateral material velocity v_{lat} and the pulse duration τ_{p}. It follows a traveling distance $\Delta s = v_{\text{m}}\tau$ for a surface element. The lateral extension a_{bifurc} of the bifurcation is approximated by the periodicity of the structures at the surface after the irradiation [98,102]. As an example, for a velocity of $v_{\text{lat}} = 124\,\text{m/s}$ and with $\tau_{\text{p}} = 55\,\text{ns}$, a moving distance of $\Delta s = 12\,\mu\text{m}$ is approximated.

3.7 Conclusions

The chapter shows the fundamental physical processes taking place during irradiation of materials with lasers. Heating and vaporization have been explained in relation to interaction times and have been calculated by means of heat transfer modeling and the Knudsen layer model. Lattice dynamics, electron-phonon coupling, phase transitions, and electromagnetic wave propagation have been described and related to the material properties. Plasma development and the formation of shock waves were shown too. The describing formulation offers additional information about reacting pressure induced forces and recondensation effects. Transport phenomena like convection or melt ejection (Piston effect) have been explained as well. Summarized, the chapter gives a detailed insight into the physics occurring during laser material interaction.

Acknowledgements A significant part of this work was financially supported by the Deutsche Forschungsgemeinschaft (grants DFG Scha 632/3, /4, /9, /10, and /11), which is gratefully acknowledged.

References

1. D. Bäuerle, *Laser Processing and Chemistry*. Springer Series in Materials Science (Springer, Berlin, 1996)
2. J.F. Ready, J. Appl. Phys. **36**, 462 (1965)
3. J.F. Ready, *Effects of High-Power Laser Radiation* (Academic, New York, 1971)
4. M. von Allmen, J. Appl. Phys. **47**, 5460 (1976)

5. M. von Allmen, *Laser Beam Interactions with Materials*, *Springer Series in Materials Science*, vol. 2. (Springer, Berlin, 1987)
6. Y.P. Raizer, Sov. Phys. JEPT **31**, 1148 (1970)
7. D. Bäuerle, *Chemical Processing with Lasers*. Springer Series in Materials Science (Springer, Berlin, 1986)
8. M. von Allmen, A. Blatter, *Laser-Beam Interactions with Materials*. Springer Series in Materials Sciences (Springer, Berlin, 1994)
9. A. Einstein, Physikal. Zeitschrift **18**, 121 (1917)
10. T.H. Maimann, Nature **187**, 493 (1960)
11. M. Bertolotti (ed.), *Physical Processes in Laser-Materials Interactions*. (Plenum, New York, 1983)
12. M. Bass (ed.), *Laser Materials Processing*, *Materials processing – Theory and Practices*, vol. 3. (North Holland Publishing Company, Amsterdam, 1983)
13. B.L. Mordike (ed.), *Laser treatment of materials, Proc. 1st European Conference on Laser Treatment of Materials, ECLAT 1986, Bad Nauheim, Germany* (DGM Informationsgesellschaft, Oberursel, 1987)
14. W. Waidelich (ed.), *Laser, Optoelektronik in der Technik, Proc. 8. International Congress 'LASER87', München, Germany* (Springer, Berlin, 1987)
15. H. Sossenheimer, G. Sepold (eds.), *Proc. 2nd European Conference on Laser Treatment of Materials, ECLAT 1988, Bad Nauheim, Germany* (DVS-Verlag, Düsseldorf, 1988)
16. H.W. Bergmann, R. Kupfer (eds.), *Proc. 3rd European Conference on Laser Treatment of Materials, ECLAT 1990, Erlangen, Germany* (Sprechsaal Publishing Group, Coburg, 1990)
17. H. Gobrecht, *Optik*, *Bergmann-Schäfer: Lehrbuch der Experimentalphysik*, vol. 3. (Verlag Walter de Gruyter, Berlin, 1978)
18. K. Tradowski, *Laser: Grundlagen, Technik, Anwendungen* (Vogel-Verlag, Würzburg, 1979)
19. H. Weber, G. Herziger, *Laser – Grundlagen und Anwendungen* (Physik-Verlag, Weinheim, 1979)
20. F.K. Kneubühl, M.W. Sigrist, *Laser* (Teubner Taschenbücher Physik, Stuttgart, 1995)
21. H.W. Bergmann, S.Z. Lee, Opto Elektronik Magazin **3**, 623 (1987)
22. O. Svelto, *Principles of Lasers* (Springer, New York, 1998)
23. M. Bass, in *Laser Materials Processing*, *Materials processing – Theory and Practices*, vol. 3 ed. by Bass (North Holland Publishing Company, Amsterdam, 1983), chap. 1, pp. 1–14
24. I.J. Spalding, in *Physical Processes in Laser-Materials Interactions*. ed. by (Plenum, New York, 1983), pp. 1–47
25. T. Manzur, T. de Maria, W. Chen, C. Roychoudhuri, Proc. SPIE **2703**, 490 (1996)
26. U. Sowada, H.J. Kahler, D. Basting, World Lasers Almanac **1**, 50 (1988)
27. K.J. Schmatjko, G. Endres, World Lasers Almanac **1**, 46 (1988)
28. M. von Allmen, A. Blatter, *Laser-Beam Interactions with Materials.* (Springer, Berlin, 1998)
29. N.W. Ashcroft, N.D. Mermin, *Solid State Physics.* (Saunders College, Philadelphia, 1976)
30. D. Pines, P. Nozières, *The Theory of Quantum Liquids.* (Benjamin, New York, 1966)
31. M. Wolf, T. Hertel, E. Knoesel, G. Ertl, Phys. Rev. Lett. **76**, 535 (1996)
32. R. Burgermeister, M. Aeschlimann, R. Knorren, K.H. Bennemann, Phys. Rev. B **61**, 9427 (2000)
33. G. Grimvall, *The Electron–Phonon Interaction in Metals* (North-Holland, Amsterdam, 1981)
34. P.B. Allen, Phys. Rev. Lett. **59**, 1460 (1987)
35. P.B. Allen, Phys. Rev. B **36**, 2920 (1987)
36. B.L. Kapeliovich, S.I. Anisimov, T.L. Perel'man, Sov. Phys. JETP **39**, 375 (1975)
37. L.H. Acioli, E.P. Ippen, C.-K. Sun, F. Vallée, J.G. Fujimoto, Phys. Rev. B **50**, 15337 (1994)
38. R. Sprik, R.H.M. Groeneveld, A. Lagendijk, Phys. Rev. B **51**, 11433 (1995)
39. D. Bejan, G. Raşeev, Phys. Rev. B **55**, 4250 (1997)
40. V.E. Gusev, O.B. Wright, Phys. Rev. B **57**, 2878 (1999)
41. A.V. Lugovskoy, I. Bray, Phys. Rev. B **60**, 3279 (1999)
42. M. Achermann, S. Tzortzakis, D. Christofilos, N. Del Fatti, C. Voisin, F. Vallée, Phys. Rev. B **61**, 16956 (2000)

43. M. Vicaneck, B. Rethfeld, A. Kaiser, G. Simon, Phys. Rev. B **65**, 214303 (2002)
44. M. Lisowski, P.A. Loukakos, U. Bovensiepen, J. Stähler, C. Gahl, M. Wolf, Appl. Phys. A **78**, 165 (2004)
45. E. Carpene, Phys. Rev B **74**, 024301 (2006)
46. A. Daunois, E. Beaurepaire, J.-C. Merle, J.Y. Bigot, Phys. Rev. Lett. **76**, 4250 (1996)
47. I.M. Lifshitz, M.I. Kaganov, L.V. Tanatarov, Sov. Phys. JETP **4**, 173 (1957)
48. C. Kittel, *Introduction to Solid State Physics* (Wiley, New York, 1971)
49. S. Funk, M. Wolf, S.S. Wellershoff, M. Bonn, D. N. Denzler, J. Hohlfeld, Phys. Rev. B **61**, 1101 (2000)
50. CRC, *Handbook of Chemistry and Physics, 63 rd. Edition* (CRC, Boca Raton, 1982/1983)
51. J.R. Bettis, Appl. Opt. **31**, 3448 (1992)
52. V. Letokhov, Appl. Phys. B Lasers Opt. **46**(3), 237 (1988)
53. D. von der Linde, K. Sokolowski-Tinten, J. Bialkowski, Appl. Surf. Sci. **109–110**, 1 (1997)
54. C. Chou, S. Polyakov, A. Kuzmich, H. Kimble, Phys. Rev. Lett. **92**(21), 213601 (2004)
55. T. Mayer-Kuckuk, *Atomphysik* (BG Teubner, Stuttgart, 1997)
56. M.F. Allmen, in *Physical Processes in Laser-Materials Interactions*, ed. by M. Bertolotti (Plenum, New York, 1983) chap. 2, pp. 49–75
57. P. Grosse, *Freie Elektronen in Festkörpern.* (Springer, Berlin, 1979)
58. G.E.R. Schulze, *Metallographie.* (Springer, Wien-New York, 1974)
59. W. Amende, *Härten von Werkstoffen und Bauteilen des Maschinenbaus mit dem Hochleistungslaser*. Technologie Aktuell 3 (VDI-Verlag, Düsseldorf, 1985)
60. J.D. Jackson, *Klassische Elektrodynamik.* (Verlag Walter de Gruyter, Berlin, 1983)
61. D. Bäuerle, *Laser Processing and Chemistry* (Springer, Heidelberg, 2000)
62. V.G. Gregson, in *Laser Materials Processing*, *Materials processing – Theory and Practices*, vol. 3, ed. by Bass (North Holland Publishing Company, Amsterdam, 1983), chap. 4, pp. 201–233
63. H.F. Mark (ed.), *Encyclopedia of Chemical Technology / Kirk-Othmer* (Wiley, New York, 1978)
64. C.A.J. Fletcher, *Computational Techniques for Fluid Dynamic 1.* (Springer, Berlin, 1988)
65. S. Fähler, H.U. Krebs, Appl. Surf. Sci. **96–98**, 61 (1996)
66. C. Illgner, P. Schaaf, K.P. Lieb, R. Queitsch, J. Barnikel, J. Appl. Phys. **83**(6), 2907 (1998)
67. C. Illgner, Untersuchungen zum Lasernitrieren von Eisen. Ph.D. thesis, Universität Göttingen, Göttingen (1997)
68. F. Landry, Lasernitrieren von Armco-eisen und Eisenwerkstoffen. Ph.D. thesis, Universität Göttingen, Göttingen (1999)
69. E. Carpene, P. Schaaf, Phys. Rev. B **65**, 224111 (2002)
70. Y.S. Touloukian, C.Y. Ho (eds.), *Thermophysical Properties of Matter*, vol. 1 and 4. (Plenum, New York, 1970)
71. S. Higashi, T. Sameshima, Jpn. J. Appl. Phys. **40**, 480 (2001)
72. M. Hatano, S. Moon, M. Lee, K. Suzuki, C.P. Grigoropoulos, J. Appl. Phys. **87**, 36 (2001)
73. S.I. Anisimov, V.A. Khokhlov, *Instabilities in Laser-Matter Interaction.* (CRC, Boca Raton, London, Tokyo, 1995)
74. S.I. Anisimov, Sov. Phys. JETP **27**, 182 (1968)
75. Y.P. Raizer, Sov. Phys. JETP **21**, 1009 (1965)
76. A. Pirri, Phys. Fluids **16**, 1435 (1973)
77. A.A. Boni, F.Y. Su, Phys. Fluids **17**, 340 (1974)
78. Y.P. Raizer, Sov. Phys. Usp. **23**, 789 (1980)
79. Y.P. Raizer, Sov. Phys. Quantum Electron. **14**, 40 (1984)
80. B.N. Chichkov, C. Momma, S. Nolte, F.V. Alvensleben, A. Tünnermann, Appl. Phys. A **63**, 109 (1996)
81. G. Marowsky, C.K. Rhodes, Appl. Phys. B **66**, 475 (1998)
82. A.N. Pirri, R.C. Root, P.K.S. Wu, AIAA J. **16**, 1296 (1978)
83. A.A. Boni, F.Y. Su, P.D. Thomas, H.M. Musal, Theoretical study of laser-target interactions. Final Tech. Report SAI 77-77-567-LJ, Science Application Inc., La Jolla, California (1977)
84. L.I. Sedov, *Similarity and Dimensional Methods in Mechanics* (Academic, New York, 1959)

85. N. Ferriter, D.E. Maiden, A.M. Winslow, J.A. Fleck, AIAA J. **5**, 1597 (1977)
86. R. Poprawe, Materialabtragung und Plasmaformation im Strahlungsfeld von UV-Lasern. Dissertation, Technische Hochschule Darmstadt (1984)
87. B.S. Holmes, C. Tarver, D.C. Ehrlich, H.E. Lindberg, The mechanical loads from LSD waves and their simultation. Final Report F29601-74-C-0051, Stanford Research Institute (1976)
88. R.G. Root, in *Laser-Induced Plasmas and Applications*, eds. by L.J. Radziemski, D.A. Cremers (Marcel Dekker Inc., New York, 1992)
89. K. Schutte, Prozessdiagnostik und technologische Untersuchungen zur Materialbearbeitung mit Excimerlasern. Ph.D. thesis, Universität Erlangen-Nürnberg, Nürnberg (1993)
90. J.P. Reilly, A. Ballantyne, J.A. Woodroffe, AIAA J. **17** (10), 1098 (1979)
91. H. Ishiguro, K. Ohyama, H. Nariai, T. Teramoto, J. Nucl. Sci. Technol. **27**(12), 1115 (1990)
92. V. Semak, A. Matsunawa, J. Phys. D: Appl. Phys. **30**, 2541 (1997)
93. R. Kelly, R.W. Dreyfus, Nucl. Instr. Methods B **32**, 341 (1988)
94. R. Kelly, J.E. Rothenberg, Nucl. Instr. Methods B **7/8**, 755 (1985)
95. R. Kelly, A. Miotello, B. Braren, C.E. Otis, Appl. Phys. Lett. **60** (24), 2980 (1992)
96. R. Bellantone, Y. Hahn, J. Appl. Phys. **78**, 1436 (1994)
97. A. Luft, U. Franz, A. Emsermann, J. Kaspar, Appl. Phys. A **63**, 93 (1996)
98. V.N. Anisimov, V.Y. Baranov, L.A. Bolshov, A.I. Ilyin, C.V. Kopetskii, V.S. Kraposhin, D.D. Malyuta, L.A. Matveeva, V.D. Pismennyi, A.Y. Sebrant, Phys. Chem. Mech. Surf. **3** (9), 2756 (1985)
99. E. D'Anna, G. Leggieri, A. Luches, Thin Solid Films **218**, 219 (1992)
100. I.N. Mihailescu, N. Chitica, L.C. Nistor, M. Popescu, V.S. Teodorescu, I. Ursu, A. Andrei, A. Barborica, A. Luches, M. Luisa de Giorgi, A. Perrone, B. Dubreuil, J. Hermann, J. Appl. Phys. **74**, 5781 (1993)
101. V.N. Anisimov, R.V. Arutyunyan, V.Y. Baranov, L.A. Bolshov, E.P. Velikhov, V.A. Dolgov, A.I. Ilyin, A.M. Kovalevich, V.S. Kraposhin, D.D. Malyuta, L.A. Matveeva, V.S. Mezhevov, V.D. Pismennyi, A.Y. Sebrant, Y.Y. Stepanov, M.A. Stepanova, Appl. Opt. **23**, 18 (1984)
102. E. D'Anna, G. Leggieri, A. Luches, M. Martino, A.V. Drigo, I.N. Mihailescu, S. Ganatsios, J. Appl. Phys. **69**, 1687 (1991)

Chapter 4
Laser–Plasma Interactions

Ion N. Mihailescu and Jörg Hermann

Abstract The purpose of the present chapter is to give an introduction into the physics of laser plasma interactions that govern the coupling of laser energy into the matter. Processes induced by laser pulses of nano- and femtosecond durations are discussed in the framework of different applications. In particular, the roles of non-linear absorption and avalanche ionization in plasma heating are discussed and a critical review of related experimental and theoretical studies is given.

4.1 Introduction

Both lasers and plasmas have unique properties that offer a multitude of applications through their interactions. There are presently several different approaches of the basic physical phenomena involved in the laser–plasma interactions. The interaction between the laser radiation and plasma can be firstly described in terms of resonant and nonresonant processes. The resonant interaction demands either that the photon energy matches with a precise transition between two energy levels of a plasma atom or molecule, or that the laser frequency equals the plasma frequency, a situation known as "resonant absorption." The nonresonant process is characterized by the interaction of the electromagnetic laser radiation with the free charges in plasma. The electrons basically interact with laser radiation due to their definitely higher mobility as compared with the ions. Another classification starts from the duration of laser pulses involved in the interaction processes. In the case of extensively investigated generation and heating of plasmas by typically nanosecond

I.N. Mihailescu (✉)
National Institute for Lasers, Plasma and Radiation Physics, Lasers Department, "Laser-Surface-Plasma Interactions" Laboratory, PO Box MG-54, RO-77125, Bucharest-Magurele, Romania
e-mail: ion.mihailescu@inflpr.ro

J. Hermann (✉)
Laboratoire Lasers, Plasmas et Procédés Photoniques, LP3 UMR 6182 CNRS - Université Aix-Marseille II, Campus de Luminy, Case 917, 13288 Marseille Cedex 9, France
e-mail: hermann@lp3.univ-mrs.fr

pulses, the interaction of laser radiation with the plasma occurs in density gradients with a scale length of tens or hundreds of laser wavelengths. Conversely, with very short pico- and femtosecond laser pulses and higher intensities, the density gradients become exceedingly sharp. It is therefore possible to study the interaction of laser radiation with a density discontinuity from vacuum to a solid in a distance which is short compared with the optical wavelength. The coupling of high intensity laser radiation to plasmas has been the subject of thoughtful experimental investigations for many years. Dedicated experiments have focused on measuring a broad range of phenomena, such as:

1. Resonance and collisional absorption
2. Filamentation
3. Density profile and particle distribution modification
4. Growth and saturation of various parametric instabilities

These phenomena depend on both the laser radiation characteristics (intensity, wavelength, and pulse duration) and the plasma properties (density, temperature, velocities). The efficient coupling of the laser beam energy to a given target is essential for both fundamental and applied laser–matter interaction research. Thus, the intense laser beam can drive parametric instabilities which scatter laser radiation primarily in the backward direction, resulting in a loss of laser energy incident to the target. We collected in this chapter some recent results and development trends in the laser–plasma interactions domain related to materials processing and organized the next overview in sections dealing with the basic phenomena in the field and the specific processes in the plasma interactions with nano- and femtosecond laser pulses, respectively.

4.2 Fundamentals of Laser–Plasma Interaction

A plasma is an ionized gas containing neutral, positively, and negatively charged particles. It is characterized by its degree of ionization that is unity in the case of complete ionization when no neutral particles are present in the plasma. The plasma is globally neutral due to the high electron mobility (small mass) and the strong Coulomb interaction between charged particles. Although the Coulomb force has a long range interaction, the latter is reduced in a plasma due to electrostatic shielding. This is characterized by the **Debye shielding length**.

$$\lambda_D = \sqrt{\frac{\varepsilon_0 k T_e}{e^2 n_e}}. \tag{4.1}$$

Here, ε_0 is the vacuum permittivity, k is Boltzmann's constant, e is the elemental charge, T_e and n_e are the electrons temperature and density, respectively. The Debye length is the maximum length on which a decay from neutrality is possible or an external electrostatic field can penetrate the plasma. The so-called ***plasma parameter***, commonly defined as the ratio between the potential and kinetic energies of

electrons, is related to the number of electrons inside the Debye sphere having a volume $V_D = \frac{4}{3}\pi\lambda_D{}^3$.[1] We have

$$g = \frac{U}{kT_e} = \frac{1}{n_e\,\lambda_D{}^3}. \tag{4.2}$$

For $kT_e >> U$ ($g << 1$), a large number of electrons are inside the Debye sphere and the collective interactions dominate over binary collisions within the plasma. The most common form of collective interactions are plasma oscillations. A perturbation due to a strong electrostatic field initiates a local decay from neutrality and drives the electrons to reestablish neutrality, causing oscillations around their equilibrium positions. The characteristic ***plasma frequency*** is determined by the Debye length and the thermal electron velocity υ_e:

$$\omega_p = \frac{\upsilon_e}{\lambda_D} = \sqrt{\frac{e^2 n_e}{\varepsilon_0 m}}, \tag{4.3}$$

where m is the mass of the electron. Oscillations of angular frequency $\omega < \omega_p$ can not propagate into the plasma due to the fast electron response that neutralizes the electrostatic field. For plasmas excited by radiation of angular frequency ω, the electron density for which $\omega_p = \omega$ is called ***critical density*** n_{crit} (Fig. 4.1). Then, strong reflection and absorption occur in the plasma sheet close to the zone of critical density.

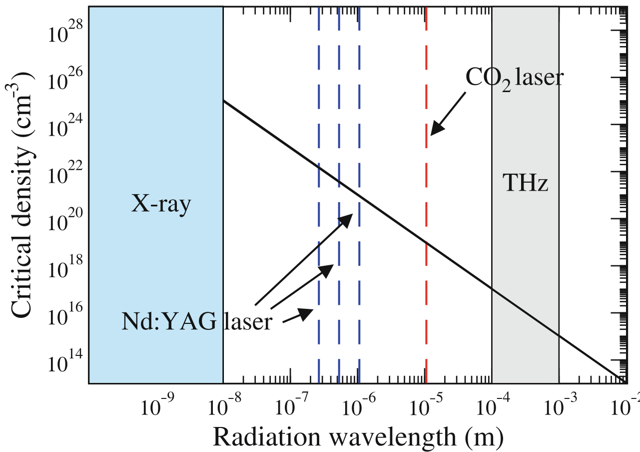

Fig. 4.1 Critical electron density vs. radiation wavelength. The wavelengths of CO_2 laser, Nd:YAG laser and it's second and fourth harmonics are indicated by the *dashed lines*. The spectral ranges of X-rays and THz radiation are presented by the colored boxes

[1] Alternative definitions of the plasma parameter can be found in literature. Some authors use the term ***plasma parameters*** for the general plasma properties.

The critical density is presented in Fig. 4.1 as a function of radiation wavelength.

The generation of a plasma through the absorption of laser radiation may occur via collisional and noncollisional processes. In the former process, called ***inverse bremsstrahlung (IB)***, charged particles absorb laser energy during collisions. The amount of energy being absorbed in a collision due to this effect can be derived from the energy of oscillation of a free electron in an electromagnetic field. The so-called ***quiver energy*** or ***ponderomotive potential*** is [1]

$$E_{\mathrm{q}} = \frac{e^2\mathcal{E}^2}{m\omega^2}, \tag{4.4}$$

where $\mathcal{E}$ is the root-mean-square electric field of laser radiation. Indeed, during a collision an amount of energy of about E_{q} is transformed into kinetic energy of the electron. The rate of growth of the electron energy ε is inferred by multiplying the energy gained per collision by the collision frequency ν_{c}. In a cold neutral gas, collisions are binary and we have $\nu_{\mathrm{c}} = n\upsilon_{\mathrm{e}}\sigma$, where n is the atomic number density and σ the cross section for $\pi/2$ scattering collisions, also called transport cross section. In a plasma, a particle interacts simultaneously with several particles, each causing a weak change of the particle's trajectory. When introducing the ***effective collision frequency*** ν_{eff}, that is, the equivalent frequency of $\pi/2$ scattering collisions,

$$\nu_{\mathrm{eff}} = n\upsilon_{\mathrm{e}}\sigma, \tag{4.5}$$

the growth rate of electron energy is obtained from [2]

$$\frac{\mathrm{d}\varepsilon}{\mathrm{d}t} = \frac{e^2\mathcal{E}^2}{m\omega^2}\nu_{\mathrm{eff}}\frac{\omega^2}{\omega^2 + {\nu_{\mathrm{eff}}}^2}\ . \tag{4.6}$$

The term $\omega^2\left(\omega^2 + {\nu_{\mathrm{eff}}}^2\right)^{-1}$ shows that the electron heating rate via inverse bremsstrahlung diminishes at large collision frequencies. However, at optical laser frequencies, this term can be neglected for gas pressures up to several atmospheres as $\nu_{\mathrm{eff}} << \omega$. The expression (4.6) is valid for all types of electron collisions being characterized by ν_{eff}. Plasma breakdown generally starts with electron heating during collisions with neutral atoms. Later, when the ion density is sufficiently large, the electron–ion IB overcomes the heating due to collisions with neutrals because of the long-distance Coulomb interaction between charged particles. The effective frequency of electron–ion collisions was given by Spitzer [3].

$$\nu_{\mathrm{ei}} = \frac{4}{3}\frac{\sqrt{2\pi}\, e^4 Z^2 n_{\mathrm{i}} \ln\Lambda}{(kT_{\mathrm{e}})^{3/2}\sqrt{m}}. \tag{4.7}$$

Here, Z and n_{i} are the mean charge and density of ions, respectively, and $\ln\Lambda$ is the Coulomb logarithm. By inserting ν_{ei} in (4.6) and multiplying by n_{e}, we obtain the

absorption coefficient due to electron–ion IB in its most common form in cgs units [4]:

$$\alpha_{\rm BI}^{\rm ei} = 3.69 \times 10^8 \frac{Z^3 {n_{\rm i}}^2}{\sqrt{T_{\rm e}}\,\nu^3}\left(1 - e^{-h\nu/kT_{\rm e}}\right), \tag{4.8}$$

where $\nu = \omega/2\pi$ and h is Planck's constant. The term in brackets was added to take into account the lowering of absorption due to induced emission. This term can be neglected when $h\nu >> kT_{\rm e}$. In the high temperature range of particular interest for thermonuclear fusion, the plasma heating efficiency is reduced according to $\alpha_{\rm BI}^{\rm ei} \propto {T_{\rm e}}^{-3/2}$.

Alternatively to the microscopic collisional view, the optical properties of a dense plasma can be derived from the collective behavior of particles. Performing calculations based on the Vlasov equation, Dawson and coworkers obtained [5]

$$\alpha_{\rm BI}^{\rm ei} = \frac{\nu_{\rm ei}\,{\omega_{\rm p}}^2}{c\omega\sqrt{\omega^2 - {\omega_{\rm p}}^2}}. \tag{4.9}$$

For $\omega_{\rm p} = \omega$, the plasma reaches the critical density and becomes completely opaque for the incident laser radiation. One expects a large fraction of incident laser energy being reflected by the critical density plasma. However, most of the laser energy is absorbed in a zone adjacent to the plasma layer of critical density. The fraction of energy reflected by the plasma strongly depends on its density gradient. Thus, the reflection is larger for plasma generation by short laser pulses. The use of mode-locked high intensity laser sources gives rise to noncollisional ionization processes. The ***Keldysh parameter***, that is, the ratio between excitation and tunneling frequencies [6]

$$\gamma = \frac{\omega}{\omega_{\rm tunnel}} = \sqrt{\frac{\Delta_{\rm ion}}{2E_{\rm q}}}, \tag{4.10}$$

classifies the domains of validity of the involved processes. In (4.10), $\Delta_{\rm ion}$ is the ionization energy of atoms. At moderate laser intensities ($\gamma \gg 1$), the tunneling frequency is small with respect to the laser frequency and the ionization proceeds through ***multiphoton absorption***. When the frequencies are almost equal ($\gamma \approx 1$), the ***tunneling ionization*** dominates [7]. If the laser frequency is much lower than the tunneling frequency ($\gamma << 1$), field ionization is the most prominent mechanism. The ionization rates can be computed using the theory of Keldysh [6] or the Ammosov–Delone–Krainov (ADK) model [8] that was shown to give more precise data [9]. A rough estimation of the ionization probability is possible using the simple expression proposed by Morgan [10]:

$$\alpha_k = \frac{{\sigma_{\rm ph}}^N}{\nu^{N-1}\,(N-1)!}\Phi^N. \tag{4.11}$$

Here, N is the number of simultaneously absorbed photons, $\sigma_{\rm ph}$ is the photoionization cross section, and Φ is the photon flux.

After initiation, the plasma relaxes via collisional and radiative processes. Laser plasmas have generally large densities and the collisional excitation and desexcitation dominate the radiative decay. This favors the instauration of ***local thermal equilibrium (LTE)***. As the collisional processes are dominated by the light electrons, the LTE state requires a minimum electron density. According to the criteria proposed by Griem [11] or Drawin [12], LTE is established in plasmas of most elements whenever $n_e > 10^{16}\,\text{cm}^{-3}$. Because plasmas generated by pulsed lasers are transitory, additional conditions have to be fulfilled. The characteristic time of plasma property variation Δt_{cin} has to be large with respect to the relaxation times of all elementary processes. The thermalization of the first excited state being generally the slowest process, the additional criterion is [13]

$$\Delta t_{cin} \geq \frac{0.1 g_1}{A_{21} g_2} \frac{n_i}{n_i + n_n} e^{E_2/kT}. \tag{4.12}$$

Here, g_1 and g_2 are the statistical weights of the ground and resonance levels, respectively, A_{21} is the radiative decay of the transition and E_2 the upper level energy, and n_n is the number density of neutral atoms. Strongly ionized atmospheric plasmas are in LTE if $\Delta t_{cin} \geq 1\,\text{ns}$. Plasma variations have to be two orders of magnitude slower for $n_e = 10^{17}\,\text{cm}^{-3}$. These conditions being fulfilled for many laser-produced plasmas, the LTE hypothesis is valid and a simplified statistical description based on the equilibrium laws is possible [14]. Moreover, plasmas produced by the interaction of pulsed lasers with condensed matter may be in ***complete thermal equilibrium*** during the early stage of expansion. According to the initial large density, they are optically thick over the entire radiation spectrum from infrared to the near ultraviolet range [15]. The emission spectrum is therefore a blackbody continuum given by Planck's formula. At a typical plasma temperature of a few eV, the maximum of radiation power is emitted in the near UV spectral range. Due to the strong coupling of UV radiation with most materials, the plasma can act as a wavelength converter during processing with infrared lasers. Using short laser pulses of very high intensity, plasmas of temperatures in the range of keV can be generated, giving rise to the emission of VUV and X-rays [16].

After the excitation by a pulsed laser, the plasma rapidly expands, converting its thermal energy into kinetic energy during a quasi-adiabatic initial expansion stage. During this stage, the density and temperature decrease rapidly and the plasma emission changes from the blackbody continuum to a spectrum of atomic lines and molecular bands characteristic of the emitting plasma species. The emission intensities of bremsstrahlung and recombination continua vary as $\propto n_e{}^2$ and decrease therefore much faster in time than the spectral line emission intensities that linearly depend on n_e. That is the reason why the material analyses via *laser-induced breakdown spectroscopy (LIBS)* are generally performed with a gated detector to start the measurements with a delay of the order of 1 μs after plasma ignition [17].

4.3 Processes in Nanosecond Laser–Plasma Interactions

4.3.1 Laser-Induced Gas Breakdown

Two mechanisms are responsible for the transformation of a neutral gas in a plasma by laser radiation absorption: the electrons heating by IB and multiphoton ionization. In the case of nanosecond laser pulses, the initiation of a laser plasma in a gas, also known as ***"optical breakdown,"*** is dominated by the electron heating process by IB. The word *"optical"* indicates that there are other breakdown types, as discharges induced by a static electric field or by microwave radiation.

Breakdown is the transformation of a gaseous environment, non- or poorly ionized, in a highly ionized plasma by igniting an ionization avalanche. The avalanche is induced via heating of free electron by a static electric field or high-power radiation (IB effect) [18]. The breakdown is defined as the achievement of a final ionization status, starting from an initial electron density. In ambient air, this initial electron density is of about $10^3\,\mathrm{cm}^{-3}$ [19].

The optical laser breakdown in gases at atmospheric pressure is usually reached by the multiplication of the initial electron density by a factor of 10^{13} during the laser pulse [2, 20]. Whenever the generation of electrons by multiphoton ionization is absent, the breakdown develops solely by avalanche ionization and each initial electron has to produce $10^{13} = 2^{43}$ electrons. The 43 generations of electrons are driven by IB heating of electrons during collisions with neutral atoms. When the ionization degree becomes larger than 10^{-4}, the Coulomb interaction between electrons and ions dominates the collisional processes and the plasma is quasi instantaneously completely ionized due to the efficient electron–ion IB heating (4.6 and 4.7).

The breakdown threshold values in literature differ from source to source, due to numerous experimental parameters such as the waist and spatial distribution of the beam, the laser pulse duration, etc. An accurate breakdown modeling was developed by Chan and Moody [21] based upon the Boltzmann equation.

In the simplest case, neglecting the electron energy losses, the breakdown threshold is obtained by integrating the energy growth rate for one electron by IB $\mathrm{d}\varepsilon/\mathrm{d}t|_{\mathrm{IB}}$ given by (4.6) over the laser pulse duration τ_{las},

$$\int_0^{\tau_{\mathrm{las}}} \left.\frac{\mathrm{d}\varepsilon}{\mathrm{d}t}\right|_{\mathrm{IB}} \mathrm{d}t \geq 43\,\Delta_{\mathrm{ion}}. \tag{4.13}$$

rate for one electron by IB given by (4.6).

In the general case, when electron energy losses are significant, breakdown occurs if [2, 20]

$$\frac{e^2\mathcal{E}^2}{m}\frac{\nu_{\mathrm{eff}}}{\omega^2+\nu_{\mathrm{eff}}{}^2} \geq \underbrace{\frac{43\Delta_{\mathrm{ion}}}{\tau_{\mathrm{las}}}}_{\text{(i)}} + \underbrace{\Delta_{\mathrm{ion}}\frac{D}{\Lambda^2}}_{\text{(ii)}} + \underbrace{\frac{2m}{M}\langle\varepsilon\rangle\,\nu_{\mathrm{eff}}}_{\text{(iii)}} + \underbrace{\Delta_{\mathrm{ion}}\gamma_{\mathrm{ci}}\nu_{\mathrm{eff}}}_{\text{(iv)}} + \underbrace{\Delta_{\mathrm{ion}}h_{\mathrm{a}}\nu_{\mathrm{eff}}}_{\text{(v)}}. \tag{4.14}$$

Here, M is the molecular mass of the gas, $\langle \varepsilon \rangle$ the electrons mean energy, γ_{ci} a numerical constant that depends on the atomic structure of the gas particles, D and Λ are the diffusion coefficient and diffusion length of free electrons, respectively, and h_a the attachment efficiency. The terms (ii), (iii), (iv), and (v) represent the energy losses by elastic collisions, inelastic collisions, diffusion, and attachment, respectively. Because during the avalanche ionization, the ion density is small compared to the neutral density, the losses by recombination could be omitted in the (4.14). It results the following breakdown criterion:

$$I_{las} \geq \frac{m\,c\,\Delta_{ion}}{4\pi e^2 \ln 2} \frac{\omega^2 + \nu_{eff}{}^2}{\nu_{eff}} \left(\overset{(i)}{\frac{43}{\tau_{las}} \ln 2} + \overset{(ii)}{\frac{D}{\Lambda^2}} + \overset{(iii)}{\frac{2m}{M} \frac{\langle \varepsilon \rangle}{\Delta_{ion}} \nu_{eff}} + \overset{(iv)}{\gamma_{ci} \nu_{eff}} \right). \quad (4.15)$$

In the (4.15), I_{las} stands for the incident laser intensity. We note that the terms (iii)–(v) in (4.14) are proportional to effective collision frequency, which in turn is given by (4.5). Because ν_{eff} is proportional to the gas pressure P_g, the loss terms (iii)–(v) in (4.14) increase linearly with P_g. For high pressures, the terms (i) and (ii) in (4.14) can be neglected. If, at the same time, P_g is sufficiently low so that $\nu_{eff}^2 << \omega^2$, the heating by IB is proportional to P_g and the breakdown threshold is independent of P_g in this limited pressure range.

Considering the entire pressure range, (4.14) shows that the rate of energy gain increases linearly with pressure for $\nu_{eff}^2 \ll \omega^2$ and decreases as P_g^{-1} for $\nu_{eff}^2 \gg \omega^2$. The breakdown threshold passes therefore through a minimum for a pressure P_g^* as shown in Fig. 4.2.

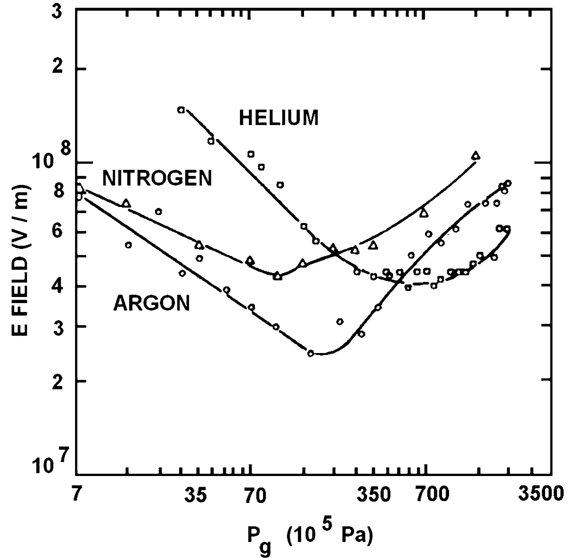

Fig. 4.2 Breakdown threshold vs. gas pressure for 694 nm ruby laser radiation of 50 ns pulse duration [22] and different gases. The threshold is expressed in terms of the peak electric field

For low pressure and especially for a small waist, the diffusion losses are prevalent. The free electron diffusion coefficient is given by

$$D = \frac{1}{3}\frac{\upsilon_e^2}{\nu_{\text{eff}}} = \frac{2}{3}\frac{\langle \varepsilon \rangle}{m\,\nu_{\text{eff}}}. \tag{4.16}$$

Evseyenko et al. [23] determined the diffusion length Λ based upon the assumption that the focal volume is a cylinder of radius r and length L resulting from

$$r = \frac{f\,\Theta}{2}, \quad L = 2\left(\sqrt{2}-1\right)\frac{f^2\,\Theta}{B}. \tag{4.17}$$

Here, f is the focal length of the lens, Θ is the laser beam divergence, and B is the beam diameter on the lens surface. For a Gaussian laser beam, we have

$$\frac{1}{\Lambda^2} = \left(\frac{2.405}{r}\right)^2 + \left(\frac{\pi}{L}\right)^2. \tag{4.18}$$

In case of a large numerical aperture ($\geq f/5$), (4.18) simply reads $\Lambda = r/2.405$ [20]. The influence of electron diffusion on the breakdown process can be evaluated by comparing the loss rates due to electron diffusion and elastic collisions [terms (ii) and (iii) in (4.14)]. Using the expressions (4.16)–(4.18), the following criterion is obtained:

$$\frac{4.810}{\sqrt{3}}\frac{\sqrt{\Delta_{\text{ion}}M}}{mf\,\Theta} << \nu_{\text{eff}}. \tag{4.19}$$

The diffusion losses are negligible whenever the inequality (4.19) is fulfilled. We mention that for $f < 50$ mm the electron losses due to diffusion become dominant and the breakdown threshold increases with the numerical aperture.

Chan et al. [20] and Nielsen et al. [24] studied the influence of the focal spot size on the breakdown threshold. It was shown that even for large beam waist, the loss terms still account and the breakdown threshold is not completely time dominated (Fig. 4.3).

Tomlinson et al. [25] and Vladimirov et al. [26] associated the small threshold observed at low gas pressure to the preionization due to electron emission from optical surfaces or the walls of the interaction chamber. Due to a small amount of electrons remanent from the previous breakdown, the threshold value can be further reduced [20].

Young and Hercher [28] and also Chin and Isenor [29] observed a decrease of the breakdown threshold when introducing impurities in the ambient gas. Two mechanisms can stay at the origin of this decrease: the Penning effect and multiphoton ionization. At high pressures, when the time between atom–atom collisions is small compared with the characteristic duration of the ionization avalanche, the Penning effect may cause the lowering of the breakdown threshold. Under these conditions, Smith and Haught [27] observed a significant threshold reduction by the Penning effect during the breakdown induced by ruby laser radiation. With respect

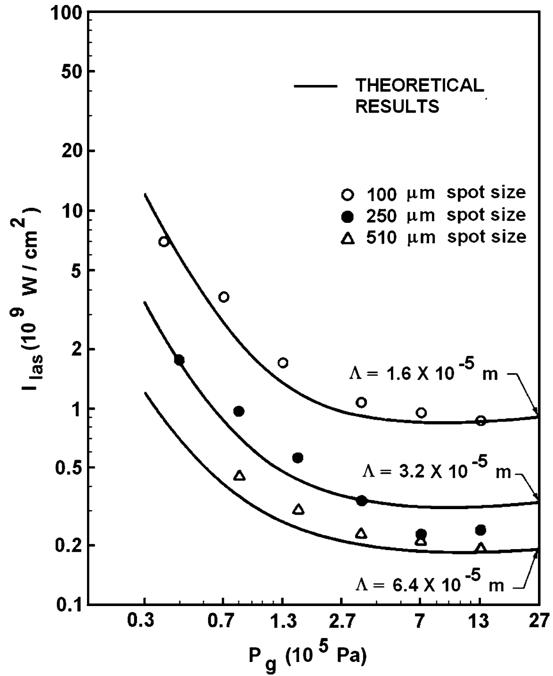

Fig. 4.3 Variation of CO_2 laser breakdown threshold in Ar as a function of gas pressure for spot sizes of 100, 250, and 510 µm [20]

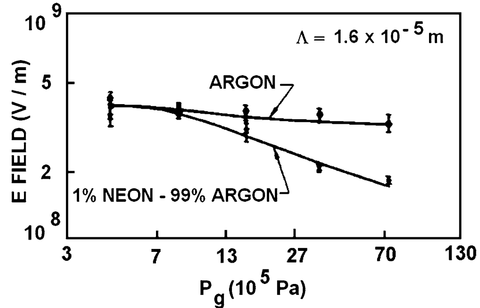

Fig. 4.4 Pressure dependence of breakdown threshold induced by a Q-switched Nd:YAG laser in pure argon and in a mixture of Ar and 1% Ne [27]

to breakdown in pure argon, they noticed a significant decrease of the threshold when adding 1% Ne in the Ar atmosphere (Fig. 4.4). The effect was explained by a resonant excitation of Ne and the Penning ionization via collisions between excited Ne and Ar atoms.

The electron gain via multiphoton ionization is

$$\frac{\partial n_{\mathrm{e}}}{\mathrm{d}t} = \alpha_k \, n_{\mathrm{gas}}, \tag{4.20}$$

where α_k is the multiphoton ionization rate that can be estimated by (4.11). In [10, 20, 30], multiphoton ionization was shown to contribute to the breakdown ignition under the action of ruby or neodymium laser sources. Damany et al. [31] studied

the multiphoton ionization effect in Xe at high pressure, using a frequency accordable UV laser source. In [28], the breakdown was studied for He, Ne, Ar, Kr with several ppm hydrocarbon impurities of low ionization potential, using single mode ruby laser radiation. It was observed that at low pressures, multiphoton ionization of impurities plays a definite role in the ignition of laser-induced gas breakdown.

4.3.2 *Plasma Shielding During Laser Material Processing*

Numerous studies [32–36] have shown that the breakdown plasma threshold in a free gas is significantly lowered when initiated in front of a solid target. Under these conditions, only a fraction E_s from the initial laser pulse energy E_{las} is reaching the target surface. This results from $E_s = E_{las}\, e^{-\tau}$, where τ is the plasma's optical thickness at the laser wavelength. For infrared radiation, τ can be much larger than unity and the plasma can almost completely decouple the target from the next action of laser radiation, a phenomenon usually described as plasma shielding of the target [37]. In the visible and UV spectral ranges, however, τ is smaller than unity and the plasma remains partly transparent to the laser radiation, depending on experimental parameters and sample nature [38].

The reduction of the breakdown threshold is explained by the shock wave induced by the intense vaporization of the target under the action of a laser pulse. The shock wave heats the gas near the target's surface, which is thus converted to the plasma state.

The breakdown process of the gas in front of a solid target is characterized by three thresholds: (a) the target's vaporization threshold, I_{vap}, (b) the breakdown threshold in the vapor, I^*_{vap}, and (c) the breakdown threshold in the gas, I^*_{gas}.

4.3.2.1 Target Vaporization

The first stage of breakdown in front of a solid target consists in its heating by the laser pulse. Under some hypotheses, analytical solutions may be found, allowing to roughly describe the heating process and to estimate the vaporization thresholds [19]. One can first assume that the laser beam is spatially uniform and the diameter of its spot on the surface, d_0, is definitely larger than the depth affected by the laser heating:

$$d_0 >> \delta_{abs}/\delta_{th}. \tag{4.21}$$

Here $\delta_{abs} = \alpha_{abs}^{-1}$ is the ***absorption length*** or ***optical penetration depth***, $\delta_{th} = \sqrt{\chi \tau_{las}}$ is the ***heat diffusion length***, and χ is the thermal diffusivity which depends on thermal conductivity K_{th}, heat capacity C_p, and density ρ as $\chi = K_{th}/C_p\,\rho$. When the relation (4.21) is fulfilled, the heat flow is unidimensional. We distinguish two cases:

1. The ***surface heating source***, when $\delta_{th} >> \delta_{abs}$, and the laser beam absorption takes place in a thin layer close to the target's surface. Assuming a simplified

laser pulse of rectangular temporal shape, the breakdown threshold is given by [32, 39]:

$$I_{vap} = \frac{\Delta H}{1-R}\sqrt{\frac{\chi}{\tau_{las}}}. \tag{4.22}$$

Here $\Delta H = \Delta H_{T_0 \to T_{vap}} + \Delta H_{fus} + \Delta H_{vap}$ is the increase of total enthalpy per volume unit, which includes heating from ambient temperature T_0 up to the evaporation temperature T_{vap}, ΔH_{fus}, and ΔH_{vap} the latent heats for melting and vaporization, respectively.

2. The ***volume heating source***, when $\delta_{th} << \delta_{abs}$, and the laser beam absorption occurs in the target's bulk. Then, the breakdown threshold is written [32] as:

$$I_{vap} = \frac{\Delta H}{\alpha_{abs}\,(1-R)\,\tau_{las}}. \tag{4.23}$$

In the case of nanosecond laser pulses, (4.22) is valid for metals, which strongly absorb the laser radiation within a few nanometers due to their large electron density [19]. In return, (4.23) applies to nonmetallic materials, which have low absorption coefficients. The surface reflectivity R is a key parameter for the lasersolid interaction. R and α_{abs} are related to the free electron density in the material. According to Drude's model [40], we have:

$$R \cong 1 - \sqrt{\frac{8\omega\varepsilon_0}{\sigma_0}} \quad \alpha_{abs} \cong \sqrt{\frac{2\omega\sigma_0}{c^2\varepsilon_0}} \tag{4.24}$$

Here, σ_0 is the electrical conductivity, proportional to the free electron density in the material. The relations (4.24) show that a material with a large density of free electrons is characterized by high values of R and α_{abs}.

4.3.2.2 Plasma Ignition in the Vapor

In comparison with the breakdown in a cold gas, the transformation of the vapor ejected from the surface in a plasma is favored due to the much larger initial electron density (see Sect. 4.3.1). This is caused by the thermal electrons of the hot vapor, on one hand, and electrons emitted by the thermoionic effect from the surface, on the other hand. In the case of metals, characterized by high evaporation temperatures, the ionization degree of the vapor is $10^{-5} \ldots 10^{-4}$. The vaporization of a metallic target by a laser pulse, typically with $I_{las} > I_{vap}$, is always accompanied by plasma formation because of both the difficulty to vaporise metals (large I_{vap}) and of the readiness to ionize metallic vapors (small Δ_{ion}) [19]. Voss et al. [41] give breakdown threshold values for CO_2 laser radiation in front of Al_2O_3 and ZrO_2 samples of $120 \ldots 170$ and $66\,\mathrm{MW\,cm^{-2}}$, respectively. These values were obtained in low pressure atmospheres ($P_g < 10^2$ Pa). The thresholds diminish with increasing gas pressure due to the vapor confinement [36].

4.3.2.3 Plasma Ignition in the Ambient Gas

When the breakdown in the gas is initiated by the vaporization of a solid target, the number of electron generations necessary to reach complete ionization (4.13) is significantly reduced ($<< 43$). The characteristic breakdown time is in this case much shorter than that of a cold gas and the term (a) may be neglected in the (4.15). The losses by diffusion (b) may be equally neglected due to the large volume of gas preionized by the shock-wave. When, furthermore, the losses by attachment and by elastic collisions are negligible (the case of rare gases), the evolution of the ionization avalanche is determined by the balance between the gain by IB and the losses due to elastic collisions. One therefore obtains [36]:

$$I^*_{\mathrm{gas}}\left[\mathrm{MW\,cm^{-2}}\right] = 2 \times 10^3 \frac{\Delta_{\mathrm{ion}}\,[\mathrm{eV}]}{\lambda^2\,[\mu\mathrm{m}^2]\ \ M\,[\mathrm{amu}]}. \tag{4.25}$$

Barchukov et al. [32] obtain the same criterion, excepting the numerical coefficient, which was three times larger. This difference comes from the average electron energy, which was supposed to be equal to the gas ionization potential, while the hypothesis $\langle\varepsilon\rangle = \Delta_{\mathrm{ion}}/3$ was applied by Hermann et al. [36]. Equation (4.25) gives $I^*_{\mathrm{gas}} = 110$ and $20\,\mathrm{MW\,cm^{-2}}$ for CO_2 laser-induced breakdown in He and Xe, respectively. We note that this criterion is independent of pressure, while it remains valid within the pressure range where $\nu^2_{\mathrm{eff}} << \omega^2$. At very high pressure, I^*_{gas} increases with P_{g} due to the reduction of the IB efficiency (via ν_{eff}) according to (4.6).

4.3.2.4 The Role of Surface Defects

Many studies showed that the occurrence of gas breakdown in the vicinity of a solid target is possible even for $I_{\mathrm{las}} << I_{\mathrm{vap}}$ [34, 35].

Bloembergen [42], Apostol et al. [43], and other authors [34, 35, 44] explained the breakdown phenomenon for $I_{\mathrm{las}} << I_{\mathrm{vap}}$ by the presence of surface defects. They can be vaporized easier than a solid with a perfect flat and defect-free surface. The vaporization of these defects induces shock-waves in the gas which is thus heated and converted to the plasma state [34]. One distinguishes between two types of defects: (a) impurities easy to be vaporized (like metal oxides, present on most metal surfaces, as Al, Ti, Fe, etc.) (see Fig. 4.5); (b) defects which extend beyond the plane of the surface and are therefore more or less thermally isolated from the bulk (Fig. 4.6). Because the heat diffusion toward the material's bulk is reduced, the vaporization of the defects is preferential. This type of defects usually exhibits a peak, which can increase the local electric field of the laser radiation by two orders of magnitude or more [34].

It is difficult to quantify the role of defects in the initiation of the breakdown plasma due to the incomplete knowledge about their characteristics (density, size, composition), which depend in turn on the sample's *"history"* before the irradiation

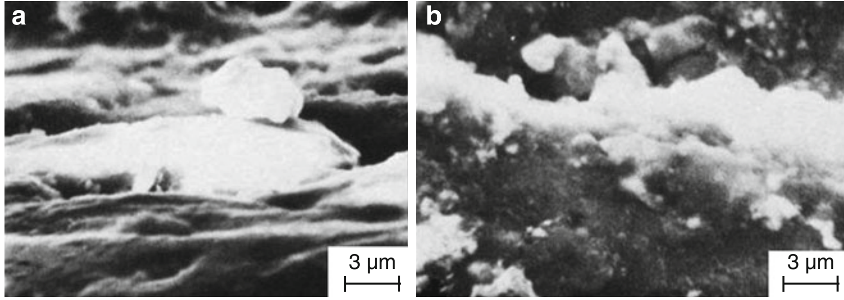

Fig. 4.5 Aluminum target surface before laser irradiation observed by SEM at oblique (**a**) and normal (**b**) incidence. The light zones were identified as Al oxides

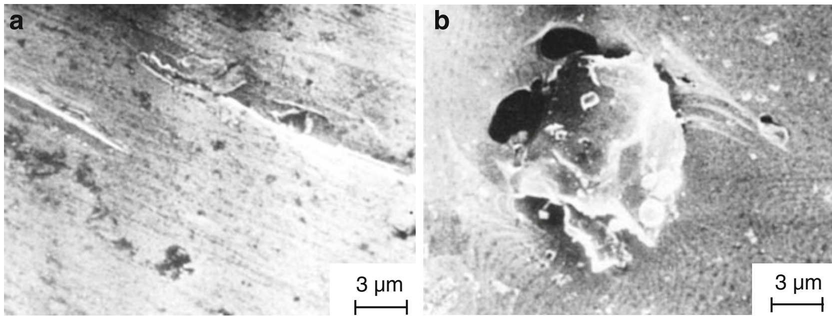

Fig. 4.6 SEM micrographs showing typical defects on the surface of a Cu target: grooves (**a**), flakes and pores (**b**)

process (polishing, sand-blasting, etc.). The laser pulse irradiation modifies the state of the surface. It can either remove defects as in laser cleaning [45], or induce them increasing damage [34], depending on the interaction conditions.

The vaporization threshold of a defect of size d_{def}, thermally isolated from the target, may be estimated from [46]

$$I_{\mathrm{vap}}^{\mathrm{def}} = \frac{\Delta H}{1-R}\frac{d_{\mathrm{def}}}{\tau_{\mathrm{las}}}. \tag{4.26}$$

Hence, the vaporization threshold reduction for a metal can be estimated from:

$$\frac{I_{\mathrm{vap}}^{\mathrm{def}}}{I_{\mathrm{vap}}} = \frac{2d_{\mathrm{def}}}{\sqrt{\chi\tau_{\mathrm{las}}}} = \frac{4d_{\mathrm{def}}}{\delta_{\mathrm{th}}}. \tag{4.27}$$

For irradiation of titanium by CO_2 laser pulses of 100-ns duration, defects of $1-\mu$m size decrease the vaporization threshold by a factor of three [46]. This can support the breakdown plasma generation for laser intensities below the vaporization threshold of a flat, defect-free target.

Boufendi et al. [47] studied the laser-induced explosive evaporation of nanoparticles in suspension in the gas. They showed that it is possible to vaporize particles of nanometric size within the focal volume of a nanosecond excimer laser beam. For $2\pi r/\lambda >> 1$, particle heating occurs via Mie absorption. The presence of these particles in the gas should provoke a decrease of the breakdown threshold similar to that induced by surface defects.

4.3.3 Laser-Supported Absorption Waves

4.3.3.1 Definition and Modeling

As explained in previous section, the laser-induced explosive vaporization of a solid material's surface or surface defects generates shock waves that heat up and ionize the surrounding gas, initiating the breakdown plasma. If the plasma reaches the critical density (see Fig. 4.1), it absorbs most of the laser energy and starts propagating toward the laser source as a wave, called ***laser-supported absorption wave (LSAW)***.

The development of absorption waves was observed in numerous experimental studies using pulsed CO_2 laser sources [32, 46, 48]. The absorption wave vanishes whenever $I_{las} < I^*_{LSAW}$, where I^*_{LSAW} is the intensity required to sustain the absorption wave. For $I_{las} < I^*_{LSAW}$, the plasma becomes transparent and the laser beam reaches again the target surface.

When P_g decreases, the propagation velocity increases and the absorption wave life-time is shortened. The I^*_{LSAW}-value equals the threshold of preionized gas breakdown given by (4.25) [46]. The threshold is independent of pressure if $P_g > P_{dif}$, where P_{dif} is the minimum pressure for which the initiation of an absorption wave is still possible. We can consider accordingly that the diffusion losses are negligible for $P_g > P_{dif}$. For $P_g < P_{dif}$, the diffusion losses slow down the ionization avalanche and I^*_{LSAW} increases.

A theoretical description of laser-induced breakdown and its propagation was given by Raizer [49] using a hydrodynamic model that considers four steps of the absorption wave propagation. They are in order:

1. A tiny plasma volume reaches near critical density and becomes strongly absorbent
2. The electron density in the neighbor region increases
3. The preionized neighbor region is heated by the laser beam and becomes absorbent
4. The absorption region thus propagates towards the laser source

Indeed, according to [50], breakdown in front of a perspex $(C_5O_2H_8)_n$ slab by Nd:YAG laser pulses of 35 ps duration leads to the absorption of 80% of the incident laser energy. The efficient absorption was attributed to a narrow region where the electron density ranges from 0.8 n_{crit} to n_{crit}.

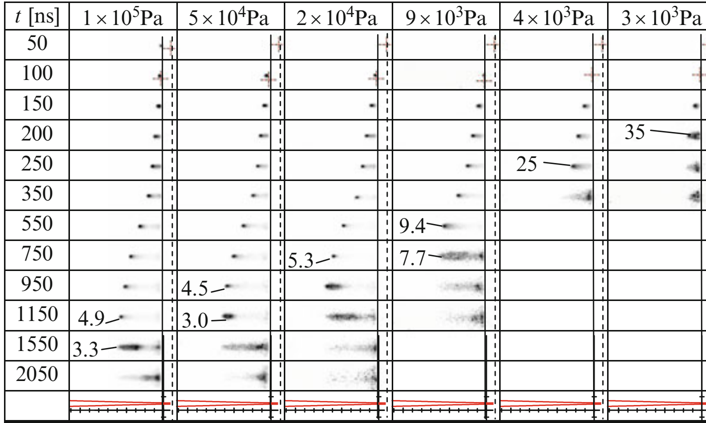

Fig. 4.7 Images of the plasma plume generated by laser irradiation of a Ti target in argon for various gas pressures and different delays with respect to the beginning of the CO_2 laser pulse. The positions of target surface and focus are indicated by the *continuous* and *dashed vertical lines*, respectively. The focussing geometry is shown in the last row. The laser intensity corresponding to the absorption wave cut-off is displayed in units of MW cm^{-2} for each pressure

Also, Offenberger and Burnett [48] measured the reflected and transmitted intensities of TEA-CO_2 laser pulses during breakdown in hydrogen. The reflected laser energy fraction was found to be smaller than 2% and attributed to strong absorption in the region adjacent to the plasma sheet of critical density. The absorption wave propagation was monitored during TEA-CO_2 laser-generated breakdown in He, Ar, and Xe by Hermann and LeFloch [46] using fast plasma imaging. Typical images are displayed in Fig. 4.7. Each column presents the plasma temporal evolution for a given value of the gas pressure. The plasma ignition corresponds to the advent of a bright point on the target's surface for $t \leq 100$ ns. It follows the plasma taking-off from the surface and its propagation toward the laser source. The LSAW expands up to 300 μm in diameter. The brightest zone originates from the plasma volume of near critical density (see Fig. 4.1), where most of the laser energy is absorbed. The gas behind the absorption front is not exposed to the laser beam, as proved by its low emission. Figure 4.7 shows that the absorption wave can be initiated for P_g much lower than the atmospheric pressure. Limit pressures P_{dif} of 3×10^3 Pa for Ar and 7×10^2 Pa for Xe were observed [46], corresponding to atomic densities of 1×10^{18} and 1.6×10^{17} cm^{-3}, respectively. We note that in gases with such a low atomic density, is impossible to reach the critical density for CO_2 laser radiation of $1 \times 10^{19}$$cm^{-3}$ (Fig. 4.1). The critical density can be attained in this case only by gas compression under the action of the shock wave.

4.3.3.2 Propagation Modes

Three different propagation modes are characteristic to absorption waves.

Breakdown wave. The breakdown primarily occurs in the region where I_{las} is maximal and it is postponed in the regions with lower intensity. The velocity of the breakdown wave is given by [49]

$$D = \frac{w_0}{\tau_{\mathrm{b}} \tan \varphi}, \tag{4.28}$$

where w_0 is the minimum radius of the focused laser beam, τ_{b} is the characteristic time of the initial breakdown, and φ is the opening angle of the laser beam.
Detonation wave. The gas within the high absorption region is rapidly heated and initiates a shock wave which isotropically propagates into the surrounding zone. This shock wave is heating up the gas around the absorption region. Next, the hot and partially ionized gas starts absorbing the laser energy and becomes opaque. Then, the absorption zone, known as detonation wave, follows the shock wave. The velocity of the detonation wave is given by [49]

$$D = \left[2\left(\gamma^2 - 1\right)\frac{I_{\mathrm{las}}}{\rho_0}\right]^{\frac{1}{3}}. \tag{4.29}$$

Here, ρ_0 and γ are the specific mass and the adiabatic coefficient of the gas, respectively. The specific energy that is injected into the gas is [49]

$$\varepsilon_{\mathrm{D}} = \frac{\gamma}{(\gamma^2 - 1)(\gamma + 1)} D^2. \tag{4.30}$$

The velocity of the detonation wave and the injected specific energy are independent of the gas ionization potential. The gas influences the propagation of the detonation wave only by its mass density and adiabatic constant.

We present in Fig. 4.8 the dependence of the absorption wave propagation velocity vs. laser intensity, deduced from time-resolved plume imaging (see Fig. 4.7). The continuous lines represent the detonation wave velocity computed on the base of Raizer's model according to (4.29). In the case of Xe, the experiment and theory are in good agreement, whereas the measured velocity in Ar is lower than that predicted by Raizer. This deviation can be assigned to energy losses which are particularly important near threshold and which are not taken into account by Raizer's model.
Radiation wave. For $I_{\mathrm{las}} > 10^{10}\,\mathrm{W{\cdot}cm^{-2}}$, the plasma temperature reaches values $\geq 10\,eV$. The plasma acts in this case as a powerful radiation source in the UV and soft X-ray spectral ranges that efficiently ionizes the surrounding gas. The preionized gas placed along the trajectory of the laser beam absorbs the radiation. The absorption wave is described in this case as radiation wave.

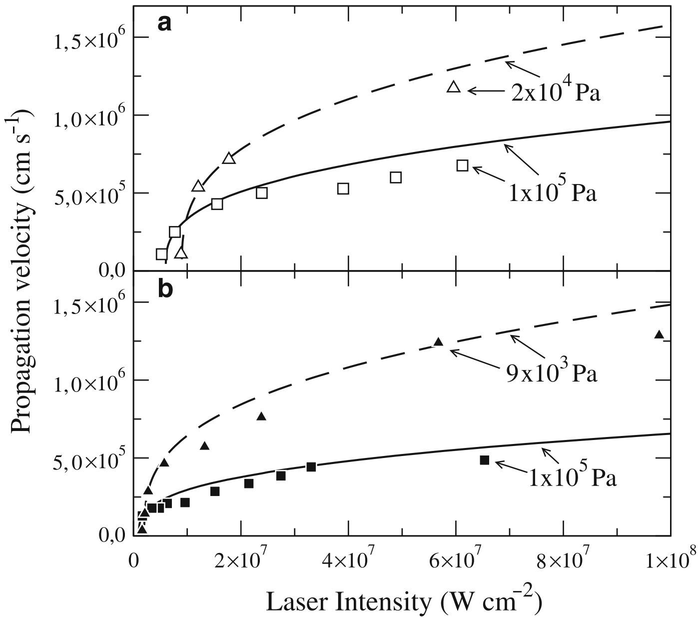

Fig. 4.8 Absorption wave propagation velocity as a function of laser intensity for Ar (**a**) and Xe (**b**) and different gas pressures

The prevalent propagation mechanism of the absorption wave depends on the experimental conditions. The breakdown waves are dominating in case of very small opening angle of the focused laser beam, whereas radiation waves occur at very high laser intensities. For moderate intensities and sufficiently wide opening angle, the optical breakdown propagates as a detonation wave.

Thus, Aguilera et al. [51] studied the atomic and ionic line emission from the breakdown plasma induced in front of a steel target by Nd:YAG laser pulses of 5 ns duration and different intensities. They observed a laser-supported detonation wave for $I_{\text{las}} = 3 \times 10^9\,\text{W}\,\text{cm}^{-2}$ and a laser-supported radiation wave for intensities in excess of $4 \times 10^{10}\,\text{W}\,\text{cm}^{-2}$.

4.3.4 *Plasma Shutter for Optical Limitation*

4.3.4.1 Mechanisms and Characteristic Times

Whenever the breakdown plasma reaches the critical density, it becomes opaque for the further coming laser radiation [48, 50, 52] (see Sect. 4.2), a process described in literature as plasma shutter.

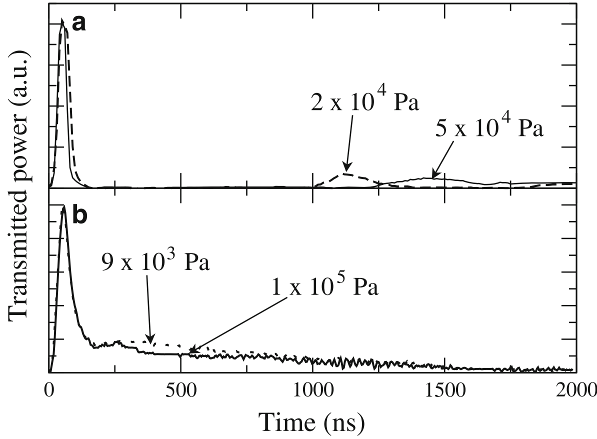

Fig. 4.9 Temporal shape of transmitted laser pulse during breakdown in Ar at different pressures. The aperture was located at 1 (**a**) and 10 mm (**b**) distance before the focus

In [46], the physical mechanisms involved into the action of a plasma shutter in the medium infrared spectral range were studied using pulsed CO_2 laser radiation. The laser beam was passed through an iris of 170-μm radius placed in center of a Ti target. The plasma shutter operation was characterized by fast plume imaging and measurements of energy and temporal shape of the transmitted laser pulse. A parametric study was performed by varying the irradiation geometry, nature, and pressure of the ambient gas, as well as the position of the iris along the laser beam axis.

Figure 4.9 presents the temporal shape of the transmitted laser pulse recorded during the breakdown in Ar at different gas pressures for various positions of the iris with respect to the focal point. When the target was placed at a distance of $d = 1$ mm in front of the focus (Fig. 4.9a), the laser beam was completely absorbed by plasma after a delay time $\tau_s = 50$ or 38 ns, respectively, for $P_g = 2 \times 10^4$ or 5×10^4 Pa. The shutter duration is pressure-dependent and increases from 1.0 to 1.2 μs for P_g varying from 2×10^4 to 5×10^4 Pa. When the target is shifted to $d = 10$ mm, the laser intensity decreases and is only slightly larger than I^*_{LSAW} for $P_g = 10^5$ Pa. Accordingly, the shutter action is delayed and has a low efficiency (Fig. 4.9b). Furthermore, for $P_g = 9 \times 10^3$ Pa, $I^*_{\mathrm{LSAW}} > I_{\mathrm{las}}$ and the plasma remains transparent for the laser radiation.

It was also shown that for $d = 1$ mm, τ_s was independent of the gas nature and pressure. For a larger distance (i.e., 3.5 or 6 mm), the gas nature and pressure determined the value of τ_s. When the breakdown is sufficiently fast (high gas pressure, low vaporization, and ionization thresholds of target material), the shutter delay time can be evaluated as $\tau_s = \tau_{\mathrm{vap}} + \tau_b$, where the vaporization time τ_{vap} obtained from (4.26) and the breakdown time τ_b write

$$\tau_{\mathrm{vap}} = \frac{\Delta H d_{\mathrm{def}}}{(1-R)\, I_{\mathrm{las}}} \quad (a), \qquad \tau_b = \eta \frac{\Delta_{\mathrm{ion}}}{I_{\mathrm{las}} - I^*_{\mathrm{EC}} - I_{\mathrm{dif}}} \quad (b). \tag{4.31}$$

Table 4.1 Laser pulse duration τ_{las}, breakdown threshold I_b, intensity to sustain the absorption wave I_{LSAW} and fraction of nontransmitted laser intensity $(I_{las} - I_t)/I_{las}$ for plasma shutter action in ambient air with preionization from different solid targets

Material	τ_{las} (μs)	I_b (MW cm^{-2})	I_{LSAW} (MW cm^{-2})	$(I_{las} - I_t)/I_{las}$
K8 glass	2	0.7	2.85	0.8
	10	0.17	0.57	0.8
Duralumin	2	1.1	2.25	0.7
	10	0.65	0.75	0.9
PMMA	2	4.5	6.75	0.6
Quartz	2	1.8	7	0.7
LiF	2	4	11	0.5

In (4.31b), η is a numerical constant, I_{EC}^* is the intensity consumed by elastic collisions, and I_{dif} is the intensity necessary to compensate the diffusion losses. It follows that τ_s is inversely proportional to the incident intensity, I_{las}. In particular, for the conditions in Fig. 4.9a, we obtain $\tau_s \cong 30$ ns, in reasonable accordance with the experimental evidence.

For given temporal and spatial distributions of the laser beam, the transmitted energy is independent of incident laser energy. However, the transmitted intensity, I_t, which is proportional to τ_s^{-1}, increases linearly with the incident laser intensity or energy.

A similar setup was used in [37] where the interaction was studied between the pulsed CO_2 laser radiation and the optical breakdown plasma generated in ambient air in front of glass, duralumin, polymethylmetacrylate, quartz, and lithium fluoride targets. The shutter action appeared for laser intensity I_{LSAW}, which was shown to depend on pulse duration, aperture diameter, and material nature (Table 4.1). The fraction $(I_{las} - I_t)/I_{las}$ of intensity nontransmitted through the plasma reaches the saturation at values ranging from 0.5 to 0.9. It follows that the transmitted fraction I_t/I_{las} increases with the incident laser intensity, i.e., with the decrease of pulse duration, from 10 down to 2 μs (see second row in Table 4.1).

4.3.4.2 Plasma Shutter Applications

Plasma shutters are used for the protection of optical components against damage by intense infrared laser pulses, as an effect of the strong absorption of IR radiation by the breakdown plasma [53]. Following the considerations in Sects. 4.3.1 and 4.3.2, the best operation of a plasma shutter is obtained in a mono-atomic gas of low ionization potential and large atomic mass, using the breakdown initiation from a solid target with low ablation threshold. According to literature [37,46], the lowest breakdown threshold of a gas in front of a metal target is of the order of 10^6 W cm^{-2} (see duralumin in Table 4.1). Nevertheless, τ_{vap} and τ_b are rather large for intensities close to this threshold, and in order to be efficient, a plasma shutter requires intensities $\geq 10^7$ W cm^{-2}. The best performance was obtained in case of a CO_2 laser radiation for Xe at atmospheric pressure, using TiO_2 as target material [46]. In this

particular case, most of the laser energy was absorbed by the plasma and re-emitted in the visible and near UV spectral ranges. The reflected laser energy was of about 1% for $I_{las} < 10^9\,W\,cm^{-2}$. This optical shutter transmitted an amount of 1-mJ laser energy only, independently of the incident laser pulse energy.

Plasma shutters were also applied to reduce the laser pulse duration. A pulse generated by a CO_2 laser source was directed to a cell containing hot CO_2 gas [54,55]. An equilibrium was reached, for which $E_{in} + E_{mol} \approx 0$, where E_{in} is the laser generated electrical field and E_{mol} is the field generated by the vibrating CO_2 molecules. If suddenly E_{in} goes to 0 due to the action of the plasma shutter, the molecules continue to generate E_{mol} for a certain relaxation time. A pulse is then emitted of the same amplitude, but with a duration of the order of the characteristic molecular collision time (controlled by the amount of hot CO_2 in the cell). This way, laser pulses with a duration downto a few tens of picoseconds have been generated [56]. Zhang et al. [57] used plasma shutters to control the duration of pulses generated by a frequency-doubled Nd:YAG laser source with 11 ns initial duration. For a total pulse energy output of 250 mJ, a short pulse of 3.2 ns duration was obtained without using a delay generator. When using a delay generator, the pulse duration was further shortened down to 1.5 ns.

It is expected that plasma shutters will allow for the development of a new generation of laser sources emitting pulses of an adjustable duration within a large time domain, ranging from μs down to sub-ps. The considerations in this chapter apply to timescales larger than the characteristic time of energy exchange between electrons and heavy particles when the hydrodynamic motion plays a significant role. Let us note that these shutters operate in transmission, to the difference of a new type of ultrafast optical switches which work in reflection (Sect. 4.4.3).

4.4 Plasma Interactions with Femtosecond Laser Pulses

4.4.1 Laser Beam Filamentation

4.4.1.1 Mechanisms and Processes

The interaction of laser radiation with matter at large distances from the focusing optics is usually limited due to the difficulty to focus the beam tightly. For a beam radius R and a lens of focusing length f, the diffraction limited minimum waist is $w_0 = \lambda f/\pi R$. Thus, focusing a Gaussian beam of visible radiation over a distance of 1 km to a spot of about 1 mm diameter requires a lens of 20 cm diameter. In the regime of high power laser pulses, however, the nonlinear interaction of radiation with matter may cancel the limitation of laser beam propagation due to diffraction. The so-called laser beam filamentation is possible since laser sources of sufficiently high power are available [58].

The nonlinear character of interaction between radiation and matter, being at the origin of filamentation, has been predicted by Fresnel in 1818. In a letter, addressed to the French Academy of Sciences, Fresnel noted that the proportionality between

vibration of light and subsequent vibration of matter was only true because no high intensities were available [59]. It was thus necessary to wait for the discovery of the laser to start nonlinear optics.

Microscopically, an electromagnetic wave tends to separate positive and negative charges in the material, inducing a macroscopic polarization

$$\mathbf{P} = \varepsilon_0 \left[\chi^{(1)} \cdot \mathbf{E} + \chi^{(2)} \cdot \mathbf{E}\mathbf{E} + \chi^{(3)} \cdot \mathbf{E}\mathbf{E}\mathbf{E} + \ldots \right]. \tag{4.32}$$

Here, $\chi^{(n)}$ are the n-th order susceptibilities and $\mathbf{E}$ is the electric field. The first term describes the linear interaction, whereas the higher order terms express the non-linear optical response of matter. The propagation of a laser pulse in a transparent medium is described by Maxwell's equations. Its temporal evolution reads

$$E\,(t) = \varepsilon\,(t)\,\mathrm{e}^{\mathrm{i}(\omega t - \varphi)}, \tag{4.33}$$

where $\varepsilon\,(t)$ is the temporal shape of the laser pulse and ω, is the angular frequency. According to Heisenberg's uncertainty principle $\Delta t\ \Delta\omega \geq 1/2$, a short laser pulse should be spectrally large. The angular frequency is a function of time $\omega\,(t)$ that is called ***pulse chirp***. The spectral distribution is given by the Fourier transform of $E\,(t)$. For a Gaussian temporal shape, we obtain $E_0\,(\omega) = \exp\left[-\left(\omega - \omega_0\right)^2/4\Gamma\right]$ and the change of the spectral shape after propagation is given by

$$E\,(\omega, x) = E_0\,(\omega)\,\mathrm{e}^{\pm \mathrm{i}\,k(\omega)x}. \tag{4.34}$$

For $\Delta\omega << \omega_0$, the frequency dependent propagation factor is

$$k\,(\omega) = k\,(\omega_0) + \left.\frac{\mathrm{d}k}{\mathrm{d}\omega}\right|_{\omega_0} (\omega - \omega_0) + \frac{1}{2}\left.\frac{\mathrm{d}^2k}{\mathrm{d}\omega^2}\right|_{\omega_0} (\omega - \omega_0)^2 + \ldots, \tag{4.35}$$

where $k'' = \mathrm{d}^2k/\mathrm{d}\omega^2$ is the group velocity dispersion parameter.

Under exposure to intense electromagnetic radiation, the refractive index of matter varies with the radiation intensity I as

$$n = n_0 + n_2\,I, \tag{4.36}$$

The Kerr effect is characterized by the second order nonlinear refractive index n_2. According to the spatial distribution of the laser intensity, the largest increase of the refractive index typically occurs along the optical axis with a progressive decrease with distance from the axis. For most media including air, we have $n_2 > 0$ and the interaction with intense laser radiation leads to the formation of a collimating lens. For a radiation power larger than the critical power [60]

$$P_{\text{crit}} = \alpha \frac{\lambda^2}{4\pi n_0 n_2}, \tag{4.37}$$

self-focusing exceeds diffraction. As the laser beam starts to be focused, the intensity increases and the Kerr effect is further amplified. Finally, the laser beam is strongly focused. In (4.37), α is a beam geometry dependent form factor. For the propagation of a Gaussian beam ($\alpha = 1.862$) of 800-nm wavelength in air, we have $n_0 \cong 1$ and $n_2 = 3 \times 10^{-19}\,\mathrm{cm^2\,W^{-1}}$ [61] and the critical power is of about 2 GW. Thus, an energy larger than 200 µJ is required for a laser pulse of 100-fs duration. It is stressed that, although the refraction index depends on the intensity, the self-focusing threshold depends on the laser power. However, the distance of self-focusing depends on I_{las} [62]. Due to the increased intensity of the self-focused laser radiation, higher order nonlinear mechanisms are triggered. For intensities ranging from 10^{13} to $10^{14}\,\mathrm{W\,cm^{-2}}$, multiphoton ionization of atoms and molecules leads to plasma formation [10]. In a quasi-transparent plasma, where $n_{\mathrm{e}} << n_{\mathrm{crit}}$, the refractive index inferred from the Drude model is [1]

$$n_0 = \sqrt{1 - \frac{n_{\mathrm{e}}}{n_{\mathrm{crit}}}}. \tag{4.38}$$

Characterized by a refractive index < 1, the plasma acts like a defocusing lens. Combining *self-focusing* and *plasma defocusing*, laser beam filamentation is the result of compensation between both effects [60]:

$$n_2\,I = \Delta n_{\mathrm{Kerr}} = \Delta n_{\mathrm{plasma}} \cong \frac{n_{\mathrm{e}}}{2\,n_{\mathrm{crit}}}. \tag{4.39}$$

A large fraction of the laser energy is transported through a surrounding *"photon bath"* of about 2-mm diameter that continuously exchanges energy with the filament (see Fig. 4.10). The photon bath acts as an energy reservoir that sustains the filament propagation over long distances [63]. For a filament diameter of 100 µm and a 15- eV average ionization potential of air molecules, a laser pulse energy of 1 mJ is large enough to produce a filament of several hundreds of meters length.

Laser beam filamentation in air was firstly observed in 1995 [58], 10 years after the invention of the ***chirped pulse amplifier (CPA)*** by Strickland and Mourou [64]. The CPA revolutionized the technology of short pulse lasers and high powers in the TW range became accessible.

Several models have been proposed to describe laser beam filamentation. Among them, we mention the *"moving focus"* where the different temporal components

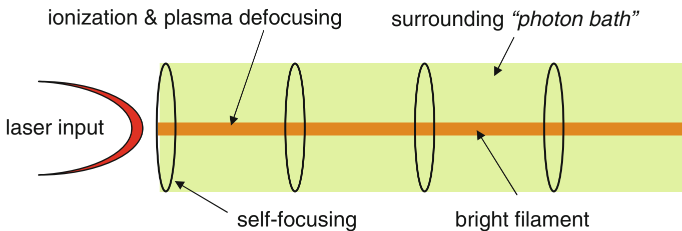

Fig. 4.10 Scheme of laser beam filament and surrounding photon bath

of the laser pulse are focused at different distances [65]. According to the *"self-guiding"* model, the interplay between Kerr effect and plasma defocusing generates a waveguide structure that consists of a weakly ionized core surrounded by a layer of larger refractive index [58, 66]. Numerical simulations led to the development of the *"dynamical restocking"* model that is based on the energy exchange between the surrounding photon bath and the filament [67].

Because the spectral components travel with different velocities through a dispersing medium, a short laser pulse undergoes a change of its temporal shape. For normal dispersing media such as air, the refraction index decreases with wavelength and the red components propagate faster than the blue ones. For 800-nm radiation in air, the velocity group dispersion parameter is $k'' = 20\,\mathrm{fs}^2\mathrm{m}^{-1}$ [68]. Accordingly, a laser pulse of 100-fs duration undergoes temporal broadening of the order of 1 ps after propagation over a distance of 1 km. One can exploit the spectral dispersion by inverting the temporal order of the spectral components in the laser pulse. If the faster propagating red components are placed behind the slower blue ones, the laser pulse will be compressed during its propagation. The so-called ***anti-chirped laser pulse*** is generated using two gratings placed in a subtractive diffraction geometry [69].

An anti-chirped laser pulse of an initial duration of the order of 1 ps may propagate in air over a distance up to a few km while it progressively compresses. When the pulse duration is sufficiently short, the intensity is large enough and self-focusing leads to laser beam filamentation. The distance after which the filamentation starts is controlled by adjusting the initial laser pulse temporal shape. The nonlinear response of matter under high radiation intensities does not only induce a spatial modification of the laser pulse but also changes its temporal shape. Analogous to the Kerr effect, the high intensity components of the laser pulse propagate with velocities different from those of the lower intensity components. As a result, temporal dephasing, commonly called ***self-phase modulation*** [70], leads to the distortion of the laser pulse temporal shape as shown in Fig. 4.11. The instantaneous frequency being proportional to the derivative of the phase, the change of the temporal shape leads to the generation of new frequencies. In particular, lower and higher frequencies are generated during the rising and falling edge of the laser pulse, respectively. A broadening from the ultraviolet up to infrared spectral range has been observed from TW laser filamentation in air [71]. The generated white light is also called ***conical emission*** due its narrow angular distribution [72]. A significant fraction of the white light is emitted backwards in the direction of the laser source. The retrodiffused emission is attributed to the density variation of the laser-produced plasma and the associated longitudinal gradient of the refractive index.

4.4.1.2 Applications of Laser Beam Filamentation

The unique features of laser beam filaments make them prospective for atmospheric measurements. Indeed, the possibility of generating filaments at controlled distance and the narrow angular distribution of the retrodiffused white light make this

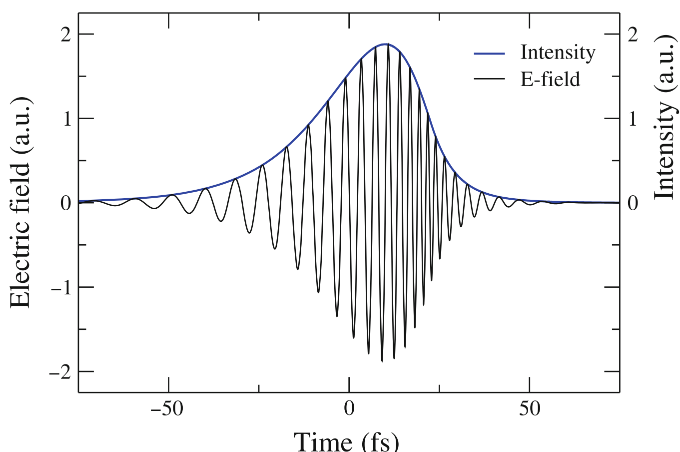

Fig. 4.11 Temporal distribution of electric field and intensity of a femtosecond laser pulse after propagation through a dispersing medium. The changes of rising and falling edge generate lower and higher frequencies, respectively

technique efficient for three-dimensional concentration mapping of pollutants in air. In contrast to the classical ***Light Detection and Ranging (LIDAR)*** technique [73], where the laser-generated retrodiffused emission allows for the detection of one pollutant only, several pollutants can be monitored simultaneously by the ***white light LIDAR***. In addition, the narrow angular distribution of the retrodiffused white light makes the technique more sensitive and measurements up to 12 km distance have been performed. White light LIDAR measurements require a TW laser source and a telescope for the collection of the laser-generated photons. For this purpose, the first mobile TW laser was developed in the framework of the *Teramobile* project, associating French and German research groups [74]. Since 1999, the *Teramobile* research consortium performed atmospheric analyses in many European cities and international sites (see Fig. 4.12). A typical absorption spectrum recorded for an altitude of 4.5 km using the white light LIDAR is shown in Fig. 4.13. Within the selected spectral range, molecular bands of water vapor are observed at 720 and 830 nm, as well as the (0,0) band of the O_2 Atmospheric system ($b^1\Sigma_g^+ \leftrightarrow X^3\Sigma_g^-$ transition). By analyzing the intensity distribution of the spectra, the authors determined temperature, water vapor concentration and thus the relative humidity. These data are precious for the understanding of the fundamental mechanisms involved into cloud formation in the atmosphere. According to the large spectral domain of the white light LIDAR ranging from the UV up to several μm, a large number of molecular species is detectable: SO_2, O_2, O_3, H_2O, CH_4, NO_2, and several volatile organic components [75].

Another challenging application of the white light LIDAR is the detection of aerosols. Classical LIDAR measurements of aerosols require the use of at least two laser sources of different wavelengths [76]. The white light LIDAR takes here

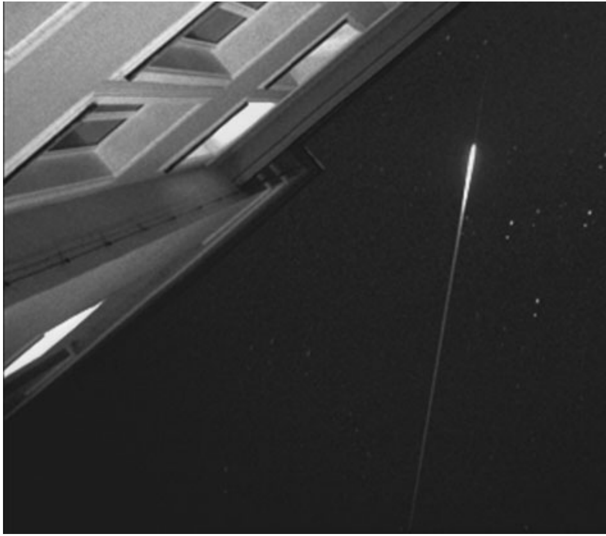

Fig. 4.12 Photograph of the white light filament produced in air by TW femtosecond laser pulses (Téramobile, C. Wedekind). The increase of brightness at large distance is due to diffusion by aerosols

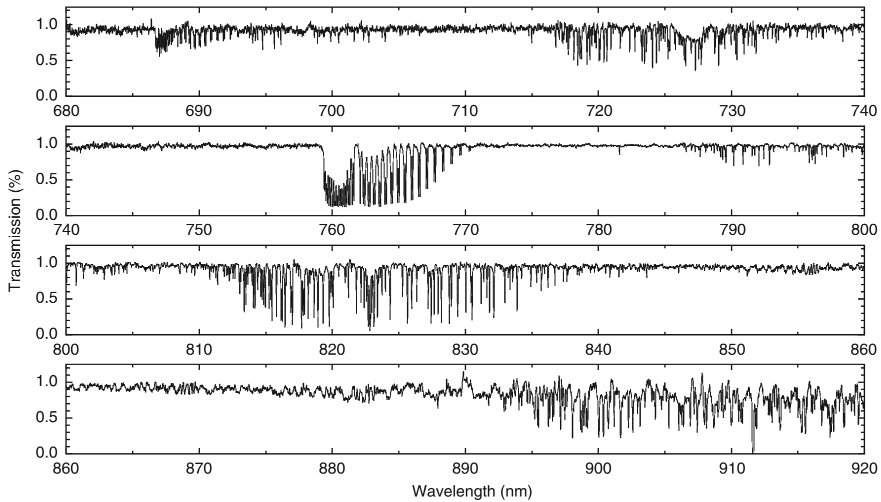

Fig. 4.13 Absorption spectrum of the atmosphere recorded for an altitude of 4.5 km using the *white light* LIDAR [71]

advantage of the large spectrum and the small angular distribution of the conical emission, to make this technique much more sensitive.

Laser-triggered lightning is another promising application of laser beam filamentation. It is an old dream of humanity to control lightning and the first tentative

using a laser beam has been performed in the 1970s when powerful nanosecond lasers pulses became available [77]. However, due to strong bremsstrahlung absorption, it is impossible to generate an ionization channel over a long distance. Contrarily, the femtosecond laser-induced filament is a partially ionized plasma channel with a length equal to the typical altitude of clouds in the atmosphere. By now, successful experiments have been only performed in laboratories [78].

Laser-produced filaments are also sources of ***THz radiation***. The emission in the long wavelength spectral range is attributed to the shift of the ionization front along the filament axis [79]. Similar to the conical emission in the visible spectral range, the THz radiation is characterized by a shallow angular distribution. As filaments have a plasma frequency in the THz range, they are completely opaque and strongly reflect this radiation. An arrangement of several filaments in a tubular configuration may therefore be used as an optical guide for THz radiation. Usually limited by its absorption in air to the propagation of several meters, the propagation on much larger distances would be so possible, opening new applications for this kind of radiation [80].

4.4.2 Generation of XUV Radiation by Laser Plasma

4.4.2.1 Pulsed XUV Radiation Sources: A Review

Radiation sources in the short wavelength spectral range are of crucial interest for scientific research and numerous applications. On one hand, the reduced diffraction limit makes short wavelength radiation interesting for micro- and nanostructuring of materials. In microelectronic fabrication for example, XUV-lithography makes the miniaturization of future integrated circuits and electronic devices accessible [81, 82]. On the other hand, XUV radiation is characterized by a much larger critical density than that of visible radiation (see Fig. 4.1), allowing thus its propagation through dense media. Short wavelength radiation is therefore suitable to characterize dense plasmas [83], but also materials in solid or liquid state [84, 85].

Discovered in 1947, ***synchrotron radiation*** was the first and – up to the 1970s – unique available pulsed XUV emission source [86]. Synchrotron radiation is a particular kind of bremsstrahlung that is generated by the deceleration of relativistic electrons. According to Einstein's relativistic theory, it has the particularity to be emitted along the direction of the electron propagation, in contrast to usual bremsstrahlung being radiated perpendicularly to the electron motion [87]. Synchrotron devices deliver pulses of low energy at high repetition frequency. The main drawback lies in the rather long pulse duration of about 100 ps [88] that is at least two orders of magnitude larger than that of laser-based sources (see Table 4.2). Recently, the so-called ***slicing*** technique was applied to shorten the pulse duration of synchrotron radiation [89]. This technique is based on the interaction of a powerful femtosecond laser with the bunch of electrons.

Table 4.2 Energy E_{XUV}, pulse duration τ_{pulse}, repetition frequency f_{rep} and levels of spatial and temporal coherence of pulsed XUV radiation sources

Radiation source	E_{XUV} (μJ)	τ_{pulse} (ps)	f_{rep} (Hz)	Spatial/Temporal coherence
Synchrotron	10^{-6}	100	10^6	Partial/Weak
Synchrotron slicing	10^{-3}	< 1	10^4	Good/Good
FEL	1	10^{-3}	10	Good/Partial
X-ray laser	$1 \ldots 10^3$	1	10	Partial/Good
Plasma	1	$0.1 \ldots 10^3$	10^4	Non/Non
Laser plasma	1	$0.1 \ldots 10^3$	10^4	Non/Non
HHG	$10^{-3} \ldots 1$	$10^{-4} \ldots 10^{-1}$	10^4	Good/Good

Similar to the synchrotron, the ***free-electron laser (FEL)*** uses magnetically confined relativistic electrons to generate radiation [90]. Nevertheless, the FEL is operated as a laser in which free electrons play the role of the amplifying medium. It has, however, the advantage to be tunable over a wide spectral range from microwaves [91] up to soft X-rays [92]. Like the synchrotron, the FEL represents a very heavy and costly installation as it requires a high-energy particle accelerator.

In the past decade, significant progress in the development of *"tabletop"* laser-based XUV radiation sources of extremely short pulse duration made accessible new domains of scientific research. Time-resolved analysis of crystallographic changes [93], ultrafast phase transformations [94] or chemical reactions [95] became possible. Application to high-resolution time-resolved in-vivo imaging of biological systems in their natural environment has seen a growing interest [96]. Finally, the generation of high energetic photons in wave packets of subfemtosecond duration allows for real-time studies of atomic and molecular systems [97].

Among the recently developed sources, the X-ray laser is a tabletop apparatus that operates in principle as longer wavelength gas lasers [98]. The difference lies in the short and energetic excitation of the amplifying medium, producing the population inversion of highly energetic transitions that involve inner shell electrons [99]. The pumping is provided by large energy short laser pulses [100] or by pulsed electrical discharges, such as a capillary Z-pinch [101]. The X-ray laser is limited to a relative low repetition rate (see Table 4.2) due to the large amount of required pumping energy [102]. For many applications that do not require coherent laser radiation, a high temperature plasma represents an ideal XUV source [103, 104]. With respect to the X-ray laser, the energy conversion from pumping toward XUV radiation is much larger and tabletop systems with high repetition rates are available for both laser and discharge pumping [16]. The use of tightly focused short laser pulses supplies here advantage of a temporally and spatially well localized radiation source that allows for X-ray imaging with high temporal and spatial resolution [105].

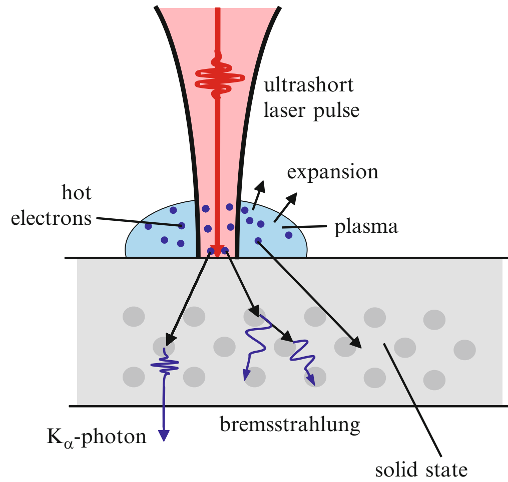

Fig. 4.14 Scheme of a laser plasma X-ray radiation source by M. Silies [109]. The radiation is generated by the interaction of energetic plasma electrons with the thin metal foil via bremsstrahlung and excitation of high energetic atomic levels

4.4.2.2 Laser Plasma X-Ray Sources

To generate a high temperature plasma using subpicosecond laser pulses, the excitation medium has to be sufficiently dense so that the collision frequency is large enough to ensure heating of electrons via IB (4.5)–(4.7). These sources are therefore based on the interaction of laser pulses with condensed matter. Different types of targets, such as liquids [106], thin foils [107], or nanoparticle expansion jets [104, 108], have been employed to generate X-ray plasmas with high repeatability at large repetition frequency.

The principle of a laser-induced X-ray plasma source is presented in Fig. 4.14. In the given example, the plasma is produced by the interaction of an intense femtosecond laser beam with a thin metallic foil. The generated high energy electrons interact with the metal via bremsstrahlung and direct excitation of inner shell electrons. Consequently, the resulting X-ray spectrum is characterized by a bremsstrahlung continuum and spectral lines of the excited high energy transitions as illustrated in Fig. 4.15.

In the given example, the quiver energy estimated from (4.4) is of about 200 eV and electrons undergo a large number of collisions to acquire energies in the multi-keV range. The energy distribution of the emission spectrum strongly depends on both laser parameters and target material. The intensity ratio between spectral line emission and the bremsstrahlung continuum depends on the electron temperature and therefore on laser pulse duration and intensity [111].

4.4.2.3 High-Order Harmonic Generation

Based on the nonlinear interaction of intense short laser pulses with gases or plasmas, high-order harmonic generation (HHG) represents another promising tabletop

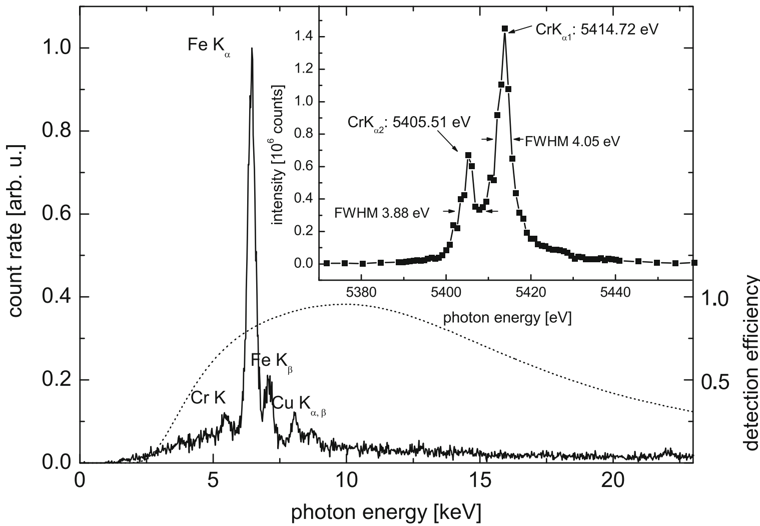

Fig. 4.15 X-ray emission spectrum recorded by Witte et al. [110] when focusing Ti:Sapphire laser pulses of 30-fs duration on a thin foil containing Fe, Cu, and Cr to $I_{\mathrm{las}} = 1.5 \times 10^{19}\,\mathrm{W\,m^{-2}}$. The Cr K¸ doublet is shown in the inset with larger spectral resolution

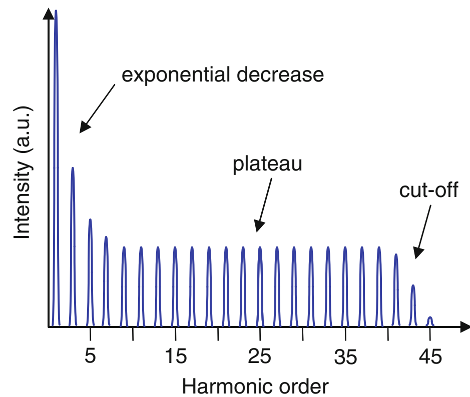

Fig. 4.16 Scheme of a typical spectrum of high-order harmonics. The cut-off for a harmonic number of 33 corresponds to the interaction of short pulse laser radiation with krypton atoms (see Table 4.3)

XUV radiation source. First reported in 1987 [112], the HHG sources have recently attracted a strongly growing interest, pushed forward by the progress in the technology of femtosecond laser sources. In contrast to the “thermal radiation” of the laser plasma X-ray source presented in the previous section, the HHG is due to the noncollisional interaction of short laser pulses with a diluted medium [113].

An HHG spectrum presents only odd harmonic numbers as shown in Fig. 4.16. It is characterized by a strong decrease of intensity with the harmonic order for small values, followed by a plateau of constant intensity up to large harmonic numbers. Finally, a sudden intensity decrease is observed at the so-called *“cut-off.”*

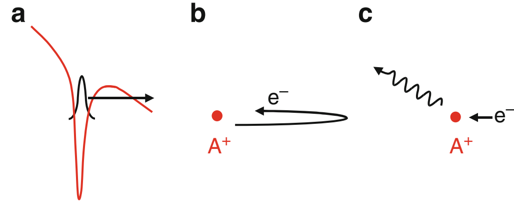

Fig. 4.17 Schematic presentation of the three steps of high-order harmonic generation (HHG): (**a**) Tunneling ionization, (**b**) Acceleration in the laser radiation field. (**c**) Radiative recombination

Table 4.3 Gas ionization potential Δ_{ion}, saturation intensity I_{sat}, cut-off harmonic order $n_{cut-off}$ and conversion efficiency ε_{conv} for HHG in different rare gases [115]

Gas	Δ_{ion} (eV)	I_{sat} (W cm^{-2})	$n_{cut-off}$	ε_{conv}
Xe	12.1	8×10^{13}	27	10^{-4}
Kr	14.0	1×10^{14}	33	3×10^{-5}
Ar	15.8	1.5×10^{14}	44	10^{-5}
Ne	21.6	1×10^{15}	211	10^{-7}
He	24.6	2×10^{15}	403	3×10^{-9}

The peculiarities of the HHG are well described by the semi-classical *"three-step model"* proposed by Corkum [114]. In this model, the atom is considered as an ensemble consisting of an ion and an electron, the electron being confined inside the potential well of the ion.

In the first step, the potential well is distorted under the action of the laser electric field, leading to tunneling ionization as shown in Fig. 4.17a. In the second step (b), the electron is accelerated by the alternating laser electric field. Finally, the electron recombines with the ion in the third step (c), emitting a photon that carries out the energy the electron gained in the laser field. Thus, the photon energy depends on the moment of tunneling with respect to the phase of the laser electric field. At maximum, the electron can gain a kinetic energy $E_{kin} \cong 3.17 E_q$, where E_q is the quiver energy given by (4.4). Consequently, the maximum available photon energy that defines the HHG cut-off (see Fig. 4.16) is [114]

$$h\nu = \Delta_{ion} + 3.17\, E_q. \tag{4.40}$$

The absence of even harmonics is due to the centrosymmetric atomic structure that can only generate odd multiples of the exciting laser angular frequency. For a typical laser intensity of 10^{15} W cm^{-2}, the cut-off photon energy is of about 200 eV, corresponding to a emitted wavelength of 6 nm.

However, the efficiency of the HHG process is limited by the probability of radiative recombination that depends on both laser intensity and ionization potential. For laser intensities larger than certain saturation threshold, multiphoton ionization dominates and the HHG efficiency decreases due to plasma defocusing. The saturation intensity increases with the ionization potential as shown in Table 4.3, allowing thus the generation of shorter wavelength. However, the conversion efficiency from the energy at the fundamental wavelength to XUV energy strongly diminishes.

When generating high-order harmonics in a preionized plasma, the plasma defocusing effect can be compensated, increasing thus the saturation intensity and the conversion efficiency [116, 117].

The harmonic generation is accompanied by the production of attosecond radiation pulses. This is due to the fact that the released electron can return close to the parent ion after every half-cycle of the laser electric field only. A photon can be emitted at this instant and the harmonic generation is constituted of a train of extremely short pulses. The period of this pulse train is the half-cycle of the laser radiation, that is 1.33 fs for a Ti:Sapphire laser. Recent effort has been paid to reduce the number of attosecond pulses within the pulse train [118]. Using a laser pulse of 5-fs duration, the generation of a single pulse as short as 100 as was demonstrated [119].

In conclusion, the recent progress in the field of HHG opened the doors to the new field of attosecond science. The international scientific community is presently entering in this new area, where time-resolved analyses of elemental processes such as the electron movement around the atomic nucleus become accessible [97, 120].

4.4.3 Plasma Mirror

4.4.3.1 Short Laser Pulse "cleaning" by Plasma Mirrors

Nowadays, the highest-intensity laser pulses of short duration are generated by Ti:Sapphire laser systems based on the chirped-pulse amplifying technique [64]. The main drawback of the CPA systems comes from the fact that some fractions of the generated laser energy are delivered before and after the main pulse of subpicosecond duration. The ***amplified spontaneous emission (ASE)*** leads in this case to the formation of a pedestal, which is characterized by the association of intensities of picosecond and long duration nanosecond timescales. The ratios between these intensities and the intensity of the subpicosecond pulse are called ***picosecond*** and ***long duration contrasts***, respectively [121].

Because the fraction of laser energy delivered out of the main pulse may worsen the laser pulse interaction with matter, the contrast has to be as large as possible, in particular in the case of high intensity laser pulses in the relativistic interaction regime. In most applications, it is sufficient to reduce the intensity of the pedestal before the main pulse, often called ***prepulse***.[2] For example, the efficient generation of XUV radiation from a laser plasma is only possible when a high intensity short laser pulse interacts with matter of solid-state density (Sect. 4.4.2.2). If the laser

[2] In CPA laser systems, the oscillator delivers pulses at much higher repetition frequency than the amplifier. Due to the use of Pockels cells for pulse injection in and ejection out of the amplifier, CPA systems deliver low energy replica of the laser pulse several nanoseconds before and after the selected pulse. These low energy replica are called by some authors ***"pre-"*** and ***"postpulses"*** and were sometimes confused with the pedestal. Their intensities can be easily reduced using additional Pockels cells.

energy of the prepulse is sufficiently large, the material's hydrodynamic expansion is initiated before the arrival of the main pulse. Consequently, instead of depositing the laser energy in a thin layer on the target surface, the main pulse is gradually attenuated at the vacuum-target interface, characterized by a reduced density gradient. As a result, the plasma temperature is lowered and its emission spectrum is shifted toward larger wavelengths.

To overcome this drawback of CPA short laser pulse systems by increasing the contrast, a solution based upon the laser beam reflection on a plasma mirror has been proposed. Instead of focusing the laser beam directly onto the target, a dielectric material is interposed into the path of the partially collimated laser beam in order to reflect the high intensity main pulse. The operation of the plasma mirror is based on the nonlinear response of the dielectric material. At moderate intensities, the dielectric material remains transparent. For sufficiently large intensities, the *Kerr effect* leads to a change of the materials refraction index [see (4.36)]. When further increasing the intensity, higher-order nonlinear effects appear and multiphoton-, tunneling- or strong field ionization cause the instantaneous transformation of the transparent solid into a plasma of supercritical density. Assuming an unsteady flow into vacuum, the hydrodynamic expansion velocity of the laser-heated material can be estimated from [122]

$$u_0 = \frac{2}{\gamma - 1} \frac{Z\,kT_e}{M}, \tag{4.41}$$

where $\gamma = C_p/C_v$, C_p, and C_v being the heat capacities at constant pressure and volume, respectively, Z is the effective ion charge, and M is the atomic mass. For large laser intensities, the electron temperature may reach values of the order of 10^3 eV, and the laser-produced plasma expands with a velocity of about 0.1 nm fs^{-1}. Thus, during the subpicosecond laser pulse, the plasma expands over a small distance only, in respect with the laser wavelength. Consequently, only a small fraction of the incident laser energy is absorbed in the narrow region close to the critical surface, oppositely to supercritical plasmas produced by nanosecond laser pulses that absorb a large fraction of energy due to the much smaller density gradients (see Sect. 4.3.3.1). Because the expansion distance of the laser-produced plasma during the subpicosecond laser pulse keeps much smaller than the laser beam diameter, the plasma can be considered flat. The supercritical plasma behaves therefore like a metal surface, characterized by a mirror-like specular reflection.

The first application of the plasma mirror to the *"cleaning"* of short laser pulses was reported in 1991 [121]. Kapteyn et al. irradiated a glass plate with 150-fs laser pulses at 45° incidence and obtained 50 and 5% reflection for the main and the prepulse ASE pedestal, respectively. Accordingly, the prepulse contrast of the reflected beam was ten times larger than that of the incident beam. The benefic effect of laser pulse "cleaning" was demonstrated by the efficient generation of a X-ray emission plasma. It was shown, using an X-ray streak camera, that the duration of X-ray emission was reduced by an order of magnitude when the plasma mirror was interposed into the beam path. The laser energy of the cleaned pulse was deposited in a thinner plasma sheet, causing a larger initial electron temperature and faster cooling by adiabatic expansion.

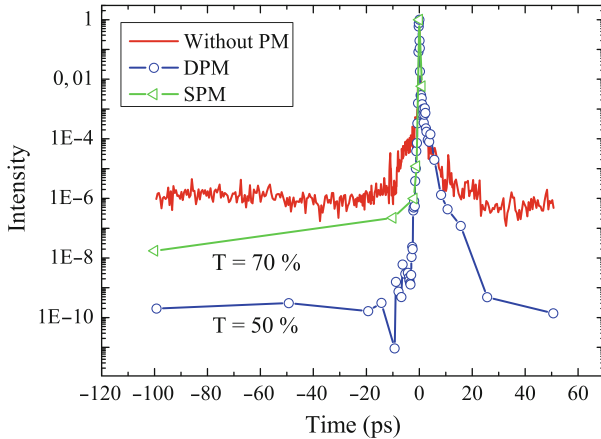

Fig. 4.18 Intensity temporal profile of femtosecond laser pulses before (without symbol) and after (*triangles*) reflection by the plasma mirror. The contrast is increased after reflection on a second plasma mirror (*circles*). The measurements were performed using a third-order cross correlator [123]

Stimulated by the numerous applications of the high intensity short pulse laser systems, the plasma mirror attracted a growing interest over the last decade [124–126]. For optimized conditions, the reflection increase up to 90% of the main pulse was demonstrated, resulting in a prepulse contrast enhancement of hundred times [125]. A further contrast improvement has been demonstrated when using two plasma mirrors (Fig. 4.18).

4.4.3.2 Harmonic Generation by Plasma Mirror

Under given conditions, the reflection by a plasma mirror can lead to the generation of high-order harmonics [127, 128], similar to the HHG in a gas (Sect. 4.4.2.3). Nevertheless, in contrast to the harmonic generation in gases, producing odd multiples of the fundamental laser frequency solely, the spectrum of radiation produced by the interaction with the plasma mirror contained both even and odd harmonics (see Fig. 4.19). This discrepancy indicates that the physical mechanism involved into HHG by a plasma mirror is different from the three-step model proposed for HHG in gases.

To describe the mechanism of HHG by the plasma mirror, two models have been proposed, corresponding to different laser intensity ranges. The oscillating mirror model [130, 131] was proposed to describe the regime of large intensities ($I_{las} > 10^{18}$ W cm^{-2}), for which the HHG was firstly observed. In this regime, the laser field drives an oscillation of the plasma's critical density surface, giving rise to periodic phase modulation of the reflected beam. This model predicts a strong dependence of the energy conversion efficiency on the incident laser intensity.

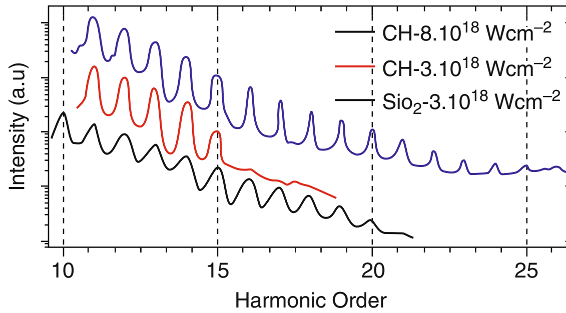

Fig. 4.19 High-order harmonics observed by Thaury et al. [129] after reflection of short laser pulses by a plasma mirror generated on plastic for two different laser intensities and on silica

However, within the moderate intensity range ($10^{15}\,\mathrm{W\,cm^{-2}} < I_{las} < 10^{17}\,\mathrm{W\,cm^{-2}}$), HHG was observed with conversion efficiencies much larger than those expected from the oscillating mirror model. Consequently, to describe HHG by plasma mirrors within the moderate intensity regime, Quéré and co-workers [132] proposed an alternative model named coherent wake emission. According to this model, the electrons are accelerated by vacuum heating [133]. The energetic electrons bunch temporally when penetrating the overdense plasma, exciting thus plasma oscillations. These plasma-wake oscillations emit bursts of radiation. In good agreement with experimental evidence, the coherent wake emission is less sensitive to the incident laser intensity than the oscillating mirror mechanism. It is therefore foreseen to dominate in the moderate intensity regime.

The performance to generate harmonics at much larger laser intensities than those applied for the saturation limited HHG in gases imposes the plasma mirror as a challenging prospective to produce intense attosecond pulses of short wavelength [134]. This new research field is of huge interest for the future investigation of the fundamental mechanisms of laser–plasma interactions under extreme conditions, when ultrashort laser pulses generate supercritical plasmas with steep density gradients [129].

4.5 Conclusion

A long time after its discovery in the early 1960s, the plasma generated and supported by high intensity laser radiation was still considered an important loss channel and so, a strong impediment in the development of efficient laser processing technologies of materials. In time however, it became clear that the plasma not only controls the complex interaction phenomena between the laser radiation and various media but can be also exploited in view of improving laser radiation coupling and eventually the efficient processing of materials submitted to intense laser beams. Our understanding of laser–plasma interactions rapidly evolved during

the years, along with the diversification of laser wavelengths from the infrared to the ultraviolet and recently to the XUV spectral ranges, and with the shortening of the laser pulse durations from microseconds in first years downto nano-, pico-, femto-, and recently attoseconds. New dramatic developments are further expected in the following years when laser pulses of attosecond duration and wavelengths in the nanometer range will be available for research in laser–matter interaction. The incoming field of "attosecond science" will cover novel laser–plasma interaction mechanism such as the direct coupling of laser radiation to nuclei and the initiation of new non-linear phenomena.

Acknowledgements Ion N. Mihailescu is grateful to Carmen Ristoscu and Andrei Popescu for the precious help in typewriting his contribution to this chapter. Jérôme Kasparian, Henrik Witte, Martin Silies, and Fabien Quéré are acknowledged for their kind help and advice in preparing Sect. 4.4.

References

1. D.V. Giovanielli, R.P. Godwin, Am. J. Phys. **43**, 808 (1975)
2. C. DeMichelis, IEEE J. Quant. Elect. **5**, 188 (1969)
3. L.J. Spitzer, *Physics of Fully Ionized Gases.* (Wiley, New York, 1962)
4. R.K. Singh, J. Narayan, Phys. Rev. B **41**, 8843 (1990)
5. J. Dawson, P. Kaw, B. Green, Phys. Fluids **12**, 875 (1969)
6. L.V. Keldysh, Sov. Phys. JETP **20**, 1307 (1965)
7. J. Wood, Central Laser Facility Annual Report (2005)
8. M.V. Ammosov, N.B. Delone, V.P. Krainov, Zh. Eksp. Teor. Fiz. **91**, 2008 (1986)
9. C.W. Siders, G. Rodriguez, J.L.W. Siders, F.G. Omenetto, A.J. Taylor, Phys. Rev. Lett. **87** (2001)
10. C.G. Morgan, Rep. Prog. Phys. **38**, 621 (1975)
11. H.R. Griem, *Principles of Plasma Spectroscopy* (University Press, Cambridge, 1997), p. 214
12. H.D. Drawin, in *Progress in Plasma and Gas Electronics* (Akademie, Berlin, 1974), p. 590
13. H.R. Griem, *Principles of Plasma Spectroscopy* (University Press, Cambridge, 1997), p. 219
14. J. Hermann, C. Dutouquet, J. Appl. Phys. **91**, 10188 (2002)
15. H.C. Liu, X.L. Mao, J.H. Yoo, R.E. Russo, Spectrochim Acta Part B At. Spec. **54**, 1607 (1999)
16. F. Dorchies, M. Harmand, D. Descamps, C. Fourment, S. Hulin, S. Petit, O. Peyrusse, J.J. Santos, Appl. Phys. Lett. **93**, 121113 (2008)
17. R. Noll, H. Bette, A. Brysch, M. Kraushaar, I. M¨onch, L. Peter, V. Sturm, Spectrochim. Acta Part B At. Spec. **56**, 637 (2001)
18. S. Rand, Phys. Rev. B **136**, 231 (1964)
19. A.M. Prokhorov, V.I. Konov, I. Ursu, I.N. Mihailescu, *Laser Heating of Metals* (Adam Hilger, Bristol, 1990)
20. C.H. Chan, C.D. Moody, W.B. McKnight, J. Appl. Phys. **44**, 1179 (1973)
21. C.H. Chan, C.D. Moody, J. Appl. Phys. **45**, 1105 (1974)
22. D.H. Gili, A.A. Dougal, Phys. Rev. Lett. **15**, 845 (1965)
23. V.P. Evseyenko, V.E. Mitsuk, V.A. Chernikov, Proceedings of 12th ICPIG p. 905 (1975)
24. P.E. Nielsen, G.H. Canavan, J. Appl. Phys. **44**, 4224 (1973)
25. R.G. Tomlinson, E.K. Damon, H.T. Buscher, *The Breakdown of Noble and Atmospheric Gases by Ruby and Neodym Laser Pulses, in Physics of Quantum Electronics* (McGraw-Hill, New York, 1966), p. 520
26. V.I. Vladimirov, G.M. Malyshev, G.T. Razdobarin, V.V. Semerov, Sov. Phys. Tech. Phys. **12**, 1277 (1968)

27. D.C. Smith, A.F. Haught, Phys. Rev. Lett. **16**, 1085 (1966)
28. M. Young, M. Hercher, J. Appl. Phys. **38**, 4393 (1967)
29. S.L. Chin, N.R. Isenor, Phys. Rev. **158**, 93 (1967)
30. N.K. Berejetskaya, G.S. Voronov, N.P. Donskaya, Proceedings of 9th ICPIG p. 43 (1969)
31. N. Damany, P. Laporte, J.L. Subtil, H. Damany, Phys. Rev. A **32**, 3418 (1985)
32. A.I. Barchukov, F.V. Bunkin, V.I. Konov, A.A. Lyubin, Sov. Phys. JETP **39**, 469 (1974)
33. D.E. Evans, Proceedings of 12th ICPIG p. 652 (1975)
34. A.S. Kovalev, A.M. Popov, A.T. Rakhimov, J. Phys. **C7**, 759 (1979)
35. I. Ursu, M. Stoica, I.N. Mihailesu, D. Craciun, Infrared Phys. **29**, 9 (1989)
36. J. Hermann, C. Boulmer-Leborgne, I.N. Mihailescu, B. Dubreuil, J. Appl. Phys. **73**, 1091 (1993)
37. Y.M. Vas'kovskǐ, A.S. Korenev, R.E. Rovinskii, I.S. Tsenina, Sov. J. Quant. Electron. **20**, 1246 (1990)
38. J.M. Vadillo, J.M.F. Romero, C. Rodriguez, J.J. Laserna, Surf. Interface Anal. **27**, 1009 (1999)
39. D.D. Duley, *CO_2 Lasers: Effects and Applications* (Academic, New York, 1976)
40. M. von Allmen, A. Blatter, *Laser-Beam Interactions with Materials* (Springer, Berlin, 1987), p. 14
41. A. Voss, J. Funken, M. Alunovic, H. Sung, E.W. Kreutz, Thin Solid Films **220**, 116 (1992)
42. N. Bloembergen, Appl. Opt. 661 (1973)
43. I. Ursu, I. Apostol, D. Craciun, M. Dinescu, I.N. Mihailescu, L. Nistor, A. Popa, V.S. Teodorescu, A.M. Prokhorov, V.I.K. N. I. Chapliev, J. Phys. D Appl. Phys. **17**, 709 (1984)
44. V.S. Vorob'ev, S. Maksimenko, Sov. J. Quant. Elec. **18**, 1595 (1988)
45. Y. Nakai, K. Hattori, A. Okano, T. Taguchi, J. Kanasaki, N. Itoh, Surf. Sci. **283**, 169 (1993)
46. J. Hermann, T.L. Floch, J. Appl. Phys. **96**, 3084 (2004)
47. L. Boufendi, J. Hermann, A. Bouchoule, B. Dubreuil, E. Stoffels, W.W. Stoffels, M.L. de Giorgi, J. Appl. Phys. **76**, 148 (1994)
48. A.A. Offenberger, N.H. Burnett, J. Appl. Phys. **43**, 4977 (1972)
49. Y.P. Raizer, Sov. Phys. Usp. **8**, 650 (1966)
50. J.A.Z. T. P. Donaldson, J. E. Balmer, J. Phys. D **13**, 1221 (1980)
51. J.A. Aguilera, C. Aragon, F. Penalba, Appl. Surf. Sci. **127**, 309 (1998)
52. R.G. Meyerand, A.F. Haught, Phys. Rev. Lett. **13**, 7 (1964)
53. F. Figueira, S.J. Czuchlewski, C.R. Phipps, S.J. Thomas, Appl. Opt. **20**, 838 (1981)
54. R.G. Brewer, R.L. Shoemaker, Phys. Rev. A **6**, 2001 (1972)
55. E. Yablanovitch, J. Goldhar, Appl. Phys. Lett. **25**, 580 (1974)
56. E. Yablanovic, *The Physics of Laser-Plasma Interaction in Gaseous Targets, in Laser Interaction and Related Plasma Phenomena*, vol. 4a (Plenum, New York, 1977), p. 367
57. F. Zhang, Q. Lou, J. Dong, W. Han, Y. Xing, W. Zhang, F. Dou, Y. Hu, Y. Shen, Optik **120**, 237 (2009)
58. A. Braun, G. Korn, X. Liu, D. Du, J. Squier, G. Mourou, Opt. Lett. **20**, 73 (1995)
59. C. Hirlimann, *Laser basics, in Femtosecond Laser Pulses: Principles and Experiments* (Springer, Berlin, 1998), p. 25
60. J. Kasparian, R. Sauerbrey, S.L. Chin, Appl. Phys. B Lasers Opt. **71**, 877 (2000)
61. L. Bergé, S. Skupin, F. Lederer, G. Méjean, J. Yu, J. Kasparian, E. Salmon, J.P. Wolf, M. Rodriguez, L. Wöste, R. Bourayou, R. Sauerbrey, Phys. Rev. Lett. **92**, 225002 (2004)
62. J.H. Marburger, E. Dawes, Phys. Rev. Lett. **21**(8), 556 (1968)
63. F. Courvoisier, V. Boutou, J. Kasparian, E. Salmon, G. Méjean, J. Yu, J.P. Wolf, Appl. Phys. Lett. **83**, 213 (2003)
64. D. Strickland, G. Mourou, Opt. Commun. **56**, 219 (1985)
65. A. Brodeur, C.Y. Chien, F.A. Ilkov, S.L. Chin, O.G. Kosareva, V.P. Kandidov, Opt. Lett. **22**, 304 (1997)
66. H.R. Lange, A. Chiron, J.F. Ripoche, A. Mysyrowicz, P. Breger, P. Agostini, Phys. Rev. Lett. **81**, 1611 (1998)
67. L. Bergé, Phys. Rep. Rev. Sec. Phys. Lett. **303**, 260 (1998)
68. I. Alexeev, A. Ting, D.F. Gordon, E. Briscoe, J. Penano, R.F. Hubbard, P. Sprangle, Appl. Phys. Lett. **84**, 4080 (2004)

69. C. Hirlimann, *Laser basics, in Femtosecond Laser Pulses: Principles and Experiments* (Springer, Berlin, 1998), p. 38
70. R.R. Alfano, S.L. Shapiro, Phys. Rev. Lett. **24**, 592 (1970)
71. J. Kasparian, M. Rodriguez, G. Méjean, J. Yu, E. Salmon, H. Wille,R. Bourayou, S. Frey, Y.B. André, A. Mysyrowicz, R. Sauerbrey, J.P. Wolf, L. Wöste, Science **301**, 61 (2003)
72. O.G. Kosareva, V.P. Kandidov, A. Brodeur, C.Y. Chien, S.L. Chin, Opt. Lett. **22**, 1332 (1997)
73. G. Fiocco, L.D. Smullin, Nature **199**, 1275 (1963)
74. H. Wille, M. Rodriguez, J. Kasparian, D. Mondelain, J. Yu, A. Mysyrowicz, R. Sauerbrey, J.P. Wolf, L. Wöste, Eur. Phys. J. Appl. Phys. **20**, 183 (2002)
75. J. Kasparian, *Some Properties of Femtosecond Laser Filamentation Relevant to Atmospheric applications II. Large-scale filamentation, in Progress in Ultrafast Intense Laser Science II* (Springer, Berlin, 2007), p. 312
76. H. Müller, H. Quenzel, Appl. Opt. **24**, 648 (1985)
77. L.M. Ball, Appl. Opt. **13**, 2292 (1974)
78. N.L. Aleksandrov, E.M. Bazelian, N.A. Bogatov, A.M. Kiselev, A.N. Stepanov, Plasma Phys. Rep. **34**, 1059 (2008)
79. C. D'Amico, A. Houard, M. Franco, B. Prade, A. Mysyrowicz, Phys. Rev. Lett. **98**, 235002 (2007)
80. A.E. Drmidonov, V.V. Valuev, V.L. Dmitriev, S.A. Shlenov, V.P. Kandidov, SPIE Proc. **6733**, S7332 (2007)
81. Y. Kato, S.H. Be, Appl. Phys. Lett. **48**, 686 (1986)
82. M. Rothschild, T.M. Bloomstein, N. Efremow, T.H. Fedynyshyn, M. Fritze, I. Pottebaum, M. Switkes, MRS Bull. **30**, 942 (2005)
83. S. Dobosz, G. Doumy, H. Stabile, P. D'Oliveira, P. Monot, F. Réau, S. Hüller, P. Martin, Phys. Rev. Lett. **95**, 025001 (2005)
84. T. Pfeifer, C. Spielmann, G. Gerber, Rep. Prog. Phys. **69**, 443 (2006)
85. H.W. K. Yamanaka, T. Yamaguchi, J. Chem. Phys. **101**, 9830 (1994)
86. F.R. Elder, A.M. Gurewitsch, R.V. Langmuir, H.C. Pollock, Phys. Rev. **71**, 829 (1947)
87. J. Schwinger, Phys. Rev. **75**, 1912 (1949)
88. M. Saes, C. Bressler, R. Abela, D. Grolimund, S.L. Johnson, P.A. Heimann, M. Chergui, Phys. Rev. Lett. **90**, 047403 (2003)
89. R.W. Schönlein, S. Chattopadhyay, H.H.W. Chong, T.E. Glover, P.A. Heimann, C.V. Shank, A.A. Zholents, M.S. Zolotorev, Science **287**, 2237 (2000)
90. D.A.G. Deacon, L.R. Elias, J.M.J. Madey, G.J. Ramian, H.A. Schwettman, T.I. Smith, Phys. Rev. Lett. **38**, 892 (1977)
91. G.B. F. Hartemann, Phys. Fluids **30**, 3283 (1987)
92. R. Treusch, J. Feldhaus, Euro. Phys. J. D **26**, 119 (2003)
93. A. Cavalleri, C. Tóth, C.W. Siders, J.A. Squier, F. Ráksi, P. Forget, J.C. Kieffer, Phys. Rev. Lett. **87**, 237401 (2001)
94. S. Fourmaux, A. Rousse, C. Rischel, I. Uschmann, S. Sebban, P. Balcou, G. Grillon, E. Forster, J.C. Gauthier, D. Hulin, SPIE Proc. **4504**, 26 (2001)
95. A. Plech, M. Wulff, S. Bratos, F. Mirloup, R. Vuilleumier, F. Schotte, P.A. Anfinrud, Phys. Rev. Lett. **92**, 125505 (2004)
96. M.W. Westneat, J.J. Socha, W.K. Lee, Ann. Rev. Physiol. **70**, 119 (2008)
97. F. Krausz, M. Ivanov, Rev. Mod. Phys. **81**, 163 (2009)
98. D.L. Matthews, P.L. Hagelstein, M.D. Rosen, M.J. Eckart, N.M. Ceglio, A.U. Hazi, H. Medecki, B.J. MacGowan, J.E. Trebes, B.L. Whitten, E.M. Campbell, C.W. Hatcher, A.M. Hawryluk, R.L. Kauffman, L.D. Pleasance, G. Rambach, J.H. Scofield, G. Stone, T.A. Weaver, Phys. Rev. Lett. **54**, 110 (1985)
99. R.A. London, M.D. Rosen, M.S. Maxon, D.C. EDER, P.L. Hagelstein, J. Phys. B At. Mol. Opt. Phys. **22**, 3363 (1989)
100. J. Dunn, Y. Li, A.L. Osterheld, J. Nilsen, J.R. Hunter, V.N. Shlyaptsev, Phys. Rev. Lett. **84**, 4834 (2000)
101. J.J. Rocca, D.P. Clark, J.L.A. Chilla, V.N. Shlyaptsev, Phys. Rev. Lett. **77**, 1476 (1996)

102. D. Zimmer, B. Zielbauer, V. Bagnoud, U. Eisenbarth, D. Javorkova, T. Kuehl, Opt. Exp. **16**, 10398 (2008)
103. P. Audebert, P. Renaudin, S. Bastiani-Ceccotti, J.P. Geindre, C. Chenais-Popovics, S. Tzortzakis, V. Nagels-Silvert, R. Shepherd, I. Matsushima, S. Gary, F. Girard, O. Peyrusse, J.C. Gauthier, Phys. Rev. Lett. **94**, 025004 (2005)
104. Y. Fukuda, A.Y. Faenov, T. Pikuz, M. Kando, H. Kotaki, I. Daito, J. Ma, L.M. Chen, T. Homma, K. Kawase, T. Kameshima, T. Kawachi, H. Daido, T. Kimura, T. Tajima, Y. Kato, S.V. Bulanov, Appl. Phys. Lett. **92**, 121110 (2008)
105. B.L. Mesler, P. Fischer, W. Chao, E.H. Anderson, D.H. Kim, J. Vac. Sci. Techn. B **25**, 2598 (2007)
106. C. Reich, C.M. Laperle, X. Li, B. Ahr, F. Benesch, C.G. Rose-Petruck, Opt. Lett. **32**, 427 (2007)
107. M. Silies, S. Linden, H. Witte, H. Zacharias, Appl. Phys B Lasers Opt. **87**, 623 (2007)
108. A.I. Magunov, T.A. Pikuz, I.Y. Skobelev, A.Y. Faenov, F. Blasco, F. Dorchies, T. Caillaud, C. Bonte, F. Salin, C. Stenz, P.A. Loboda, I.A. Litvinenko, V.V. Popova, G.V. Baidin, G.C. Junkel-Vives, J. Abdallah, JETP Lett. **74**, 375 (2001)
109. M. Silies, Zeitaufgelöste röntgenbeugung an GaAs und $TiSe_2$. Ph.D. thesis, Westfälische Wilhelms-Universität Münster, Germany (2009)
110. H. Witte, M. Silies, T. Haarlammert, J. Hüve, J. Kutzner, H. Zacharias, Appl. Phys. B Lasers Opt. **90**, 11 (2008)
111. C.L. Rettig, W.M. Roquemore, J.R. Gord, Appl. Phys. B Lasers Opt. **93**, 365 (2008)
112. A. McPherson, G. Gibson, H. Jara, U. Johann, T.S. Luk, I.A. McIntyre, K. Boyer, C.K. Rhodes, J. Opt. Soc. Am. B Opt. Phys. **4**, 595 (1987)
113. M. Ferray, A. L'Huillier, X.F. Li, L. Lompré, G. Mainfray, C. Manus, J. Phys. B At. Mol. Opt. Phys. **21**, L31 (1988)
114. P.B. Corkum, Phys. Rev. Lett. **71**, 1994 (1993)
115. M.D. Grazia, Applications du rayonnement harmonique à l'interaction UVX-solide. Ph.D. thesis, Université Paris XI, France (2007)
116. D.M. Gaudiosi, B. Reagan, T. Popmintchev, M. Grisham, M. Berrill, O. Cohen, B. Walker, M.M. Murnane, H.C. Kapteyn, J.J. Rocca, Phys. Rev. Lett. **96**, 203001 (2006)
117. R.A. Ganeev, J. Phys. B At. Mol. Opt. Phys. **40**, R 213 (2007)
118. I.P. Christov, M.M. Murnane, H.C. Kapteyn, Phys. Rev. Lett. **78**, 1251 (1997)
119. G. Sansone, E. Benedetti, F. Calegari, C. Vozzi, L. Avaldi, R. Flammini, L. Poletto, P. Villoresi, C. Altucci, R. Velotta, S. Stagira, S. De Silvestri, M. Nisoli, Science **314**, 443 (2006)
120. P.B. Corkum, F. Krausz, Nat. Phys. **3**, 381 (2007)
121. H.C. Kapteyn, M.M. Murname, A. Szoke, R. Falcone, Opt. Lett. **16**, 490 (1991)
122. Y.B. Zel'dovich, Y.P. Raizer, *Physics of Shock Waves and High Temperature Phenomena* (Academic, New York, 1966)
123. A. Lévy, T. Ceccotti, P. D'Oliveira, F. Reau, M. Perdrix, F. Qurere, P. Monot, M. Bougeard, H. Lagadec, P. Martin, J.P. Geindre, P. Audebert, Opt. Lett. **32**, 310 (2007)
124. M.D. Perry, D. Pennington, B.C. Stuart, G. Tietbohl, J.A. Britten, C. Brown, S. Herman, B. Golick, M. Kartz, J. Miller, H.T. Powell, M. Vergino, V. Yanovsky, Opt. Lett. **24**, 160 (1999)
125. P. Monot, G. Doumy, S. Dobosz, M. Perdrix, P. D'Oliveira, F. Quéré, F. Reau, P. Martin, P. Audebert, J.C. Gauthier, L.P. Geindre, Opt. Lett. **29**, 893 (2004)
126. Y. Nomura, L. Veisz, K. Schmid, T. Wittmann, J. Wild, F. Krausz, New J. Phys. **9**, 9 (2007)
127. D. von der Linde, T. Engers, G. Jenke, P. Agostini, G. Grillon, E. Nibbering, A. Mysyrowicz, A. Antonetti, Phys. Rev. A **52**(1), R 25 (1995)
128. B. Dromey, M. Zepf, A. Gopal, K. Lancaster, M.S. Wei, K. Krushelnick, M. Tatarakis, N. Vakakis, S. Moustaizis, R. Kodama, M. Tampo, C. Stoeckl, R. Clarke, H. Habara, D. Neely, S. Karsch, P. Norreys, Nat. Phys. **2**, 456 (2006)
129. C. Thaury, F. Quéré, J.P. Geindre, A. Levy, T. Ceccotti, P. Monot, M. Bougeard, F. Reau, P. D'Oliveira, P. Audebert, R. Marjoribanks, P.H. Martin, Nat. Phys. **3**, 424 (2007)

130. S.V. Bulanov, N.M. Naumova, F. Pegoraro, Phys. Plasma **1**, 745 (1994)
131. R. Lichters, J. MeyerterVehn, A. Pukhov, Phys. Plasma **3**, 3425 (1996)
132. F. Quéré, C. Thaury, P. Monot, S. Dobosz, P. Martin, J.P. Geindre, P. Audebert, Phys. Rev. Lett. **96**, 125004 (2006)
133. M.K. Grimes, A.R. Rundquist, Y.S. Lee, M.C. Downer, Phys. Rev. Lett. **82**, 4010 (1999)
134. F. Quéré, C. Thaury, J.P. Geindre, G. Bonnaud, P. Monot, P. Martin, Phys. Rev. Lett. **100**, 095004 (2008)

Chapter 5
Laser Ablation and Thin Film Deposition

Christof W. Schneider and Thomas Lippert

Abstract One of the most versatile deposition techniques in solid-state physics and analytical chemistry is the vaporization of condensed matter using photons. A short-pulsed high-power laser beam is focused onto a sample surface thereby converting a finite volume of a solid instantaneously into its vapor phase constituents such as ions and neutrals. Subsequently, the vapor moves away from the target at a high velocity and can be sampled either to grow a film or being analyzed by various spectroscopic techniques. In this chapter, the focus is on general properties of pulsed laser ablation relevant for solid-state physics like the initial ablation processes, plume formation, and plume properties. Next, oxide thin film growth will be discussed and the growth of $LaAlO_3/SrTiO_3$ heterostructures is presented as one example of tailoring oxide interfaces with surprising properties. The final discussion is on the topic of polymer ablation.

5.1 Pulsed Laser Ablation

Pulsed laser deposition (PLD) is a growth technique in which the photon energy of a laser characterized by pulse duration and laser frequency interacts with a bulk material [1–3]. As a result, material is removed from the bulk depending on the absorption properties of the target materials. The principle of PLD is shown in Fig. 5.1a. A laser pulse is focused onto the surface of a target (solid or liquid) in a vacuum chamber and thereby removes material. A significant removal of materials occurs above a certain threshold power density, and the ejected, partially ionized material forms a luminous ablation plume. The threshold power density required to create such a plasma depends on the absorption properties of the target material, the laser wavelength, and pulse duration. Typical for excimer laser is a pulse length

C.W. Schneider (✉)
Paul Scherrer Institut, Materials Group, General Energy Research Department,
CH-5232 Villigen PSI, Switzerland
e-mail: christof.schneider@psi.ch

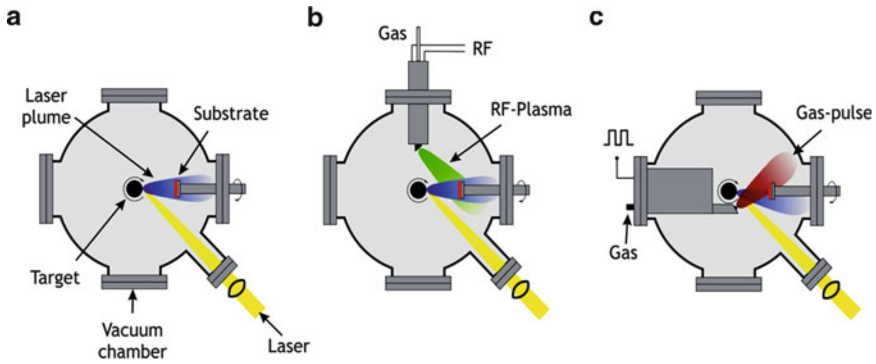

Fig. 5.1 (**a**) Schematic of pulsed laser deposition (PLD). The incoming laser beam is focused onto a target, thereby vaporizing the material of the surface region. The ejected material is partially ionized and forms the ablation plume which is directed towards the substrate. (**b**) Schematic of a RF-plasma enhanced pulsed laser deposition [4]. (**c**) Schematic of a gas-pulse set-up combined with PLD also known as pulsed reactive crossed beam laser ablation (PRCLA) [5]. The two beams merge after passing the interaction zone and expand together

of 10 ns, for femtosecond excimer lasers it is in the range of 500 fs. The removed material is directed towards a substrate where it recondenses to form a film. The growth kinetic of such films depends on the material flux, repetition rate, growth temperature, substrate material, pressure, and background gas (vacuum, reactive). To enhance the reactivity of the background gas with the ablated species, either a RF-plasma source [4] (Fig. 5.1b) or a gas pulse configuration [5] (Fig. 5.1c) are used.

An interesting development from conventional laser ablation is pulsed reactive crossed beam laser ablation (PRCLA, see Fig. 5.1c). The main feature of PRCLA is the interaction between the ablated plume and a pulsed gas. The purpose of the pulsed gas valve is to use a reactive gas when transfer and deposition of material occurs, but also to provide a higher partial pressure during the interactions, yet to maintain a defined and low background pressure. This can be achieved experimentally by using a distance of at most 1 cm between the nozzle and the ablation point on the target, which results in a strong degree of scattering between the gas and the plume species also called interaction region (see Fig. 5.1c). After passing the interaction region, the initial two beams merge and expand together almost collision-free while maintaining their reactivity for the film growth [6]. One application of the gas pulse is to provide more reactive oxygen by injecting N_2O into the laser plume. As a result, the oxygen content in an oxide film can be improved [7]. Another example is the controlled substitution of ions in a growing film like N-doped $SrTiO_3$ [8, 9]. Here, PRCLA is used to provide reactive nitrogen to the background gas and surprisingly, it worked more efficient compared to N-doped $SrTiO_3$ films grown by RF-plasma assisted PLD.

To use PLD for thin film growth has advantages for a number of reasons:

- The flexibility in wavelength and power density allows to ablate almost any material or materials combination.
- The laser is not part of the vacuum system. Therefore, a considerable degree of freedom in the ablation geometry is possible.
- The use of a pulsed laser beam enables a precise control over the growth rate.
- The congruent transfer of the composition can be achieved for most ablated material or materials combinations.
- Moderation of the kinetic energy of evaporated species to control the growth properties and growth modes of a film.

There are also disadvantages to perform PLD. Some of them are of a technical nature; some are intrinsic to the ablation process and the electromagnetic interaction between photons and matter [2]:

- The large kinetic energy of some plume species causes resputtering and likewise defects in the substrate surface and growing film.
- An inhomogeneous energy distribution in the laser beam profile gives rise to an inhomogeneous energy profile and angular energy distribution in the laser plume.
- Light elements like oxygen or lithium have different expansion velocities and angular distributions in a plume as compared to heavier elements. Therefore, an addition source to supplement these elements to obtain the desired film composition is required, e.g., adequate background gas or an adapted target composition.
- Due to the high laser energies involved, macroscopic and microscopic particles from the target can be ejected which can be detrimental to the desired properties of films and multilayers.

The latter point can partially be overcome by working with very dense polycrystalline or even single crystalline targets, but it also depends on the absorption and mechanical properties of the target material and laser fluence used.

5.2 Lasers Used for Laser Ablation

Many types of pulsed lasers have been used for the ablation of solid materials and ruby lasers were among the first to be applied. At present, laser ablation systems are equipped with either Nd:YAG or excimer lasers. Solid-state Nd:YAG systems are employed because they are relatively inexpensive, require little maintenance, there is hardly any divergence of the laser beam, and they can be easily incorporated into small commercial ablation systems. In addition, the beam profile at the base frequency is in most cases close to a Gaussian or a super-Gaussian distribution. Excimer lasers are based on halogen gas-filled laser cavities rather than solid-state crystals. Handling issues demand greater care and laser devices are rather bulky. However, excimer laser have a much bigger power output and typically provide a better defined beam profile.

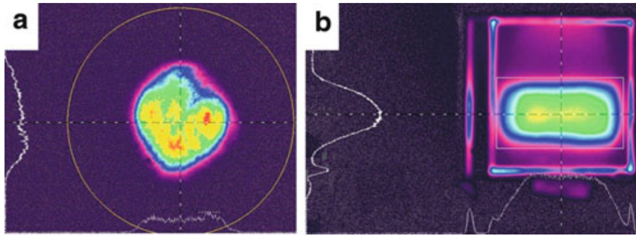

Fig. 5.2 (**a**) Beam profile of a Nd:YAG operating at $\lambda = 532$ nm. (**b**) Beam profile of a KrF excimer laser operating at $\lambda = 248$ nm. One horizontal and vertical line-scan through the beam profile is shown for each image. Images courtesy of Sven Kern, Spiricon GmbH

To illustrate the differences of the laser beam profile, beam profiles for a Nd:YAG (Quantel Brilliant BW) with $\lambda = 532$ nm and a KrF excimer laser (LPX 100) with $\lambda = 248$ nm are shown in Fig. 5.2. The beam profile for the Nd:YAG at the base frequency of $\lambda = 1{,}064$ nm seems to have not an ideal Gaussian shape which is also observed for the higher harmonics. Several hot-spots are clearly visible in the beam profile in Fig. 5.2a. Contrary to the YAG profile is the flat-top energy distribution for an excimer laser. Such a profile is more homogeneous and hence the energy distribution in a laser plume becomes better defined. The square fringes in Fig. 5.2b are due to the limited size of the image plate used.

The laser wavelength is an important parameter for the ablation process. In general, with decreasing laser wavelength an increase in the ablation rate is expected. For Nd:YAG lasers, the fundamental wavelength is in the near-infrared at 1,064 nm. Optical frequency doubling, tripling, quadrupling, and quintupling (wavelengths at 532, 355, 266, and 213 nm) of the Nd:YAG lasers have been achieved. For excimer lasers, the operating gas determines the lasing wavelength. The excimer laser wavelengths available are at 351, 308, 248, 222, 193, or 157 nm, using XeF, XeCl, KrF, KrCl, ArF, or F_2, respectively.

A shorter wavelength offers a higher photon energy which is more suitable for an efficient vaporization and ionization of the solid sample. The equivalent photon energy for a laser wavelength at 266, 213, and 157 nm, is 4.66, 5.83, and 7.90 eV, respectively. However, the absorption properties of a target material will finally decide which laser frequency can be employed. In addition, the chosen wavelength and likewise the pulse length (ns or fs) will affect the laser-induced plasma. In the case of a fs laser-pulse, there is no laser–plasma interaction because the pulse duration is shorter than the time required for a plume to develop.

5.3 Initial Ablation Processes and Plume Formation

When a photon interacts with matter, the photon energy is coupled to the lattice through electronic processes. The photon absorption by a material occurs in general over an optical depth of several nanometres where the energy in metals is

transferred to the electronic system directly and in nonmetallic systems typically to the lattice. Electronic relaxation processes are very fast with a typical lifetime of 10^{-14}–10^{-13} s. For metals it has been shown, that the time scale for the electron energy transfer to the lattice is of the order 1.5 ps and strongly dependent on the thermal conductivity, specific heat, and electron–phonon coupling [6]. For nonmetallic systems, the relaxation time varies between 10^{-12} and 10^{-3} s. Here, the absorption process occurs on a much shorter time scale compared to the thermal diffusion process, which gives rise to vaporization and plasma formation during the time scale of the pulse duration. The vaporization process can be described by the heat flow theory where the surface temperature of the target at the end of the laser pulse is determined by the light absorption and thermal diffusivity. It is therefore expected that the laser ablation mechanisms for nanosecond and femtosecond ablation are different.

5.3.1 Femtosecond Laser Irradiation

The use of fs pulses in the ablation process, and in particular for nanoparticle synthesis, has been successfully demonstrated [10, 11]. The fs ablation has several advantages compared to longer pulse lengths. First, for a given fluence, higher temperatures and pressures are obtained as compared to ns ablation because the laser energy is delivered before significant thermal conduction occurs. Second, there are no secondary interactions between the laser beam and the ablated material. A higher photon density also means a larger kinetic energy for plume species due to the so-called Coulomb explosion. This is often detrimental for thin film growth as a result of a high-energy ion bombardment of the substrate and growing film. In addition, nanoparticle formation is observed [11–13].

5.3.2 Nanosecond Laser Irradiation

Irradiating a solid with a ns pulse, there is enough time for a thermal wave to propagate into the bulk material thereby causing a melting and evaporation of the material. Two dominant mechanisms are involved in the plume absorption, i.e., inverse Bremsstrahlung and photoionization. These phenomena induce vapor ionization and excitation through collisions with excited and ground state neutrals. ns ablation of metals and ceramics may result at high fluences in the formation of a liquid phase, which is the reason for the ejection of droplets which are embedded in a film. As already pointed out, these drawbacks can be reduced and ns lasers are nowadays a useful tool to grow a large variety of materials.

Having described, how material is ejected from a target upon interaction with the laser photons, the plume formation, and the differences of the ablation process in vacuum and in the presence of a background gas will be discussed next.

When PLD is performed under vacuum conditions, two main aspects are different from sputtering or conventional thermal evaporation techniques. First, pulses of high vapor fluxes ($\sim$1 ms) are separated by periods of no vapor flux ($\sim$100 ms). Second, relatively high vapor arrival energies at the substrate. There may be ions with energies up to the keV range and neutral atoms with energies of several eV.

When PLD is performed in the presence of a background gas like oxygen, two effects are expected during the film formation: (a) the reduction of the kinetic energy of the vapor flux; (b) it provides a high flux of background oxygen molecules bombarding the surface during deposition. This high flux could change the film and substrate surface energies and will increase the oxygen content, like in oxide thin films. Changing the background gas to other gases such as NH_3 to provide reactive nitrogen, the composition of a film can be substantially changed [8,9]. Likewise, the introduction of CH_4 as background gas to form Si–C or C–N has been successfully demonstrated [14].

5.4 Plume Expansion

5.4.1 Plume Expansion in Vacuum

The plume expansion in vacuum is considered adiabatic, as long as there is no mass and energy transfer to the ablation plume and hence the plume expansion is called almost collision free. According to the Anisimov model [15], the plume expansion is characterized by an ellipsoid. As the ablation rate (in ns ablation) exceeds 0.1 monolayer per second, high particle densities are formed at the target surface. Multiple scattering between plume species tends to thermally equilibrate the plasma, resulting in the formation of the so-called Knudsen layer [2]. This Knudsen layer modifies the Maxwell–Boltzmann distribution to a shifted function, which includes the centre of mass velocity given by (5.1):

$$f(v) = A\left(\frac{m}{2\pi k}\right)^{\frac{3}{2}} v^n \exp\left(\frac{-m(v-u)^2}{2kT}\right)\mathrm{d}v, \tag{5.1}$$

where m is the mass of the particles, k is the Boltzmann constant, v is the speed along the propagation direction, u is the stream velocity, T is the stream speed, which describes the angular distribution of the propagation, and n is an integer (typically 3–4).

5.4.2 Plume Expansion into a Background Gas

A background gas can be utilized to reduce the kinetic energy of the plume species and to increase the number of chemical reactions between the plume and gas

molecules thereby forming atomic (N, O) and diatomic species. The plume dynamics is affected by the gas type and gas pressure. At a low background pressure (<1 Pa), the plume expansion is similar to the ablation in vacuum. At intermediate background pressures (10–100 Pa), the background gas influences progressively the plume dynamics. During the plume expansion in a background gas, it pushes gas away thereby introducing a compression of the gas and of the plasma plume. If the mean free path of the plume species is reduced, a shock wave is formed and the plume pressure equalizes the background pressure [16]. According to the model of Zeldovich and Raizer, the plume mass can be determined as follows:

$$M_p \approx \frac{2}{3}\pi R_{\mathrm{SKW}}^3 \rho_{\mathrm{g}}, \tag{5.2}$$

where ρ_{g} represents the gas density and R_{SKW} is the distance at which the hemispherical shock wave starts.

The spherical expansion, calculated using the blast wave model can be described as

$$R_{\mathrm{b.w.}}(t) = \varepsilon_0 \left(\frac{2E_0}{\rho_{\mathrm{g}}}\right)^{\frac{1}{5}} t^{\frac{2}{5}}, \tag{5.3}$$

where ε and ρ are constants determined by the specific heat ratio and the mass density of the layer.

At pressures larger than 100 Pa, a strong confinement of the plume with a short stopping distance takes place. For the laser ablation of $LaMnO_3$, a stopping distance smaller than 1 cm was reported [10].

5.4.3 *Imaging*

Having discussed in the previous sections the properties of the laser plume expansion, we discuss next the laser plume expansion in vacuum and in a background gas. The laser plume expansion by imaging the emission of neutral Mn-plume species (Mn I) in vacuum and at a background pressure of 20 Pa oxygen at different times after the laser pulse strikes the target are shown in Fig. 5.3 [17]. Here, a laser with $\lambda = 248$ nm was focused on a rotating $LiMn_2O_4$ target at an incident angle of 45° with a laser fluence 2 Jcm^{-2} and a spot size on the target of 1 mm^2. Emission spectra measurements were performed in a high vacuum chamber at a base pressure of $\sim 10^4$ Pa and recorded with an intensified charged couple device (ICCD, DH520-18F, Andor technology) gated for an interval of 40 ns.

The emission images for Mn I in vacuum are shown in (Fig. 5.3a), with the delay time indicated in each frame. A hemispherical expansion of the Mn I plume is observed for all time frames except at longer times when the plume becomes more elongated. For the ionized Mn species (Mn II), the plume expansion is comparable in time with Mn I. For Li I however, the initial hemispherical expansion becomes elongated which is attributed to the high velocity of the expanding species (see

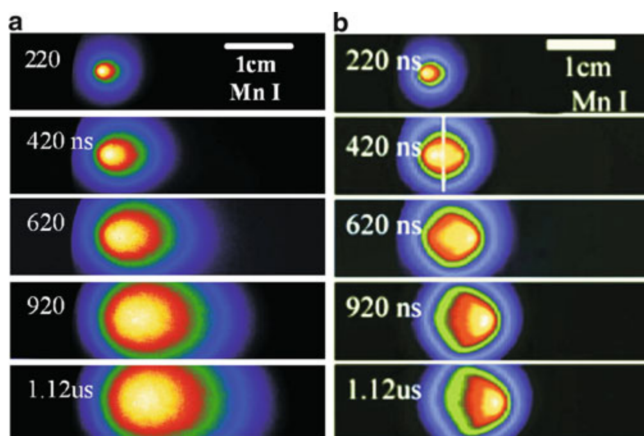

Fig. 5.3 ICCD emission images of neutral Mn-plume species as obtained by ablating $LiMn_2O_4$ in (**a**) vacuum and (**b**) at 20 Pa of oxygen. Each image is normalized with respect to the maximum intensity. The laser fluence for the KrF-laser was set to 2 Jcm^{-2} with a laser spot on the target of 1 mm^2 [17]

Table 5.1 Excited state lifetime and the expansion velocities in vacuum and in an oxygen background for neutral Mn and Li-species are given [17]

Species	Excited state lifetime (nsec)	Expansion velocity in vacuum (m/s)	Expansion velocity in 20 Pa O_2 (m/s)
Mn I	5	1.2 (±0.01)×10^4	7.8 (±0.01)×10^3
Li I	27	1.8 (±0.01)×10^4	1.6 (±0.01)×10^4

Table 5.1). The plume images for Li I also indicate an increased angular broadening of the plume compared to Mn I.

The plume emission evolution at 20 Pa oxygen background pressure (Fig. 5.3b) for Mn I is very different compared to a vacuum expansion. Here, the plume undergoes multiple scattering with the gas species which results in a sharpening of the plume front. The plume is progressively decelerated, which is revealed by the increase in the emission intensity at the plume front. In addition, interaction of the plasma plume with the background gas leads to a separation of the plume into two main components (Fig. 5.3b, 420 ns). The peak appearing at the plume front gains intensity in time with respect to the peak close to the target surface, while at later times, the two peaks merge. In addition, the velocity of the species slow down and become comparable at the later observation time. The data in Fig. 5.3b also indicate that the emission intensity profiles of Mn I in the background gas are sharper as compared to the emission profiles in vacuum. This is attributed to the confinement of the plume, induced by the collisions of the species in the plume with the background gas.

In Table 5.1, the lifetime of the exited states for Li I and Mn I is given. The lifetime for Li I is ∼5 times longer than for Mn I; however, the time over which the plume excitation can be observed is much longer. In optical emission

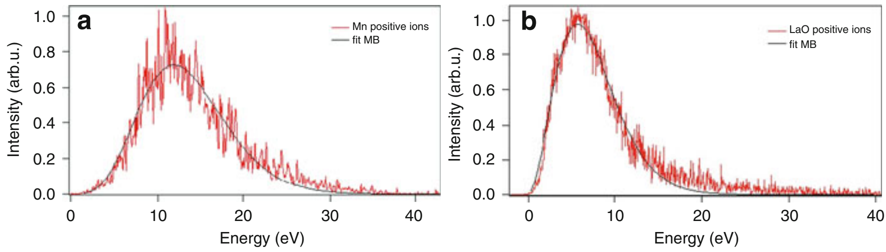

Fig. 5.4 Kinetic energy distributions of (**a**) Mn^+ and (**b**) LaO^+ species are measured during the ablation of $La_{1-x}Ca_xMnO_3$ in vacuum with a laser fluence of 1 J/cm^2 and a laser wave length of λ =193 nm. The fit to the experimental data is based on a shifted Maxwell–Bolzmann (MB) distribution [21]. Images courtesy of Stela Canulescu

spectroscopy, not only excited species created during the ablation process are detected, but also species formed and excited during plume expansion. The observation of plume species over a few hundred ns indicates that excitation processes occurs during the plume expansion. A likely mechanism for an extended observation time is the recombination and reexcitations of plume species due to collisions with electrons and other plume species. This allows for a prolonged detection as shown in Fig. 5.3.

5.4.4 Kinetic Energy of Plume Species

The kinetic energy and angular distribution of ablated species are the main parameters which determine the plume characteristics and to a large extent the growth mode of a film. In vacuum, the kinetic energy of plume species was found to vary between a few eV and up to ~80 eV [18]. In the case of the double and triple charged C-species, generated from a graphite target, the mean value of the energy distributions was found to be around 160 and 240 eV, respectively [19]. Also, kinetic energies of up to 100 eV were reported for the ablation of Si, Ge, and Cu. Here, the kinetic energy was found to vary almost linear with the ion charge.

The kinetic energy of laser plume species can be measured using an electrostatic energy analyzer coupled with a quadrupole mass spectrometer (EEA–QMS). The plume species of interest are detected by their energy per charge ratio (ε/q) and subsequently selected in the QMS due to the charge to mass ratio (q/m). Hence, this method provides a direct measurement of the kinetic energy distribution for a given mass. An example for a measurement of the kinetic energy of different plume species is given in Fig. 5.4. The kinetic energy distribution was measured for two different positive ions (Mn^+ and LaO^+) while ablating $La_{1-x}Ca_xMnO_3$ in vacuum with a ArF-Laser and a laser fluence of 1 J/cm^2 [20].

Fitting the Maxwell–Bolzmann distribution to the experimental data in Fig. 5.4 allows to extract an effective temperature of the species along the expansion

direction, the centre of mass velocity as well as the so-called most probable energy E_p, which corresponds to the maximum peak position of the energy distribution. In vacuum, the ionic species exhibit a centre of mass velocity between 2.5×10^3 and 1×10^4 m/s while the velocity of the neutral species varies between 2.4×10^3 and 4.4×10^3 m/s. It is interesting to note that in this experiment the oxygen species are among the fastest species in the plume. The most probable kinetic energy for the different species varies between 5 and 10 eV with tails extending well beyond 30 eV. Values obtained for the effective temperature for ionic species are in the range of $1-1.2\times10^4$ K ($\sim$1 eV) and for neutral species of the order $2-3\times10^3$ K ($\sim$0.3 eV). These extracted numbers underline the fact that the chemistry in such a plasma is far from the chemical equilibrium. To achieve under the described deposition conditions, the correct chemical composition in a film can be difficult due to very different expansion velocities and angular distributions for different species. It is also interesting to point out that the mean kinetic energy for species is comparable or smaller than typical values obtained for sputtering (several 10 eV and larger) but larger than for molecular beam epitaxy ($\sim$0.1 eV). However, the tail end of the kinetic energy distribution can be high and result in detrimental effects on the growth of a film and the corresponding properties. Consequences of the latter point will be illustrated in the section on tailoring interfaces in oxides.

5.4.5 Thin Film Growth

Growing oxide thin films involves a number of requirements. Often, epitaxial growth of a material is preferred and therefore the choice of the appropriate substrate material is important. Basic requirements are a good crystallographic lattice match between film and substrate, the substrate material should be chemically compatible to the film, it should have comparable thermal expansion coefficients, and a thermodynamically and chemically stable surface. Essential for some applications is to choose selectively the chemical termination of the surface [22, 23]. Examples are $SrTiO_3$ substrates with a TiO_2-termination (B-site termination) [22] or $NdGaO_3$ with a NdO-termination (A-site termination) [24]. Such surfaces allow the growth of a material from a chemically well-defined surface which minimizes, e.g., line defects in $YBa_2Cu_3O_{7-\delta}$ typically occurring in these films when grown on a surface with a mixed termination [25]. In Fig. 5.5, the growth of (001) oriented $SrRuO_3$ on TiO_2-terminated (001) $SrTiO_3$ is depicted. On the left side, the atomic structure of TiO_2-terminated (001) $SrTiO_3$ is shown. When growing $SrRuO_3$, the growth will start with a SrO layer compatible to the cubic $SrTiO_3$ lattice followed by a layer of RuO_2 rotated by 45° to the initial SrO layer. Only thereafter, the atomic arrangement of $SrRuO_3$ is as expected for the orthorhombic $SrRuO_3$ unit cell.

When species of the plume arrive at a substrate surface, the first arriving pulse causes the nucleation of a high density of smaller clusters. These subcritical clusters tend to dissociate into mobile species that will nucleate new clusters of a different size during the time of no vapor arrival. The next pulse will initiate the same process

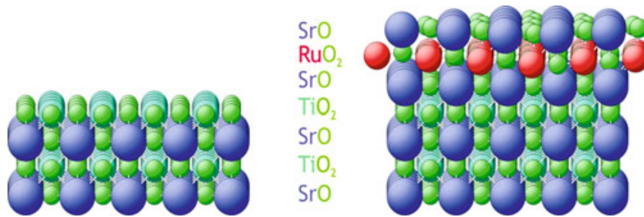

Fig. 5.5 Atomic model of TiO_2-terminated (001) oriented $SrTiO_3$ (*left*). On the right hand side, the initial growth of (001) $SrRuO_3$ on (001) $SrTiO_3$ is depicted. Images courtesy of Izabela Czekaj

again, with the difference that some of the mobile atoms will reach the previous formed clusters. What is the influence of laser wavelength, power density, repetition rate, substrate temperature, and background pressure on the growth properties of a film?

As already discussed, wavelength and power density will determine if the evaporation of the target material will be a thermal or a nonthermal evaporation process. It also determines the ratio between neutral and ionized species in a plume. The repetition rate will determine the degree of supersaturation of the evaporated material on the surface of the substrate which has a direct influence on the growth mode of a growing film. The substrate temperature is important to ensure a sufficient surface mobility of the arriving species to support epitaxial growth. To obtain the correct film composition, the background pressure and gas is another parameter which needs to be controlled. For most oxides, an oxygen atmosphere is necessary for the correct oxygen content in a film, some materials require a reducing atmosphere, like for $LaTiO_{3-x}$ [26, 27]. The chemistry of a film can also be controlled by the background gas as discussed for the growth of oxynitrates [8, 9]. Another example is the growth of NbN in a nitrogen atmosphere using PLD [28] or growing NbN/MgO heterostructures [29], where the background gas has to be changed for each material.

What are the different growth modes for epitaxial films [30, 31]? Ideally, the free energy of the substrate surface which depends on the crystalline orientation of the surface, the free energy of the film surface and the free energy of the interface need to be minimized. The latter point includes the misfit between substrate and film. This leads either to the ideal 2D layer-by-layer growth of a film (Fig. 5.6a), an island growth mode (Fig. 5.6b), or a layer-by-layer growth followed by an island growth mode (Fig. 5.6c). An island growth occurs when atoms or molecules in a growing film are more strongly bound to each other than to the substrate thereby forming clusters. A layer-by-layer growth requires species with a high mobility on a surface provided by the kinetic energy of the arriving species and the surface temperature of the substrate. In addition, a good lattice match is necessary. The surface roughness is the result of the incomplete coverage during the growth of one monolayer. A 2D growth followed by an island growth is often the result of a strain release of a growing film due to the lattice mismatch between substrate and film.

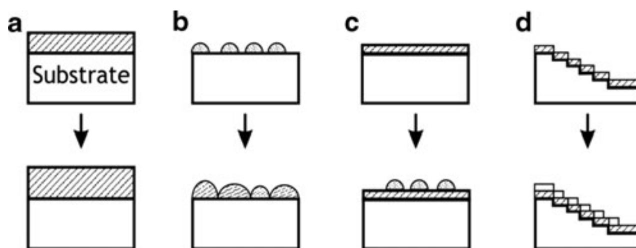

Fig. 5.6 Schematic illustrating four different growth modes for epitaxial growth: (**a**) 2D layer-by-layer growth (Frank–van der Merwe), (**b**) 3D island growth (Volmer-Weber), (**c**) layer-by-layer followed by an island growth (Stranski–Krastanov), and (**d**) step-flow growth

The surface of a crystal or the crystal itself is often not ideal. Defects are present which promote, e.g., the growth of screw dislocation in a film as a mechanism to accommodate the defect structure of the seed crystal. One example is the formation of screw dislocations in $YBa_2Cu_3O_{7-\delta}$ grown on $SrTiO_3$ [32]. The surface is never ideally flat, but has a certain miscut and hence the surface consists of terraces with a finite width. If the distance mobile species can move on a surface is larger than the terrace width, step-flow growth occurs (Fig. 5.6d). This type of growth mode depends on the growth temperature, substrate miscut, and the supersaturation of the arriving species. The degree of supersaturation can also switch between screw dislocation mediated growth and step-flow growth [33].

Another type of relaxation mechanism is the strain release via misfit-dislocations. If a heteroepitaxially grown film is thinner than a critical thickness t_c, it grows coherent and highly strained (tensile or compressive strain). For films with $t > t_c$, the strain is released by a build-in misfit-layer. In case the tension cannot be relaxed by a misfit layer, such a film will develop cracks when reaching t_c. An example for crack formation in a highly strained film is shown in Fig. 5.7b. Here, 102 uc of $LaAlO_3$ have been grown epitaxially on TiO_2-terminated (001) oriented $SrTiO_3$. In Fig. 5.7a, 5 uc of $LaAlO_3$ have been grown epitaxially on $SrTiO_3$ in a 2D growth mode, monitored using high pressure RHEED (reflective high-energy electron diffraction) [34]. The 2D growth, expressed here as the step and terrace growth of $LaAlO_3$ can be maintained even to a layer thickness of 102 uc. At a threshold thickness t_c of 25 uc, crack formation starts and becomes very pronounced with increasing t with the underlying substrate terraces still clearly to be observed (Fig. 5.7b). In Fig. 5.7c, the STEM cross-sectional image of such a layered structure shows a highly coherent and strained layer of $LaAlO_3$ on $SrTiO_3$ with the unit cell lattice parameter of $LaAlO_3$ (a(LAO) = 0.3,791 nm) equals that of $SrTiO_3$ (a(STO) = 0.3,906 nm). Despite the high biaxial tensile strain of $\approx 3\%$, $LaAlO_3$ grows over tens of nm without a visible defect even for thicker layers of $LaAlO_3$.

Another type of defect, inherent to the epitaxial growth of oxide thin films is twinning. Growing a material with an orthorhombic structure like $YBa_2Cu_3O_{7-\delta}$ on a cubic seed lattice ($SrTiO_3$), there will be no preferential orientation for the in-plane lattice parameters of the orthorhombic film. Hence, such a film will be twinned. To

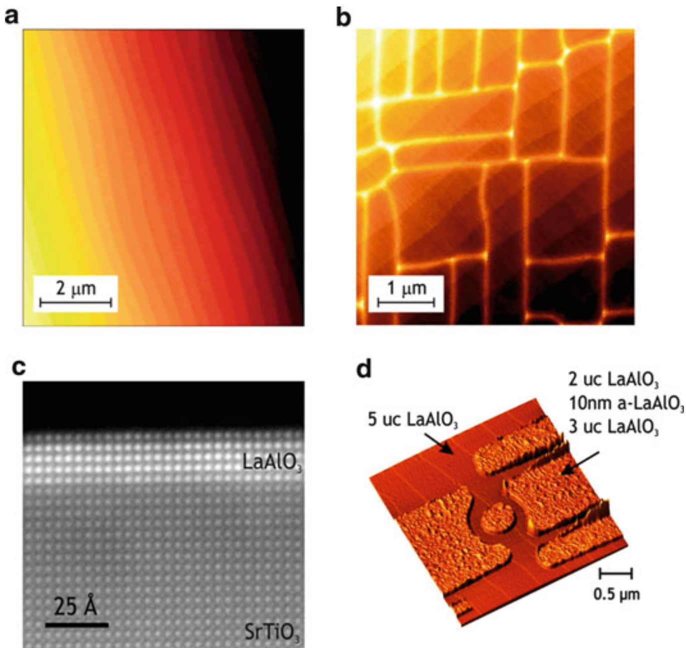

Fig. 5.7 (**a**) Topographic AFM-image of a 5 uc $LaAlO_3$ thick layer on a TiO_2 terminated $SrTiO_3$ substrate. The uc high terraced structured of the substrate is preserved in the $LaAlO_3$ layer. (**b**) Topographic image of a 102 uc $LaAlO_3$ thick layer on a TiO_2-terminated $SrTiO_3$ substrate. Like in (**a**), the terraced structure of the substrate is preserved. In addition, a very pronounced crack formation in the $LaAlO_3$-layer has taken place. The critical thickness for cracks to appear is 25 uc. (**c**) Cross-sectional high angle annular dark field (HAADF) STEM image of a 5 uc thick layer of $LaAlO_3$ (*bright*) on a (001) oriented $SrTiO_3$ substrate (*greyish*). The contrast between $LaAlO_3$ and $SrTiO_3$ is dominated by a chemical contrast. (**d**) AFM image of a ring as defined by the sequential deposition of epitaxial and amorphous $LaAlO_3$. The epitaxially grown area defines a 2D electron gas inside the ring with a diameter of $\approx 1.2\,\mu m$ and a track width of of $\approx 200\,nm$ [35]. AFM images courtesy of S. Thiel, G. Hammerl, and J. Mannhart, University of Augsburg (Germany). STEM image courtesy of L. Fitting Kourkoutis and D.A. Muller, University of Cornell (USA)

achieve in the ideal case a twin-free growth, the substrate lattice constant can be matched to the lattice of the orthorhombic film with a defined miscut of the substrate in one crystallographic direction. This idea of a defined substrate matching has been successfully demonstrated for the growth of $YBa_2Cu_3O_{7-\delta}$ thin films on $SrTiO_3$ with a substrates miscut of $\approx 1°$ either along the (100) or (010) direction. The grown $YBa_2Cu_3O_{7-\delta}$ films are almost twin-free with single crystalline normal state and superconducting transport properties [36, 37].

Film growth and properties of $LaAlO_3$/$SrTiO_3$ interfaces

An outstanding example of surface engineering and the influence of the proper interface termination has been discovered in the $LaAlO_3$/$SrTiO_3$, $LaTiO_3$/$SrTiO_3$, and $LaVaO_3$/$SrTiO_3$ system [38–40], where a metallic-like interface conductivity is confined to a few unit-cells at the interface [41]. One way to explain the

observed conductivity is by oxygen defects which cause conductivity in $SrTiO_3$ [42–44]. Considering the stacking sequence of $LaAlO_3$ on $SrTiO_3$, there is an alternative explanation of this interface conductivity which is based on the polarity discontinuity at the interface between the TiO_2-terminated $SrTiO_3$ and the homoepitaxially grown $LaAlO_3$ [45]. Looking at the $SrTiO_3$ sub-unit cells, the charge neutral SrO^0 is followed by TiO_2^0, whereas for $LaAlO_3$, positively charged LaO^+ is followed by negatively charged AlO_2^-. At such an interface (Fig. 5.8a), a Coulomb potential of several eV can build up. One way to lower the potential barrier is to move charge from the top surface to the interface corresponding to an electronic reconstruction at the interface (Fig. 5.8b). Another way to explain the conductivity is that defects holding a charge like oxygen vacancies can be moved to the interface by force due to the strong electrostatic potential. This is also known as ionic compensation.

All three mechanisms to explain the interface conductivity have observable consequences based on how these stacking sequences are grown. This will be discussed in the following paragraphs. Typical deposition parameters for $LaAlO_3$ are a deposition temperature ≈750–770°C, a laser fluence of ≈1 J/cm^2 and an oxygen background pressure of 2×10^{-5} mbar [34, 38, 39, 46]. The growth mode for $LaAlO_3$ is 2D (Fig. 5.7a). With these parameters, a quasi-2 dimensional conductivity associated with the interface is observed with a charger carrier density of $\approx 3\times10^{13}$/cm^2 between room temperature and 4.2 K and a metallic like temperature dependence for the resistivity [34, 38, 39, 46]. These interfaces even become superconducting when cooled below 200 mK [41, 47]. In the superconducting state, an estimate for the conducting sheet layer thickness reveals an upper limit of 4 nm verifying the 2-dimensional character of the conducting layer [41, 47].

With increasing background pressure up to $\approx 10^{-2}$ mbar, the film surface becomes rougher and the resistivity larger as compared to interfaces grown in the 10^{-5} mbar range. The increase in roughness and in resistivity indicates the presence

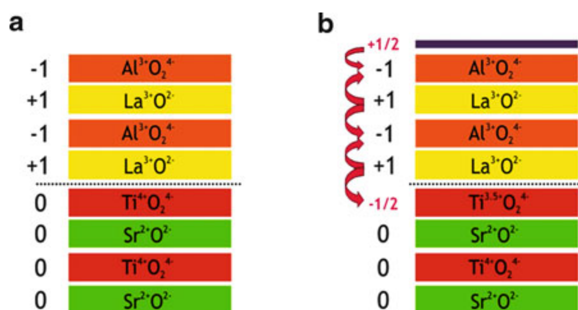

Fig. 5.8 Illustration of an atomically sharp interface between (001) $LaAlO_3$ and (001) $SrTiO_3$. (**a**) Stacking sequence of an unreconstructed n-type interface between neutral SrO and TiO_2 planes followed by charged LaO^+ and AlO_2^- planes. This stacking sequence causes a diverging potential at the interface with an increasing number of LaO^+ and AlO_2^- planes. (**b**) The diverging potential can be avoided by the transfer of ½ an electron per unit cell from the top surface to the top TiO_2 layer [48]

of defects in the $LaAlO_3$ layer due to a change in supersaturation and surface mobility of the arriving species during the deposition. However, at present there are different pressure regimes reported at which significant changes to the electrical and surface properties take place [46, 49]. The role of defects on the transport properties for the 2D-conducting layer has been studied [50]. It is reported that a dislocation in a $SrTiO_3/LaAlO_3$ heterostructure is a scattering center with an insulating and charge-depleted cross section of $\approx$5 nm. One consequence of the presence of defects on the conducting properties of the interface is a significant change in the temperature dependence of the resistance at low temperatures [50]. Similar changes to transport properties in addition with magnetic field-dependent measurements of the resistance are associated with ferromagnetic properties of this interface [46].

Ablating $LaAlO_3$ in a pressure regime well below 10^{-5}mbar, the kinetic energy of the arriving species becomes more important. As already discussed, the tail end of such an energy distribution can easily reach several tens of eV. Such a medium to higher energy ion-bombardment of $SrTiO_3$ is detrimental to the surface properties. First, a sputtering of the surface creates a finite roughness; second, the ion-damage leads to charged vacancies and hence to a well conducting surface. In addition, the combination of a very low pressure and high temperature is responsible of some oxygen loss and hence oxygen defects near the $SrTiO_3$ surface. Extended defect structures for interfaces prepared at such low pressure have been reported in [43]. The charge carrier density of these heterostructures is of the order $10^{16}/cm^2$ and comparable to numbers measured for oxygen reduced $SrTiO_3$. If such structures are annealed sufficiently long in oxygen, the conductivity originally measured disappears. Subjecting the heterostructures with 2D-conducting interface layers to an extended oxygen heat treatment, the resistance can be changed but the charge carrier density remains effectively unchanged.

There is also the question if the interface is atomically sharp, or is there some intermixing of La and Ti. The STEM image in Fig. 5.7c suggests that the interface is atomically sharp. It is a high angle annular dark field (HAADF) STEM image, where the contrast between the 5 uc $LaAlO_3$ and $SrTiO_3$ is largely due to the chemical difference between La (light) and Sr (dark). If there is some intermixing of La and Sr, it is limited to at most 1 uc. The atomic reconstruction of the $LaAlO_3/SrTiO_3$ interface based on x-ray surface diffraction studies suggests a finite intermixing over at least 1 uc [51]. Further studies to clarify this issue are necessary.

The $SrTiO_3/LaAlO_3$ stacking sequence for the interface as illustrated in Fig. 5.8a has an interesting consequence. The appearance of an interface potential due to the polar nature of the interface will drive an electronic reconstruction only if the build-in potential becomes large enough. Therefore, it can be expected that there will be a threshold thickness for $LaAO_3$ at which a diverging potential due to the increasing number of $LaAlO_3$ layers will drive an electronic reconstruction. In order to bring the potential back to zero, the nominal charge of e/2 has to be transferred from the top-most AlO_2^- layer to the interface as illustrated in Fig. 5.8b [45, 48]. In case, the diverging potential cannot be brought back to zero via a charge transfer to the interface, the structure remains insulating. The existence of such a critical

$LaAlO_3$ layer thickness was verified by Thiel et al. [34] and also confirmed for $LaVaO_3/SrTiO_3$ interfaces [40].

So far, there is no hard experimental indication that an ionic compensation mechanism is the driving force to generate interface conductivity. One way to invoke such a scenario is by applying an external electric field to the $LaAlO_3/SrTiO_3$ heterostructure with the $LaAlO_3$ layer thickness smaller than the critical thickness. There, a threshold voltage is required to obtain the conducting interface [34, 52]. Once, the conducting state is reached and the gate voltage removed, the conducting state is stable in time over several minutes to hours. This is particularly striking for electric field induced AFM written nanostructures, which are stable up to one day at room temperature [52, 53].

Most electrical measurements on this interface have been done on large area samples. For electrical transport measurements, however, a lithographically defined structure would be useful. Ion beam etching of the heterostructure is not practical due to the defect-induced conductivity at the $SrTiO_3$ surface. A useful and simple route to pattern the interface without exposing it to chemicals needed for patterning is provided by the critical layer thickness [35]. The delicate interface is protected prior patterning by two monolayers of epitaxially grown $LaAlO_3$. After the definition of the measurement structure, a second epitaxial layer of $LaAlO_3$ is grown on top of the protecting $LaAlO_3$ layer to obtain the conducting interface wherever it is required. One example of such a pattern is shown in Fig. 5.7d. It is interesting to note, that $LaAlO_3$ can be grown homoepitaxially and in sufficient quality on top of each other despite the extensive use of chemicals on the first $LaAlO_3$ surface.

5.5 Laser Ablation of Polymers

Polymers are a class of materials which require low threshold fluences for a gentle processing (reduced energy and heat transfer). This makes them suitable candidates for low power laser ablation. First studies on the laser ablation of polymers were reported in 1982 by Srinivasan [54] and by Kawamura [55] on polyethylene terephtalate and polymethyl methacrylate, respectively. Since, the ablation of polymers developed a variety of applications, ranging from drilling [56] to ophthalmology [57]. For ablation, the UV region of the spectrum is of interest, because it allows involving photochemical degradation which is intrinsically more precise than thermal decomposition. The short wavelength is also advantageous for a precision processing operating at the diffraction limit.

Most commercial polymers absorb below $\lambda = 250$ nm and these polymers can be ablated with the corresponding excimer or Nd:YAG lasers. However, by applying shorter wave length chemical bonds like C-bonds can be broken leading to a carbonization of the surface of these polymers. Therefore, it is advantageous to work in the UV range above $\lambda = 250$ nm. In this frequency range, triazene and pentazadiene chromophores have a high absorption around 300 nm and a XeCl excimer laser ($\lambda = 308$ nm) can be used for ablation. Incorporating triazene and pentazadiene

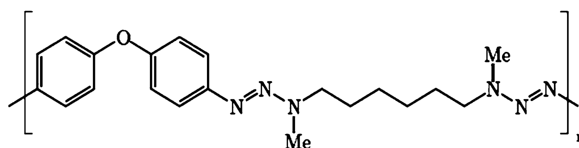

Fig. 5.9 Chemical structure of the triazene polymer

into the polymer main chain, this yields several related compounds [58]. The most promising candidate for laser ablation, an aryltriazene polymer, is shown in Fig. 5.9. This holds also true if compared to selected commercial or polymers designed for laser ablation, such as polyimides, polyesters [59,60], or polyurethanes [61,62].

The aryltriazene polymers show very high ablation rates per pulse, the lowest threshold fluence compared to other polymers and debris-free ablation. These properties make them a promising candidate for an application as a dynamic release layer (DRL) for laser-induced forward transfer (see below).

5.5.1 Ablation Mechanism

While the ablation of polymers is well established, several fundamental aspects of the ablation process are still debated. The difficulty to model the laser ablation of polymers is related to their complex nature (large molecules, possible reactive pathways, etc.) when compared to metals or oxides. Several models have been proposed, which are reviewed in [63,64] but up to now, these models are only able to describe well the experimental observations for a single class of polymers, i.e., Kapton™.

There are a range of different models to explain the ablation process. They can be divided into photochemical models [65–70], photothermal models [71–74], and photophysical models [75]. There is an effort to combine the presented models because they only partially predict aspects of the ablation of polymers. Some attempts have been made to describe the ablation process by combining the features of the different models mentioned above, thereby creating mixed model [76]. However, this appears to be a very difficult task because the details of the ablation process will always depend on the laser parameters like wavelength, fluence, pulse duration, and the chemical structure of the polymer in question.

What are the applications for polymer ablation? There are at present four directions which can be identified: (a) material removal, (b) deposition, (c) analysis, and (d) miscellaneous. (a) Material removal involves everything related to surface and volume modification with a high lateral and depth resolution. This includes direct patterning of structures thereby combining the definition and etching of a structure in a single step. (b) The deposition of a material on a substrate can either take place as a single continuous film or involves the direct transfer of a pattern. The latter point, also called laser induced transfer, will be discussed separately. (c) The removal of material from a sample can be used for analytical purposes. The ablated plume is imaged and analyzed optically using emission

spectroscopy. The constituents of a plume can also be measured using mass spectrometry, inductively coupled plasma mass spectrometry [77–79], or matrix-assisted laser desorption/ionization–time of flight analysis. All techniques allow the investigation of the initial composition of the target. (d) The fourth direction for applications include plasma thruster for microsatellites, shock wave generation and others niche applications.

5.5.2 Polymer Film Ablation

Like for metals and oxides the direct ablation of polymers in vacuum to deposit polymer films has been achieved [48, 80–82] (Fig. 5.10a). Due to the nature of the ablation process, this works only for certain polymers such as Teflon [81] and PMMA [40, 83, 84]. These polymers depolymerize upon irradiation and subsequently polymerize with a different, most probably lower molecular weight on the substrate. Alternatively, it is proposed that after the depolymerization intact chains are transferred directly onto a substrate [40, 83, 84].

The direct application of a pulsed laser beam is critical when used on sensitive compounds due to the direct irradiation of the material and the absorption of the laser energy. To prevent this, a technique was developed, called matrix-assisted pulsed laser evaporation (MAPLE). The method, shown in Fig. 5.10b, uses a frozen solvent (the matrix) target containing the material to be deposited. Upon irradiation, the solvent is evaporated and forms a plume together with the molecules of interest. Films grown on a substrate consist of dried molecules previously solvated in the matrix [82, 85–87], although recent data have shown that solvent molecules are also trapped in these films [85]. The method is mainly applied to biological molecules (e.g., proteins) or sensitive organic molecules. To avoid or reduce the aforementioned depolymerization, a possibly more gentle transfer of conductive polymers such as MEH-PPV [88, 89] and PEDOT:PSS [90] has been proposed when using a free-electron laser in the mid-infrared domain at the resonant frequency of the solvent.

Although PLD and MAPLE are very useful techniques to prepare thin organic films, they do not conserve the spatial information from the laser impact spot and

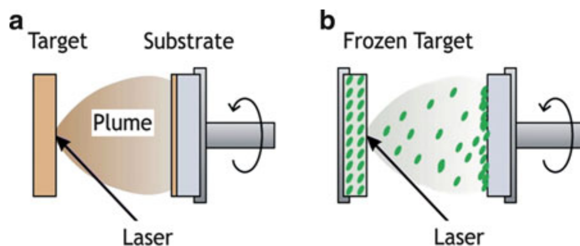

Fig. 5.10 Polymer film deposition by (**a**) PLD and (**b**) matrix-assisted pulsed laser evaporation (MAPLE). Image courtesy of Romain Fardel

do not allow the deposition of patterns, except when using a mask. To overcome this problem, the laser-induced forward transfer for organic material has been developed [91, 92]. Here, the laser forward transfer is realized by positioning a receiver substrate in front of the donor film to recover the ejected material by irradiating from the back.

5.5.3 *Film Pattern Transfer*

The defined shape of an excimer laser beam enables to transfer precise patterns, i.e., transfer of a layer from a donor to a receiver substrate while conserving the shape defined by the laser spot. This technique is called laser-induced forward transfer (LIFT) and is illustrated in Fig. 5.11a. The donor substrate is prepared by coating a film onto a transparent plate. The receiver substrate, where the material will be deposited, is placed in front of the donor film. To obtain a shape conserving transfer of the donor material, it is illuminated from the back of the substrate with the laser beam. The material is ejected as a flyer and redeposited onto the receiver substrate. Ideally, the ablation conditions for the donor film are such that the film is ejected in a compact flyer and collected in one piece on the receiver substrate. This is shown in the shadowgraphy images in Fig. 5.12 where a stable and planar polymer flyer is observed up to 0.8 μs, at a later time, the flyer starts to disintegrate [93]. The distance between the donor and receiver substrate must also be optimized to prevent a lateral spread of the ablated material. In this way, the shape of the deposited pattern corresponds to the ablated spot, and the technique allows the transfer of a structure without using a masking technique. This technique is known as a direct writing technology [94]. The main disadvantage of this method is the direct ablation of the transfer material at the interface of the transfer. This may have a detrimental effect, i.e., decomposition, on the transfer material, especially if sensitive materials are used.

To reduce or even completely avoid the thermal decomposition of the ablated polymer, a sacrificial layer can be added to the polymer layer which absorbs all the laser energy, decomposes, and the pressure build-up transfers the polymer across a gap onto the receiver substrate. Likewise, a pattern transfer can be achieved with the receiver substrate in contact with the film. This sacrificial layer is also called a DRL and the working principle is illustrated in Fig. 5.11b. The DRL can be a metal, ceramic, or a polymer depending on the application. A polymer has the advantage

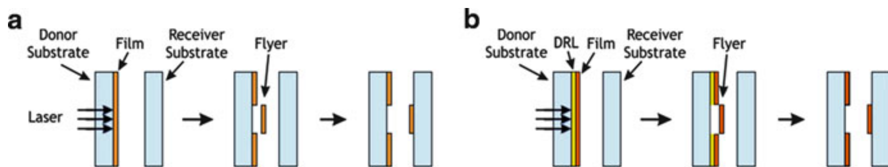

Fig. 5.11 Working principle of (**a**) the laser-induced forward transfer and (**b**) the dynamic release layer laser-induced forward transfer (DRL-LIFT). Images courtesy of Romain Fardel

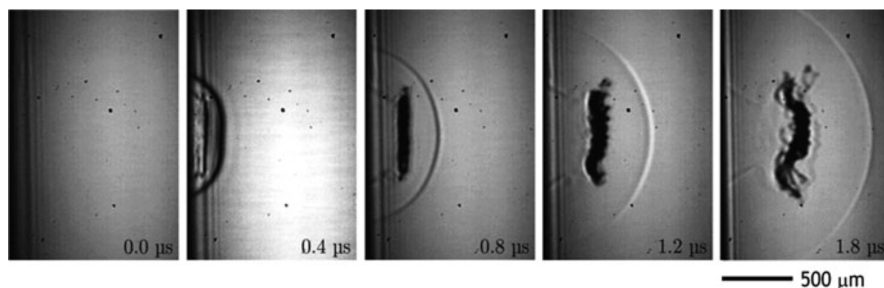

Fig. 5.12 Sequence of pictures taken for back side ablation of a 460 nm triazene polymer film at a laser fluence of 110 mJ/cm^2. The time delays are indicated on the frames [93]

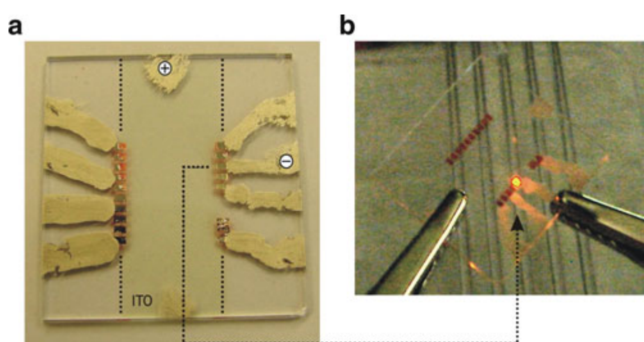

Fig. 5.13 Overview of an organic light emitting diode (OLED) pixel realized by laser transfer. (**a**) top view of the lay-out, (**b**) pixel in operation under inert atmosphere. Noncontacted pixels also visible. Images courtesy of Romain Fardel

that upon complete decomposition into gaseous products, no contaminants can be incorporated into the transferred film while the application of UV-light reduces the thermal load to the transferred film.

Combining the UV sensitivity of triazene-polymers with the laser-induced forward transfer, the preparation of organic light emitting diode (OLED) based on polymers has been successfully demonstrated. These polymer OLEDs are fully functional without thermal or UV degradation [95] (Fig. 5.13). In Fig. 5.13a, a top view of the layout is shown indicating the pixel which is operated in Fig. 5.13b. The glass substrate is coated with a strip of indium-tin-oxide (ITO) as a transparent, conducting bottom electrode. The same approach using DRL-LIFT has been utilized to transfer biological material [96], nano-quantum dots [97], metals [98], and ceramics [99].

5.6 Conclusions

In this chapter, the evaporation of matter based on pulsed lasers has been introduced and advantages as well as disadvantages of this technique discussed. Next, the initial ablation processes and plume formation were introduced and the plume formation and expansion in vacuum and with a background pressure were presented in detail. Often, PLD is a tool to grow thin epitaxial films. Therefore, models and examples of thin film growth have been presented. The growth of $LaAlO_3/SrTiO_3$ heterostructures has been discussed separately to show one example for interface engineered thin film structures with remarkable properties where many aspects of thin film growth can be studied and discussed. Finally, the last section discusses the ablation of polymers which holds quite some promise for, e.g., the controlled deposition of polymer OLED pixels.

Acknowledgements The authors would like to thank S. Heiroth, I. Marozau, R. Fardel, M. Nagel, F. Nüesch, P.R. Willmott, S.A. Pauli, S. Thiel, G. Hammerl, J. Mannhart, L. Fitting Kourkoutis, and D.A. Muller for valuable discussions and interactions and also providing us with figures. Financial support of the Paul Scherrer Institut and the Swiss National Science Foundation are greatly acknowledged.

References

1. D. Chrisey, G.K. Hubler, *Pulsed Laser Deposition of THIN Films*, vol. 154–155 (Wiley, New York, 1994)
2. P.R. Willmott, J.R. Huber, Rev. Mod. Phys. **72**, 315 (2000)
3. X. Yang, Y. Tang, M. Yu, Q. Qin, Thin Solid Films **358**, 187 (2000)
4. M. Braic, M. Balaceanu, A. Vladescu, A. Kiss, V. Braic, G. Epurescu, G. Dinescu, A. Moldovan, R. Birjega, M. Dinescu, Appl. Surf. Sci. **253**, 8210 (2007)
5. P.R. Willmott, R. Timm, J.R. Huber, J. Appl. Phys. **82**, 2082 (1997)
6. X.Y. Wang, D.M. Rice, Y.S. Lee, M.C. Downer, Phys. Rev. B **50**, 8016 (1994)
7. M.J. Montenegro, K. Conder, M. Döbeli, T. Lippert, P.R. Willmott, A. Wokaun, Appl. Surf. Sci. **252**, 4642 (2006)
8. I. Marozau, A. Shkabko, G. Dinescu, M. Döbeli, T. Lippert, D. Logvinovich, M. Malle-pell, C.W. Schneider, A. Weidenkaff, A. Wokaun, Appl. Surf. Sci. **255**, 5252 (2009)
9. I. Marozau, M. Döbeli, T. Lippert, D. Logvinovich, M. Mallepell, A. Shkabko, A. Wei-denkaff, A. Wokaun, Appl. Phys. A **89**, 933 (2007)
10. V. Vitiello, S. Amoruso, A. Sambri, X. Wang, Appl. Surf. Sci. **252**, 4712 (2006)
11. S. Amoruso, G. Ausanio, C. de Lisio, V. Iannotti, M. Vitiello, X. Wang, L. Lanotte, Appl. Surf. Sci. **247**, 71 (2005)
12. S. Amoruso, G. Ausanio, R. Bruzzese, M. Vitiello, X. Wang, Phys. Rev. B **71**, 033406 (2005)
13. J. Perrière, C. Boulmer-Leborgne, R. Benzerga, S. Tricot, J. Phys. D Appl. Phys. **40**, 7069 (2007)
14. T. Ishiguro, T. Shoji, H. Inada, Appl. Phys. A **69**, 149 (1999)
15. S.I. Anisimov, B.S. Luk'yanchuk, A. Luches, Appl. Surf. Sci. **96–98**, 24 (1996)
16. S. Amoruso, R. Bruzzese, N. Spinelli, R. Velotta, J. Phys. B At. Mol. Opt. Phys. **32**, 131 (1999)
17. S. Canulescu, E.L. Papadopoulou, D. Anglos, Th. Lippert, C.W. Schneider, A. Wokaun, J. Appl. Phys. **6**, 493 (2009)
18. S. Amoruso, V. Berardi, R. Bruzzese, N. Spinelli, X. Wang, Appl. Surf. Sci. **127–129**, 953 (1998)

19. L. Torrisi, F. Caridi, D. Margarone, A. Picciotto, A. Mangione, J.J. Beltrano, Appl. Surf. Sci. **252**, 6383 (1990)
20. S. Canulescu, Th. Lippert, A. Wokaun, Appl. Phys. A **93**, 771 (2008)
21. J.C.S. Kools, T.S. Baller, S.T. DeZwart, J. Dieleman, J. Appl. Phys. **71**, 4547 (1999)
22. M. Kawasaki, K. Takahashi, T. Maeda, R. Tsuchiya, M. Shinohara, O. Ishiyama, T. Yonezawa, M. Yoshimoto, H. Koinuma, Science **226**, 1540 (1994)
23. G. Koster, B.L. Kropman, G. Rijnders, D.H.A. Blank, H. Rogalla, Appl. Phys. Lett. **73**, 2920 (1998)
24. T. Ohnishi, K. Takahashi, M. Nakamura, M. Kawasaki, M. Yoshimoto, H. Koinuma, Appl. Phys. Lett. **74**, 2531 (1999)
25. S. Bals, G. Rijnders, D.H.A. Blank, G. Van Tendeloo, Phys. C **355**, 225 (2001)
26. A. Schmehl, F. Lichtenberg, H. Bielefeldt, J. Mannhart, Appl. Phys. Lett. **82**, 3077 (2003)
27. M. Huijben, G. Rijnders, D.H.A. Blank, S. Bals, S. Van Aert, J. Verbeeck, G. Van Tendeloo, A. Brinkman, H. Hilgenkamp, Nat. Mater. **5**, 556 (2006)
28. R.E. Teece, J.S. Horwitz, J.H. Claassen, D.B. Chrisey, Appl. Phys. Lett. **65**, 2860 (1994)
29. G. Cappuccio, U. Gambardella, A. Morone, S. Orlando, G.P. Parisi, Appl. Surf. Sci. **109–110**, 399 (1997)
30. J.L. Batsone, *Atomic Level Properties of Interface Materials*, vol. 83 (Chapman and Hall, London, 2008), p. 38003
31. J.A. Venables, G.D.T. Spiller, M. Hanbucken, Rep. Prog. Phys. **47**, 399 (1984)
32. C. Gerber, D. Anselmetti, J.G. Bednorz, J. Mannhart, D.G. Schlom, Nature **350**, 279 (1991)
33. I. Sunagawa, P. Bennema, *Preparation and Properties of Solid State Materials*, vol. 7 (Dekker, New York, 1982)
34. S. Thiel, G. Hammerl, A. Schmehl, C.W. Schneider, J. Mannhart, Science **313**, 1942 (2006)
35. C.W. Schneider, S. Thiel, G. Hammerl, C. Richter, J. Mannhart, Appl. Phys. Lett. **89**, 122101 (2006)
36. J.M. Dekkers, G. Rijnders, S. Harkema, H.J.H. Smilde, H. Hilgenkamp, H. Rogalla, D.H.A. Blank, Appl. Phys. Lett. **83**, 5199 (2003)
37. J.R. Kirtley, C.C. Tsuei, A. Ariando, C.J.M. Verwijs, S. Harkema, H. Hilgenkamp, Nat. Phys. **2**, 160 (2006)
38. A. Ohtomo, D.A. Muller, J.L. Grazul, H.Y. Hwang, Nature **419**, 378 (2002)
39. A. Ohtomo, H.Y. Hwang, Nature **427/441**, 423/120 (2004/2006)
40. Y. Hotta, T. Susaki, H.Y. Hwang, Phys. Rev. Lett. **99**, 236805 (2007)
41. N. Reyren, S. Thiel, A.D. Caviglia, L. Fitting-Kourkoutis, G. Hammerl, C. Richter, C.W. Schneider, T. Kopp, A.-S. Rüetschi, D. Jaccard, M. Gabay, D.A. Muller, J.-M. Tris-cone, J. Mannhart, Science **317**, 1196 (2007)
42. G. Herranz, M. Basletic, M. Bibes, C. Carrétéro, E. Tafra, E. Jacquet, K. Bouzehouane, C. Deranlot, A. Hamzic, J.-M. Broto, A. Barthtélémy, A. Fert, Phys. Rev. Lett. **98**, 216803 (2007)
43. A. Kalabukhov, R. Gunnarsson, J. Börjesson, E. Olsson, T. Claeson, D. Winkler, Phys. Rev. B **75**, 121404 (2007)
44. W. Siemons, G. Koster, H. Yamamoto, W.A. Harrison, G. Lucovsky, T.H. Geballe, D.H.A. Blank, M.R. Beasley, Phys. Rev. Lett. **98**, 196802 (2007)
45. S. Okamoto, A.J. Millis, Nature **428**, 630 (2004)
46. A. Brinkman, M. Huijben, M. van Zalk, J. Huijben, U. Zeitler, J.C. Maan, W.G. van der Wiel, G. Rijnders, D.H.A. Blank, H. Hilgenkamp, Nat. Mater. **6**, 493 (2007)
47. A.D. Caviglia, S. Gariglio, N. Reyren, D. Jaccard, T. Schneider, M. Gabay, S. Thiel, G. Hammerl, J. Mannhart, J.-M. Triscone, Nature **456**, 624 (2008)
48. J. Mannhart, D.H.A. Blank, H.Y. Hwang, A.J. Millis, J.-M. Triscone, MRS Bull. **30**, 1027 (2008)
49. S. Thiel, C.W. Schneider, F.L. Kourkoutis, D.A. Muller, N. Reyren, A.D. Caviglia, S. Gariglio, J.-M. Triscone, J. Mannhart, Phys. Rev. Lett. **102**, 046809 (2009)
50. S. Thiel, Study of interface properties in $LaAlO_3/SrTiO_3$ heterostructures. Ph.D. thesis, University of Augsburg (2009)

51. P.R. Willmott, S.A. Pauli, R. Herger, C.M. Schlepütz, D. Martoccia, B.D. Patterson, B. Delley, R. Clarke, D. Kumah, C. Cionca, Y. Yacoby, Phys. Rev. Lett. **99**, 155502 (2007)
52. C. Cen, S. Thiel, J. Mannhart, J. Levy, Science **323**, 1026 (2009)
53. C. Cen, S. Thiel, G. Hammerl, C.W. Schneider, K.E. Andersen, C.S. Hellberg, J. Mannhart, J. Levy, Nat. Mater. **7**, 298 (2008)
54. R. Srinivasan, V. Mayne-Banton, Appl. Phys. Lett. **41**, 576 (1982)
55. Y. Kawamura, K. Toyoda, S. Namba, Appl. Phys. Lett. **40**, 374 (1982)
56. A. Schawlow, Science **149**, 13 (1965)
57. G.A. Moo-Young, West J. Med. **143**, 745 (1985)
58. T. Lippert, A. Wokaun, J. Stebani, O. Nuyken, J. Ihlemann, Angew. Makromol. Chem. **206**, 97 (1993)
59. T. Lippert, Adv. Polym. Sci. **168**, 51 (2004)
60. T. Lippert, J. Dickinson, Chem. Rev. **103**, 453 (2003)
61. K. Suzuki, M. Matsuda, T. Ogino, N. Hayashi, T. Terabayashi, K. Amemiya, Excimer Lasers Opt. Appl. **2992**, 98 (1997)
62. N. Hayashi, K. Suzuki, M. Matsuda, T. Ogino, Y. Tomita, Excimer Lasers Opt. Appl. **2992**, 129 (1997)
63. S. Anisimov, B. Luk'yanchuk, Physics-Uspekhi **45**, 293 (2002)
64. N.M. Bityurin, B. Luk'yanchuk, M. Hong, T. Chong, Chem. Rev. **103**, 519 (2003)
65. M. Prasad, P.F. Conforti, B.J. Garisson, J. Appl. Phys. **101**, 103113 (2007)
66. N. Mansour, K. Jamshidi-Ghaleh, J. Phys. D Appl. Phys. **38**, 852 (2005)
67. M. Castex, N.M. Bityurin, Appl. Surf. Sci. **197–198**, 805 (2002)
68. H. Schmidt, J. Ihlemann, B. Wolff-Rottke, K. Luther, J. Troe, J. Appl. Phys. **83**, 5458 (1998)
69. G. Pettit, R. Sauerbrey, Appl. Phys. A **56**, 51 (1993)
70. M. Hauer, D.J. Funk, T. Lippert, A. Wokaun, Appl. Surf. Sci. **208**, 107 (2003)
71. G. Bounos, A. Selimis, S. Georgiou, E. Rebollar, M. Castillejo, N.M. Bityurin, J. Appl. Phys. **100**, 114323 (2006)
72. N.M. Bityurin, in *Proc. SPIE*, vol. 4423 (Chapman and Hall, London, 2001), p. 197
73. N. Arnold, N.M. Bityurin, D. Bäuerle, Appl. Surf. Sci. **138–139**, 212 (1999)
74. N.M. Bityurin, N. Arnold, B. Luk'yanchuk, D. Bäuerle, Appl. Surf. Sci. **127–129**, 164 (1998)
75. B. Luk'yanchuk, N.M. Bityurin, S. Anisimov, A.Y. Malyshev, N. Arnold, D. Bäuerle, Appl. Surf. Sci. **106**, 120 (1996)
76. N. Arnold, N. Bityurin, Appl. Phys. A **68**, 615 (1999)
77. C. Latkoczy, D. Günther, J. Anal. At. Spectrom. **17**, 1264 (2002)
78. J. Koch, M. Wälle, J. Pisonero, D. Günther, J. Anal. At. Spectrom. **21**, 932 (2006)
79. M. Tanner, D. Günther, J. Anal. At. Spectrom. **21**, 941 (2006)
80. N. Matsumoto, H. Shima, T. Fujii, F. Kannari, Appl. Phys. Lett. **71**, 2469 (1997)
81. G. Blanchet, Macromolecules **28**, 4603 (1995)
82. D. Chrisey, A. Piqué, R. McGill, J. Horwitz, B. Ringeisen, D. Bubb, P. Wu, Chem. Rev. **103**, 553 (2003)
83. E. Süske, T. Scharf, T. Junkers, M. Buback, H.U. Krebs, J. App. Phys. **100**, 014906 (2006)
84. B. Lösekrug, A. Meschede, H.U. Krebs, Appl. Surf. Sci. **254**, 1312 (2007)
85. D. Chrisey, A. Piqué, J. Fitz-Gerald, R. Auyeung, R. McGill, H. Wu, M. Duignan, Appl. Surf. Sci. **154–155**, 593 (2000)
86. A. Purice, J. Schou, P. Kingshott, N. Pryds, M. Dinescu, Appl. Surf. Sci. **253**, 7952 (2007)
87. A. Purice, J. Schou, P. Kingshott, N. Pryds, M. Dinescu, Appl. Surf. Sci. **253**, 6451 (2007)
88. S. Johnson, C. Bowie, B. Ivanov, H. Park, R. Haglund Jr., Proc. SPIE **6486**, 64860 (2007)
89. B. Toftmann, M.R. Papantonakis, R.C.Y. Auyeung, W. Kim, S.M. O'Malley, D.M. Bubb, J.S. Horwitz, J. Schou, P.M. Johansen, R.F. Haglund, Thin Solid Films **453–454**, 177 (2004)
90. S.L. Johnson, H.K. Park, R.F. Haglund Jr., Appl. Surf. Sci. **253**, 6430 (2007)
91. J. Bohandy, B.F. Kim, F.J. Adrian, J. Appl. Phys. **60**, 1538 (1986)
92. K. Kyrkis, A. Andreadaki, D. Papazoglou, I. Zergioti , *Recent advances in Laser Processing of Materials*, vol. 241 (Elsevier, Amsterdam, 2006)
93. R. Fardel, M. Nagel, F. Nüesch, T. Lippert, A. Wokaun, Appl. Surf. Sci. **255**, 5430 (2009)
94. C. Arnold, P. Serra, A. Piqué, MRS Bull. **32**, 23 (2007)

95. R. Fardel, M. Nagel, F. Nüesch, T. Lippert, A. Wokaun, Appl. Phys. Lett. **91**, 061103 (2007)
96. A. Doraiswamy, R. Narayan, T. Lippert, L. Urech, A. Wokaun, M. Nagel, B. Hopp, M. Dinescu, R. Modi, R. Auyeung, D. Chrisey, Appl. Surf. Sci. **252**, 4743 (2006)
97. J. Xu, J. Liu, D. Cui, M. Gerhold, A.Y. Wang, M. Nagel, T.K. Lippert, Nanotech. **18**, 025403 (2007)
98. R. Fardel, M. Nagel, T. Lippert, F. Nüesch, A. Wokaun, Appl. Surf. Sci. **254**, 1322 (2007)
99. D.P. Banks, K. Kaur, R. Gazia, R. Fardel, M. Nagel, T. Lippert, R.W. Eason, Europhys. Lett. **83**, 38003 (2008)

Chapter 6
Processing with Ultrashort Laser Pulses

Jürgen Reif

Abstract This chapter reviews the peculiarities of ultrashort laser pulse interaction with materials and the consequences for materials processing. After a short introduction, presenting time scales of typical processes and comparing previous results for femtosecond and nanosecond laser pulses, we start with the fundamentals of laser-material coupling. Then we describe energy dissipation dynamics and direct follow-up processes and finish with a consideration of bulk and surface relaxation and structure formation on a time scale much longer than the pulse duration.

6.1 Introduction and General Considerations

This chapter is devoted to the application of ultrashort laser pulses (100 femtoseconds or less) for materials processing and the peculiarities related to that short interaction time. Generally, laser materials processing can be classified in a series of processes: the laser energy is coupled to the material; there, it is dissipated and, finally, results in a material reaction like photochemistry [1], melting [2], ablation [3], and phase transformation [4]. In addition, there may be interactions outside the target material, like absorption of laser energy in an ablation plume (cf. Chap. 4) with subsequent plasma sputtering [5]. Further, postinteraction phenomena can play a role in processing, like self-organized structure formation [6], diffusion, (re-) crystallization, and annealing [7]. The time scales involved may range from a few femtoseconds to several microseconds or even longer (cf. Chap. 3): the basic light absorption occurs instantaneously during illumination. It starts during the first optical cycles or femtoseconds. Photochemistry can set in instantaneously and last for nanoseconds after the illumination stops. Both ablation and melting start around one picosecond after the onset of energy input and then may go on for a considerably

J. Reif
Brandenburgische Technische Universität (BTU) Cottbus and Cottbus JointLab,
Universitätsstrasse 1, 03046 Cottbus, Germany
e-mail: reif@tu-cottbus.de, www.physik.tu-cottbus.de/physik/xp2

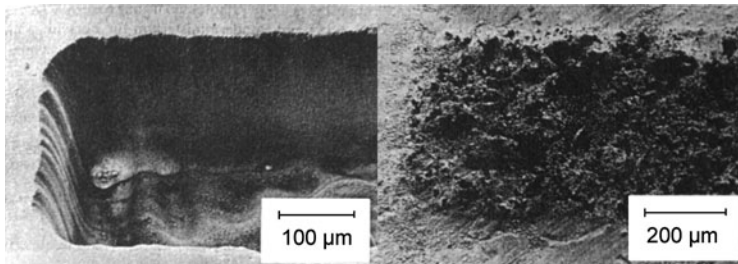

Fig. 6.1 SEM photographs of ablated spots on Teflon for 248-nm-pulses of different duration. *Left panel*: 300 fs (240 pulses at 1 J/cm^2); *Right panel*: 16 ns (50 pulses at 2 J/cm^2) (from [10])

long time. Phase transformation as well as crystallization and annealing may result either from refreezing of the melt or from high ablation-recoil pressure, going on for several microseconds. Usually, laser pulses with a duration of several (ten) nanoseconds are used for materials processing. There, the illumination continues while the material modification already proceeds; i.e., the incident light hits a target with changing (optical) properties. In contrast, pulses of subpicosecond duration open new potentials for laser processing [8]. It becomes possible to concentrate the illumination to only the first steps in the series of processes [9] when a significant material modification has not yet started. Further, the high intensity available at comparably low energy may have implications on both the coupling and the type of materials modification obtainable, as we will show later. Already in the very first reports on materials processing by ultrashort laser pulses [10], a distinct effect was observed: the definition of processed area was, obviously, much cleaner than by processing with nanosecond pulses (cf. Fig. 6.1). This was attributed to the idea that the heat affected zone in the material around the illuminated area was negligibly small, due to an extremely short heat diffusion length during the pulse duration.

To date, it appears, in fact, confirmed that the application of ultrashort laser pulses provides finer, more precise, and better defined results than the use of longer pulses.

6.2 Laser-Material Coupling

As was already addressed in Chap. 3, laser materials processing relies, essentially, on the deposition of light energy into the target, via heating of conduction band electrons or excitation of electrons across the band gap. In principle, band-to-band absorption occurs if the photon energy, $\hbar\omega$, matches the energy gap. Then, the absorbed energy is given by the product of photon energy, $\hbar\omega$, and number, N, of absorbed photons. N is given by the product of absorption probability, $\wp$, and photon density, ρ:

$$W_{\text{abs}} = N\hbar\omega = \wp\rho\hbar\omega. \tag{6.1}$$

For a practical use, it is more convenient to express the absorbed energy in terms of incident fluence, F, i.e., energy area density, and macroscopic absorption cross section, σ:

$$W_{\text{abs}} = \sigma F. \tag{6.2}$$

Classically, σ is a material constant, depending on the absorption strength of the respective transition and on the energy mismatch between photon and material energy structure. All material energy structure depends, however, on *Coulomb* interaction between electrons and atomic cores. Therefore, at very high incident intensity, I, the electric light field

$$E_{\text{light}} = \sqrt{2I/(c\varepsilon_0)} \tag{6.3}$$

may severely perturb the internal *Coulomb* potential and thus influence, transiently, the interaction cross section which is no longer a constant but depends on the laser electric field or rather intensity:

$$\sigma = \sigma(E_{\text{light}}) = \sigma'(I) \tag{6.4}$$

The consequence of this intensity dependent cross section is a nonlinear absorption which will be detailed in the next paragraph.

6.2.1 Nonlinear Absorption

As the electric light field may be considered as a perturbation of the static electronic properties, the nonlinear cross section may be developed in a power series of the incident intensity:

$$\sigma'(I) = \sum_n \sigma^{(n)} I^{n-1}; \quad n = 1, 2, ... \tag{6.5}$$

with $\sigma^{(1)}$ being the "classical," intensity independent, absorption cross section. As a consequence, the absorbed energy becomes:

$$W = \sigma' F = \left(\sum_n \sigma^{(n)} I^{(n-1)}\right) F = \left(\sum_n \sigma^{(n)} I^{(n-1)}\right) I\tau = \sum_n \sigma^{(n)} I^n \tau, \tag{6.6}$$

where τ is the pulse duration[1] and the fluence is $F = I \cdot \tau$. Assuming an incident field $E = E_0 \cdot \exp\{\mathrm{i}(\omega t - \mathbf{kr})\}$, the local component ($r = 0$), $E^{(n)} = E^n$, of the perturbing field contains contributions at frequency $n \cdot \omega$, i.e., the interaction energy

[1] For simplicity, here only pulses with rectangular shape in time are considered.

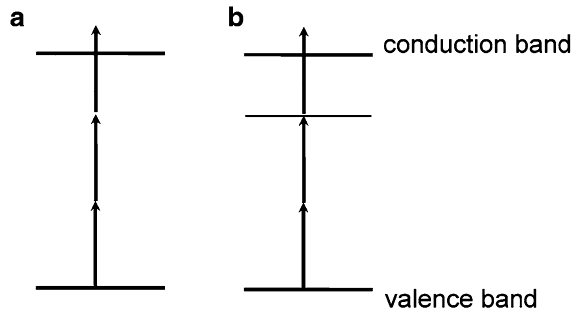

Fig. 6.2 Multiphoton absorption across the band gap. (**a**) Three photon absorption; (**b**) resonance enhancement by defect state

is n times the photon energy. Correspondingly, the interaction may be considered as the simultaneous work of n photons and is termed a "multiphoton" transition. Thus, a nominally "transparent" material can absorb light (Fig. 6.2). The absorption can even be enhanced if there are localized defect states within the band gap.

6.2.2 Hot Electron Generation

If electrons are already present in the conduction band (from multiphoton absorption or intrinsic [metals, semiconductors]), these electrons can be heated by the laser energy and then, potentially, create more hot electrons by avalanche and Auger processes [9,11]. Because of the short pulse duration, the electron heating is much faster than any energy transfer to the lattice, and a "two-temperature" regime is established (high temperature of the electron gas, low lattice temperature) [9, 11]. Target modification, i.e., actual processing, occurs, usually, only after the return to a thermal equilibrium between lattice and electrons which depends on the electron–phonon collision rate.

6.2.3 Incubation

An interesting phenomenon is observed for processing under multiple-pulse irradiation. In particular, in the case of multiphoton absorption, the coupling efficiency increases significantly with successive pulses (Fig. 6.3) In a first attempt to understand this incubation a merely statistical model was introduced [12], assuming the ablation threshold I_t to decrease inversely proportional to a power of the number of pulses N: $I_t(N) \sim 1/N^{\alpha}$. A more "physical" model, assuming an exponential increase of the number of defects (responsible for the threshold reduction), was presented in [13], postulating $I_t(N) \sim \exp(-\alpha N)$. In fact, as is shown in Fig. 6.3, recent experimental results favor this exponential model [14].

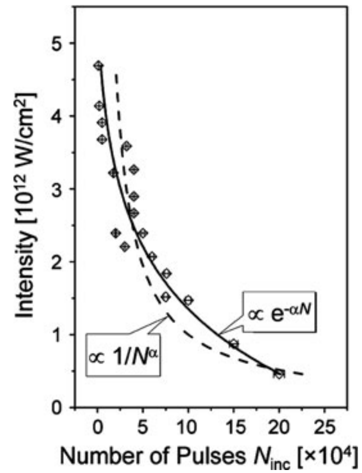

Fig. 6.3 Multipulse (N-on-1) desorption threshold intensity as a function of number N of subsequent pulses [14]. The comparison with the "physical" exponential model (*solid line*) and the statistical model (*dashed line*) confirms the idea of increasing defect generation as the origin of incubation

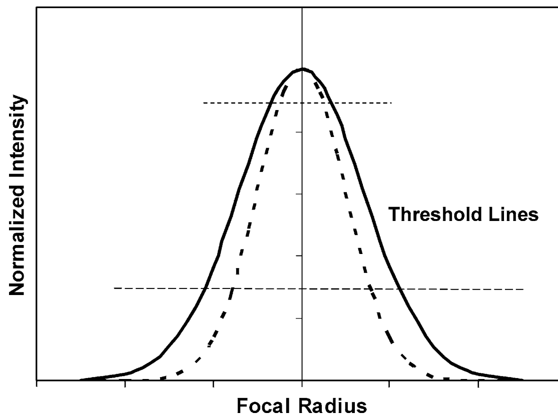

Fig. 6.4 Focal beam profile (*normalized*) for Gaussian beam (*solid line*) and squared Gaussian beam (*dashed line*). The dashed horizontal line indicates the threshold intensity. Obviously, the squared-beam radius is smaller than the diffraction limit, given by the Gaussian beam. The dotted line indicates the situation where only the most intense central part of the beam profile overcomes the action threshold

6.2.4 Resolution Below the Diffraction Limit

Another interesting consequence of multiphoton absorption is the possibility of generating structures below the diffraction limit [15]. This is schematically illustrated in Fig. 6.4 for a two-photon transition: As the absorption cross-section depends, in this case, on the square of the local intensity, the effective spatial beam profile is the square of the original pulse.

Even stronger confinement of the surface interaction region can be obtained by using an optical near-field microscope [16]. Another possibility consists in adjusting the laser pulse peak intensity in the focal region just only slightly above the

threshold for material modification (Sect. 6.5 and Chaps. 3, 5, 7, 8). Then, only the very top of the beam profile will act, thus significantly reducing the modified spot size [17] (cf. dotted line in Fig. 6.4).

6.3 Dissipation Dynamics

Once the laser energy is deposited in the target electronic system, it will be dissipated and transferred to the lattice. Only then, in fact, material modification and processing can take place.

6.3.1 Dissipation Channels

The only direct action of the laser energy input is an ionization of the interaction volume. For further energy dissipation from the electrons to the lattice there are, in principle, two channels: (1) thermodynamic equilibration between electron bath and lattice by electron–phonon collisions [9, 11, 18] and (2) perturbation of crystalline bonds when binding electrons are excited from their state of equilibrium. For channel (2) molecular dynamics calculations [19, 20] and tight-binding simulations [21] indicate that within a few 10 fs the crystalline lattice starts to be severely disturbed and dissolved. The dissolution can go so far that atoms start to leave the crystal surface and, thus, initiate ablation. The subsequent route for channel (1) is more complicated: since the dissipation occurs very rapidly, the temperature can, occasionally, rise accordingly, and homogeneous nucleation may take place in the interaction volume, giving rise to a phase explosion [9, 22, 23]. Usually, the time scale of the actual explosion, i.e., material removal, is at the order of a few nanoseconds. This is significantly *after* the end of energy input. However, the lattice excitation, via both routes (1) and (2), does not necessarily result in ablation. It can, as well, relax via classical thermodynamic pathways into the liquid state and, then, end in (re-)crystallization, again on a time scale much longer than the pulse duration.

6.3.2 Transient Material Modification

As was just indicated, a main feature of materials processing with ultrashort laser pulses is the temporal separation between energy input and (macroscopic) action. This implies that during and immediately after the laser pulse the material is in a transiently modified state. Similar to the effect of incubation, this modified state can result in a changed response to a second laser pulse following immediately after, as shown in Fig. 6.5.

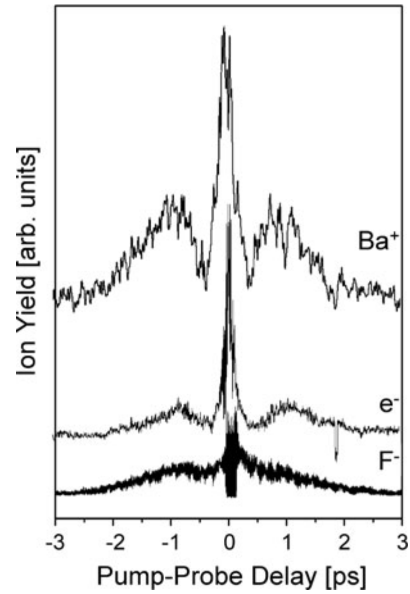

Fig. 6.5 Transient modification of material response: pump-probe investigation of femtosecond laser desorption from BaF_2. For a second pulse about 700 fs after irradiation with a first laser pulse, desorption is significantly enhanced, indicating an increased absorption which, subsequently, decays again

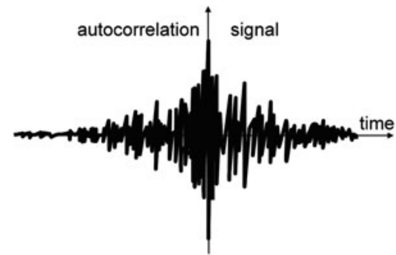

Fig. 6.6 Typical autocorrelation of an "optimally shaped" pulse after phase modulation of a femtosecond pulse in a programmable spatial light modulator (SLM)

This transient modification can be successfully exploited by sending appropriately shaped pulses [24] to the target, which can be considered to produce modulated trains of pulses over a certain range of time (Fig. 6.6). It has been demonstrated [24] that thus the processing result can be optimized.

A particular type of transient material modification is the possibility of driving the target out of thermal equilibrium [6, 25]. Then, classical thermodynamics is no longer a good way of describing the evolution of the system. In fact, pump-probe x-ray diffraction [26–28] indicates the presence of such nonequilibrium systems, also termed "nonclassical liquids," exhibiting the loss of near order but keeping far order. As will be shown later, relaxation from this instability results in a very special type of materials processing, namely self-organized surface structure formation.

6.4 Desorption/Ablation

6.4.1 Concept

One of the most dramatic effects of the laser impact is the removal of material from the target surface. At moderate pulse energy only individual ions or clusters come off, frequently attributed to Coulomb explosion of an electrostatically destabilized surface. However, this "desorption" is, normally, too weak for materials processing. The much stronger removal for this purpose, termed "ablation," occurs only beyond an (empirical) threshold pulse energy. The corresponding processes are more complex than for desorption and combine Coulomb explosion, phase explosion and, potentially, plasma expansion. This plasma is the consequence of an extremely high excitation, with a high density of hot electrons, directly within the target. In contrast to the interaction of longer pulses it does not result from an excitation of the ablation plume in front of the target. Laser ablation is, certainly, the base of the most important field of laser materials processing. Cutting, drilling, lithography but also pulsed-laser-deposition (PLD) rely on this phenomenon. As suggested already by the first experiments [10], the ultra-short-pulse results appear, in most cases, much cleaner and better defined than those obtained with longer pulses [29–42]. Taking into account the timescales and processes involved, the early explanation of a reduced heat affected zone (HAZ) appears evident. Because the energy input is terminated before particle emission occurs, all excited material is ejected, and no additional energy is deposited in the surrounding target region (Fig. 6.7). This has been confirmed experimentally [43].

However, this scenario only holds as long as the initial excitation is not too large. Otherwise, the dissipation rate can be faster than the ablation process, and a larger region than originally irradiated is affected, leading to a heat affected zone similar to the case of long-pulse irradiation.

Once ablated, the material can be recondensed on a substrate in the ablated particle stream. This is the basic idea of pulsed laser deposition of thin films, which is the subject of Chap. 5 of this volume. The peculiarities of using femtosecond laser ablation may be that the ablation plume consists of higher-energetic ions than for longer pulses [44]. On the other hand, the droplet content in the plume is strongly reduced while there is a large amount of ionic clusters [45, 46], resulting in new properties of the deposited films.

6.4.2 Applications

One application of ultrafast (multiphoton-)ablation is, certainly, the direct writing of fine, well-defined structures with a feature size below 1 μm, such as holographic gratings [47] or Fresnel lenses [48] (Fig. 6.8).

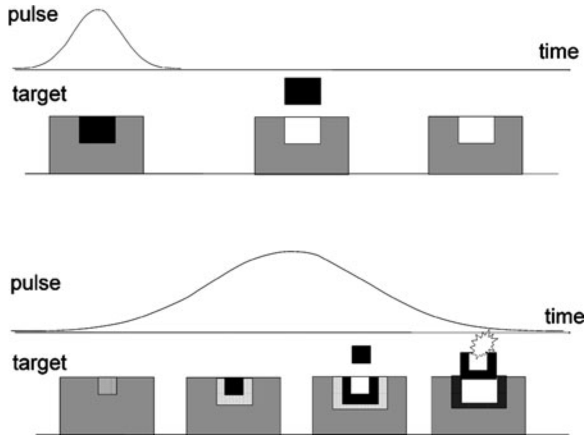

Fig. 6.7 Difference between femtosecond (*upper*) and long-pulse (*lower*) ablation. (The shaded area is the excited region. The darker the shading, the stronger is the excitation). For the short pulse, the irradiated area is immediately highly excited. After a dissipation delay, the whole excited volume is ablated. For the long pulse, at the beginning, only the central part is weakly excited. For increasing pulse duration, the central-part excitation increases above threshold, the surrounding area is weakly excited. Still later (yet during the pulse), the central area material leaves the target, the surrounding reaches the threshold and a still wider range is weakly excited. At the same time, the ablated plume still absorbs laser light, generating a plasma which, for still longer pulse duration, is heated by inverse bremsstrahlung and, then, sputters back to the surface

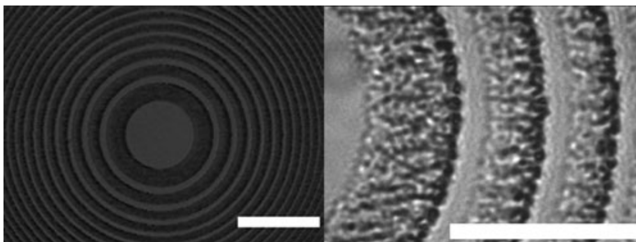

Fig. 6.8 Direct writing of well defined structures with femtosecond laser: Fresnel phase plates infused silica [48], Overview (*left*) and detail (*right*). The white bar corresponds to 100 μm in both panels

Another field is the structuring of thin films on supporting substrates [49]. Of particular interest is the repair of defects in photomasks, e.g., Cr on quartz [40], without affecting the substrate. In another application, tiny pores were introduced in a protective TiN thin film to improve its tribological performance [50] (Fig. 6.9). Again, the low thermal budget of femtosecond processing was necessary to prevent delamination of the thin film.

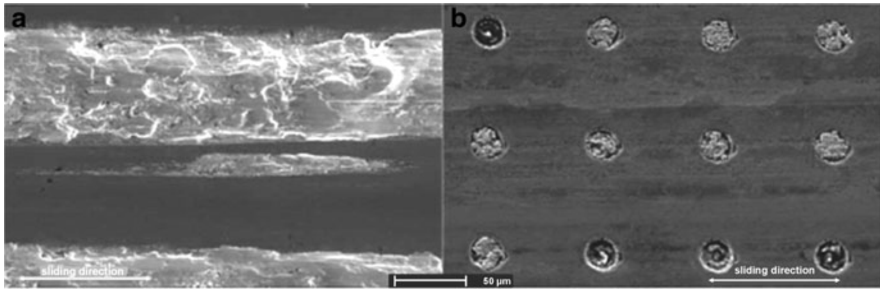

Fig. 6.9 Wear traces on TiN protective film. (*left*: unpatterned; *right*: femtosecond patterned [50])

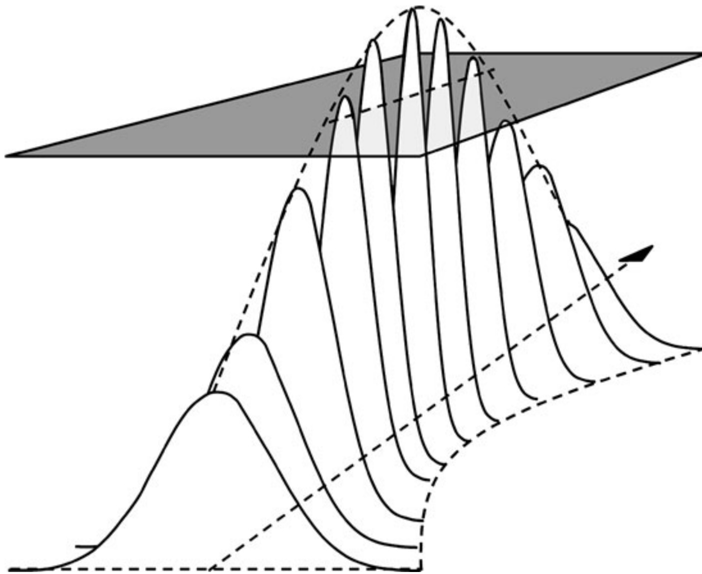

Fig. 6.10 Sketch of the intensity variation in the focal region. The *shaded section* represents the action threshold. It is easily seen, that the threshold intensity is exceeded is only in a limited volume (*unshaded*). Depending on focussing conditions and multiphoton order (cf. Fig. 6.4) this volume can be minimized in 3-D

6.5 3-D Bulk Modifications, Waveguide Writing

Because of the high intensity available at relatively low fluence, the possibility to easily rely on multiphoton absorption with femtosecond pulses opens new channels also for processing in the bulk of a material. Restricting the action volume, where the threshold intensity is exceeded, by tight focussing, even three-dimensional processing becomes feasible (Fig. 6.10).

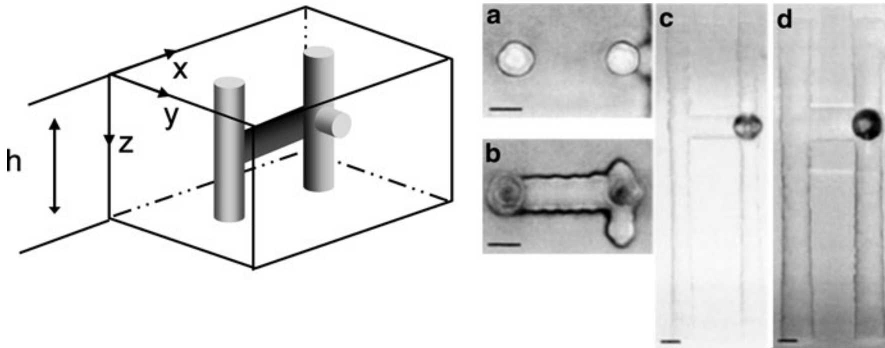

Fig. 6.11 Writing of 3-D structures in fused silica [51]. *Left*: The laser is tightly focused inside the transparent sample. In the focal region, a void is generated after multiphoton absorption and subsequent bond breaking. To write the structure, the sample – and thus the focus – is moved in 3-D. The *right* panel shows the adjacent voids aligned to obtain a trace

6.5.1 Bulk Structuring, Waveguide Writing

This effect is exploited to write structures inside the bulk of a transparent material [51, 52]. The principle is shown in Fig. 6.11.

The laser is focussed into the bulk of the transparent target. Only in the confocal region, the intensity is high enough to allow multiphoton absorption. The resulting ionization, subsequent local plasma formation and lattice destabilization result in a rearrangement of the material, e.g., the generation of voids, on the one hand, and a local densification on the other hand. By moving the focus inside the sample, complex structures can be written [53–56]. An important application of such bulk modification is the writing of micro-channels for lab-on-chip applications [57] and integrated optical waveguides [58–61] and even more complex photonic devices [52].

6.5.2 Multiphoton Polymerization

Even more complicated structures can be produced, not only in the bulk, by exploiting a photochemical reaction, also induced by multiphoton absorption. Light-induced polymerization, usually, requires UV light to induce the reaction. By multiphoton absorption, however, the same transitions in the precursor of the polymer can be used, with the advantage of precise 3-D-localization. Thus, by moving the focal point inside the precursor, complex structures can be polymerized [53, 56, 57, 62–64]. A particularly useful group of materials are photosensitive glasses like, e.g., Ormocer® [65].

6.6 Phase Transformation, Laser Annealing

One of the consequences of the ultrafast perturbation of the target lattice is that the material after relaxation does not return to the phase it was before. Thus, amorphous material can be crystallized if the cooling from the (super-)liquid phase is sufficiently slow [66] (laser annealing). On the other hand, if the cooling is very rapid, an initially crystalline material can turn into the amorphous phase [67]. Both effects have been observed on silicon. The main difference appears to be the surrounding condition: at the surface, crystallization was found, in deep drilled holes the material became amorphous. In any case, the advantage of femtosecond pulses appears to be the very rapid generation of an electron–hole plasma instead of a "regular" liquid as the state of crystal perturbation.

6.7 Medical Applications

An important field of laser materials processing are applications in medicine and biology. The specific point for the application of ultrashort laser pulses lies, again, in the fact that high intensity, enough to enable multiphoton processes, can be obtained at relatively low fluence. Thus, localized action can be achieved without thermally overloading (and potentially destroying) the target. This is particularly important for the isolation and manipulation of single biological cells [68, 69], nanosurgery of cells and tissue [70, 71], or material transfer [72]. But also in more mechanical field, the treatment of dental and bone material, femtosecond lasers are successfully applied [73,74]. Here the advantage lies in the fact that the high intensity achievable makes multiphoton absorption almost as efficient as single photon absorption. Also the interaction is extremely short. Therefore, complex materials, like dental and bone tissue, are ablated simultaneously, independent of their detailed composition.

6.8 Nanostructures and Nanoparticles

As the irradiated target surface is, usually, in a state well away from thermal equilibrium, the emitted material is neither atomized nor does it consist of large droplets from the melt (cf. PLD with femtosecond pulses). If the deposited energy is sufficiently low, so that no hot electron–hole plasma is generated, the ablated material can consist of a mixture of atomic ions, considerably large clusters and even nanoparticles. The latter are, especially, observed, when the ablation takes place under a liquid environment, i.e., the free expansion of the ablation plume

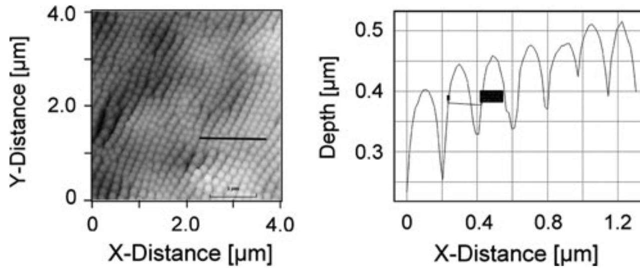

Fig. 6.12 Self-organized regular nanostructure (ripples) upon femtosecond laser ablation with circularly polarized laser light. The *left panel* shows an AFM image of a part of the ablated area, the *right panel* is an analysis along the *black line* in the *right panel*

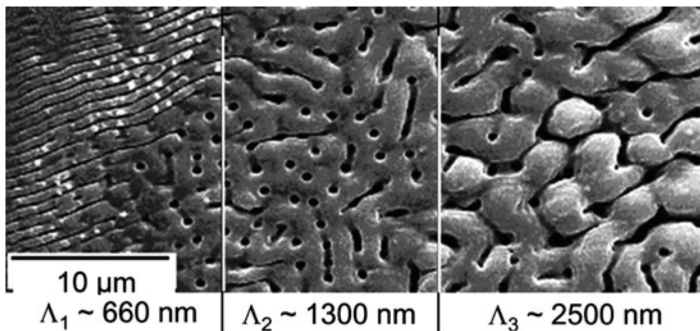

Fig. 6.13 Ripples produced with linearly polarized light on silicon. The image shows a part of the ablated spot, with the spot center at the right and the spot edge to the left. With increasing intensity along the beam profile, the structure becomes coarser, changing in distinct steps of period doubling

is hindered by the surrounding medium [75]. This appears to be a promising way to produce gold colloids which may be used for drug delivery [76, 77]. But even in vacuum, silicon nanoparticles have been produced [78]. Another consequence of the thermodynamic instability, induced in the target upon the rapid energy input, is the phenomenon of self-organized structure formation in the area where ablation took place [6] (Fig. 6.12).

The dynamics of the formation of these structures, called "ripples", is still not fully understood. Their features depend, however on the absorbed energy dose. Typical for self-organization, they exhibit, e.g., phenomena like period doubling under an increase of energy across the beam profile (Fig. 6.13).

It has been shown, recently, that it is possible to produce arrays of ripples structures, coherently covering larger areas [79–81]. Such larger areas can, then, be used as stencils to produce replica showing a maximized hydrophobicity, the so-called "lotus-effect" [82].

6.9 Conclusions

Materials processing using ultrashort laser pulses provide some distinct features of interest, compared to the application of longer pulses. First of all, the energy input is usually separated from the subsequent steps leading to materials modification. Second, the high intensity at comparably low fluence facilitates, on the one hand, multiphoton interaction and reduces, on the other hand, the thermal load on the target. The second point is responsible for the outstanding precision and cleanliness of the processing, the first point accounts for the finesse of possible results, well confined and smaller than the diffraction limit.

Acknowledgements The author gratefully acknowledges fruitful discussions with Markus Ratzke, Florenta Costache, Taznimir Arguirov, Michael Bestehorn, and Olga Varlamova.

References

1. H. Sato, S. Nishio, J. Photochem. Photobiol. C Photochem. Rev. **2**, 139 (2001)
2. L.S. Penn, R. Lin, B.S. Yilbas, Opt. Lasers Eng. **27**, 297 (1997)
3. see, e.g., the proceedings of the *Conferences on Laser Ablation (COLA)*:
   J.C. Miller, R.F. Haglund (eds.), *Laser Ablation: Mechanisms and Applications*, Lecturer Notes in Physics **389**, (Springer, Heidelberg, 1991)
   J.C. Miller, D.B. Geohegan, (eds.), *Laser Ablation: Mechanisms and Applications - II*, AIP Conference Proceedings **288** (American Institute of Physics, New York, 1994)
   E. Fogarassy, D.B. Geohegan, M. Stuke (eds.), *Proceedings of Symposium F: Third International Symposium on Laser Ablation of the 1995 E-MRS Spring Conference*, Appl. Surf. Sci. **96–98**, 1 (1996)
   R.E. Russo, D.B. Geohegan, R.F. Haglund, R.F. Haglund Jr., K. Murakami (eds.), *Proceedings of the 4th Conference on Laser Ablation*, Appl. Surf. Sci. **127–129**, 1 (1998)
   J.S. Horwitz, H.U. Krebs, K. Murakami, M. Stuke (eds.), *Laser Ablation V*, Appl. Phys. A **69**(Supplement 1) (1999)
   K. Murakami, A. Yabe, J.S. Horwitz, C. Fotakis, J.T. Dickinson (eds.), *Proceedings of the 6th Conference on Laser Ablation*, Appl. Surf. Sci. **197–198**, 1 (2002)
   C. Fotakis, H. Koinuma, D. Lowndes, M. Stuke, (eds.), *Laser Ablation VII*, Appl. Phys A **79**(4–6), 713 (2004)
   B. Luk'yanchuk, S. Juodkazis, T. Lippert (eds.), *Special Issue: Laser Ablation Fundamentals*, Appl. Phys. A **92**, 743 (2008)
   P. Schaaf, R. Serna, J.G. Lunney, E. Fogarassy (eds.), *Laser synthesis and processing of advanced Materials*, Appl. Surf. Sci. **254(4)**, 789 (2007)
4. A. Kaplan, Chap. 3 in *The Theory of Laser Materials Processing*, Springer Ser. Mater. Sci ed. by J. Dowden (Springer, 2009), p. 119
5. S. Eliezer, K. Mima (eds.), *Applications of Laser-Plasma Interactions*, Series in Plasma Physics, (CRC, 2009)
6. J. Reif, F. Costache, M. Bestehorn, Chap. 9 in *Recent Advances in Laser Processing of Materials*, ed. by J. Perriere, E. Millon, E. Fogarassy (Elsevier, 2006) p. 275
7. I.W. Boyd, J.I.B. Wilson, Nature **287**, 278 (1980)
8. R.R. Gattass, E. Mazur, Nat. Photonics **2**, 219 (2008)
9. D. von der Linde, K. Sokolowski-Tinten, Appl. Surf. Sci. **154–155**, 1 (2000)
10. S. Küper, M. Stuke, Appl. Phys. Lett. **54**, 4 (1989)

11. B. Rethfeld, K. Sokolowski-Tinten, D. von der Linde, S. Anisimov, Appl. Phys. A **79**, 767–769 (2004)
12. Y. Jee, K. Becker, R.M. Walser, J. Opt. Soc. Am. B **5**, 648 (1988)
13. S. Petzoldt, A.P. Elg, J. Reif, E. Matthias, Proc. SPIE **1438**, 180 (1989)
14. F. Costache, S. Eckert, J. Reif, Appl. Phys. A **92**, 897 (2008)
15. A. Ostendorf, F. Korte, G. Kamlage, U. Klug, J. Koch, J. Serbin, N. Baersch, T. Bauer, B.N. Chichkov, Chap. 12 in *3D Laser Microfabrication: Principles and Applications*, ed. by H. Misawa, S. Joudkazis (Wiley, 2006)
16. S. Nolte, B.N. Chichkov, H. Welling, Y. Shani, K. Lieberman, H. Terkel, Opt. Lett. **24**, 914 (1999)
17. F. Korte, S. Adams, A. Egbert, C. Fallnich, A. Ostendorf, S. Nolte, M. Will, J.-P. Ruske, B.N. Chichkov, A. Tünnermann, Opt. Express **7**, 41 (2000)
18. S.-S. Wellershoff, J. Hohlfeld, J. Güdde, E. Matthias, Appl. Phys. A **69**, S99 (1999)
19. P. Lorazo, L.J. Lewis, M. Meunier, Phys. Rev. Lett. **91**, 225502 (2003)
20. Z. Lin, L.V. Zhigilei, Phys. Rev. B **73**, 184113 (2006)
21. H.O. Jeschke, M.E. Garcia, M. Lenzner, J. Bonse, J. Krüger, W. Kautek, Appl. Surf. Sci. **197–198**, 839 (2002)
22. N. Bulgakova, I.M. Bourakov, Appl. Surf. Sci. **197–198** (2002)
23. R. Kelly, A. Miotello, Phys. Rev. E **60**, 2616 (1999) A. Miotello and R. Kelly, Appl. Phys. Lett. **67**, 3535 (1995) A. Peterlongo, A. Miotello, and R. Kelly, Phys. Rev. E **50**, 4716 (1994)
24. R. Stoian, A. Mermillod-Blondin, S.W. Winkler, A. Rosenfeld, I.V. Hertel, M. Spyridaki, E. Koudoumas, P. Tzanetakis, C. Fotakis, I.M. Burakov, N.M. Bulgakova, Opt. Eng. **44**, 051106 (2005)
25. P. Saeta, J.-K. Wang, Y. Siegal, N. Bloembergen, E. Mazur, Phys. Rev. Lett. **67**, 1023 (1991)
26. A.M. Lindenberg, S. Engemann, K.J. Gaffney, K. Sokolowski-Tinten, J. Larsson, D. Reis, P. Lorazo, J.B. Hastings, SPIE Proc. **7005**, 700504 (2008)
27. A. Lindenberg, S. Engemann, K. Gaffney, K. Sokolowski-Tinten, J. Larsson, P. Hillyard, D. Reis, D. Fritz, J. Arthur, R. Akre, M. George, A. Deb, P. Bucksbaum, J. Hajdu, D. Meyer, M. Nicoul, C. Blome, Th. Tschentscher, A. Cavalieri, R. Falcone, S. Lee, R. Pahl, J. Rudati, P. Fuoss, A. Nelson, P. Krejcik, D. Siddons, P. Lorazo, J. Hastings, Phys. Rev. Lett. **100**, 135502 (2008)
28. M. Ligges, I. Rajkovic, P. Zhou, O. Posth, C. Hassel, G. Dumpich, D. von der Linde, Appl. Phys. Lett. **94**, 101910 (2009)
29. S. Preuss, A. Demchuk, M. Stuke, Appl. Phys. A **61**, 33 (1995)
30. P.P. Pronko, S.K. Dutta, J. Squier, J.V. Rudd, D. Du, G. Mourou, Opt. Commun. **114**, 106 (1995)
31. C. Momma, B.N. Chichkov, S. Nolte, F. von Alvensleben, A. Tünnermann, H. Welling, Opt. Commun. **129**, 134 (1996)
32. B.C. Stuart, M.D. Feit, S. Herman, A.M. Rubenchik, B.W. Shore, M.D. Perry, J. Opt. Soc. Am. B **13**, 459 (1996)
33. W. Kautek, J. Krüger, M. Lenzner, S. Sartania, C. Spielmann, F. Krausz, Appl. Phys. Lett. **69**, 3146 (1996)
34. B. Chichkov, C. Momma, S. Nolte, F. von Alvensleben, A. Tünnermann, Appl. Phys. A **63**, 109 (1996)
35. S. Nolte, C. Momma, H. Jacobs, A. Tünnermann, B.N. Chichkov, B. Wellegehausen, H. Welling, J. Opt. Soc. Am. B **14**, 2716 (1997)
36. F. Korte, S. Nolte, B.N. Chichkov, T. Bauer, G. Kamlage, T.Wagner, C. Fallnich, H. Welling, Appl. Phys. A **69**, S7 (1999)
37. N. Bärsch, K. Körber, A. Ostendorf, K.H. Tönshoff, Appl. Phys. A **77**, 237 (2003)
38. G. Kamlage, T. Bauer, A. Ostendorf, B.N. Chichkov, Appl. Phys. A **77**, 307 (2003)
39. S. Ameer-Beg, W. Perrie, S. Rathbone, J. Wright, W. Weaver, H. Champoux, Appl. Surf. Sci. **127–129**, 875 (1998)
40. R. Haight, D. Hayden, P. Longo, J. Vac. Sci. Technol. B **17**, 3137 (1999)
41. K. Ozono, M. Obara, A. Usui, H. Sunakawa, Opt. Commun. **189**, 103 (2001)

42. N.H. Rizvi, Riken Rev. **50**, 107 (2003)
43. R. LeHarzic, N. Huot, E. Audouard, C. Jonin, P. Laporte, placeS. Valette, A. Fraczkiewicz, R. Fortunier, Appl. Phys. Lett. **80**, 3886 (2002)
44. F. Garrelie, A.S. Loir, C. Donnet, F. Rogemont, R. LeHarzic, M. Belin, E. Audouard, F. Laporte, Surf. Coat. Technol. **163–164**, 306 (2003)
45. R. Eason, *Pulsed Laser Deposition of Thin Films* (Wiley, 2007)
46. F. Garrelie, C. Donnet, A.S. Loir, N. Benchikh, SPIE Proceedings **6261**, 62610L (2006)
47. K. Kawamura, N. Sarukura, M. Hirano, N. Ito and H. Hosono, Appl. Phys. Lett. **79**, 1228–1130 (2001)
48. J. Bonse, P. Rudolph, J. Krüger, S. Baudach, W. Kautek, Appl. Surf. Sci. **154–155**, 659 (2000)
49. G. Dumitru, V. Romano, Y. Gerbig, H.P. Weber, H. Haefke, Appl. Phys. A **80**, 283 (2005)
50. A. Marcinkevicius, S. Juodkazis, M. Watanabe, M. Miwa, S. Matsuo, H. Misawa, J. Nishii, Opt. Lett. **26**, 277 (2001)
51. K. Minoshima, A.M. Kowalevicz, I. Hartl, E.P. Ippen, J.G. Fujimoto, Opt. Lett. **26**, 1516 (2001)
52. M. Masuda, K. Sugioka, Y. Cheng, T. Hongo, K. Shihoyama, H. Takai, placeI. Miyamoto, K. Midorikawa, Appl. Phys. A **78**, 1029 (2004)
53. K. Miura, Jianrong Qiu, S. Fujiwara, S. Sakaguchi, K. Hirao, Appl. Phys. Lett. **80**, 2263 (2002)
54. Ken-ichi Kawamura, Masahiro Hirano, Toshio Kamiya, Hideo Hosono, Appl. Phys. Lett. **81**, 1137 (2002)
55. F. Korte, J. Serbin, J. Koch, A. Egbert, C. Fallnich, A. Ostendorf, B.N. Chichkov, Appl. Phys. A **77**, 229 (2003)
56. K. Sugioka, M. Masuda, T. Hongo, Y. Cheng, K. Shihoyama, K. Midorikawa, Appl. Phys. A **79**, 815 (2004)
57. K.M. Davis, K. Miura, placeN. Sugimoto, K. Hirao, Opt. Lett. **21**, 1729 (1996)
58. S. Nolte, M. Will, J. Burghoff, A. Tuennermann, Appl. Phys. A **77**, 109 (2003)
59. R. Osellame,G. Della Valle, N. Chiodo, S. Taccheo, P. Laporta,O. Svelto, G. Cerullo, Appl. Phys. A **93**, 17 (2008)
60. L. Shah, A.Y. Arai, S.M. Eaton, P.R. Herman, Opt. Express **13**, 1999 (2005)
61. L. Li, J.T. Fourkas, Mater. Today **10**, 30 (2007)
62. J. Serbin, A. Egbert, A. Ostendorf, B.N. Chichkov, R. Houbertz, G. Domann, J. Schulz, C. Cronauer, L. Fröhlich, M. Popall, Opt. Lett. **28**, 301 (2003)
63. Y. Cheng, K. Sugioka, K. Midorikawa, M. Masuda, K. Toyoda, M. Kawachi, K. Shihoyama, Opt. Lett. **28**, 1144 (2003)
64. Fraunhofer-Institut für Silicatforschung, Wuerzburg, Germany
65. J.-M Shieh, Z.-H. Chen, B.-T. Dai, Y.-C. Wang, A. Zaitsev, C.-L. Pan, Appl. Phys. Lett. **85**, 1232 (2004)
66. J. Jia, M. Li, C.V. Thompson, Appl. Phys. Lett. **84**, 3205 (2004)
67. Y. Hosokawa, H. Takabayashi, S. Miura, C. Shukunami, Y. Hiraki, H. Masuhara, Appl. Phys. A **79**, 795 (2004)
68. W. Supatto, D. Débarre, B. Moulia, E. Brouzés, J.-L. Martin, E. Farge, E. Beaurepaire, PNAS **102**, 1047 (2005)
69. A. Vogel, J. Noack, G. Hüttmann, G. Paltauf, Appl. Phys. B **81**, 1015 (2005)
70. A. Heisterkamp, I.Z. Maxwell, E. Mazur, J.M. Underwood, J.A. Nickerson, S. Kumar, D.E. Ingber, Opt. Express **13**, 3690 (2005)
71. K. König, O. Krauss, I. Riemann, Opt. Express **10**, 171 (2002)
72. I. Zergioti, A. Karaiskou, D.G. Papazoglou, C. Fotakis, M. Kapsetaki, D. Kafetzopoulos, Appl. Phys. Lett. **86**, 163902 (2005)
73. K. Ozono, M. Obara, Appl. Phys. A **77**, 303 (2003)
74. J. Serbin,T. Bauer, C. Fallnich, A. Kasenbacher, W.H. Arnold, Appl. Surf. Sci. **197–198**, 737 (2002)
75. S. Eliezer, N. Eliaz, E. Grossman, D. Fisher, I. Gouzman, Z. Henis, S. Pecker, Y. Horovitz, M. Fraenkel, S. Maman, Y. Lereah, Phys. Rev. B **69**, 144119 (2004)
76. Andrei V. Kabashin, Michel Meunier, Christopher Kingston, and John H.T. Luong, J. Phys. Chem. B **107**, 4527 (2003)

77. A.V. Kabashin, M. Meunier, J. Appl. Phys. **94**, 7941 (2003)
78. S. Amoruso, R. Bruzzese, N. Spinelli, R. Velotta, M. Vitiello X. Wang, G. Ausanio, V. Iannotti, L. Lanotte, Appl. Phys. Lett. **84**, 4502 (2004)
79. R. Wagner, J. Gottmann, A. Horn, E.W. Kreutz, Appl. Surf. Sci. **252**, 8576 (2006)
80. N. Sanner, N. Huot, E. Audouard, C. Larat, J.-P. Huignard, Opt. Las. Eng. **45**, 737 (2007)
81. M. Zamfirescu, M. Ulmeanu, F. Jipa, O. Cretu, A. Moldovan, G. Epurescu, M. Dinescu, R. Dabu, J. Laser Micro/Nanoeng. **4**, 7, 2009
82. G.R.B.E. Römer, A.J.Huis in't Veld, J. Meijer, M.N.V. Groenendijk, CIRP Ann. Manufact. Technol. **58**, 201 (2009)

Chapter 7
Creating Nanostructures with Lasers

Paolo M. Ossi and Maria Dinescu

Abstract Lasers represent an efficient and versatile tool to produce and to arrange in organized dispositions nanometer-sized particles, obtaining extended nanostructures with increasing degrees of complexity. In the first part of the chapter, the basic mechanisms of nanoparticle formation for nanosecond laser ablation in an ambient gas atmosphere and femtosecond ablation in vacuum are considered. In the former case, atomic or molecular clusters grow during the propagation through the ambient gas of the plasma plume resulting from target irradiation. Plume expansion is affected by laser wavelength and fluence, nature and pressure of the background gas, target to substrate distance. Cluster size and kinetic energy, together with the related distributions at landing onto the substrate depend on plasma dynamics and determine relevant differences of morphology and nanostructure of the growing film. Popular models for the propagation of an ablation plume through a gas at increasing pressure are recalled before deducing the average asymptotic size of particles nucleated in the plume, to be compared with available data from selected experiments. The synthesis of spatially uniform distributions of spherical metal particles with controlled size, size distribution, and number density, resulting in films with differentiated morphologies and optical properties is discussed.

In recent years, increasing attention and efforts have been devoted to the controlled synthesis of nanostructured materials. The nanostructure plays a fundamental role in determining electronic, optical, magnetic, and mechanical material properties. It is in principle possible to engineer new functional systems by carefully tailoring their structure at the atomic and nanometer scales. One of the more exciting routes adopted to synthesize nanostructured thin films is the controlled assembling of clusters.

Among different chemical and physical assembling techniques, laser processing plays an important role: laser ablation, pulsed laser deposition, laser micromachining, laser etching, and laser-assisted chemical vapor deposition are only some

P.M. Ossi (✉)
Dipartimento di Energia, Politecnico di Milano, Italy
e-mail: paolo.ossi@polimi.it

examples of recently introduced techniques that are reviewed with emphasis on the degree of control of the resulting artificial nanostructures.

7.1 Introduction

The word nanostructure is largely used in the scientific and technical literature with a variety of meanings. In the initial part of this chapter, by nanostructure, we mean the result of the assembling procedure, with a bottom-up strategy of nanometer-sized particles, or briefly nanoparticles (NPs). Thus, our attention is focused onto the mechanisms whereby NPs are formed in a laser-generated plasma. Our goal is to identify conditions suitable to drive the synthesis of NPs with controlled properties and their assembling in an organized, convenient spatial disposition, up to a cluster-assembled (CA) film. Particle properties of interest range from the size and its distribution, to the composition, the chemical and thermal stability, the transport, mechanical, and chemical properties with their peculiar size dependence.

The plasmas produced by laser ablation yield large amounts of particles with typical size in the few nanometer range [1, 2]: the possibility to separately manage laser pulse features, irradiation geometry and radiation – matter interaction allows modifying the complex dynamics within matter ejected from the irradiated target surface. Thus, it is possible to understand and in part to control the mechanisms of NP formation and their relative efficiency.

We move from the considerable activity of the last decade on NP synthesis following irradiation of a solid target with laser pulses, to underline some differences between femtosecond (fs) and nanosecond (ns) pulses that have important effects on NP synthesis. A femtosecond pulse releases its energy to matter adiabatically with respect to thermal conduction. Thus, an intense, ultra-short pulse locally brings to supercritical conditions the target while it preserves a solid density. The extreme temperature – pressure regions explored, together with the fast-quenching conditions associated to material expulsion, constitute ideal conditions to synthesize metastable phases otherwise unattainable. Further to this, ultrashort pulses do not interact with the material ejected from the target; therefore the fundamental thermodynamics – hydrodynamics of NP formation can be considered. By contrast, pulses lasting picoseconds or longer times strongly interact with the nascent high-density cloud of matter evaporated from the target. The resulting photoionization and collisional heating mechanisms have significant effects on particle formation.

In fs ablation, NP formation usually occurs during free plasma expansion *in vacuum*: hydrodynamics suggests that the severe strain experienced at very high strain rate by a rapidly expanding, highly pressurized fluid leads to mechanical fragmentation: such a mechanism is essential to *quantitatively* interpret NP formation [3]. By contrast, an *ambient gas* strongly favors NP synthesis in ns ablation [1]: clustering of species in the expanding plume critically depends on the relative weight of interaction mechanisms between ablated species and ambient gas, including scattering, slowing down, diffusion, recombination, shock wave formation, and

propagation. All these mechanisms are affected by ambient gas nature and pressure. The above differences suggest to separately discuss NP formation when ns and fs laser pulses are used.

For both irradiation timescales to manage the production of NPs, it is essential to know *how* and *when* they are formed. This is our goal. A difficulty to answer such questions stems from a long-standing separation between two approaches to analyze pulsed laser ablation experiments. On the one hand, film properties are correlated to deposition parameters such as target to substrate distance, laser wavelength, fluence, intensity at the target surface, number of pulses [4, 5], atomic mass, and pressure of the ambient gas [6]. On the other hand, plasma expansion dynamics is studied. Several time- and space-resolved plasma diagnostics yield details on the dynamics of the vaporized species escaping from the target: they include optical emission spectroscopy (OES) [7], optical time of flight measurements (TOF) [8], Langmuir probes [9], and fast photography, using an intensified charge coupled device (ICCD) [1, 10], from which plasma front position and velocity are obtained, besides the size and shape of the expanding plasma. Although the two classes of investigations are complementary to each other, only recently plasma plume studies were carried out at conditions suitable to have a feedback on film deposition.

We first review the phenomena associated to the propagation through an ambient gas of a plasma plume produced by a nanosecond laser pulse. The strengths and weaknesses of the most popular models adopted to interpret plasma expansion are recalled and the phenomenological model of mixed-propagation for plume dynamics in the ambient gas is introduced. Recent results on the deposition under different conditions of CA films of carbon, tantalum, and silver are interpreted. It is shown that the average NP asymptotic sizes deduced by mixed-propagation model, agree with those of *as-deposited* NPs, measured by transmission electron microscopy (TEM). The morphology, as investigated by scanning electron microscopy (SEM) and the related optical properties of deposited silver films evolve through well-differentiated stages that were controlled by changing the number of laser pulses and the ambient gas pressure. Selected experimental results on NP formation upon fs ablation mainly of elemental targets are presented, highlighting the nature and the dynamic properties of plasma constituents. The data are discussed in the frame of current models and simulations to describe the mechanisms of ultra-fast ablation relevant to NP synthesis.

7.2 Fundamentals

7.2.1 Plasma–Gas Interaction at Increasing Gas Pressure in ns PLD: Experiments and Modeling

When a laser pulse is absorbed by a solid target, the irradiated surface undergoes intense heating at a rate of the order of $10^{12}\,\mathrm{K s^{-1}}$ in most materials and violent matter evaporation occurs: a high density, strongly anisotropic vapor cloud

is formed, which lies just above the irradiated surface. Initially, the vaporized matter behaves like a high pressure, high temperature, strongly collisional fluid interacting with the laser radiation. An isothermally expanding plasma results up to the pulse end. Heavy laser – plasma interaction, triggered by intense ionization of plasma species, stimulates additional plume expansion. Particle ejection from the target surface stops at the end of the laser pulse.

Both in vacuum and at low ambient gas pressure (up to about 1 Pa), plasma propagation is similar to a supersonic free expansion with a *linear* relation between the delay time and the position of plume front [11]. Ablation can be considered as an extension of thermal desorption, monolayers being evaporated from the target surface one by one under quasi-equilibrium conditions. A condensation model [12] explains the presence of nanoparticles in the plume, of which they are a minor constituent.

When gas pressure increases, the collisions between the species ejected from the target and ambient gas atoms slow down plume propagation and lead to *shock wave* formation. The high density of the surrounding gas makes plume braking most relevant in the direction normal to the target as compared to the radial directions. Thus, the observed shape of the propagating plume rapidly tends to *spherical*. At relatively low (below 10 Pa) ambient gas pressure, the *initial* plume expansion is similar to that in vacuum [13], but at times longer than 1 μs at most, ambient gas spatially confines the plume, and a slowing down of its front is observed [14]. At larger times plume sharpens and its front shows an oscillatory behavior persisting up to ambient gas pressures of a few tens of Pascal. Generally, the effect occurs at earlier times with increasing gas pressure. At ambient gas pressures beyond about 10^2 Pa, plasma oscillations disappear.

In Fig. 7.1, pictures taken at the same delay times of C plumes ablated from a graphite target allow for comparing propagation in vacuum (Fig. 7.1a) to shock wave formation during expansion in N_2 at a pressure of 13.3 Pa (Fig. 7.1b). The role of ambient gas mass is clear from Fig. 7.1c, where the plume expands in a N_2+Ar (1/9) mixture, at the same total pressure as for the propagations in Fig. 7.1b.

At intermediate gas pressures, between 30 and 50 Pa, plume sharpening is associated to increasing confinement of the emission to plume front. In this pressure range, the slowing down of plume front begins after a few microseconds and continues until a stationary behavior is achieved. At the same time, the rear edge of the plume moves *backwards* towards the target. Such a behavior marks a transition to a *diffusion-like* propagation of plume species through the ambient gas typical of longer times, for pressures in the tens of Pascal range. During this stage, the plume is characterized by important interpenetration of plasma species and ambient gas that leads to plume *splitting*, besides sharpening [15]. Ions and neutrals split into *two* velocity populations. The faster group, which travels practically at the same velocity as in vacuum, consists of particles that move through the ambient gas nearly collision less. The dynamic properties of the slower, delayed population result from the interaction between ablated species and background gas atoms. The effect was observed by TOF distribution analysis of the ablated species and affects both ions [16] and neutrals [17]. During the regime of mutual penetration of the laser-generated plasma and ambient gas, a considerable fraction of kinetic energy is

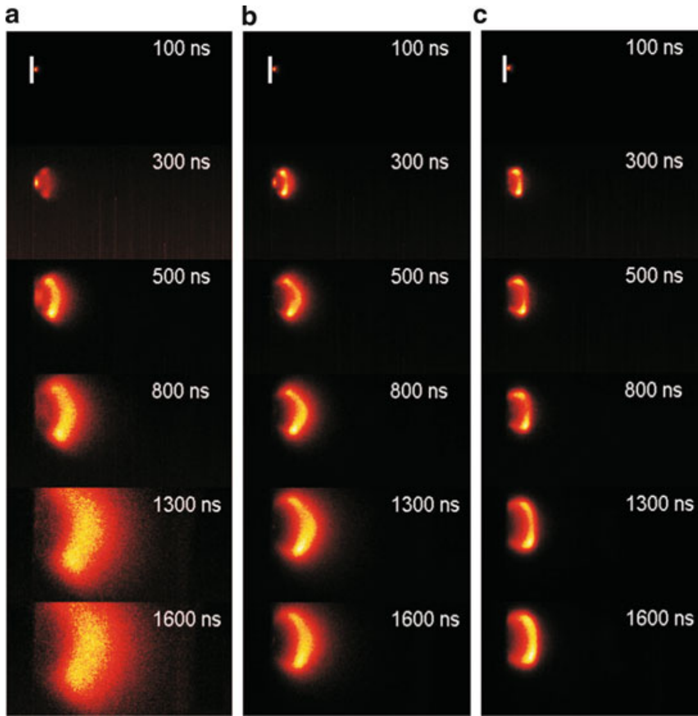

Fig. 7.1 ICCD fast photography pictures of C ablation plumes expanding from a high purity graphite target irradiated with pulses from a KrF excimer laser (wavelength 248 nm, pulse width 25 ns, repetition rate 10 Hz, fluence 2.0 J cm^{-2}). The bars mark the position of target surface. The laser beam was focused at an incident angle of 45° onto the target, placed on a rotating holder. Ablation was carried out: (**a**) in vacuum (residual pressure better than 1×10^{-4} Pa); (**b**) in high purity N_2 ambient gas at 13.3 Pa; (**c**) in mixed N_2+Ar atmosphere, with pressure ratio 1/9, at 13.3 Pa total pressure. Notice the different evolution of plasma size and shape, indicating different degrees of plasma confinement and the development of a shock wave (courtesy of Dr. S. Trusso, CNR-Istituto per i Processi Chimico-Fisici, Sez. di Messina, Italy)

converted into heat, in turn increasing both gas and radiation temperature. At pressures around 10^2 Pa, *turbulence* is observed in the decelerating plume front [18]. By further increase of the gas pressure, the mutual penetration zone contracts and the plasma front is compressed.

The above-illustrated path of propagation behavior of the ablation plume is met independently of the specific combination target – ambient gas – process conditions, although the pressure ranges typical of the different propagation regimes are quite broad and not always the complete sequence of phenomena just discussed is observed.

The interaction of the ablation plasma with an ambient gas is by far a more complex gas dynamic phenomenon than an expansion into vacuum. The gas affects plume dynamics and the spatial distribution, kinetic energy, and kinetic energy distribution of its constituents. As a consequence, cluster nucleation and evolution, as well as cluster energy distribution in the plume are influenced.

When the mass m_g of ambient gas displaced from plume periphery is at least comparable with plume mass M_p, we observe relevant deviations from free expansion of the plume [12]. For a supposed hemispherical plume, the radius r_p is related to plume mass and gas pressure as

$$r_p = [(3M_p k_B T_g)/(2\pi m_g)]^{1/3} p_g^{-1/3}, \tag{7.1}$$

with k_B the Boltzmann constant and T_g, p_g the ambient gas temperature and pressure.

Considering the features of plume expansion, it is unrealistic to search for a single model with general validity to accurately describe the whole above phenomenology, and each analytical model is adequate to represent a specific expansion stage.

Historically, three *analytical* models, the *drag* model [19, 20], the *shock-wave* model [12, 20], and the *diffusion* model [21] were introduced. Summarizing from a recent review [22], drag model, particularly in its delayed version [20], fits well the *early* plasma expansion stage, but when gas pressure and time exceed about 10^2 Pa and about 4 μs, respectively, plume velocity is underestimated. The plume is expected to stop at a distance $x_{st} \cong 4 - 5\lambda$ from the target [23], with $\lambda = (n_g\sigma)^{-1}$ the mean free path of the ablated species in the gas, σ being the relevant scattering cross section. Therefore, beyond a lower threshold value, ambient gas pressure gives rise to a nonlinear dependence of the position of plasma front edge on the distance from the target. Shock wave model, again in the delayed version [20], fits experimental data at *large* values of time and ambient gas pressure. The classical diffusion model [21] systematically underestimates the distance traveled by the plume.

A few gas-dynamic *numerical* models [23–25] fit specific experiments, but their applicability is limited by the specific validity of the required approximations and the complexity of the mathematical treatments.

The analytical models just recalled offer *a posteriori* interpretations of experimental data, yet they have no predictive capability concerning plasma dynamics, due to their dependence on numerical fitting parameters. We now move to a two-stage analytical approach that describes plume propagation under rather wide conditions. We take into account that the high values of temperature and particle number densities in the first stage of plasma propagation [23], with the associated quasi-explosive initial plume expansion, result in a Knudsen layer [26] where the leading contribution is the particle flux velocity. We assume that the particles ejected from the target, with a dominant velocity component directed normal to the surface, undergo diffusive motion. This corresponds to diffusion through the ambient gas whose *effective* number density n_{eff} is considerably reduced with respect to the value n_g deduced from gas pressure p_g. In the resulting *modified diffusion* model, the diffusion coefficient [27] is

$$D' = K\lambda v_0 = K v_0 (n_g\sigma)^{-1}, \tag{7.2}$$

where v_0 is the ejection velocity from the target of the *fastest* group of ablated particles. v_0 is obtained from the initial slope of the measured distance – time curve

for plumes produced and propagating under specified conditions. The choice of the particle group with maximum flux velocity v_0 instead of the usual thermal velocity v of the particles is an *ansatz* of the model to enhance the relevance of flux velocity. Although plume front slows down during expansion (see Figs. 7.2 and 7.3 below), modified diffusion model fits reasonably well experimental data, particularly beyond the initial plume expansion stage. This means that flux velocity indirectly affects plume propagation also at comparatively *large* distances from the target.

For elemental C, Si, Sn, Ag, Ta, and W targets, literature data on the velocity of expansion through different gases of UV laser-generated ablation plumes were analyzed. The integer K values that better fit the data scale with the target atomic mass, from $K = 2$ (light elements: C, Si) to $K = 6$ (intermediate mass elements: Ag, Sn) to $K = 8$ (heavy elements: Ta, W). Thus, given the target mass, K value is *uniquely* identified.

To reproduce the experimentally observed initial linear behavior of plume expansion (see, e.g., [28] for C), drag model is most suited. We study for simplicity a one-dimensional plume expansion along the principal plume axis x. When we consider the diffusion dynamics of a fluid of classical particles in the presence of viscosity, whose effect is embodied in a coefficient ξ [29] (ξ is a diffusion coefficient multiplied by time), with the initial conditions $x(0) = 0$ and $(\mathrm{d}x/\mathrm{d}t)(0) = v_0$, the position *x(t)* of an atom is

$$x(t) = \frac{v_0 D'}{\xi}\left[1 - \mathrm{e}^{\left(-\frac{\xi \cdot t}{D'}\right)}\right] \tag{7.3}$$

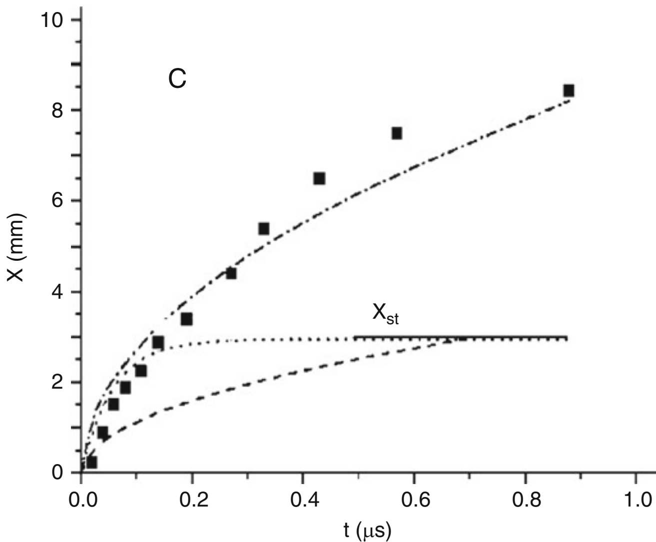

Fig. 7.2 Position x (*full squares*) of the front edge of carbon plumes propagating through N_2 [28] as a function of time. *Dashed curve*: diffusion model; *dashed-dotted curve*: modified diffusion model; *dotted curve*: modified drag model. x_{st}: stopping distance

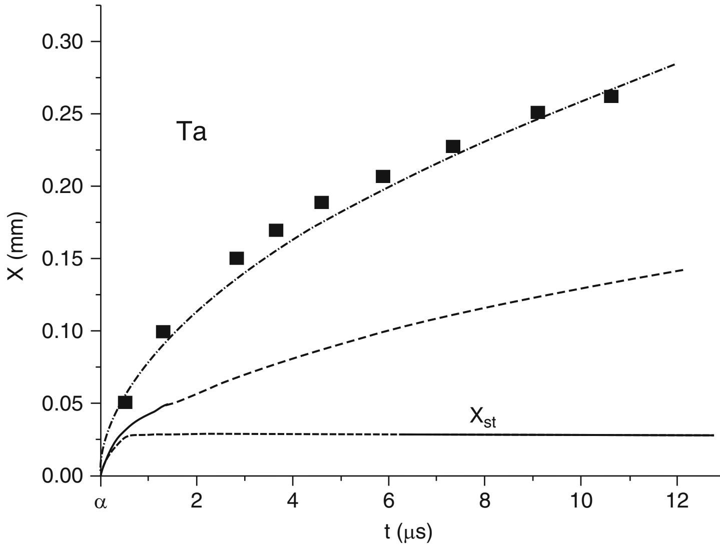

Fig. 7.3 Model analysis of tantalum plume propagation through O_2 vs. time [35]. General information as for Fig. 7.2

Equation 7.3 describes *modified drag* model, where both the slowing down coefficient $b = \xi D'^{-1}$ and the stopping distance $x_{st} = v_0 D' \xi^{-1}$ have a clear physical meaning.

Initially, the number density n_a of the ablated particles is larger than n_g, but the fast plume expansion leads to the condition $n_a = n_g$, corresponding to the formation of a stable shock wave front and to a change of expansion regime. The inequality $n_a < n_g$ is established in the body of the plume and ambient gas atoms are heavily scattered by fast plume constituents (normally, positive ions) that are slowed down and *aggregate* themselves with the slower particles initially grouped in the plume body and tail.

The sequence of such complex phenomena is mimicked combining modified diffusion and modified drag models that result in *mixed-propagation model*. The unphysical discontinuity of plume propagation at x_{st} coincides with the region where the viscous slowing down of plume front leads to formation of a stable shock wave front. At distances $x < x_{st}$ modified drag model holds, while for $x \geq x_{st}$ modified diffusion model holds. The x_{st} value is chosen according to the estimate $x_{st} \cong 4\lambda$ [23] and it is calculated using the n_g and pertinent σ values.

At ambient gas pressure lower than 1 Pa, x_{st} is often much larger than the usual values of target to substrate distance x_{T-S} (a few centimeters) and modified drag model is adequate to describe plume dynamics.

Mixed-propagation model has been tested against literature data on the dynamics of ablation plumes from different targets, propagating in different ambient gases at various pressures [30–34]. The model offers a highly simplified description of plasma expansion, but its easily accessible input parameters v_0, σ, n_g, and n_a make it

Table 7.1 Collection of data from ablation experiments on C [28], Ta [35] and Ag [34]

Target	λ (nm)	E(J cm^{-2})	τ (ns)	x_{t-s} (mm)	p_g (Pa)	T(K)	n_g (cm^{-3})
C	248	38	20	50	30; N_2	300	7.2×10^{15}
Ta	532	5.0	6	30	20; O_2	300	4.8×10^{15}
Ag	248	2.0	25	35	10; Ar	300	2.4×10^{15}
					40; Ar		9.7×10^{15}
					100; Ar		2.4×10^{16}

Table 7.2 Collection of parameter values for mixed-propagation model (see text)

Target	$< n_a >$(cm^{-3})	σ_{a-g}(cm^2)	σ_{a-a}(cm^2)	$< v >$ (cm µs^{-1})	t_f (µs)	x_{aggr} (cm)
C	1.7×10^{17}	7.4×10^{-16}	1.5×10^{-15}	4.5	1.8	2.5
Ta	5×10^{15}	3.7×10^{-15}	7.5×10^{-15}	0.7	0.7	3.3
Ag_{10Pa}	7.1×10^{14}	3.8×10^{-15}	3.7×10^{-15}	0.5	0.8	0.7
Ag_{40Pa}	1.4×10^{15}	3.8×10^{-15}	3.7×10^{-15}	0.3	3.3	0.5
Ag_{100Pa}	2.8×10^{15}	3.8×10^{-15}	3.7×10^{-15}	0.2	7.4	0.4

useful to predict general trends of plume behavior. Here, we discuss the propagation of C in molecular nitrogen [28], Ta in molecular oxygen [35], and Ag in argon [34]. In Tables 7.1 and 7.2 are collected data from ablation experiments and parameter values used in mixed-propagation model, respectively.

In Fig. 7.2, data on the propagation of the front of carbon plumes in N_2 (full squares) [28] are compared with predictions of diffusion model (dashed curve), modified diffusion model (dashed-dotted curve), and modified drag model (dotted curve). The latter fits well the first stage of plume expansion. It predicts that plume is stopped at x_{st}. Diffusion model appears inaccurate. Its modified version well fits the data at intermediate and delayed times, but slightly overestimates plume expansion velocity in the neighborhood of the target. From a fit on available data [36, 37] on carbon ablation with excimer lasers in vacuum, or at low ambient gas pressure, over the energy density interval between 1 and 10^2 J cm^{-2}, the initial velocity is $v_0 = 5.2$ cm µs^{-1}. Mixed-propagation model successfully fits experimental data on carbon plume expansion for different gas pressures and laser energy densities (50 Pa, 12 J cm^{-2} [28]; 66 Pa, 6 J cm^{-2} [38]). Taking $x_{st} = 4\lambda$, an estimate for the slowing down coefficient is obtained from $b = v_0(4\lambda)^{-1}$. For C, $K = 2$.

In Fig. 7.3 are displayed the results of the fitting procedure to the expansion of tantalum plumes in oxygen [32, 35], starting from optical emission spectroscopy data. The v_0 value used in the fits is 1.5 cm µs^{-1} [35] and $K = 8$. The trend of the fits is similar to that discussed for carbon. No data are available on the early plume expansion stage of Ta. Experimental data fall beyond the stopping distance x_{st} so that modified diffusion model is enough to describe plume dynamics. The fit obtained by mixed-propagation model is of equivalent quality to that of the literature analysis [35].

For silver fast photography pictures of the laser-generated plasma at several time delays were analyzed: from a fitting on propagation distances traveled by plume front versus time in the initial, linear plasma propagation stage v_0 values of 1.11,

1.04, and 0.86 cm μs^{-1} were obtained for expansions in Ar at 10, 40, and 100 Pa [34]. The adopted K value is 6.

For the discussed targets, mixed-propagation model fits to experimental data are of accuracy comparable, or slightly better than existing approaches. The model can be applied to analyze data obtained for a wide range of ablation conditions and it does not require fitting parameters, apart from K, whose value can be easily chosen, as discussed. The results of mixed-propagation model are particularly useful as input parameters to model the growth of nanoparticles in the expanding ablation plasma.

7.2.2 Nanoparticle Synthesis

We focus on low-energy landing (energy of the order of fractions of eV at.$^{-1}$) of plasma plume onto the substrate. In such conditions, the particles possibly carried by the plume diffuse and aggregate together on the substrate surface [39] until, beyond a critical degree of surface coverage, coalescence in larger NPs occurs. Such a deposition path is attractive to produce CA materials that can "remember" the properties of their precursor building blocks. In spite of being an important parameter, the kinetic energy of the deposited species was rarely allowed for. In particular, the kinetic energy of Au species was changed from several tens to fractions of eV at.$^{-1}$ by adjusting gas pressure and target to substrate distance in PLD experiments [40], but neither evidence of fragmentation nor of soft landing of the particles following impact onto the substrate was reported.

CA Pt films deposited changing both the kinetic energy of the plume and the number of laser pulses, thus changing the degree of substrate coverage with NPs, were later observed by STM [41]. The average particle diameter increases with increasing film thickness, following a power law with an exponent similar to that observed for metals grown by MBE. This is taken as evidence that NPs grow *on the substrate* by surface diffusion of the deposited material.

Nucleation and growth up to a critical particle size, followed by coalescence and coarsening at large degrees of substrate coverage drive the growth of Cu nanocrystals with size below 10 nm synthesized in nanocomposite films deposited by PLD in argon at low pressure, not exceeding 0.66 Pa. At higher ambient gas pressures, up to 13 Pa, again nucleation and growth mainly occur at the substrate, but the reduced surface mobility inhibits the coarsening stage, so that highly anisotropic nanocrystals form [42]. The same scheme of NP growth was reported for Fe/Mo [43], Fe/Cu(111) [44], and Au in amorphous Al_2O_3 layers [45].

By contrast, in a careful analysis of the growth of silicon NPs with narrow size distribution [46], plasma spectroscopy shows that NP nucleation and growth occurs *in the expanding ablation plume*. A more recent deposition and modeling study [25] confirms that Si NPs are nucleated and grow in the plume. Ionization processes occurring when plume propagates through an ambient gas result in very high nucleation rates and small cluster critical radii. The synthesis of C NPs in plumes expanding through He and Ar atmospheres up to pressures as high as 1 kPa was

reported and modeled [30], again keeping into account the relevant role of ionization phenomena in the interface region between the shock wave front and the ambient gas [47]. Cluster-assembled W films were deposited in different atmospheres and pressure ranges [48]. The surface morphology, bond coordination, and oxidation path of the deposited films, both when exposed to ambient atmosphere and when synthesized in dry air, were systematically studied and complement a detailed HREM analysis of structure, size, and morphology of the deposited clusters [49]. Ag nanoparticles were synthesized in a controlled way in He [50] and Ar [34] over wide pressure ranges. Scanning and transmission electron microscopy images of the samples show that they belong to CA materials. Both the growth path followed by the films, as revealed by the surface morphology and the measured NP sizes, convey a coherent picture whereby NPs form in the expanding ablation plume.

In the framework of this picture, using the parameters calculated in the analysis of plasma propagation by mixed-propagation model, the average NP asymptotic size, which is the number N of constituent atoms in a particle that reached a steady state during plume propagation, is evaluated.

It is commonly observed that NP formation proceeds through the steps of nucleation, growth, and cooling [51]. The presence of an ambient gas requires solving a set of hydrodynamic equations for plume expansion, including vapor condensation. Such an approach is out of the present calculation capability. We assume an initial seed population of tiny clusters [52] in the propagating plume. Their existence is most likely, given the high ionization degree of the plume and the ion tendency to be surrounded by neutral atoms [25]. For given ablation conditions (see Table 7.1 for the examples discussed here), the average *asymptotic* number N of atoms in a NP that attained a steady state during plume expansion is calculated in the ideal gas approximation. The plume experiences a range of internal pressures and is spatially inhomogeneous, so that growing NPs at different stages of evolution coexist in it; yet we consider averages over long times. N is given by

$$N = (\langle n_{\mathrm{a}} \rangle \cdot \sigma_{\mathrm{a-a}} \cdot \langle v \rangle \cdot t_{\mathrm{f}}) \cdot (n_{\mathrm{g}} \cdot \sigma_{\mathrm{a-g}} \cdot \langle v \rangle \cdot t_{\mathrm{f}}) \cdot x_{\mathrm{T-S}} \cdot x_{\mathrm{aggr}}^{-1} \tag{7.4}$$

when the target to substrate distance $x_{\mathrm{T-S}}$ is shorter than the distance x_{aggr} over which NPs grow in the expanding plasma and

$$N = (\langle n_{\mathrm{a}} \rangle \sigma_{\mathrm{a-a}} \langle v \rangle t_{\mathrm{f}})(n_{\mathrm{g}} \sigma_{\mathrm{a-g}} \langle v \rangle t_{\mathrm{f}}), \tag{7.5}$$

when $x_{\mathrm{T-S}}$ is larger than x_{aggr}.

In both equations, the distance x_{aggr} traveled by the plume during particle growth is deduced from optical emission data, considering the relevant species in the plume (such as TaO, for Ta ablation [35]). When such data are lacking, we adopt the relation [22]

$$\mathrm{x}_{\mathrm{aggr}} = 6 p_{\mathrm{g}}^{-1/5}. \tag{7.6}$$

Equation (7.6) gives an upper limit for the value of x_{aggr}. The monotonic dependence of particle size on p_{g} in (7.6) agrees with a number of results on Si [4, 25], in turn

well fitted by mixed-propagation model [32]. Yet we notice that the size of Si NPs grown in helium at pressures as high as 1 kPa shows a peaked dependence on gas pressure, with a maximum at about 600 Pa [53]. The choice of the value of x_{aggr} is a delicate point of mixed-propagation model, as we noticed when the measured sizes of dispersed silver nanoparticles deposited on suitable TEM grids were compared to the calculated values obtained by the model [34]. An excellent agreement was found choosing x_{aggr} as the distance at which the absolute plasma luminosity decays by three orders of magnitude with respect to the initial value. It is likely that at such a distance from the target, the plasma is non-collisional, so that at x_{aggr}, the NPs in the plume reached a steady size.

In (7.4) and (7.5) the particle formation time t_f is the time needed by the plume to travel the distance x_{aggr}. The average number density of ablated atoms $< n_a >$ is obtained from the ratio between the number of ablated atoms per pulse and the volume of the plume, deduced from fast imaging pictures of the plume taken both near the target and at a distance from the target around x_{aggr}. Increasing $< n_a >$, the collision rate between ablated atoms increases, while increasing n_g, the plume becomes more confined. Both trends favor NP formation and growth. σ_{a-a} and σ_{a-g} are the geometric cross sections for ablated particle – ablated particle and ablated particle – gas atom binary collisions. A unity sticking coefficient is assumed. Although both for ambient gas atoms and for ablated species velocity distributions should be considered, the velocity v_0 for ablated particles and the average velocity v_g for gas atoms, as deduced from the gas temperature, are assumed. The average between v_g and v_0 is taken as the representative average velocity $< v >$ of plume particles, being the impact velocity in a binary collision between a slow gas atom and a fast plume particle. With this choice, an important role in particle formation is attributed to the fastest group of ablated particles. When $< v >$ increases, the time interval between two subsequent collisions decreases, thus increasing the rate of NP growth.

In both (7.4) and (7.5), the first term ($< n_a > \cdot\sigma_{a-a}\cdot < v > \cdot t_f$) yields cluster growth and is proportional to the scattering probability between ablated particles, while all the mechanisms resulting in slowing down and confinement of the plume are embodied in the second term ($< n_g > \cdot\sigma_{a-g}\cdot < v > \cdot t_f$), which is proportional to the scattering probability between ablated particles and gas atoms.

In the first stage of plume propagation, atoms mainly aggregate together and NPs grow. Beyond the distance x_{aggr}, particle cooling, both by a dominant evaporative and by a less effective collisional mechanism, *balances* particle growth. The term $x_{T-S}x_{aggr}^{-1}$ in (7.4) and *1* in (7.5) takes into account the competition between growth and cooling mechanisms in a particle, by avoiding an indefinitely persisting, unphysical particle growth when the plume propagates over large distances, as described by (7.4).

The phenomenological model we just described for NP growth in the expanding ablation plasma is highly simplified. The contrasting experimental results on Si, the only material whose behavior was studied with some detail, although not exhaustively, indicate that the dependence of x_{aggr} on laser fluence and on ambient gas nature and pressure is a complex one. This suggests that our understanding

Table 7.3 Asymptotic number of atoms per NP, N and average NP diameters, d calculated with mixed-propagation model. For comparison, available NP diameters measured by TEM are reported

Target	p_g (Pa)	N	d_{th} (nm)	d_{exp} (nm)
C	30; N_2	5.5×10^4	10	$5 \div 10$ [30]
Ta	20; O_2	9.6×10^4	17	–
Ag	10; Ar	15	0.7	$0.9 \div 1.7$ [34]
Ag	40; Ar	158	1.7	$1.8 \div 2.2$ [34]
Ag	100; Ar	2.34×10^3	4.1	$4 \div 7$ [34]

of the combined effect on particle formation of the parameters that drive plume propagation is far from being complete.

The model of NP growth was applied to evaluate the average asymptotic *size* of NPs grown in ablation plumes of C, Ta, and Ag, propagating under the experimental conditions listed in Table 7.1. Parameter values for mixed-propagation model from Table 7.2 were used in the calculations. In all cases, x_{T-S} is larger than x_{aggr}, so (7.5) holds. The average number of atoms per particle N is reported in Table 7.3 together with the average diameter of spherical NPs: in the calculations, we used packing efficiency $\eta = 0.67$ for close-packed noncrystalline structures, based on NP structure from electron diffraction patterns taken on samples observed by TEM.

From Table 7.3, there is a reasonable agreement between calculated and observed NP sizes, when available. The effectiveness of gas pressure to NP growth is evident in the case of Ag films pulsed laser deposited keeping identical all other process conditions.

Thus, although blind with respect to the detailed interaction mechanisms among particles in the ablation plasma that propagates through the ambient gas, mixed-propagation model appears to have a degree both of interpretative and of predictive ability concerning NP growth in the expanding plasma produced by a nanosecond laser pulse.

7.2.3 *Controlled Deposition of 2D Nanoparticle Arrays: Self-Organization, Surface Topography, and Optical Properties*

We now discuss the synthesis and deposition of silver NPs produced by laser ablation in a controlled inert gas (Ar) atmosphere to show up to what extent is it possible to manage the deposition of a spatially organized two-dimensional arrangement of NPs with controlled properties (size, size distribution, number density). Selected physical properties of the obtained film can thus be tailored. As an example, the position and the full width at half maximum (FWHM) of the surface plasmon resonance of the Ag films is considered. Our study combines an investigation of plasma expansion dynamics by fast photography imaging with the modeling of NP growth by mixed-propagation model and with electron microscopy observations, both SEM

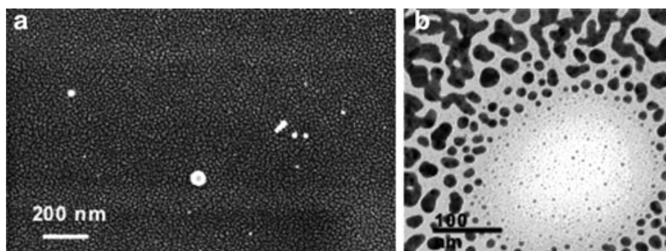

Fig. 7.4 Representative pictures of a silver film deposited at $p_{Ar} = 10$ Pa showing: (**a**) the surface morphology (SEM); (**b**) the nanostructure (TEM) [34]

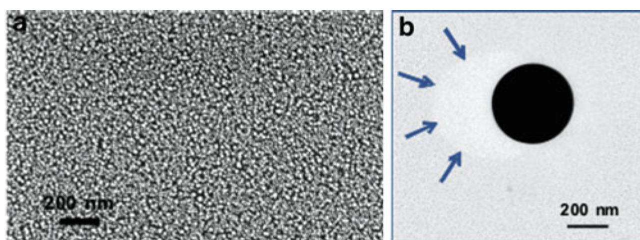

Fig. 7.5 Representative pictures of a silver film deposited at $p_{Ar} = 100$ Pa showing: (**a**) the surface morphology (SEM); (**b**) the nanostructure (TEM) (adapted from [54])

and TEM of the morphology and nanostructure of the deposited films, whose optical properties were tested by UV-vis spectrophotometry [34, 54].

For all depositions, the number of laser pulses was fixed at 10,000 and the process was stopped before the substrate surface were completely covered. In Fig. 7.4 are shown representative SEM (Fig. 7.4a) and TEM (Fig. 7.4b) pictures from the sample deposited at the lowest pressure $p_{Ar} = 10$ Pa. Film morphology consists of silver islands with smooth rounded edges, with typical size in the range of few tens of nanometers. The elongated shape of most of such islands indicates that they result from *coalescence* of definitely smaller, nearly spherical particles, some of which can be still observed as isolated NPs on the film surface. A similar morphology is observed in the sample grown at $p_{Ar} = 40$ Pa. The TEM picture in Fig. 7.4b clearly shows structures resulting from a coalescence process. Besides them, in the circular, near-center region of the image, spherical, isolated NPs with the smallest size visible to the naked eye are visible. The spatial density of the latter is low, probably due to the shadowing effect of a big spherical droplet that masked a portion of the substrate during part of the deposition process. We conclude that in the films deposited at the lower ambient gas pressures, the adopted number of laser pulses results in a particle density on the substrate surface large enough that aggregation of small NPs occurs, giving rise to coalescence into the observed big NPs besides the smaller spherical ones.

Turning to the surface of the sample grown at $p_{Ar} = 100$ Pa (Fig. 7.5a), it is mostly covered by a random distribution of *isolated* sphere-like NPs. There is

no evidence for a coalescence process. In a film grown at $p_{Ar} = 70$ Pa, a similar morphology is observed [54]. In the corresponding TEM picture in Fig. 7.5b, only near-spherical, small NPs are visible, most of them having size, evaluated by a counting software [55] in the range between 3 and 5 nm; some particles composed by two or more smaller spherical NPs can be observed. In Fig. 7.5b, three regions can be discerned. The black circular area is a micrometric droplet ejected by the liquefied target surface by pressure recoil that gently landed on the substrate surface during NP deposition. The arrows indicate the boundary between a crescent-shaped area, adjacent to the droplet on the left side, and the remaining sample area. Both these zones are covered with isolated, small, spherical NPs with quite narrow size distribution. Within the crescent, the NP number density is evidently lower than in the remaining area. The gradient of NP number density on moving away from the droplet indicates that it severely shadows a fraction of the particle flux directed at the substrate, the mechanism becoming less and less relevant on moving away from the center of the normally projected droplet shadow. Thus in a single picture, we look at snapshots of film growth at *different times*. The same reasoning holds for Fig. 7.4b. In the early stage of deposition on the substrate isolated, nanometer-sized particles are present. With increasing deposition time, NP size increases until they begin to coalesce, giving rise to larger islands that lose spherical symmetry, until lastly a percolated structure results.

It is noticeable that in the films deposited at high Ar pressures, the shape of nearly all NPs is sphere-like. For the films deposited at lower gas pressures, where particle coalescence dominates, only a *minor* fraction of *spherical* particles was identified. NP sizes reported in Table 7.3 refer to such particles.

In all the above films, most likely NPs of size near those calculated by mixed-propagation model constitute the building blocks from which kinetics and, to a lower extent, thermodynamics drive the formation of a CA film, as shown by the discussed morphology.

While mixed-propagation model that is based on the kinetic gas theory nicely predicts NP size, it does not include the kinetic evolution of mutually interacting particles on the substrate. However, some observations are in order. In particular, the adsorption energy of Ag on most substrates is low, so that also the initial sticking probability is low [56]. Thus most likely, Ag *films* grow according to the Volmer–Weber scheme, forming three-dimensional islands. The observed coalescence in the films deposited at low Ar pressure can be explained because, at fixed number of laser pulses, the number of Ag NPs impinging on the substrate increases with lowering Ar pressure. Both the progressive increase in NP areal density and the corresponding decrease in NP number density support this picture.

The well-differentiated morphologies of the deposited Ag films, thereby clustered NPs are found at $p_{Ar} = 40$ Pa, while slightly increasing the pressure up to $p_{Ar} = 70$ Pa a population of isolated NPs results open the way to obtain nanostructured metal films with finely tuned optical properties. In noble metals, a surface plasmon resonance (SPR), resulting from the coherent oscillation of surface electrons excited by an electromagnetic field, can be observed. In isolated Ag NPs with size of few nanometers a SPR peak is observed at about 400 nm [57]. The position

Table 7.4 Position ω_p and FWHM of the plasmon resonance peak for Ag films deposited with different process parameters. The films consist of NP arrays whose observed morphologies are reported

p_{Ar} (Pa)	Laser pulse #	ω_p (nm)	FWHM (nm)	Film morphology
10	10,000	632	>630	Percolated
40		560	336	Clustered NPs
100		440	150	NPs

and shape of the SPR peak critically depend on NP size, shape, and spatial distribution [58, 59]. Thus, a fine control of the morphology of a nanostructured thin film allows controlling its optical properties. In Table 7.4 are reported both the position (ω_p) and the FWHM of the SPR peak of samples deposited at different Ar pressures. Keeping fixed the number of laser pulses and decreasing p_{Ar} from 100 down to 10 Pa, the plasmon position red shifts from 440 to 643 nm while its width progressively increases from 150 nm up to more than 650 nm. Such trends indicate that the films deposited at low ambient gas pressure no more consist of isolated, spherical NPs, as confirmed by SEM and TEM pictures.

Thus, in the case of silver deposition, with the adopted parameters, playing with ambient gas (Ar) pressure, a qualitative change in the strategy of self-assembling of NPs on the substrate occurs and involves coalescence. The trend of the measured SPR of the films shows that it is possible to finely tailor the nanostructure of this family of films and concurrently their optical properties.

In conclusion, our comprehension and control of the key mechanisms of NP synthesis by ns laser ablation in an ambient gas is moving towards the stage of identifying experimental conditions suitable to deposit on a substrate arrays of dispersed NPs with predefined size and composition. This is a requisite to finely control the physicochemical properties of such NPs in the frame of a bottom-up strategy.

7.3 NP Formation in Femtosecond PLD: Experimental Results and Mechanisms

The morphology, composition, and nanostructure of films synthesized by femtosecond (fs) PLD of a solid target significantly differ from those of films obtained with ns laser pulses. In most cases, we find random stackings of nanoparticles whose sizes lie between 10 and 100 nm [2] and quite narrow size distributions [10]. By fs ablation, NPs of several elemental materials were obtained in an efficient and chemically clean way. Besides simple (Al [5, 60]), transition (Ti [2, 7], Ni [61]) noble metals (Cu [10, 60], Au [10]) and semiconductors (Si [62]), also compounds even with complex stoichiometry were synthesized as NPs. We mention MgO, $BaTiO_3$, GaAs [62], TiO_x [7], Ru_2B_3, and RuB_2 [63]. The composition of the deposited NPs in relation to that of the target is a still poorly investigated, nontrivial problem, in particular when traces of reactive gases such as oxygen are present in the deposition chamber [64].

Parallel to film deposition attention was focused to plasma analysis, mainly considering the emitted signals that characterize the species escaping from the target, ions, neutrals, and NPs. Pairs of ultrashort, time-delayed pulses were recently used to change the relative proportions and kinetic energies of ions and neutrals with respect to the preformed plasma, thus influencing NP production. The accumulated wealth of data are useful to model the dynamics of plume formation and the early stages of expansion, to identify mechanisms of particle synthesis whose relative weight as a function of irradiation conditions is discussed, often taking the deposited laser fluence E as the reference experimental parameter.

Two conceptual schemes are presently adopted to explain NP synthesis: direct cluster ejection from the target as a consequence of material disruption by a laser-induced explosion-like process, or aggregation in the flying ablation plume via a collisional mechanism [65]. Available models and simulations take care of the features of fs pulse interaction with solid matter, namely an initial ultrafast heating without changing matter density, followed by a very rapid expansion and cooling. Just this sequence is at the roots of NP formation. According to the results of hydrodynamic simulations [66, 67], a thermal wave is followed by a pressure increase and a propagating shock wave. Molecular dynamics (MD) simulations [65, 68] put into evidence mechanisms such as phase explosion, fragmentation, evaporation, and mechanical spallation. Important *quantitative* discrepancies are found when model predictions are compared with experiments, even considering the very ablation depth. This is an indication that ablation mechanisms and their relative weight for various fluence ranges are still partly unknown. In the following, we focus on a selection of reliable results and concepts concerning NP synthesis by ultrafast laser pulses.

Detailed analyses of the ablation plasma produced by ultrashort pulses were conducted mostly on elemental targets irradiated with light visible to near-IR at fluence values ranging from intermediate to modest and laser intensities between a few 10^{12} and a few 10^{14} $\mathrm{Wcm^{-2}}$. By the time of flight mass spectrometry (TOF-MS), both plasma constituents and their velocity distributions were determined for Si [69]. When fluence is large enough, being above the ablation threshold, the velocity distribution is a full-range Maxwellian whose center-of-mass velocity is attributed to collisions in the Knudsen layer. In metals, Ti being the prototype, again by TOF-MS two components are found in the ion velocity distribution at rather low fluence; kinetic energies of Ti^{+} ions in the keV range are taken to indicate that Coulomb explosion could significantly contribute to ablation [70]. Recently, time resolved optical emission spectroscopy (OES) was coupled with fast imaging of the expanding plasma: in Fig. 7.6, images of plasmas produced irradiating the same Si target with ns and fs pulses are compared to each other at comparable delays.

In some cases, the size and size distribution of the deposited dispersed NP populations were measured by atomic force microscopy (AFM). Basically, the same picture emerges: at very short delays, a plume propagates normally to the target with narrow angular aperture. According to OES, the constituents of such a plasma are atomic species, both ions and neutrals. Velocity measurements show that ions are always faster, with velocities of a few 10^4 $\mathrm{ms^{-1}}$, due to their strong coupling to

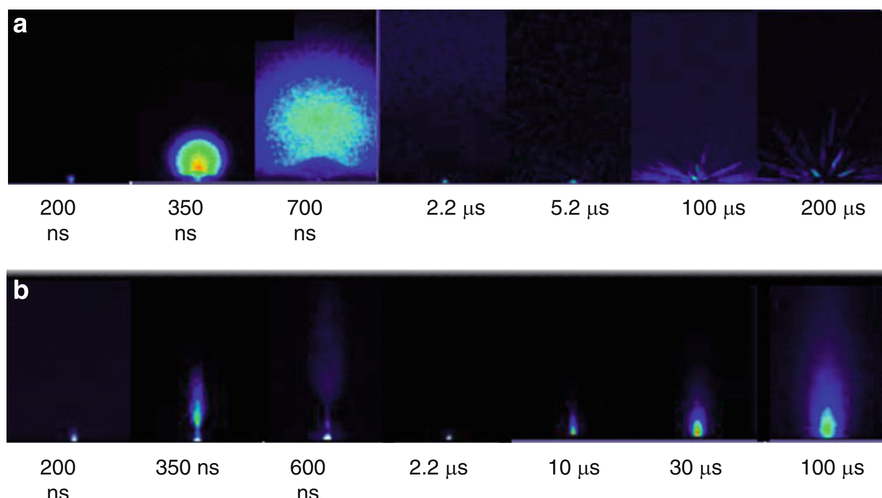

Fig. 7.6 ICCD fast photography pictures of ablation plumes from a silicon target irradiated in vacuum with (**a**), 25 ns pulses, $\lambda = 248$ nm (**b**), 100 fs pulses, $\lambda = 620$ nm (adapted with permission from [64])

electrons that escape first from the target, while atom velocities are about one order of magnitude less. Data are available for Ti [2,71], Zr, Hf [71], Au, Cu [10], Al [60]. In the latter study, plasma expansion was analyzed via space- and time-resolved X-ray absorption spectroscopy, monitoring the energy shifts and modifications of the Al $L_{II,III}$ absorption edge, similarly to an earlier investigation on Si [62].

At delays of the order of microseconds, a second plume with considerable angular aperture and rather low velocity, from a few 10^2 to a few 10^3 ms^{-1}, is observed. A typical *blackbody* spectrum, obtained by OES, leads to consider NPs as the constituents of such a plasma [2, 7, 10, 71]. Whenever film nanostructure was analyzed, SEM or AFM show random distributions of NPs [2, 10, 61]. In these studies, care was taken of depositing a submonolayer to avoid cluster self-organization on the substrate, most likely resulting in coalescence. Since the above observations are independent of the chemistry of the target (metal, semiconductor), the production of NPs appears to be associated to fs ablation.

The reported velocities of the different species are nearly constant up to considerable distances from the target (from 1 mm to centimeters [2]). Qualitatively, the ratio between atom/ion and cluster velocities is correctly reproduced in a direct simulation Monte Carlo (DSMC), where MD results were used as input parameters [72].

For both Au and Cu [10] atom velocities, measured as a function of the fluence, increase near the ablation threshold E_t, presumably due to the increased quantity of ablated matter and the related changes in the adiabatic expansion stage, while NP velocities decrease near E_t, due to changes in their size distribution. The velocities of both populations are nearly independent of fluence at values larger than E_t, showing

that in the *initial* plasma expansion, the average temperature of ablated matter is almost independent of E.

Defining atomization as the direct transformation of target material into the gas phase [73], both in Au and in Cu, the measured ablation efficiency is maximum at the fluence E_{NP} where atomization is minimum. Afterwards increasing E atomization slightly increases [10]. Such a strong correlation is explained in terms of the higher energy cost of atomization, compared to NP production. The E_{NP} value is associated to target heating regime. At fluences larger than the ablation threshold E_t, matter escapes from layers below the target surface that are progressively deeper and colder, so it cannot be energized enough to be fully atomized and a mixture gas – NPs (liquid) escapes from the target. As the ablation efficiency is much higher than the value expected for thermal vaporization (pure atomization), a considerable fraction of NPs is likely to be ejected *directly* from the target.

The shape of the deposited NPs is sphere-like and they belong to two distinct populations [10]; the smaller-sized particles are supposed to be *directly ejected* from the target. The size distribution of the larger particles scales as $r^{-3.5}$, r being their radius. This distribution is observed when a mechanism of fragmenting collisions dominates; thus, such NPs are expected to result from *in-plasma* collisional sticking.

Some attempts were made at manipulating plasma constituents with a delayed fs [2], or ns [61] pulse, playing also with the delayed pulse wavelength [61]. In particular, irradiating Ni with UV fs pulses with $\lambda = 263$ nm, the average diameters of deposited dispersed NPs measured by AFM are nearly half of those resulting upon irradiation with identical pulses, with doubled wavelength $\lambda = 527$ nm. In both cases, particle size is independent of the laser fluence, up to $1\,\mathrm{J\,cm^{-2}}$. When a further ns-UV pulse intercepts the ablation plasma at different delays, changes are caused in the size distribution of the deposited NPs. At fixed intermediate fluences (about 0.5 and $0.4\,\mathrm{J\,cm^{-2}}$, respectively) of the fs and ns pulses, NPs shrink, the effect being more marked at shorter delays. The result suggests that in the expanding plasma, NPs *group together* as a function of their size, the smaller ones traveling ahead of the bigger ones.

It is to be mentioned that at very long delays, of the order of tens of microseconds, when irradiation is performed at high fluences (about $10\,\mathrm{J\,cm^{-2}}$ and higher), *droplets* can be visible to the naked eye due to their luminous trajectories. Whenever such debris are observed, their fingerprint are micron-sized particles lying on the surface of the deposited films, evident in SEM pictures [62]. The difference in size and velocity between such species and NPs indicates that droplets are not "giant" particles, nor the two species are likely to be produced by the same mechanism. Stress confinement in the target, associated to ultrashort pulses was proposed as their origin [65].

Irrespective of the target nature, a scaling among thresholds in laser fluence holds thereby the thresholds for atomic, E_a and nanoparticle, E_{NP}, emissions are comparable, both being lower than the value E_d for droplet emission [64]

$$E_d > E_a \approx E_{NP}. \tag{7.7}$$

The main experimental results on NP synthesis can be correlated with reasonable agreement to simulations of target behavior under fs pulse irradiation. MD indicates [65] that at high deposited fluences, the main mechanism responsible for material expulsion from the target is phase explosion of matter heated above the thermodynamical critical temperature T_c. The surface region decomposes into a foam of interconnected liquid regions, containing gas molecules, liquid droplets, and small particles. At increasing depth from the target surface where matter decomposition occurs and thus in regions where the degree of overheating is progressively lower, the liquid fraction increases and big droplets form in the tail of the ablation plume. NPs segregate in different regions of the expanding plasma depending on their size, the smallest ones being grouped in the front region, while medium-sized ones are found in the middle. Two particle populations are consistently found, the smaller ones being ejected in the explosive decomposition of matter into liquid and vapor, while the larger ones result from decomposition and coarsening of the transient interconnected liquid regions.

Combining smaller scale MD and larger scale DSMC techniques, two channels of NP production are identified, namely direct ejection following laser–matter interaction and collisional condensation-evaporation in the propagating ablation plume [72]. The processes belonging to the first channel include, besides phase explosion, photomechanical spallation and fragmentation; such *volume* mechanisms produce small particles and atoms/ions.

Gas-phase collisional sticking and evaporations are the processes belonging to the second channel. They resemble those occurring in aggregation sources [74] and are favored by the huge number of seed molecules and small particles in the laser-generated plasma.

Femtosecond Al ablation was investigated in a one-dimensional hydrodynamic numerical model [73] exploring the relative weights of different decomposition processes. Moving from a thermodynamically complete equation of state, the time evolution of heavy particles is followed on a temperature-density (T-ρ) phase diagram, taking into account matter slices lying at different depths below the target surface. Ablation mechanisms are compared to each other as a function of the laser fluence E, allowing for interplay between the kinetic lifetime of the metastable liquid state and the time needed to induce mechanical fracture of the material. Atomization requires the highest initial temperatures, attainable only in a near-surface thin layer, not exceeding 15 nm, so that only a small fraction of matter is ablated via this mechanism. A metastable liquid state forms at depths between 20 and 30 nm where the thermodynamical critical temperature is reached and phase explosion occurs, but also this thermal mechanism involves a limited amount of material. Indeed the molten layer is much thicker, but most particle trajectories, although entering the metastable liquid region, reach temperatures below T_c. Matter persists for comparatively long times in a metastable state and mechanical effects prevail over thermal ones, leading to decomposition into droplets and chunks.

The fractions of material ablated by the above mechanisms depend on target nature and laser fluence E. At low E, target melts; with increasing fluence, material fragmentation [65] occurs, then mechanical and thermal mechanisms coexist, until,

at large E values atomization, phase explosion and mechanical decomposition take place at different depths in the target; the latter mechanism dominates in Al in the interval 0.1–5 J cm^{-2}.

Thus, we have evidence that ablating a solid target with ultrashort laser pulses several different thermodynamic paths in the temperature–density phase diagram of the irradiated material are followed, depending on the maximum attained temperature. The initial conditions experienced by the target uniquely determine the nature of the constituents of the ablation plasma and their relative abundances. Simulations indicate the ablation mechanisms and their dependence on the laser fluence, offering a picture of the process in qualitative agreement with experiments.

In conclusion, ultrashort laser pulses offer an efficient and clean way to synthesize NPs *in vacuum*. Although most of the systematic investigations were devoted to elemental systems, the basic mechanisms of laser–matter interaction have been identified, although their relative relevance to ablation is still under debate.

7.4 Applications

Lasers have been widely utilized in metallic materials machining since the early 1970s as well as in machining nonmetallic materials such as ceramics, plastics, various composites, and semiconductors (e.g., silicon, silicon carbide, etc.) for a number of industrial applications. The ability of lasers, especially pulsed lasers, to precisely machine micron and submicron features in otherwise difficult to machine materials such as ceramics and semiconductors has stimulated a rapidly growing interest in understanding the parameters controlling the limits and the capabilities of this process. Micromachining by laser ablation has become an alternative to other traditional micromachining methods such as photolithography. One reason is the recent developments in laser micromachining that have improved the ability to achieve well-defined 3-D structures at the micrometer scale. Situations suitable for laser micromachining are, for example, when the substrate material cannot be removed by etching (wet or dry) or when the substrate geometry is a complex one.

A large number of studies have been devoted to investigate laser-based micromachining that covered the different aspects of the machining process and the physics of laser–material interaction. The development of femtosecond (fs) lasers and their initial application to the machining of a variety of materials has created strong interest in their micromachining potential.

Current reasoning (see Sect. 7.3) suggests that the pulse duration of a femtosecond laser is so short that there is not sufficient time for any of the pulse energy to be distributed to the substrate in the form of heat. Thus, particularly for low pulse energies, there should be no heat-affected zone (HAZ) resulting from the processing.

This is in direct contrast to nanosecond (ns) machining, which has an associated HAZ. The magnitude of the HAZ is a direct result of the machining parameters and can be minimized for nanosecond micromachining. However, the HAZ is only one aspect of how a material is altered during the machining process. It is important also

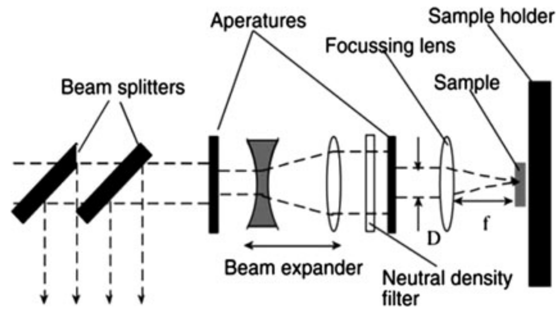

Fig. 7.7 Optical set-up for the laser machining [75]

to look at the stresses induced as a function of laser parameters. The optical set-up is simple (Fig. 7.7), involving a beam expander system (only if an ns laser is used).

We will briefly review some possible applications of laser processing. Lasers can be used for microdrilling, fine cutting, etching, thin films deposition, reshaping, etc. The pulsed lasers reported for being used for micronanomachining are working in nanosecond and femtosecond regimes. For the nanosecond lasers, there have been studies with excimer lasers, Nd:YAG, CO_2 [76–78]. There is an increased interest in using femtosecond lasers in micromachining, because of the high energy densities that can be obtained [79].

7.4.1 Direct Writing

Brodoceanu et al. [80] report on laser-induced patterning performed by "direct writing" (see Chap. 8 for a detailed description), where the laser light is just focused onto the substrate, by projection of the laser light through a mask, by direct-contact mask, or by the interference of laser beams. Nanoholes on Si(100) wafers were fabricated by using femtosecond Ti:sapphire laser radiation. A monolayer of amorphous silica microspheres of 150 nm radius is directly deposited onto the Si wafer by using a commercially available colloidal suspension. Figure 7.8 is an AFM image of the patterned Si substrate. A single pulse of 300 fs was used, at 266 nm. The fluence was $15 \pm 3.5\,\mathrm{m\,J\,cm^{-2}}$. The microspheres have a hexagonal lattice structure, and the distance between the holes represents the diameter of the spheres. The diameter at FWHM (full with at half maximum) is around 60 nm and the depth 6 nm, approximately.

7.4.2 Laser LIGA

An indirect way to use laser for microstructuring is called Laser-LIGA. This is a replication technique. It is a relatively low cost alternative to classic LIGA (using sichrotron radiation), if it is used in parallel mode. Laser LIGA makes use of the

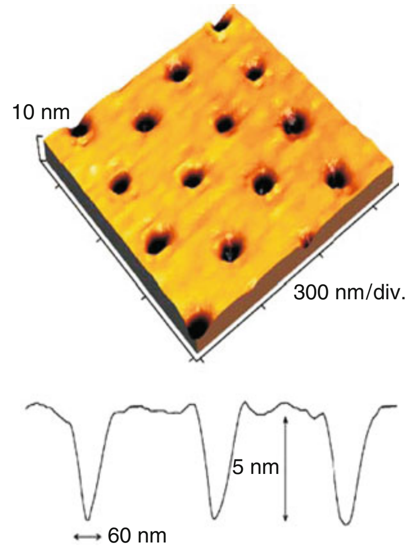

Fig. 7.8 Nanoholes fabricated on silicon by a single shot [80]

ablation of polymers (usually PMMA) followed by metallization (often with Ni or Cu). The typical processes are presented in [81] by Arnold et al. (Fig. 7.9). The main advantage of using Laser-LIGA is the fact that almost any geometry can be obtained and there is no need of masks, in most cases. The disadvantage is the fact that surface quality is better for X-ray lithography, and the maximum aspect ratios (up to 10) are considerably lower.

7.4.3 Laser Etching

Laser-assisted chemical etching is a method used for producing 3D structures *into substrates*. The laser light is used to activate a photochemical reaction. On the one hand, the laser activates the material, and on the other hand, it excites the etchant. The experiments can take place at atmospheric pressure.

Kazuyuki Minami et al. in [82] used a continuous wave Nd:YAG laser with a Q-switch unit for laser-assisted etching (LAE) of silicon. The laser worked in continuous mode because Q-switched created particles around the etched area. As etching gases, HCl, SF_6, NF_3, and CF_4 were investigated. The authors noticed that the p^+-Si can be heated and etched faster than the n-Si substrate. When the etching took place in the presence of HCl and in NF_3, there was no particle formation or redeposition. Al structures were etched in HCl, but they were not in NF_3.

Armacost et al. [83] used excimer laser at 193 nm to etch polysilicon in CF_3Br, CF_2Cl_2, and NF_3 atmosphere. There was almost no etching with CF_2Cl_2, some etching with CF_3Br, and smooth profiles were obtained with NF_3.

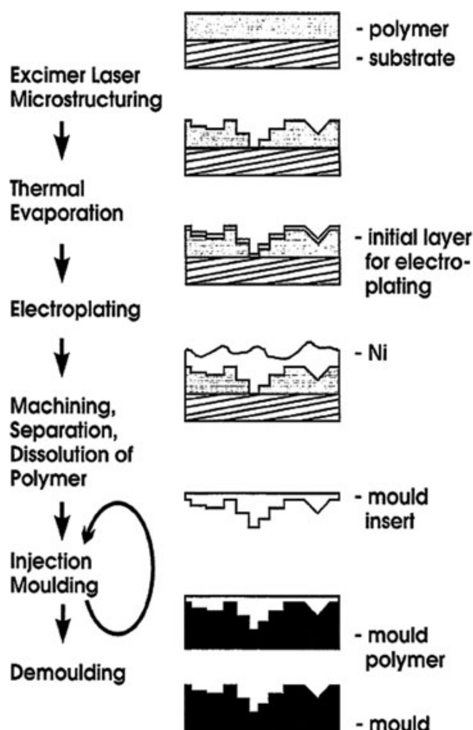

Fig. 7.9 Laser-LIGA processes [81]

Barada K. Nayak in [84] reported the etching of silicon and germanium after irradiating with femtosecond laser in sulfur hexafluoride (SF_6) and hydrogen chloride (HCl). Features with size in the nanometer range have been obtained. Figure 7.10 presents SEM images of structures formed in silicon surface by 240 laser pulses of 130 fs duration, at 0.6 J cm^{-2} in 40 kPa of (a) SF_6 and (b) HCl.

7.4.4 Pulsed Laser Deposition

Pulsed laser deposition (PLD) is particularly interesting due to its versatility in the deposition of materials, even with a complex stoichiometry [4]. PLD in vacuum permits to produce films assembled atom by atom, achieving even epitaxial growth in particular conditions (e.g., with heated substrates).

In the presence of a suitable background gas pressure, laser ablation may result in cluster formation during plume expansion. In the synthesis of nanostructured thin films, the characterization of the growth processes plays a fundamental role for the control of the film and surface properties. In particular, when the deposition technique is based on the production and assembling of nanoparticles-clusters, the

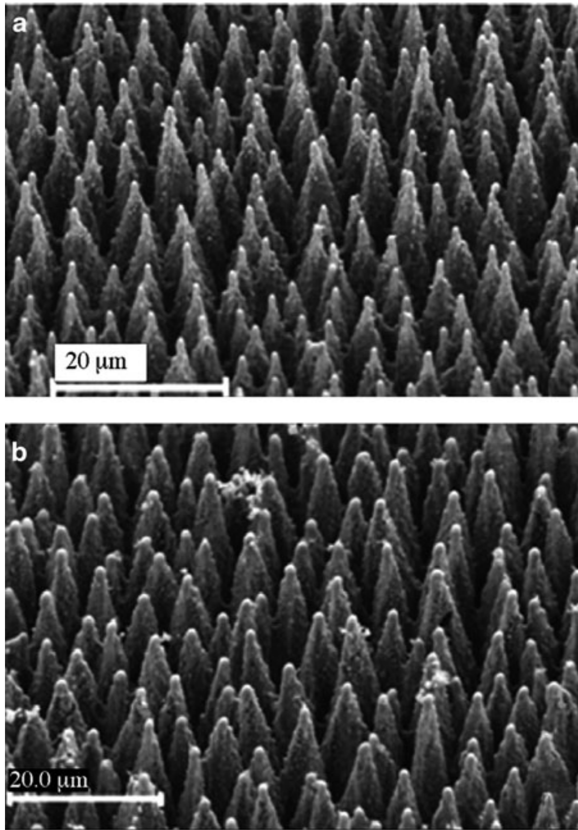

Fig. 7.10 SEM images of structures, formed in a silicon surface by 240 laser pulses of 130 fs duration, at 0.6 J cm^{-2} in 40 Pa of (**a**) SF_6 and (**b**) HCl [84]

characterization of the precursor size distribution as well as of the first stages of film formation is of fundamental importance (see Sects. 7.2.2 and 7.3).

Factors influencing the laser ablation process include the laser beam parameters, such as wavelength, energy, or fluence, and pulse length, the material properties of the target, such as melting temperature, thermal diffusion rate, optical reflectivity, and the ambient, whether a gas, or a liquid. By the correct combination of these parameters, it is possible to implement surface features with a complex 3-D geometry on virtually any material surface, and by choosing a specific micromachining environment, for example, vacuum, gas, or liquid with appropriate composition, it is possible to control the laser-induced chemical changes of the material surface.

A typical PLD set-up is described in Fig. 7.11. This consists basically of four components: a laser, a reaction chamber, a target, and a substrate. When the deposition takes place in chemically reactive gas, the ablated substance reacts with the gas molecules, and the film can differ completely from the starting material. This

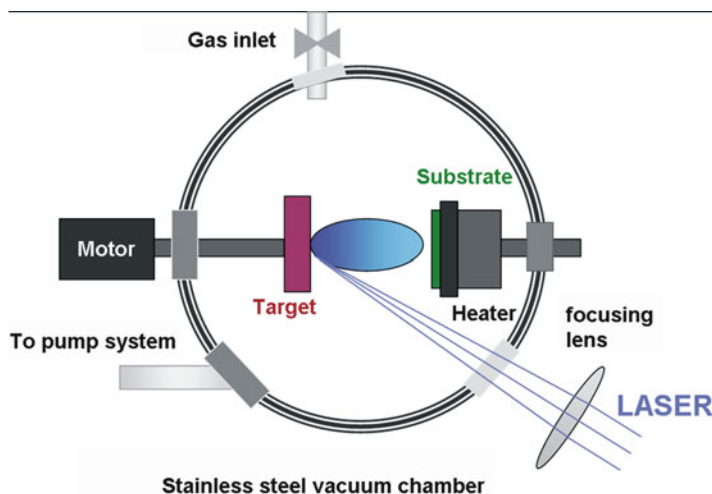

Fig. 7.11 Standard PLD set-up

method is called reactive pulsed laser deposition and is sustained by the fact that the ablated species are highly reactive and have energies between 1 and 20 eV.

Uniform ablation of the target is obtained through its rotation and translation with respect to the laser radiation. The distance between the target and substrate is generally of a few centimeters. The film uniformity can be improved if the substrate is moved with respect to the plasma direction, for example, rotating eccentrically the substrate holder.

The substrate temperature is a very important parameter for the morphology, microstructure, and crystallinity of the deposited films. For a good control of the temperature, thermocouples are placed under the substrate.

Nanoparticles play an important role in a wide variety of fields including advanced materials, biomedical field (sensors for disease detection (quantum dots), programmed release drug delivery systems), and environmental (clean up of soil contamination and pollution, biodegradable polymers, treatment of industrial emissions), electronics, pharmaceuticals, etc. Embedding nanoparticles in a matrix, complex compounds with tailored characteristics can be obtained. Combining polymers with different properties (for example optical, or electrical properties) with clusters of metals, new materials can be obtained, with new macroscopic characteristics. This class of compounds where metallic nanoclusters are embedded in polymeric matrices is suitable for packaging applications.

An interesting work on this topic has been carried out by Röder et al. in 2008 [85]. They report on the use of PLD to grow nanostructured materials formed by *metallic clusters* (Ag, Au, Pd, and Cu) and *polymeric matrices* (polycarbonate – PC and poly (methyl methacrylate) – PMMA). The metal clusters embedded in PC were grown using a KrF excimer laser with pulse duration of 30 ns, working at 248 nm, and repetition rate of 10 Hz. The work has been performed at room

temperature in UHV deposition chamber with the base pressure of 10^{-6} Pa. As reported in [85], smooth polycarbonate thin films of about 20 nm were deposited at a fluence of 70 mJ cm^{-2}. On these films, the metals were deposited at fluences in the range of 4–6 J cm^{-2} and they had an average thickness of less than 5 nm. Two processes take place during metal ablation in vacuum: deposition of metal on the polymeric surface and ion implantation some nanometers below the surface. The nanocluster dimension and shape depend both on the metal and on the polymer type. TEM investigations evidence that the nanocluster are formed inside the polymer, just below its surface, by the ion diffusion processes followed by the Volmer–Weber island formation. As it can be seen from the pictures in Figs. 7.12 and 7.13 [85], the clusters grow separately. When the number of pulses increases, fewer islands are formed, with bigger size, due to coalescence processes. The clusters are, in general, spherical, but a tendency to different shapes can be noticed, depending on the metal and/or on the polymer. J. Röder et al. concluded that the Ag clusters show larger distances on PMMA, because of a higher diffusivity of Ag on PMMA than on PC. Pd and Cu exhibit a high reactivity with the polymer. This decreases the diffusion and results in a bigger number of clusters of smaller sizes.

Tungsten oxide is a chromogenic compound with various applications in gas sensing (it detects both H_2S and H_2, and small concentrations of NO and Cl_2) [86, 87]. The sensing efficiency depends also on the surface morphology of the

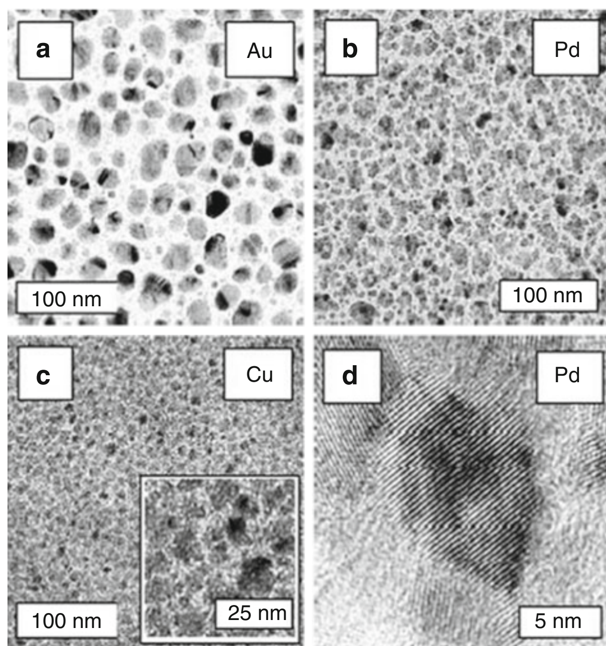

Fig. 7.12 TEM images of different metals between two 20-nm-thick PC layers with average metal amounts of (**a**) 7.3 nm for Au, (**b**) 3.3 nm for Pd, (**c**) 3.8 nm for Cu, and (**d**) 3.3 nm for Pd [85]

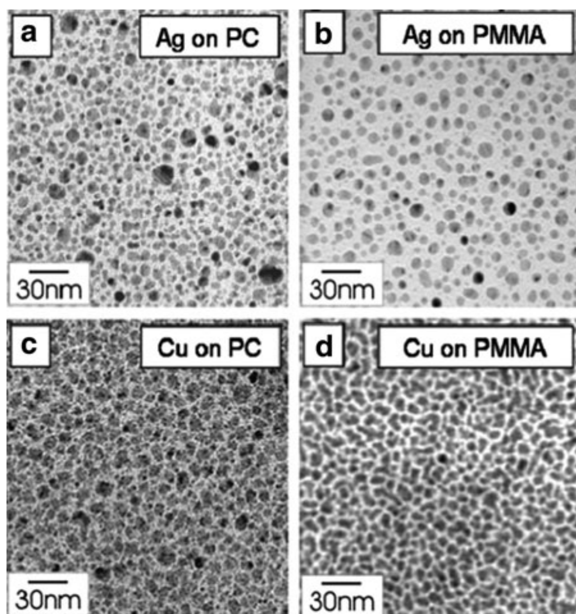

Fig. 7.13 TEM images of Ag and Cu clusters grown between two 20-nm-thick PC layers and on 15-nm PMMA, respectively, with metal amounts of (**a**) 1.9 nm for Ag on PC, (**b**) 2.0 nm for Ag on PMMA, (**c**) 3.8 nm for Cu on PC, and (**d**) 3.6 nm for Cu on PMMA [85]

active material. In particular a high-specific area value A_s is desirable. Cluster-assembled (CA) films are suitable to get high A_s values however, it is often difficult to deposit CA films in a reproducible way with an acceptable mechanical stability and adhesion to the substrate.

Filipescu et al. in [88] reported the growth of WO_x by laser ablation using a W target at room temperature in oxygen reactive pressure. A Nd:YAG laser with 4 harmonics was used, and a radiofrequency (RF) discharge system was added to increase the reactivity. The information regarding the WO_x film morphology was supplied by SEM observations.

The microstructure of some WO_x samples that were synthesized in the presence of a radio-frequency consists of a dense nanostructure made of irregularly shaped agglomerates (Fig. 7.14) whose typical size lowers with increasing O_2 pressure, from about 80 nm (sample deposited at 300 Pa) to 40 nm (sample deposited at 500 Pa) to 20 nm (samples deposited at 700 and 900 Pa). The addition of RF is efficient to induce film nanostructuring, resulting in an open microstructure much more prone to oxidation, also after the deposition is completed, than the compact films produced without RF power. Consequently, at fixed substrate temperature, the cluster ability to migrate and reciprocally aggregate giving bigger agglomerates is progressively reduced with increasing buffer gas pressure.

PLD technique can be also used for the *growth of nanowires* as presented by N. Wang et al. in [89], which is a very interesting review about the growth of

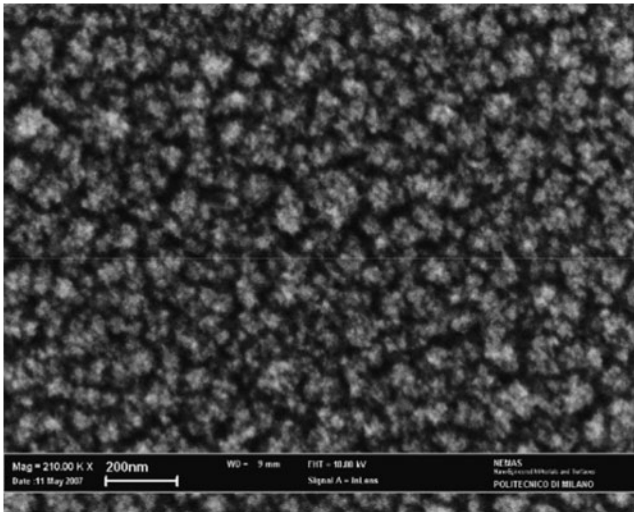

Fig. 7.14 Representative surface microstructure of a WO_x film deposited with the assistance of RF power (100 W) [88]

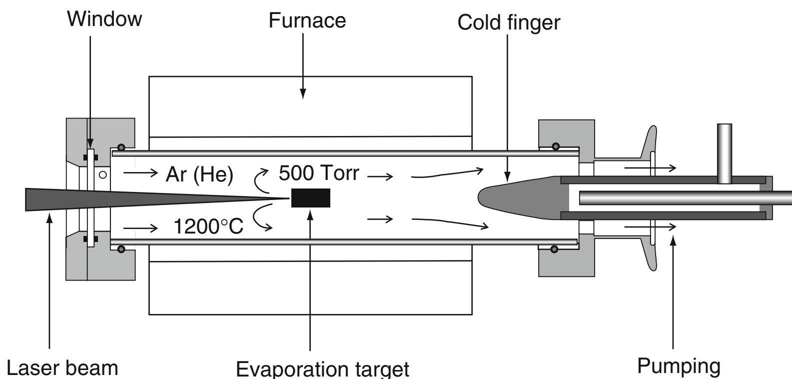

Fig. 7.15 Experimental setup for the synthesis of Si nanowires by laser ablation (Prof. I. Bello) [89]

nanowires. A schematic of a laser ablation experimental setup that can be used to grow nanowires is shown in Fig. 7.15.

Any kind of high-power pulsed laser can be used: Nd:YAG, excimer laser, femto-second lasers. For example, in [90], A.M. Morales and C.M. Lieber reported laser ablation cluster formation and vapor–liquid–solid (VLS) growth for crystalline semiconductor nanowires synthesis. Silicon and germanium nanowires with diameters of 6–3 and 3–9 nm, respectively, and lengths between 1 and 30 microns (for Si) have been obtained using a Nd:YAG laser working at 532 nm to ablate targets containing the element of the nanowire and the metal catalyst as well. Figure 7.16

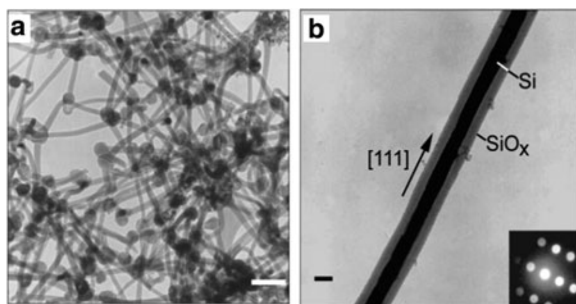

Fig. 7.16 (**a**) TEM image of the nanowires produced after ablation of a $Si_{0.9}Fe_{0.1}$ target. The scale on is 100 nm. The temperature was 1,473 K and the pressure ∼66 kPa Ar flowing at 50 SCCM. (**b**) Diffraction contrast TEM image of a Si nanowire. The scale represents 10 nm [90]

presents high resolution TEM images of individual Si nanowires. The nanowire has a uniform crystalline core covered by an amorphous coating.

7.4.5 Matrix-Assisted Pulsed Laser Evaporation (MAPLE)

The MAPLE technique used for the deposition of carbon nanostructures is described in [91]. Hunter et al. report on the deposition of carbon nanopearls (also known as nanospheres) by MAPLE and also the use of the process simultaneously with magnetron sputtering to encapsulate nanopearls within a gold film. They investigated the effects of: (a) solvent material; (b) laser repetition rate; (c) laser pulse energy; (d) substrate temperature; and (e) background pressure.

In Fig. 7.17, the carbon nanopearls, which were successfully embedded within the gold layer of approximately 1 μm in thickness can be seen. The aim of the study was to find the optimal parameters for depositing disperse, droplet-free films of carbon nanopearls with a large field of applications such as tribological coatings. These parameters were found to be toluene matrix, 700 mJ, 1 Hz, 373 K substrate temperature, and unregulated vacuum pressure or 2.67 Pa in argon.

MAPLE technique has also been successfully used for the deposition of nanostructured titania (TiO_2) nanoparticles thin films to be used for gas sensing applications as it was reported in [92]. Caricato et al. reported on the deposition of an uniform distribution of TiO_2 nanoparticles with an average size of about 10 nm on Si and interdigitated Al_2O_3 substrates (Fig. 7.18). To investigate the thin films, they used high-resolution scanning electron microscopy-field emission gun (SEM-FEG). Energy dispersive X-ray (EDX) analysis revealed the presence of only the titanium and oxygen signals and by FTIR (Fourier transform infrared) spectroscopy, the TiO_2 characteristic composition and bond were revealed.

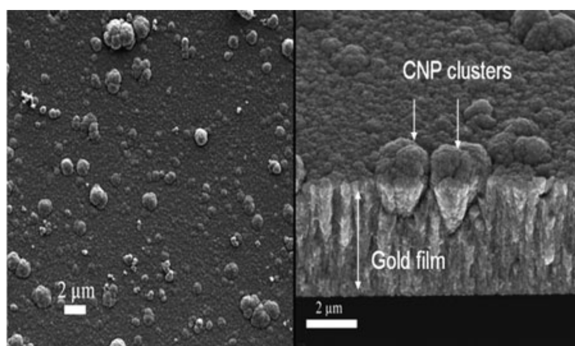

Fig. 7.17 Carbon nanopearls embedded in a gold coating synthesized using MAPLE and magnetron sputtering: *left* – top view; *right* – cross section [91]

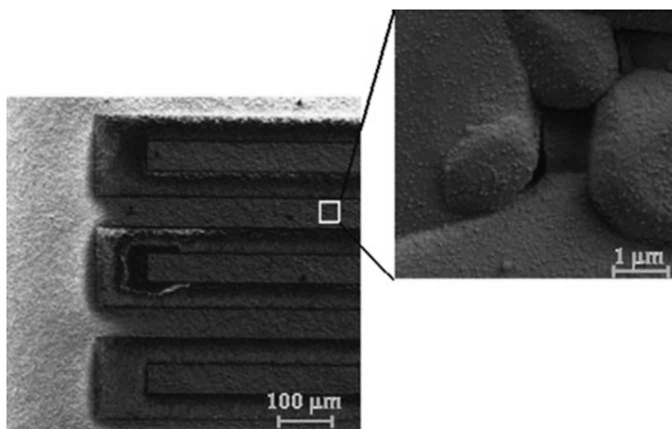

Fig. 7.18 Scanning electron microscopy images of the interdigitated sensor and of the TiO_2 film morphology on the Al_2O_3 grains [92]

7.4.6 Laser-Assisted Chemical Vapor Deposition (LA-CVD)

Single-walled nanotubes are a very important variety of carbon nanotube because they exhibit important mechanical and electrical properties and also offer great promise as active elements in the "nano-electromechanical" systems. They have a wide range of applications as high-frequency oscillators and filters, nanoscale wires, transistors and sensors.

In [93], Liu et al. reported on the nucleation and rapid growth of single-wall carbon nanotubes (SWNTs) by pulsed-laser-assisted chemical vapor deposition (PLA-CVD). The deposition system is shown in Fig. 7.19. A special high-power, Nd:YAG laser system with tunable pulse width (>0.5 ms) was used to rapidly heat ($> 3\times10^4\ \mathrm{K\,s^{-1}}$) metal catalyst-covered substrates to different growth temperatures

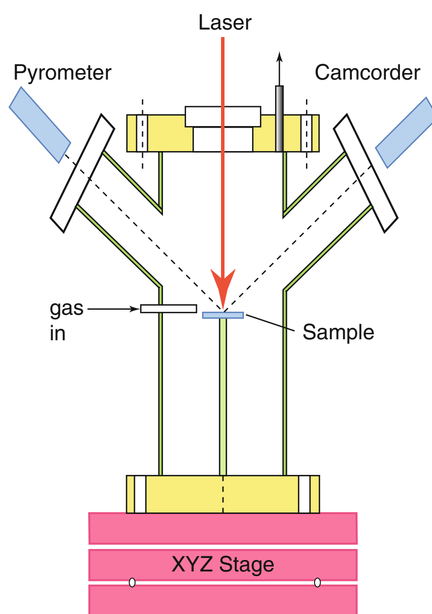

Fig. 7.19 Schematic of a PLA-CVD chamber [93]

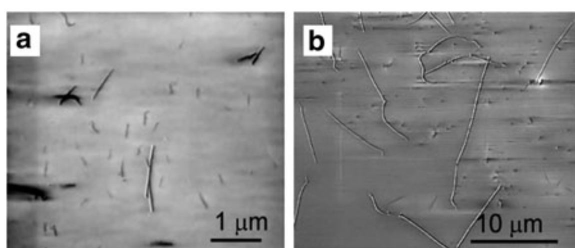

Fig. 7.20 SEM images of nanotubes grown from a single 50 ms laser pulse (52 J) using (**a**)/(**b**) Fe/Al_2O_3 thin film and ferritin as catalysts, respectively [93]

for very brief (subsecond) and controlled time intervals. SWNTs were found to grow under rapid heating conditions, with a minimum nucleation time of >0.1 s. The growth rates by single laser pulse were found to be up to 100 $\mu m\,s^{-1}$. SEM images of nanotubes obtained using thin film catalysts (a) and ferritin nanoparticles (b) are shown in Fig. 7.20.

Another example concerning the synthesis of SWNTs and SWNHs (single-walled nanohorns) is given in [94], exploring the continuous ablation regime for the growth of SWCN and the cumulative ablation regime, which is optimal for the growth of SWNTs with catalyst assistance. An industrial Nd:YAG laser (600 W, 1–500 Hz repetition rate) with tunable pulse widths (0.5–50 ms) was used. Carbon is shown to self-assemble into single-wall nanohorn structures at rates of $\sim$1 nm·ms^{-1}, which is comparable to the catalyst-assisted SWNT growth rates measured in [95]. Figure 7.21 shows TEM images of SWNHs synthesized at the optimized conditions

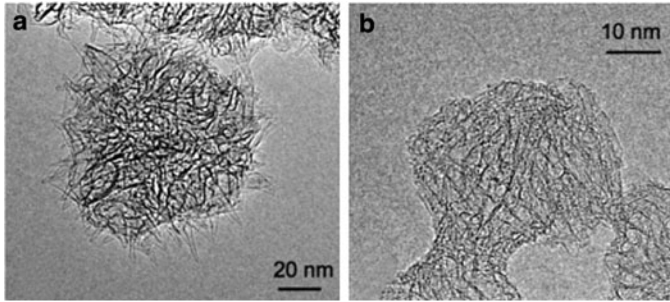

Fig. 7.21 TEM images of SWNHs synthesized using (**a**) 20 ms, 5 Hz repetition rate, and (**b**) 0.5 ms, 80 Hz laser pulses [94]

using 20 ms laser pulses at a low laser pulse repetition rate of 5 Hz and 0.5 ms pulses at 80 Hz.

7.4.7 Lasers for MEMS (Micro-Electro-Mechanical Systems)

MEMS fabrication and semiconductor industry is a very large area, searching for new technologies to assure high quality, speed, and reliability. The field of micro-electro-mechanical systems is still dominated by the silicon technology. There are also other good candidates to replace silicon as wafers like gallium arsenide, germanium, gallium phosphide, indium phosphide, sapphire, quartz etc. The laser is a very good tool for the micronanoprocessing of these materials, and also other types of materials such as metals, ceramics, and polymers can be processed.

Figure 7.22 is an example and presents a MEMS built by Sandia National Laboratories [96]. Some of the advantages of using lasers in MEMS fabrications are listed in the following:

- Reliability
- Speed
- Relatively low cost
- Selectivity (based on the fine focusing that can be achieved)

7.5 Concluding Remarks

Lasers have been demonstrated to be a clean and efficient tool to produce and/or to assist obtaining nanostructures of different materials, from simple metals to complex nanocomposites. The size, form, distribution, and density of nanostructures depend both on experimental parameters (laser wavelength, fluence and pulse duration, substrate type, and temperature) and on target material. Particles and/or nanostructures with tailored properties can be obtained by a careful control of process parameters.

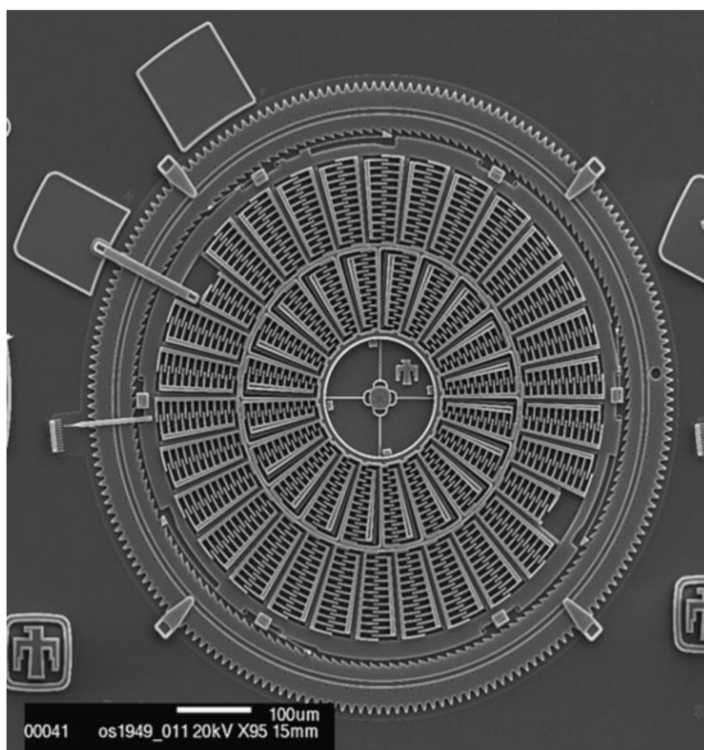

Fig. 7.22 The Torsional Ratcheting Actuator (TRA). The TRA uses a rotationally vibrating (oscillating) inner frame to ratchet its surrounding ring gear. Charging and discharging the inner interdigitated comb fingers causes this vibration (Sandia National Laboratories) [96]

NP synthesis by ns laser ablation in an ambient gas is a bottom-up strategy that is approaching the stage of designing experimental conditions to deposit on a suitable substrate arrays of dispersed NPs with predefined size and composition. Such a condition is essential to finely tune the physico-chemical properties of the NPs and those of the resulting nanostructure. Energy exchanges occurring both in the plasma and between plasma and ambient gas during plume propagation affect NP growth, besides determining the energy available to particle interaction on the substrate. Plasma interaction with ambient atmosphere is a complex gas dynamic phenomenon including scattering, slowing down, thermalization, diffusion, and recombination of the ablated particles, formation of shock waves, and particle clustering. By modeling plasma propagation, the average size of NPs grown in the plume up to their steady size can be calculated.

Ultrashort laser pulses have shown to be a conceptually simple and clean way to synthesize NPs in vacuum; the basic mechanisms of laser–matter interaction have been identified. Attention was mainly focussed onto the dependence of the different ablation mechanisms on laser fluence, yet ablation is sensitive to target

morphology, including crater formation, to the uniformity of energy distribution of the laser spot, to the size of the latter. Besides this, elemental targets were mostly investigated. Chemical effects, both concerning compound targets and interactions between plasma constituents and residual reactive gases were nearly neglected. Such topics need further investigation before fs laser ablation can be considered a reliable bottom-up strategy to prepare NP assemblies and CA films with ad-hoc designed properties.

References

1. D.B. Geohegan, A.A. Puretzky, G. Duscher, S.J. Pennycook, Appl. Phys. Lett. **72**, 2987 (1998)
2. D. Scuderi, O. Albert, D. Moreau, P.P. Pronko, J. Etchepare, Appl. Phys. Lett. **86**, 071502 (2005)
3. B. Holian, D. Grady, Phys. Rev. Lett. **60**, 1355 (1988)
4. T. Yoshida, S. Takeyama, Y. Yamada, K. Mutoh, Appl. Phys. Lett. **68**, 1772 (1996)
5. S. Eliezer, N. Eliaz, E. Grossman, D. Fisher, I. Gouzman, Z. Henis, S. Pecker, Y. Horovitz, S. Fraenckel, M. Maman, Y. Lereah, Phys. Rev. B **69**, 144119 (2004)
6. S. Amoruso, J. Schou, J.G. Lunney, Appl. Phys. A Mater. Sci. Process. **92**, 907 (2008)
7. O. Albert, S. Roger, Y. Glinec, J.C. Loulergue, J. Etchepare, C. Boulmer-Leborgne, J. Perrière, E. Million, Appl. Phys. A Mater. Sci. Process. **76**, 319 (2003)
8. X.T. Wang, B.Y. Man, G.T. Wang, Z. Zhao, B.Z. Xu, Y.Y. Zia, L.M. Mei, X.Y. Hu, J. Appl. Phys. **80**, 1783 (1996)
9. Z. Zhang, P.A. VanRompay, J.A. Nees, P.P. Pronko, J. Appl. Phys. **92**, 2867 (2002)
10. S. Noël, J. Hermann, T. Itina, Appl. Surf. Sci. **253**, 6310 (2007)
11. S.I. Anisimov, D. Bäuerle, B.S. Luk'yanchuk, Phys. Rev. B **48**, 12076 (1993)
12. Y.B. Zel'dowich, Y.P. Raizer, *Physics of Shock Waves and High-temperature Hydrodynamic Phenomena* (Academic, New York, 1966)
13. S. Amoruso, A. Sambri, X. Wang, J. Appl. Phys. **100**, 013302 (2006)
14. A.K. Sharma, R.K. Thareja, Appl. Surf. Sci. **243**, 68 (2005)
15. T.E. Itina, J. Hermann, P. Delaporte, M. Sentis, Phys. Rev. E **66**, 066406 (2002)
16. R.F. Wood, J.N. Leboeuf, D.B. Geohegan, A.A. Puretzky, K.R. Chen, Phys. Rev. B **58**, 1533 (1998)
17. G.W. Martin, L.A. Doyle, A.A. Khateeb, I. Weaver, D. Riley, M.J. Lamb, T. Morrow, C.L.S. Lewis, Appl. Surf. Sci. **127–129**, 710 (1998)
18. S.S. Harilal, C.V. Bindhu, M.S. Tillack, F. Najmabadi, A.C. Gaeris, J. Appl. Phys. **93**, 2380 (2003)
19. D.B. Geohegan, Appl. Phys. Lett. **60**, 2732 (1992)
20. J. Gonzalo, C.N. Afonso, I. Madariaga, J. Appl. Phys. **81**, 951 (1997)
21. A.V. Rode, E.G. Gamaly, B. Luther-Davies, Appl. Phys. A Mater. Sci. Process. **70**, 135 (2000)
22. P.M. Ossi, in *Laser-surface interactions for new materials production: Tailoring structure and properties*, ed. by A. Miotello, P.M. Ossi (Springer, Berlin, 2009), p. 99
23. R.F. Wood, K.N. Chen, J.N. Leboeuf, A.A. Puretzky, D.B. Geohegan, Phys. Rev. Lett. **79**, 1571 (1997)
24. V. Gusarov, I. Smurov, J. Phys. D Appl. Phys. **36**, 2962 (2003)
25. M.S. Tillack, D.W. Blair, S.S. Harilal, Nanotechnol. **15**, 390 (2004)
26. A. Peterlongo, A. Miotello, R. Kelly, Phys. Rev. E **50**, 4716 (1994)
27. A. Bailini, P.M. Ossi, Appl. Surf. Sci. **252**, 4364 (2006)
28. S. Acquaviva, M.L. De Giorgi, Appl. Surf. Sci. **186**, 329 (2002)
29. A. Quarteroni, *Modellistica Numerica per Problemi Differenziali* (Springer, Milano, 2003), p. 105

30. D. Bolgiaghi, A. Miotello, P. Mosaner, P.M. Ossi, G. Radnoczi, Carbon **43**, 2122 (2005)
31. A. Bailini, P.M. Ossi, A. Rivolta, Appl. Surf. Sci. **253**, 7682 (2007)
32. A. Bailini, P.M. Ossi, Europhys. Lett. **79**, 35002 (2007)
33. P.M. Ossi, A. Bailini, Appl. Phys. A Mater. Sci. Process. **93**, 645 (2008)
34. E. Fazio, F. Neri, P.M. Ossi, N. Santo, S. Trusso, Laser Part. Beams **27**, 281 (2009)
35. M.F. Zhou, Z.W. Fu, Q.Z. Qin, Appl. Surf. Sci. **125**, 208 (1998)
36. J.C. Orlianges, C. Champeaux, A. Catherinot, T. Merle, B. Angleraud, Thin Solid Films **453–454**, 285 (2004)
37. Y. Yamagata, A. Sharma, J. Narayan, R.M. Mayo, J.W. Newman, K. Ebihara, J. Appl. Phys. **88**, 6861 (2000)
38. C. Vivien, J. Hermann, A. Perrone, C. Boulmer-Leborgne, A. Luches, J. Phys. D Appl. Phys. **31**, 1263 (1998)
39. P. Jensen, Rev. Mod. Phys. **71**, 1695 (1999)
40. E. Irissou, B.L. Drogoff, M. Chaker, D. Guay, J. Appl. Phys. **94**, 4796 (2003)
41. R. Dolbec, E. Irissou, M. Chaker, D. Guay, F. Rosei, M.A.E. Khakani, Phys. Rev. B **70**, 201406 (2005)
42. C.N. Afonso, J. Gonzalo, R. Serna, J.C.G. de Sande, C. Ricolleau, C. Grigis, M. Gandais, D.E. Hole, P.D. Townsend, Appl. Phys. A Mater. Sci. Process. **69**, 201 (1999)
43. P.O. Jubert, O. Fruchart, C. Meyer, Surf. Sci. **522**, 8 (2003)
44. P. Ohresser, J. Shen, J. Barthel, M. Zheng, C.V. Mohan, M. Klaua, J. Kirschner, Phys. Rev. B **59**, 3696 (1999)
45. J. Gonzalo, A. Perea, D. Babonneau, C.N. Afonso, N. Beer, J.P. Barnes, A.K. Petford-Long, D.E. Hole, P.D. Townsend, Phys. Rev. B **71**, 125420 (2005)
46. W. Marine, L. Patrone, B. Luk'yanchuk, M. Sentis, Appl. Surf. Sci. **154–155**, 345 (2000)
47. A. Bailini, P.M. Ossi, Carbon **44**, 3049 (2006)
48. F. Di Fonzo, A. Bailini, V. Russo, A. Baserga, D. Cattaneo, M.G. Beghi, P.M. Ossi, C.S. Casari, A.Li. Bassi, C.E. Bottani, Catal. Today **116**, 69 (2006)
49. P.M. Ossi, A. Bailini, O. Geszti, G. Radnoczi, Europhys. Lett. **83**, 68005 (2008)
50. B. Fazio, S. Trusso, E. Fazio, F. Neri, P.M. Ossi, N. Santo, Rad. Eff. Def. Sol. **163**, 673 (2008)
51. R.W. Siegel, in *Physics of New Materials*, ed. by F.E. Fujita (Springer, Berlin, 1998), p. 66
52. D.B. Geohegan, A.A. Puretzky, Appl. Surf. Sci. **96–98**, 131 (1996)
53. D.H. Lowndes, C.M. Rouleau, T. Thundat, G. Duscher, E.A. Kenik, S.J. Pennycook, Appl. Surf. Sci. **127–129**, 355 (1998)
54. E. Fazio, F. Neri, P.M. Ossi, N. Santo, S. Trusso, Appl. Surf. Sci. **255**, 9676 (2009)
55. W.S. Rasband, ImageJ, *http://rsb.info.nih.gov/ij/* (1997–2005)
56. C.R. Henry, Surf. Sci. Rep. **31**, 231 (1998)
57. P. Mulvaney, Langmuir **12**, 788 (1996)
58. Y. Sun, Y. Xia, Science **298**, 2176 (2002)
59. R. Jin, Y.W. Cao, C.A. Mirkin, K.L. Kelly, G.C. Shatz, J.G. Zheng, Science **294**, 1901 (2001)
60. Y. Okano, K. Oguri, T. Nishikawa, H. Nakano, Appl. Phys. Lett. **89**, 221502 (2006)
61. S. Amoruso, G. Ausanio, A.C. Barone, R. Bruzzese, C. Campana, X. Wang, Appl. Surf. Sci. **254**, 1012 (2007)
62. C. Boulmer-Leborgne, B. Benzerga, J. Perrière, Proc. SPIE **6261**, 20 (2006)
63. J.V. Rau, A. Latini, A. Generosi, V.R. Albertini, D. Ferro, R. Teghil, S.M. Barinov, Acta Mater. **57**, 673 (2009)
64. C. Boulmer-Leborgne, in *Laser-surface interactions for new materials production: Tailoring structure and properties*, ed. by A. Miotello, P.M. Ossi (Springer, Berlin, 2009), p. 125
65. L.V. Zhigilei, Appl. Phys. A Mater. Sci. Process. **76**, 339 (2003)
66. K. Eidmann, J.M. ter Vehn, T. Schlegel, S. Hüller, Phys. Rev. E **62**, 1202 (2000)
67. T.E. Glover, J. Opt. Soc. Am. B **20**, 125 (2003)
68. B.J. Garrison, T.E. Itina, L.V. Zhigilei, Phys. Rev. E **68**, 041501 (2003)
69. A. Cavalleri, K. Sokolowski-Tinten, J. Bialkowski, M. Schreiner, D. von der Linde, J. Appl. Phys. **85**, 3301 (1999)
70. M.Q. Ye, C.P. Grigoropoulos, J. Appl. Phys. **89**, 5183 (2001)
71. D. Grojo, J. Hermann, A. Perrone, J. Appl. Phys. **97**, 063306 (2005)

72. T.E. Itina, K. Gouriet, L.V. Zhigilei, S. Noël, J. Hermann, M. Sentis, Appl. Surf. Sci. **253**, 7656 (2007)
73. M.E. Povarnitsyn, T.E. Itina, M. Sentis, K.V. Khishchenko, P.R. Levashov, Phys. Rev. B **75**, 235414 (2007)
74. H. Haberland, in *Clusters of Atoms and Molecules*, ed. by H. Haberland (Springer, Berlin, 1994), p. 205
75. H. Huang, H.Y. Zheng, G.C. Lim, Appl. Surf. Sci. **228**, 201 (2004)
76. C. Molpeceres, S. Lauzurica, J.J. García-Ballesteros, M. Morales, J.L. Ocaña, Microel. Eng. **84**, 1337 (2007)
77. M. Goller, N. Lutz, M. Geiger, J. Eur. Ceram. Soc. **12**, 315 (1993)
78. N.C. Nayak, Y.C. Lam, C.Y. Yue, A.T. Sinha, J. Micromech. and Microeng. **18**, 095020 (2008)
79. A.S. Holmes, Proc. SPIE, **4274**, 297 (2001)
80. D. Brodoceanu, L. Landström, D. Bäuerle, Appl. Phys. A Mater. Sci. Process. **86**, 313 (2007)
81. J. Arnold, U. Dasbach, W. Ehrfeld, K. Hesch, H. Löwe, Appl. Surf. Sci. **86**, 251 (1995)
82. K. Minami, Y. Wakabayashi, M. Yoshida, K. Watanabe, M. Seashi, J. Micromech. Microeng. **3**, 81 (1993)
83. M.D. Armacost, S.V. Babu, S.V. Nguyen, J.F. Rembetski, J. Mater. Res. **2**, 895 (1987)
84. B.K. Nayak, M.C. Gupta, K.W. Kolasinski, Appl. Surf. Sci. **253**, 6580 (2007)
85. J. Röder, J. Faupel, H.U. Krebs, Appl. Phys. A Mater. Sci. Process. **253**, 863 (2008)
86. P.V. Ashirt, G. Bader, V. Truong, Thin Solid Films **320**, 324 (1998)
87. Z. Xu, J.F. Vetelino, R. Lec, D.C. Parker, J. Vac. Sci. Technol. A **8**, 3634 (1990)
88. M. Filipescu, P.M. Ossi, M. Dinescu, Appl. Surf. Sci. **254**, 1347 (2007)
89. N. Wang, Y. Cai, R.Q. Zhang, Mat. Sci. Eng., R **60**, 1 (2008)
90. A.M. Morales, C.M. Lieber, Science **279**, 208 (1998)
91. C.N. Hunter, M.H. Check, J.E. Bultman, A.A. Voevodin, Surf. Coat. Tech. **203**, 300 (2008)
92. A.P. Caricato, S. Capone, G. Ciccarella, M. Martino, R. Rella, F. Romano, J. Spadavecchia, A. Taurino, T. Tunno, D. Valerini, Appl. Surf. Sci. **253**, 7937 (2007)
93. Z. Liu, D.J. Styers-Barnett, A.A. Puretzky, C.M. Rouleau, D. Yuan, I.N. Ivanov, K. Xiao, J. Liu, D.B. Geohegan, Appl. Phys. A Mater. Sci. Process. **93**, 987 (2008)
94. A.A. Puretzky, D.J. Styers-Barnett, C.M. Rouleau, H. Hu, B. Zhao, I.N. Ivanov, D.B. Geohegan, Appl. Phys. A Mater. Sci. Process. **93**, 849 (2008)
95. A.A. Puretzky, H. Schittenhelm, X. Fan, M.J. Lance, L.F. Allard Jr, D.B. Geohegan, Phys. Rev. B **65**, 245425 (2002)
96. *http://mems.sandia.gov/gallery/images_torsional_ratcheting_actuator.html*

Chapter 8
Laser Micromachining

Jürgen Ihlemann

Abstract This chapter deals with the laser-based fabrication of surface structures by ablative material removal. Only microstructures with typical dimensions ranging from 100 to 1 mm are treated here. Only the use of pulsed lasers, mainly in the nanosecond pulse duration regime, is described, for fs-laser micromachining see Chap. 6. Only technical materials are treated, not biological material.

8.1 Basic Considerations

Laser micromachining of materials is used here in the sense that a laser beam is directed onto a solid material in a specific manner, so that controlled material removal takes place leading to a functional surface or 3D pattern. While the fundamentals of laser-material interactions are described in Chap. 3, we concentrate here more or less on a phenomenological description of the various irradiation concepts and the resulting surface structure or surface shape. As sufficient optical absorption is the main prerequisite of precise ablative laser processing, in most cases UV-lasers are applied. The short wavelength serves for high optical resolution at the same time.

8.2 Processing Limits

Micromachining by ablative removal of material is characterized by a threshold fluence F_{T}, i.e., the minimum energy per area that is required to start ablation, and the fluence dependent ablation rate $d(F)$, i.e., the ablation depth per laser pulse. If it is assumed that ablation takes place to that depth where the fluence has decreased

J. Ihlemann
Laser-Laboratorium Göttingen e.V., Hans-Adolf-Krebs-Weg 1, 37077 Göttingen, Germany
e-mail: juergen.ihlemann@llg-ev.de

to F_T due to absorption according to the Lambert Beer law, the ablation rate should behave like:

$$d(F) = \alpha^{-1} \log(F/F_T) \tag{8.1}$$

with the absorption coefficient α.

This behavior is approximately observed for strongly absorbing polymers like polyimide, but it does not hold for materials that change their absorption due to irradiation. This change can be a permanent increase because of chemical modification of the material or color center formation leading to the so called incubation behavior, or a transient change due to the formation of transient species with different absorption. In these cases often an effective absorption coefficient α_{eff} is defined, which is derived from the experimentally measured ablation curve $d_{\text{exp}}(F)$ according to:

$$\alpha_{\text{eff}} = d_{\text{exp}}^{-1} \log(F/F_T). \tag{8.2}$$

The structure resolution which can be reached by laser micromachining is limited on the one hand by the resolution of the light intensity profile on the surface (optical resolution) and on the other hand by the thermal distribution of the absorbed energy on the time scale of the pulse duration (thermal resolution). The optical resolution is given by:

$$A = \frac{\lambda}{2NA} \tag{8.3}$$

with the laser wavelength λ and the numerical aperture NA of the optical system used for the irradiation. Thus, the optical resolution can be improved by choosing a shorter wavelength and/or using a lens with larger numerical aperture. However, the numerical aperture influences the depth of focus DOF according to

$$DOF \sim \frac{\lambda}{NA^2}, \tag{8.4}$$

so that a higher NA leads to strongly increasing requirements concerning the 'z-positioning' of the surface to be machined. Therefore, the generation of small structures with high aspect ratio (ratio depth over lateral width) is rather difficult. For such deep holes, effects like *light channelling* have to be utilized.

The resolution limit given by thermal spreading of the absorbed energy is given by the heat diffusion length

$$L = 2(D\tau)^{1/2} \tag{8.5}$$

with the laser pulse duration τ and the thermal diffusivity D given by $D = \kappa\rho c_p$ (κ thermal conductivity, ρ density, c_p specific heat capacity of the irradiated material).

In Table 8.1 the excimer laser ablation rates (ablation depth per pulse) are listed for some often used materials. The data are given for pulse lengths of about 10–30 ns and laser spot diameters of the order of 100 μm. Actually, the ablation rate depends on these parameters, too. Especially at high fluences (5 J/cm^2 is already high in that sense), the ablation rate increases with growing pulse duration and with diminishing

Table 8.1 Ablation rates in nm/pulse of various materials at specific laser wavelengths at 5 J/cm^2

Material	157 nm	193 nm	248 nm	308 nm
Polyimide (PI)		200 [1]	650 [2]	1,150 [2]
Polymethylmethacrylate (PMMA)		500 [1]	4,000 [2]	
Polycarbonate (PC)			650 [3]	1,100 [3]
Polytetrafluoroethylen (PTFE)	600			
SF11-glass		140 [4]	170 [4]	
BK7-glass		170 [4]	600 [4]	
Fused silica	100 [5]	200 [6]	1,800 [6]	–
Al_2O_3-ceramic		30 [7]	100 [8]	230 [8]
MgO-ceramic			110 [8]	50 [8]
Copper			80 [9]	
Aluminium		800 [10]		
Molybdenum			30	

spot size [11, 12] due to the screening of the expanding product plume. Most of the lasers used for micromachining operate with ns-, ps-, or fs-pulses. There are two reasons for choosing ultrashort pulses: to increase the absorption by nonlinear effects and to reduce the heat affected zone (HAZ). Whereas a fs-pulse duration is required for efficient multiphoton absorption to treat transparent materials, for the reduction of unwanted heat effects like melt rims, the use of picosecond pulses seems to be sufficient. Ultrashort pulse processing is treated in a separate chapter. The wavelengths used for micromachining are in the range from vacuum ultraviolet (157 nm) to infrared (1,064 nm). CO_2-lasers with longer wavelengths (10.6 μm) are mainly used for macromachining, because the optical resolution does not allow shaping on the μm-scale. Beam delivery is accomplished either by direct spot writing or by mask projection.

8.3 Materials and Processes

8.3.1 Polymers

Organic polymers are well suited materials for UV-laser micromachining. Especially, polymers containing aromatic constituents (polyimide, polycarbonate, polyethersulfone, polyethylene-terephthalate (PET)) absorb very well in the near UV. Their threshold fluence is rather low; ablation can be easily performed at 248, 266, 308, or 351 nm wavelength. Polymers with linear chains without aromatic ring systems (polymethylmethacrylate (PMMA), polyethylene (PE)) have an absorption edge in the deeper UV, so that a wavelength of 193 nm is required for clean ablation. For fluorocarbon polymers like polytetrafluoroethylen (PTFE) even shorter wavelengths, e.g., 157 nm have to be applied (Fig. 8.1). Some new polymer materials have been specially developed for excellent 308-nm ablation performance (Fig. 8.1).

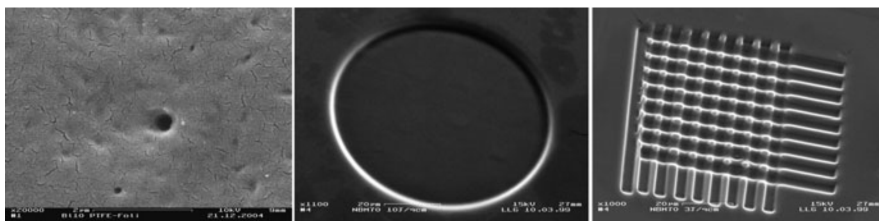

Fig. 8.1 Nanohole in PTFE ablated at 157 nm [13] (*left*) and ablation patterns in arylazophosphonate containing polymers designed for XeCl laser ablation [14] (*center, right*)

Photoablation of polymers has often been termed a ‘cold’ process, because in many cases very sharp contours with no evidence of heat effects are obtained. This does not mean that the ablated material remains cold, but because of the low thermal conductivity of the polymeric material and the efficient eduction of the absorbed energy with the ablation products, the heat effect on the remaining material is limited. Some weakly absorbing polymers exhibit a so called ‘incubation behavior.’ This means that the first few pulses do not lead to substantial ablation but to a material modification that leads to stronger absorption and substantial ablation for following pulses at the same site [15]. Even for fluences below the ablation threshold these changes may occurs. For instance, the transmission of a 40 μm thick PMMA film irradiated at 248 nm and a fluence of 40 mJ/cm^2 drops to 6% of its initial value after 1,000 pulses.

At high fluences the influence of the product plume on the ablation result becomes significant. The trailing part of a nanosecond pulse is already absorbed in the material cloud generated by the beginning part of the same pulse [2]. This leads to a saturation of the ablation rate with further increasing fluence. Furthermore, because of the 3D-expansion characteristics of the plume, the ablation rate depends on the lateral dimensions of the laser spot. A smaller spot will lead to a larger ablation rate at the same fluence. This means that even a completely homogeneous illumination of the mask in a mask projection set-up may lead to different ablated depths for different geometrical features. Similarly, changes of the pulse duration in the nanosecond regime lead to variations of the ablation depth. For instance, the ablation depth of polyimide at a laser wavelength of 248 nm and a fluence of 10 J/cm^2 amounts to 0.75 μm/pulse for a pulse duration of 20 ns, and 1.9 μm/pulse at 230 ns [2]. This can be explained by a more pronounced plume absorption in the case of shorter pulses, when the time is not sufficient for lateral dilution of the product plume.

The redeposition of ablated products (debris), which is very undesirable for most micro machining applications, can be diminished by choosing the adequate fluence. For the KrF-laser ablation of polyurethane for instance, at 100 mJ/cm^2 a lot of debris is deposited around the ablation holes. At 200 mJ/cm^2 the generated debris is greatly reduced, presumably because of the stronger fragmentation of the ablated polymer material into volatile, small molecular-weight compounds [16]. The distribution of surface debris can be further influenced by the ambient atmosphere. Lower pressure

leads to a wider, but more dilute distribution of the debris [17]. Similarly, ambient gases of low molecular weight (e.g., He) lead to a strong reduction of at least nearby debris.

The wall angle of laser generated holes or channels plays an important role for many micro machining applications. As a general rule, a higher fluence leads to a steeper wall. But in detail the wall angle can be tuned by choosing the effectively used numerical aperture of the optical system. This way even negative wall angles are possible [18]. Holes with very steep wall angles and consequently a high aspect ratio (depth over diameter) of 600 have been obtained by KrF-excimer laser ablation in various polymers like PMMA or polycarbonate [19].

8.3.2 Glass

Phenomenologically, glasses behave similar to organic polymers. Strongly absorbing glasses allow smooth ablation at low fluences, especially at 193 nm [20]. Lead glass can be machined also at 248 nm or even 308 nm [21]. CO_2-lasers can be used for polishing of lead glass [22]. But many glasses with low absorbance require high fluences to overcome the dielectric breakdown threshold. Often, in analogy to the incubation behavior of polymers, a two phase behavior with low ablation rate for the first pulses and increase of the ablation rate due to accumulation of absorbing defects is observed [6]. For highly transparent glass materials another interesting phenomenon has been observed. As the laser damage threshold at a surface is generally lower, when the beam propagates from a high refractive index material (glass) to a low refractive material (air) then the opposite way [23], a hole can be drilled from the backside into the material. There is practically no bulk absorption, ablation is initiated by rear surface absorption and continues because of the accumulation of surface defects at this rear surface. This behavior has been observed in the case of fused silica for UV-lasers [6] as well as for near-IR-lasers [24].

For extremely UV-transparent glasses like fused silica, irradiation at 193 nm leads to cracking, so that irradiation at 157 nm is required to obtain precisely machined structures (Fig. 8.2) [25]. The ablation rate can be precisely tuned between 10 and 100 nm per pulse by choosing a fluence between 1 and 10 J/cm^2, and a surface roughness of 5–15 nm rms can be achieved [5]. A 157 nm is also used to obtain smooth ablation of N-BK7 glass [26].

An important feature of glass processing is the remaining surface roughness at the bottom of ablated spots or channels. In case of ArF-laser processing of borocilicate glass (Pyrex) roughness values of $R_a = 35 \ldots 150$ nm have been obtained, depending on fluence and irradiation procedure [28].

8.3.3 Ceramics

Many ceramic materials like alumina (Al_2O_3) or magnesia (MgO) have also weak UV-absorbance. Their sintered grain structure leads to light scattering and increased

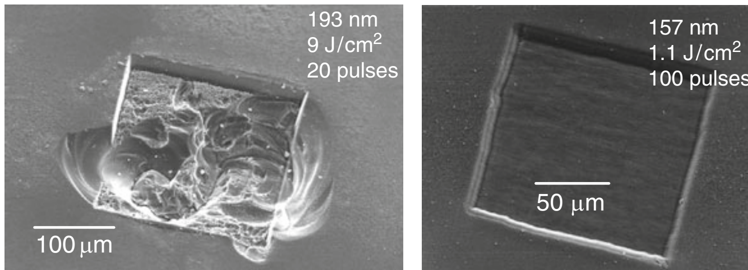

Fig. 8.2 Fused silica ablated at 193 nm and at 157 nm [27]

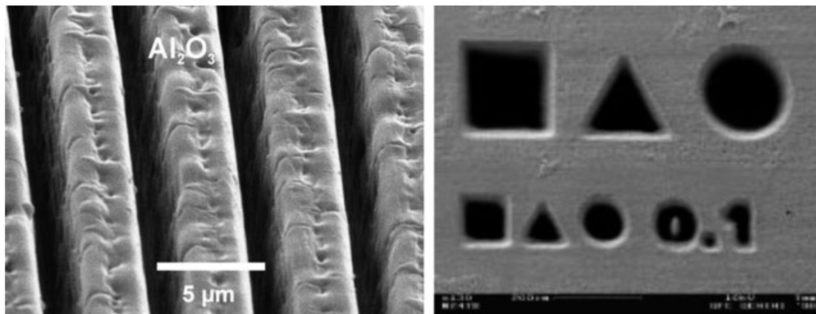

Fig. 8.3 Line pattern machined in alumina ceramic with an ArF-excimer laser [7] (*left*). Microgeometries in SiC structured with a frequency tripled YAG-laser at 355 nm [31] (*right*)

defect density compared to single crystals. High fluences (> 1 J/cm^2 at 248 nm) are necessary to obtain ablation. A plasma mediated process is observed leading to smoothing of the surface (Fig. 8.3). This plasma mediated process has been observed also for single crystal MgO [29]. Stronger absorbing nitride materials (Si_3N_4) exhibit a somewhat lower ablation threshold (< 1 J/cm^2 at 248 nm), but precise patterning is possible only at high fluences, too [30]. Precise ablation of SiC and Si_3N_4 is possible also with YAG-lasers, either at the fundamental wavelength or at the second or third harmonic [31] (Fig. 8.3). The roughness of side walls in the case of IR-laser (CO_2 and YAG) processing is significantly larger than that for excimer laser processing [32].

8.3.4 Metals

Metals exhibit high reflectivities and low penetration depths. UV-lasers are applied, because the reflectivity decreases in the UV. The penetration depth is still limited to a few 10 nm; but because of heat conduction the absorbed energy is transferred into deeper regions and the ablation rate can significantly exceed the optical absorption length. On the other hand, the high thermal conductivity leads to noticeable melt effects (Fig. 8.4) like burrs around ablated areas [33]. These observations suggest

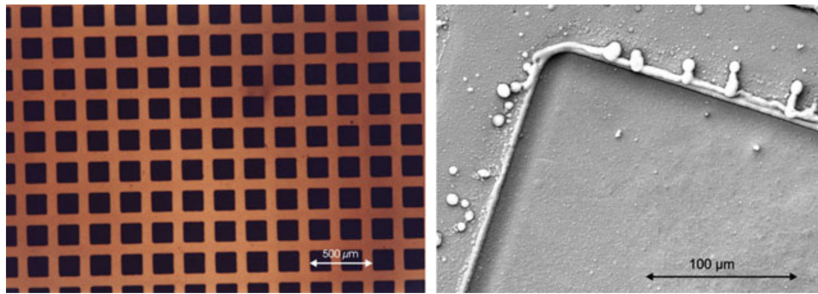

Fig. 8.4 Copper grid on fused silica made by laser micromachining, thickness of the copper layer: 500 nm; laser parameters: 193 nm, 450 mJ/cm^2, 5 pulses. (*Left*: optical microscopy, *right*: scanning electron microscopy)

strong hydrodynamic contributions to the ablation process of metals even in the UV (248 nm) [9]. The importance of the absorption and heating of the plasma plume has been pointed out [34, 35].

8.3.5 Layer Ablation

In addition to bulk micro machining, laser ablation can be used for the patterning of thin films. If the threshold fluence of the film material is significantly lower than that of the substrate material, it is easy to remove the film without damaging the substrate. This is the case for polymer films on metal or glass substrates. The substrate acts as stop layer and the process can be controlled easily, as some excessive pulses do not alter the result. On the other hand, the removal of a metal film from a polymer substrate requires more controlled conditions to avoid substrate damage [36]. In addition, it has to be taken into account, that the ablation threshold of metal films depends on the film thickness, if nanosecond laser pulses are applied [37]. This is caused by the high thermal conductivity of the metal, which serves for a rapid thermal spreading of the absorbed energy over the whole film thickness, so that thicker films get less heated compared to thinner films at the same laser fluence. The achievable resolution is limited by *edge curling* effects [38].

If the substrate is transparent at the laser wavelength, in addition to the standard *front side ablation* also a *rear side ablation* configuration is possible [39]. This means that the laser beam is absorbed in the film after passing through the transparent substrate. Fused silica substrates are sufficiently transparent to enable rear side ablation with wavelengths in the whole UV and visible range above 190 nm. For near UV and visible lasers, even other glass substrates can be applied (BK7); rear side ablation using a 157 nm-laser has been demonstrated with CaF_2-substrates [40]. If the layer system to be patterned is transparent at the laser wavelength, an underlying absorber layer can be applied, which enables rear side ablation, but does not obstruct the functionality [e.g., of a mirror layer system used in a front side application (Fig. 8.5)].

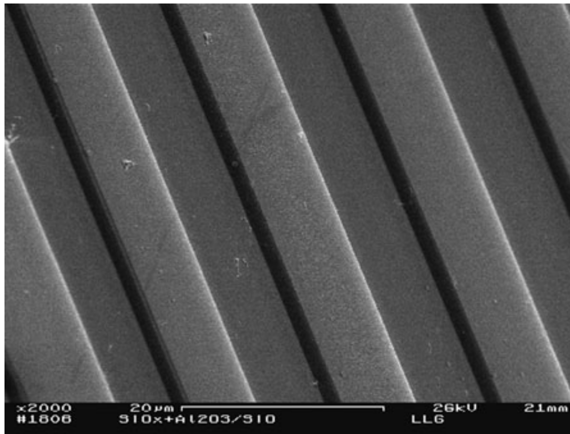

Fig. 8.5 Single pulse rear side ablation of a Al_2O_3/SiO_2-multilayer dielectric coating with underlying SiO-absorber layer on fused silica, ArF-excimer laser, 500 mJ/cm^2 [41]

8.3.6 Indirect Ablation

There are several methods of laser machining, where the laser radiation is not directly coupled into the material to be ablated, but by means of an auxiliary absorber material. This is particularly of interest, if the material is transparent at the ablation wavelength. Then the laser light can be delivered to the absorber (instead of directly to the workpiece to be machined), leading to various kinds of indirect ablation:

In the case of "laser induced backside wet etching" (LIBWE) [42] the backside of the sample to be machined is in contact with an absorbing liquid, which may be an alcoholic or aqueous solution of a dye absorbing at the laser wavelength. The energy is coupled into the rear surface of the workpiece by heating this absorber liquid. This method was successfully applied to pattern fused silica, crystalline quartz [43], and sapphire [44]. The etch rate is rather low compared to direct ablation, but this enables the precise depth profiling. Structure resolution down to 1 micron has been achieved. The main advantage of this method is, that the laser wavelength does not have to be adapted to the material to be machined, but only to the absorbing dye, so that the rather convenient wavelength 308 nm can be used for glass machining.

Another method is based on non permanent, but laser induced indirect absorption. In this process called 'laser-induced plasma-assisted ablation' (LIPAA) [45], a metallic sample is positioned behind the transparent workpiece (e.g., fused silica). The laser pulse causes a plasma plume expanding from the metal to the backside of the workpiece, which is then able to absorb light via the deposited metallic layer.

Especially for the micro machining of fused silica a variety of methods has been developed to overcome the problem of insufficient absorption. An overview on direct and indirect methods is shown in Table 8.2.

Table 8.2 Direct and indirect ablation methods for micromachining of fused silica

Method	Type	Mode of operation	References
DUV (193 nm)	Direct	(Surface-) Defect absorption	Ihlemann et al. [6]
VUV (157 nm)	Direct	Near bandgap absorption	Herman et al. [5]
Soft x-ray (10 nm)	Direct	Laser plasma soft x-rays	Makimura et al. [46]
Multiwavelength	Direct	VUV → transient absorption UV → ablation	Sugioka et al. [47]
Femtosecond	Direct	Multiphoton absorption	Varel et al. [48] Krüger et al. [49]
LIBWE	Indirect	Laser induced backside wet etching	Wang, Niino, Yabe [42]
LIPAA	Indirect	Laser induced plasma assisted ablation	Zhang, Sugioka et al. [45]
LESAL	Indirect	Laser etching at a Surface Adsorbed Layer	Zimmer et al. [50]
LIBDE	Indirect	Laser induced backside dry etching	Hopp et al. [51]

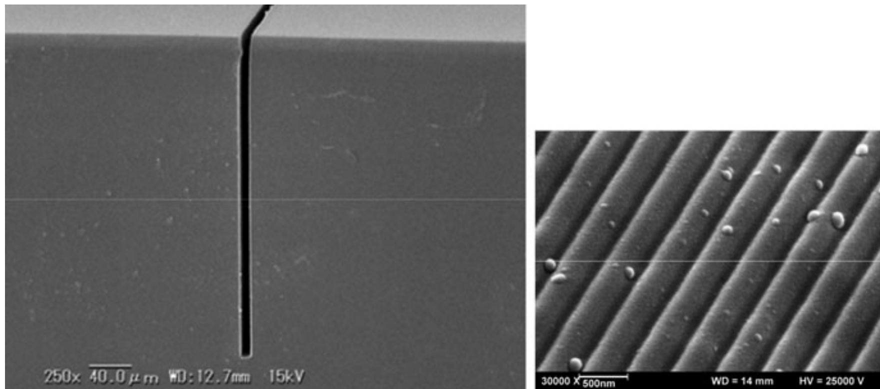

Fig. 8.6 Deep trench in silica glass fabricated by the LIBWE method; laser: 248 nm, 1 J/cm^2, 20,000 pulses (*left*) [53]. 400 nm-line pattern in fused silica made by solid-coating-absorption-mediated ablation; laser: 193 nm, 16 J/cm^2, 1 pulse (*right*) [52]

The absorbing medium for indirect ablation does not have to be a liquid. Good results have also been obtained by using adsorbed layers [50] or, for single pulse machining, metal [51] or dielectric [52] absorber layers. Whereas LIBWE seems to the optimum choice for generating deep trenches with high aspect ratio [53] (Fig. 8.6), LIBDE is more appropriate to obtain either high resolution or a large single pulse ablation rate [52, 54].

8.4 Hole Drilling

The straightforward application of laser ablation in micromachining is hole drilling. In the simplest form it is accomplished by focusing a laser beam onto the workpiece and applying as many pulses as required to obtain a via hole (through hole) or a pocket hole (blind hole). With this method a reasonable quality of the holes is obtained only, if a Gaussian laser beam is used, e.g., in the case of solid state lasers (YAG). In the case of flat top beam profiles (excimer laser), perfect quality can be achieved by mask imaging. Depending on laser energy, size of the hole and material, one hole at a time is made with a pinhole mask, or parallel processing of a multihole pattern is performed using a complex multihole mask. For comparatively large hole diameters, alternatively to this percussion mode (laser spot is fixed with regard to the work piece), the trepanning mode can be applied, where the laser spot is guided on a circle, so that a disc is cut out of the work piece. This is already the route to laser cutting, which is more or less a macromachining process and is not treated here.

An important application of micro hole drilling is the fabrication of nozzle plates for ink jet printers. In a standard process, several rows of holes are drilled simultaneously using an excimer laser and a mask projection system. These holes in polyimide have diameters of about 10–50 μm. In such configurations, it has to be taken into account, that even in the case of homogeneous illumination, nonuniform hole depths are obtained due to geometrical effects of the plume shielding [55]. Depending on the required geometries, materials and hole dimensions, holes in multilayer printed circuit boards are made by excimer laser drilling [56], or for instance in a combined process, where copper layers are drilled with a frequency tripled YAG-laser and the intermediate dielectric layers are removed by a CO_2-laser [57]. Using CO_2-lasers, hole dimensions down to 10 μm are possible in polyimide and glass material [58].

Also in semiconductor device fabrication and production of photovoltaic devices there are several applications of hole drilling. One example is the drilling of silicon carbide wafers [59]. Using a frequency tripled diode pumped solid state laser at 355 nm, through and blind holes of 60 μm diameter with aspect ratios of 5–6 have been obtained (Fig. 8.7). For the back contacting of solar cells, processes with parallel drilling of up to 5,000 holes using 1,047 nm-laser radiation have been developed [60].

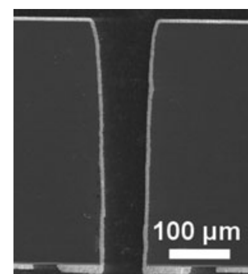

Fig. 8.7 355 nm-laser drilled hole in SiC after etching and metallization [59]

Fuel injection nozzles in steel for gasoline or Diesel engines with typical diameters of around 100 μm are made mainly by diode pumped YAG-lasers, either with the fundamental wavelength or using the second or third harmonic [61,62]. Not only size reduction but also specifically shaped holes (tapers) are of interest.

Other applications of laser hole drilling are in the biomedical field. One example is the fabrication of nozzles for the so called pulmonary drug delivery. These nozzles often have to be strongly conical with an exit diameter of about 1 μm. Excimer lasers are used to fabricate such disposable nozzle plates [63].

8.5 Patterning of Thin Films

Applications of thin film patterning include the fabrication of thin film photovoltaic cells (CIS, amorphous silicon) and flat panel displays (ITO patterning) [64]. Excimer laser patterning of Cr films on glass substrates has been investigated [65] and applied to the fabrication of Cr-masks [66, 67].

One micron thick TiN coatings on steel have been patterned using a Nd:YAP laser at 1,078 nm and at its second and third harmonic [68]. Microcraters with diameters of 3–5 micron and 1 micron depth have been obtained at all three wavelengths. By generating such microcrater arrays, the durability of lubricated sliding could be increased by 25% compared to that of the original TiN film.

By micropatterning diamond films with Nd:YAP (1,078 nm) and KrF-excimer lasers, IR-antireflection coatings could be machined [69]. The patterns consist of hole arrays or grooves with 3 micron period.

8.5.1 Dielectric Masks

A number of studies have been performed to investigate the microfabrication of masks and diffractive phase elements by laser patterning of dielectric layers. A typical application for the patterning of multilayers for optical applications is the fabrication of dielectric optical masks. Dielectric masks can be applied for high-intensity laser applications, where metal masks (Cr on quartz) would be easily damaged [70]. Multilayer stacks of alternating high refractive index and low refractive index (HfO_2/SiO_2) can be ablated by an ArF-excimer laser, because HfO_2 is absorbing at 193 nm. Although the thickness of the film is more than 1 μm, under certain conditions sub-μm edge definition is achieved in the case of rear side ablation [71].

If both materials of the dielectric layer stack are transparent at 193 nm, the ablation of these systems has to be performed either at even shorter wavelengths (Vacuum-UV) [72] or with an absorbing subsidiary layer. Thus, dielectric mirrors with high reflectivity at 193 nm consisting of a stack of alternating SiO_2- and Al_2O_3-layers were patterned by depositing a 193 nm-absorbing HfO_2- or SiO-layer

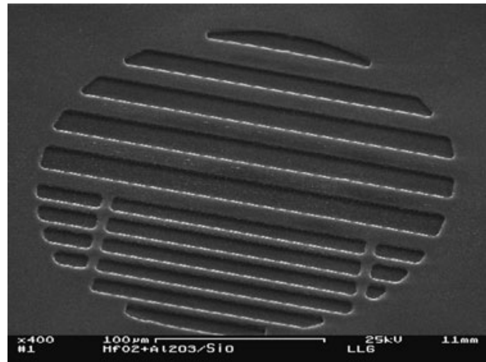

Fig. 8.8 Dielectric mask fabricated by single pulse rear side ablation of a Al_2O_3/SiO_2-multilayer dielectric coating with underlying HfO_2-absorber layer on fused silica, ArF-excimer laser, 1.3 J/cm^2 [73]

between substrate and HR-stack and ablating in a rear side configuration [73] (Fig. 8.8). It is even possible to fabricate grey level masks by ablating only a defined number of single layers instead of the whole stack [74]. As this process works only by front side ablation, the edge definition of the ablated structures is limited.

8.5.2 Diffractive Optical Elements

Laser film patterning is the ideal method for the flexible generation of diffractive optical elements (DOE). Specifically, diffractive phase elements (DPE) enable the generation of complex irradiation patterns without substantial optical system energy losses. In many cases a computer generated two-dimensional phase function is transferred into an optically effective phase controlling element by fabricating a surface relief on a transparent substrate.

Diffractive optical elements can be characterized as amplitude or phase elements. The simplest phase element to be used at a wavelength λ is a binary surface relief structure on a material of refractive index n with a depth modulation of $d = \frac{\lambda}{2(n-1)}$. Lateral structure dimensions are of the order of a few microns depending on the optical configuration and the coherence parameters of the light for which the DOE is designed. For a DOE made of a polymer material, to be used in the visible spectral range, surface structures with a depth of about 0.5 micron and lateral dimensions of 5 micron are required. These dimensions are easily accessible by excimer laser ablation. Some attempts have been made to fabricate DOEs by laser ablation, either on the basis of pixel by pixel irradiation [75,76] or image based using chrome masks [77]. Multilevel DOEs could be produced in polymers by excimer laser ablation using a half tone mask [78]. DOEs that can be used for UV laser applications require the processing of fused silica or other materials with high UV transmission. Such DOEs have been fabricated on the basis of dielectric mask projection [79].

For the fabrication of diffractive phase elements from SiO_2 without the need of direct ablation of fused silica the following three-step-method has been suggested [81]: (1) A UV-absorbing coating of silicon monoxide (SiO) is deposited on a fused

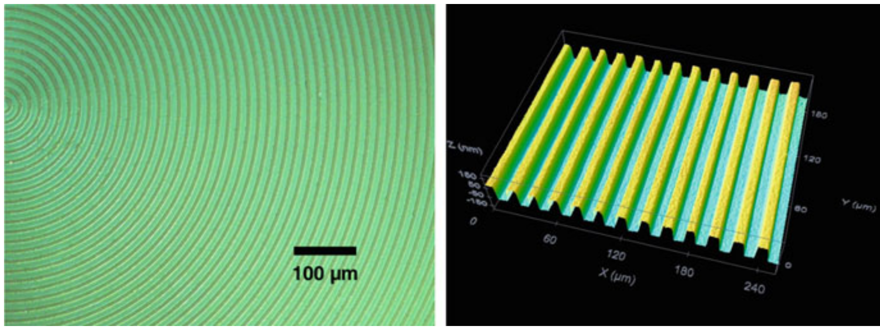

Fig. 8.9 Diffractive phase elements made by rear side ablation of SiO layers and subsequent oxidation [80]

silica substrate. (2) The SiO-coating is patterned by excimer laser ablation to form the desired phase structure. (3) The SiO-material is oxidized to UV-transparent silicon dioxide (SiO_2). Phase elements fabricated with this method are shown in Fig. 8.9.

8.6 Fabrication of Micro Optics and Micro Fluidics

One large field of laser micro machining is that of generating micro optical structures. This is understandable, because the precision or resolution required here matches roughly the ultimate precision or resolution which is possible with standard light-based manufacturing processes, both given by the wavelength scaled with a factor of the order of 1. This led to a variety of processes for fabricating optical components like micro lenses, gratings, or complex diffractive structures.

8.6.1 Gratings

Laser micromachining of optical grating structures has been a subject of study for a long time. This work aimed either at the demonstration of high resolution capability of the ablation process or at the fabrication of real gratings to be used, e.g., as coupling gratings for planar waveguides. The spatially periodic intensity pattern needed for the generation of a (one dimensional) periodic surface structure with a periodicity of the order of the wavelength of light can be understood generally as the consequence of the interference of two beams. Several optical arrangements are possible: The interfering beams may be generated by a partially reflecting beam splitter or by a diffractive beam splitter and recombined either by using beam superposition in a Talbot interferometer [82, 83] or by imaging methods, using, e.g., a Schwarzschild type objective [27]. Depending on a specific configuration, the coherence properties of the applied laser radiation may be crucial for the development of

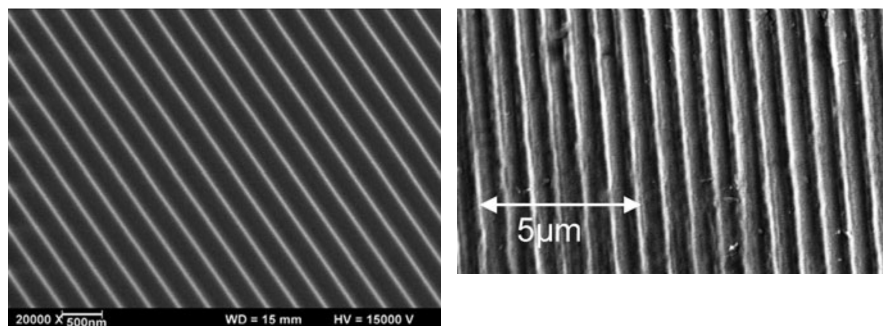

Fig. 8.10 331 nm-period grating in polyethersulfone fabricated using a KrF-laser in combination with a two grating interferometer [84] (*left*). 800 nm-period-grating in fused silica made by F_2-laser ablation [66] (*right*)

the periodic patterns. An arrangement of two gratings, where the second grating recombines the ± first diffraction orders generated at the first grating, allows for efficient submicron patterning with high contrast even with only partially coherent laser light [84].

Such grating designs are used in several micro-optic applications such as grating demultiplexers for telecommunication components, light couplers for planar optical waveguides, Bragg reflectors, and alignment grooves for liquid crystals [85, 86]. Submicron periodic structures, which are required for ultraviolet, visible, and near-infrared spectral applications, have been structured by UV-laser ablation with nanosecond (ns) duration pulses on polymer [87–90] and borosilicate glass [91] surfaces. For the fabrication of gratings on metals or crystalline optical materials femtosecond excimer lasers, for the treatment of weakly absorbing materials like fused silica [66] or metal oxide waveguides [92], F_2-lasers have been applied (Fig. 8.10).

8.6.2 *Micro Lenses*

It is very attractive to fabricate micro lenses by laser ablation, because, if the basic problems of creating a smooth, three dimensional surface in an optical material are solved, a great variety of lens shapes should be possible (aspheric etc.). The processing of cylindrical lenses is rather straightforward, if a flexible mask technology is applied [7] (Fig. 8.11). In the case of processing glass, the ablation debris is one of the major problems, which can be solved by ablating in a vacuum or by applying additional cleaning procedures. For the generation of spherical lenses, an approach based on scanning a polymer surface with an excimer beam along well-chosen multiple concentric contours was applied [93, 94]. This way microlenses of arbitrary shape can be realized. Lens arrays could be fabricated by the so

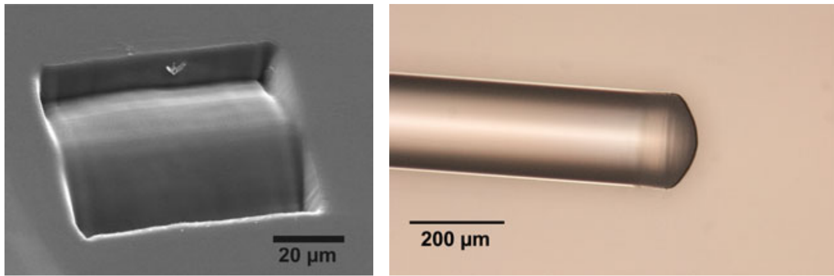

Fig. 8.11 Cylindrical microlens fabricated in BK7-glass at 193 nm with a variable mask technique [7] (*left*). Lens machined at a fused silica fiber tip by 157-nm-ablation [99] (*right*)

called synchronized-image-scanning (SIS) in combination with half tone masks [95]. Besides the fabrication of refractive lenses, also the machining of diffractive (Fresnel-type) lenses in polymers [96] and glasses [97] has been demonstrated.

There have been made some attempts to integrate microlenses in optical fiber tips by laser machining. Using a CO_2-laser the processing is more or less based on a defined melting process [98]. For precise shaping of fused silica fibers, a VUV-laser emitting at 157 nm has to be applied. Two different techniques for the fabrication of microlenses directly on the end face of multimode silica fibers have been demonstrated using a F_2-laser processing station [99]. The first method is based on a mask projection arrangement perpendicular to the fiber axis. The fiber is rotated axially while the laser cuts through the fiber, yielding a spherically shaped tip with radius defined by the mask dimensions (Fig. 8.11). For the second technique, a uniform ablation spot is projected onto the fiber end face in axial direction and steered along a trajectory of overlapping concentric circles. The lens profile is controlled by the spot size, the number of circles in the trajectory, and the scanning speed. Strong 157 nm absorption by the silica glass facilitates precise structuring without microcrack formation in both cases. The surface quality of the fiber-lenses is characterized by $\sim$40 nm rms roughness with good control of the surface profile. Optical beam profiling indicates the possibility for creating spot sizes of $1/5$ the core diameter at the fiber output. Good results have been obtained also for processing single mode fibers [100].

8.6.3 *Micro Fluidics*

To machine microfluidic devices, several aspects of channel fabrication and surface texturing have been investigated. Using ArF-excimer lasers, channels or channel systems with typical dimensions of 10–50 μm in depth and width were made in polymers [101, 102] and borosilicate glass [103] (Fig. 8.12). Even in fused silica microchannels could be fabricated using a laser wavelength of 193 nm [7]. Though with a Nd:YAG laser at 355 nm smooth channels in glass without cracks could be

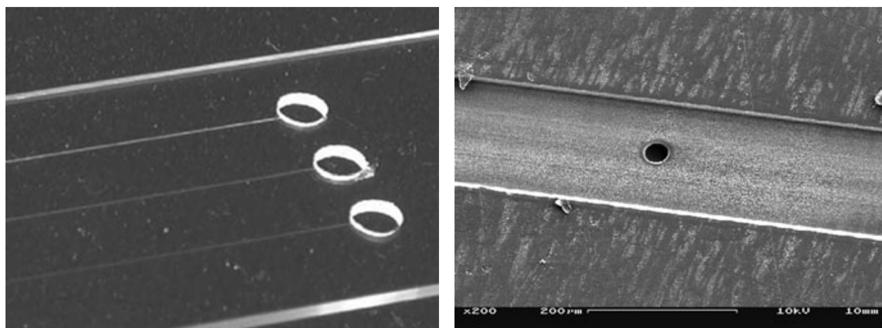

Fig. 8.12 Microchannel systems machined in glass with an ArF-laser (*left*) and in Teflon using a F_2-laser [13] (*right*)

obtained under well controlled conditions [104], and even at 532 nm the cutting of borosilicate glasses is possible [105], for the fabrication of precise grooves in weakly absorbing glasses the use of a F_2-laser seems to be more appropriate [106]. Microfeatures produced in N-BK7-glass using a F_2-laser have been replicated by polydimethylsiloxane (PDMS) moulding [107]. The obtained stamps have been used then to print arrays of fluorescent molecules with submicron fidelity. Hole arrays ablated in BK7 have been used to fabricate microneedle arrays by micromolding [20]. Such needle arrays are used in biomedical applications like gene and drug delivery.

To obtain microchannels in quartz glass with a nanosecond 1,064-nm-YAG-laser, very high laser fluences (up to 600 J/cm^2) have been applied to perform laser induced plasma processing [108].

8.7 Conclusions

Micromachining by laser ablation is a versatile tool for the generation of surface patterns and three-dimensional structures. Processing of any kind of technical materials like polymers, glass, ceramics, and metals is possible. Laser wavelength and pulse duration have to be adapted to the specific material and processing task. For precise machining of transparent materials the use of deep UV or vacuum UV wavelengths is ideal; for high-resolution patterning of metals ultrashort pulse lasers (ps or fs) are suitable. Thin films are preferably patterned by mask projection using flat top beams of excimer lasers. For the processing of transparent materials like fused silica a number of indirect ablation methods have been established, where the laser is absorbed by an auxiliary material, which is in contact with the sample surface. Laser ablation can be utilized for hole drilling and the machining of microfluidic devices like nozzles and channel systems. In addition, the fabrication of micro-optics like gratings, phase masks, micro lenses, and diffractive optical elements has been demonstrated.

References

1. V. Srinivasan, M.A. Smrtic, S.V. Babu, J. Appl. Phys. **59**(11), 3861 (1986)
2. H. Schmidt, J. Ihlemann, B. Wolff-Rottke, K. Luther, J. Troe, J. Appl. Phys. **83**(10), 5458 (1998)
3. H. Schmidt, Physikalisch-chemische Aspekte des excimerlaserinduzierten Ablationsprozesses an Polymeren. Phd, Göttingen (1994)
4. B. Wolff-Rottke, H. Schmidt, J. Ihlemann, in Laser treatment of materials (ECLAT'92), ed. by B.L. Mordike (DGM Informationsgesellschaft, 1992), pp. 615–620
5. P.R. Herman, R.S. Marjoribanks, A. Oettl, K. Chen, I. Konovalov, S. Ness, Appl. Surf. Sci. **154**, 577 (2000)
6. J. Ihlemann, B. Wolff-Rottke, P. Simon, Appl. Phys. A Mater. Sci. Process. **54**(4), 363 (1992)
7. J. Ihlemann, B. Wolff-Rottke, Appl. Surf. Sci. **106**, 282 (1996)
8. J. Ihlemann, A. Scholl, H. Schmidt, B. Wolff-Rottke, Appl. Phys. A Mater. Sci. Process. **60**(4), 411 (1995)
9. J. Arnold, F. Dausinger, in ECLAT (1990), p. 859
10. I. Horn, M. Guillong, D. Gunther, Appl. Surf. Sci. **182**(1–2), 91 (2001)
11. M. Eyett, D. Bäuerle, Appl. Phys. Lett. **51**(24), 2054 (1987)
12. B. Wolff-Rottke, J. Ihlemann, H. Schmidt, A. Scholl, Appl. Phys. A Mater. Sci. Process. **60**(1), 13 (1995)
13. M. Rauh, UV-Laser-Mikrostrukturierung von Polytetrafluorethylen für biophysikalische Anwendungen. Master, Göttingen (2005)
14. M.N. Nobis, C. Scherer, O. Nuyken, F. Beinhorn, J. Ihlemann, Macromol. Mater. Eng. **275**(2), 1 (2000)
15. S. Küper, M. Stuke, Appl. Phys. A Mater. Sci. Process. **49**(2), 211 (1989)
16. S. Küper, J. Brannon, K. Brannon, Appl. Phys. A Mater. Sci. Process. **56**(1), 43 (1993)
17. S. Küper, M. Stuke, Appl. Phys. Lett. **60**, 1633 (1992)
18. B. Burghardt, H.J. Kahlert, D. Basting, in Laser Treatment of Materials, ed. by B. Mordike (Oberursel, 1992), p. 609
19. S. Lazare, J. Lopez, F. Weisbuch, Appl. Phys. A Mater. Sci. Process. **69**, 1 (1999)
20. A.A. Tseng, Y.T. Chen, C.L. Chao, K.J. Ma, T.P. Chen, Optics and Lasers in Eng. **45**(10), 975 (2007)
21. C. Buerhop, N. Lutz, R. Weissmann, M. Geiger, in Laser Treatment of Materials (DGM Informationsgesellschaft, Oberursel, 1992), pp. 603–608
22. C. Buerhop, B. Blumenthal, R. Weissmann, N. Lutz, S. Biermann, Appl. Surf. Sci. **46**(1–4), 430 (1990)
23. M.D. Crisp, N.L. Boling, G. Dube, Appl. Phys. Lett. **21**, 364 (1972)
24. A. Salleo, T. Sands, F.Y. Genin, Appl. Phys. A Mater. Sci. Process. **71**(6), 601 (2000)
25. A.A. Tseng, physica status solidi (a) **204**(3) (2007)
26. P.E. Dyer, C.D. Walton, Appl. Phys. A Mater. Sci. Process. **79**(4), 721 (2004)
27. J. Ihlemann, M. Schulz-Ruhtenberg, T. Fricke-Begemann, in Eighth International Conference on Laser Ablation, vol. 59 (Institute of Physics Publishing, 2007), pp. 206–209
28. B. Keiper, T. Petsch, H. Exner, Excimer Laser Technology (Springer, Berlin, 2005), chap. Micro-Processing of Borosilicate Glass and Polymers, pp. 201–219
29. L. Dirnberger, P.E. Dyer, S. Farrar, P.H. Key, P. Monk, Appl. Surf. Sci. **69**(1–4), 216 (1993)
30. J. Heitz, J.D. Pedarnig, D. Bäuerle, G. Petzow, Appl. Phys. A Mater. Sci. Process. **65**(3), 259 (1997)
31. R. Weichenhain, A. Horn, E.W. Kreutz, Appl. Phys. A Mater. Sci. Process. **69**, 855 (1999)
32. I. Miyamoto, H. Maruo, in Proc. SPIE, vol. 1279 (1990), p. 66
33. D. Breitling, A. Ruf, F. Dausinger, in Proc. SPIE, vol. 5339 (2004), pp. 49–61
34. J.G. Lunney, R. Jordan, Appl. Surf. Sci. **127**, 941 (1998)
35. R. Jordan, J.G. Lunney, Appl. Surf. Sci. **127**, 968 (1998)
36. P.E. Dyer, D.M. Karnakis, P.H. Key, D. Sands, Appl. Surf. Sci. **109**, 168 (1997)

37. E. Matthias, M. Reichling, J. Siegel, O.W. Käding, S. Petzoldt, H. Skurk, P. Bizenberger, E. Neske, Appl. Phys. A Mater. Sci. Process. **58**(2), 129 (1994)
38. J.E. Andrew, P.E. Dyer, R.D. Greenough, P.H. Key, Appl. Phys. Lett. **43**, 1076 (1983)
39. J. Ihlemann, B. Wolff-Rottke, Appl. Surf. Sci. **86**(1–4), 228 (1995)
40. D. Schäfer, J. Ihlemann, G. Marowsky, P.R. Herman, Appl. Phys. A Mater. Sci. Process. **72**(3), 377 (2001)
41. J. Ihlemann, J. Békési, J.-H. Klein-Wiele, P. Simon, Laser Chemistry 2008 (2008), Article Id. 623872.
42. J. Wang, H. Niino, A. Yabe, Appl. Phys. A Mater. Sci. Process. **68**(1), 111 (1999)
43. J. Wang, H. Niino, A. Yabe, Appl. Phys. A Mater. Sci. Process. **69**, 271 (1999)
44. X.M. Ding, T. Sato, Y. Kawaguchi, H. Niino, Jap. J. Appl. Phys. Part 2-Lett. **42**(2B), L176 (2003)
45. J. Zhang, K. Sugioka, K. Midorikawa, Opt. Lett. **23**(18), 1486 (1998)
46. T. Makimura, H. Miyamoto, Y. Kenmotsu, K. Murakami, H. Niino, Appl. Phys. Lett. **86**, 103111 (2005)
47. K. Sugioka, S. Wada, Y. Ohnuma, A. Nakamura, H. Tashiro, K. Toyoda, Appl. Surf. Sci. **96**, 347 (1996)
48. H. Varel, D. Ashkenasi, A. Rosenfeld, M. Wähmer, E.E.B. Campbell, Appl. Phys. A Mater. Sci. Process. **65**(4–5), 367 (1997)
49. J. Krüger, W. Kautek, Appl. Surf. Sci. **96**, 430 (1996)
50. K. Zimmer, R. Böhme, B. Rauschenbach, Appl. Phys. A Mater. Sci. Process. **79**(8), 1883 (2004)
51. B. Hopp, C. Vass, T. Smausz, Appl. Surf. Sci. **253**(19), 7922 (2007)
52. J. Ihlemann, Appl. Phys. A Mater. Sci. Process. **93**(1), 65 (2008)
53. Y. Kawaguchi, H. Niino, T. Sato, A. Narazaki, R. Kurosaki, in Eighth International Conference on Laser Ablation, vol. 59 (Institute of Physics Publishing, 2007), pp. 380–383
54. B. Hopp, C. Vass, T. Smausz, Z. Bor, J. Phys. D: Appl. Phys. **39**(22), 4843 (2006)
55. B. Burghardt, S. Scheede, R. Senczuk, H.J. Kahlert, Appl. Phys. A Mater. Sci. Process. **69**(7), 137 (1999)
56. F.G. Bachmann, Appl. Surf. Sci **46**, 254 (1990)
57. M. Heßling, J. Ihlemann, S. Puschmann, G. Marowsky, M. Loff, M. Novotny, B. Radinger-Dombert, Laser-Praxis **3**, 14 (2001)
58. P.E. Dyer, I. Waldeck, G.C. Roberts, J. Phys. D: Appl. Phys. **30**, 19 (1997)
59. O. Krüger, G. Schöne, T. Wernicke, W. John, J. Würfl, G. Tränkle, in Eighth International Conference on Laser Ablation, vol. 59 (Institute of Physics Publishing, 2007), pp. 740–744
60. A. Schoonderbeek, R. Kling, A. Ostendorf, R. Grischke, R. Meyer, R. Brendel, in Proc. ALAC (2007)
61. J. Clarke, J. Profeta, in Advanced Laser Applications Conference & Exposition, ed. by D. Roessler, N. Uddin, B. Tang (Ann Arbor, 2004), p. 94
62. L. Herbst, J.P. Quitter, G.M. Ray, T. Kuntze, A.O. Wiessner, S.V. Govorkov, M. Heglin, in Proc. SPIE, vol. 4968 (2003), p. 134
63. T. Lizotte, Industrial Laser Solutions **17** (2002)
64. J. Chae, S. Appasamy, K. Jain, Appl. Phys. Lett. **90**, 261102 (2007)
65. S.K. Lee, S.J. Na, Appl. Phys. A Mater. Sci. Process. **68**(4), 417 (1999)
66. J. Ihlemann, S. Müller, S. Puschmann, D. Schäfer, M. Wei, J. Li, P.R. Herman, Appl. Phys. A Mater. Sci. Process. **76**(5), 751 (2003)
67. A. Yick, J. Li, P.R. Herman, in Proc. SPIE, vol. 4977 (2003), p. 400
68. T.V. Kononenko, S.V. Garnov, S.M. Pimenov, V.I. Konov, V. Romano, B. Borsos, H.P. Weber, Appl. Phys. A Mater. Sci. Process. **71**(6), 627 (2000)
69. T.V. Kononenko, V.V. Kononenko, V.I. Konov, S.M. Pimenov, S.V. Garnov, A.V. Tishchenko, A.M. Prokhorov, A.V. Khomich, Appl. Phys. A Mater. Sci. Process. **68**(1), 99 (1999)
70. J.R. Lankard, G. Wolbold, Appl. Phys. A Mater. Sci. Process. **54**(4), 355 (1992)
71. J. Ihlemann, K. Rubahn, Appl. Surf. Sci. **154**, 587 (2000)
72. D. Schäfer, J. Ihlemann, G. Marowsky, P. Herman, Appl. Phys. A Mater. Sci. Process. **72**(3), 377 (2001)

73. J. Ihlemann, K. Rubahn, R. Thielsch, in Proc. SPIE, vol. 4426 (2002), p. 437
74. K. Rubahn, J. Ihlemann, Appl. Surf. Sci. **127**, 881 (1998)
75. G.P. Behrmann, M.T. Duignan, Appl. Opt. **36**(20), 4666 (1997)
76. N.A. Vainos, S. Mailis, S. Pissadakis, L. Boutsikaris, P.J.M. Parmiter, P. Dainty, T.J. Hall, Appl. Opt. **35**(32), 6304 (1996)
77. X. Wang, J.R. Leger, R.H. Rediker, Appl. Opt. **36**(20), 4660 (1997)
78. F. Quentel, J. Fieret, A.S. Holmes, S. Paineau, in Proc. SPIE, vol. 4274 (2001), pp. 420–431
79. J. Ihlemann, D. Schäfer, Appl. Surf. Sci. **197**, 856 (2002)
80. J. Ihlemann, R. Weichenhain-Schriever, J. Laser Micro/Nanoeng. **4**, 100 (2009)
81. M. Schulz-Ruhtenberg, J. Ihlemann, J. Heber, Appl. Surf. Sci. **248**(1–4), 190 (2005)
82. H.M. Phillips, R.A. Sauerbrey, Opt. Eng. **32**(10), 2424 (1993)
83. P.E. Dyer, R.J. Farley, R. Giedl, D.M. Karnakis, Appl. Surf. Sci. **96**, 537 (1996)
84. J. Bekesi, J. Meinertz, J. Ihlemann, P. Simon, Appl. Phys. A Mater. Sci. Process. **93**(1), 27 (2008)
85. C.J. Newsome, M. O'Neill, R.J. Farley, G.P. Bryan-Brown, Appl. Phys. Lett. **72**(17), 2078 (1998)
86. M. Behdani, S.H. Keshmiri, S. Soria, M.A. Bader, J. Ihlemann, G. Marowsky, T. Rasing, Appl. Phys. Lett. **82**, 2553 (2003)
87. K.J. Ilcisin, R. Fedosejevs, Appl. Opt. **26**(2), 396 (1987)
88. H.M. Phillips, D.L. Callahan, R. Sauerbrey, G. Szabo, Z. Bor, Appl. Phys. Lett. **58**, 2761 (1991)
89. T. Lippert, T. Gerber, A. Wokaun, D.J. Funk, H. Fukumura, M. Goto, Appl. Phys. Lett. **75**, 1018 (1999)
90. K. Rubahn, J. Ihlemann, G. Jakopic, A.C. Simonsen, H.G. Rubahn, Appl. Phys. A Mater. Sci. Process. **79**(7), 1715 (2004)
91. S. Pissadakis, L. Reekie, M. Hempstead, M.N. Zervas, J.S. Wilkinson, Appl. Phys. A Mater. Sci. Process. **69**, 739 (1999)
92. M.A. Bader, C. Kappel, A. Selle, J. Ihlemann, M.L. Ng, P.R. Herman, Appl. Opt. **45**(25), 6586 (2006)
93. K. Naessens, P. Van Daele, R.G. Baets, in Proc. SPIE, vol. 4941 (2003), p. 133
94. K. Naessens, H. Ottevaere, R. Baets, P. Van Daele, H. Thienpont, Appl. Opt. **42**(31), 6349 (2003)
95. J.E.A. Pedder, A.S. Holmes, R. Allott, K. Boehlen, in Proc. SPIE, vol. 6462 (2007),
96. T. Lippert, A. Wokaun, Chimia **55**(10), 783 (2001)
97. T. Fricke-Begemann, J. Meinertz, J. Ihlemann, in EOS Topical Meeting on Micro-Optics, Diffractive Optics and Optical MEMS (Paris, 2006), p. 114
98. H.M. Presby, A.F. Benner, C.A. Edwards, Appl. Opt. **29**(18), 2692 (1990)
99. T. Fricke-Begemann, J. Li, J. Dou, J. Ihlemann, P. Herman, G. Marowsky, in Third International WLT-Conference Lasers in Manufacturing, LIM (2005), p. 733
100. J. Dou, J. Li, P.R. Herman, J.S. Aitchison, T. Fricke-Begemann, J. Ihlemann, G. Marowsky, Appl. Phys. A Mater. Sci. Process. **91**(4), 591 (2008)
101. M. Wehner, P. Jacobs, R. Poprawe, in Proc. SPIE, vol. 6459 (2007), p. 645908
102. W. Pfleging, R. Adamietz, H.J. Bruckner, M. Bruns, A. Welle, in Proc. SPIE, vol. 6459 (International Society for Optical Engineering, 2007), p. 645907
103. R. Böhme, B. Keiper, K. Zimmer, R. Ebert, H. Exner, in Proc. SPIE, vol. 5116 (2003), pp. 491–496
104. S. Nikumb, Q. Chen, C. Li, H. Reshef, H.Y. Zheng, H. Qiu, D. Low, Thin Solid Films **477** (1–2), 216 (2005)
105. D. Ashkenasi, M. Schwagmeier, in Proc. SPIE, vol. 6458 (2007), p. 64580F
106. P.R. Herman, A. Yick, J. Li, N. Munce, L. Lilge, E. Jervis, S. Krylov, in CLEO Tech. Digest CLF5 (2003), p. 3
107. P.E. Dyer, S.M. Maswadi, C.D. Walton, M. Ersoz, P.D.I. Fletcher, V.N. Paunov, Appl. Phys. A Mater. Sci. Process. **77**(3), 391 (2003)
108. S.J. Qin, W.J. Li, Appl. Phys. A Mater. Sci. Process. **74**(6), 773 (2002)

Chapter 9
Laser Processing Architecture for Improved Material Processing

Frank E. Livingston and Henry Helvajian

Abstract This chapter presents a novel architecture and software–hardware design system for materials processing techniques that are widely applicable to laser direct-write patterning tools. This new laser material processing approach has been crafted by association with the genome and genotype concepts, where predetermined and prescribed laser pulse scripts are synchronously linked with the tool path geometry, and each concatenated pulse sequence is intended to induce a specific material transformation event and thereby express a particular material attribute. While the experimental approach depends on the delivery of discrete amplitude modulated laser pulses to each focused volume element with high fidelity, the architecture is highly versatile and capable of more advanced functionality. The capabilities of this novel architecture fall short of the coherent spatial control techniques that are now emerging, but can be readily applied to fundamental investigations of complex laser-material interaction phenomena, and easily integrated into commercial and industrial laser material processing applications. Section 9.1 provides a brief overview of laser-based machining and materials processing, with particular emphasis on the advantages of controlling energy deposition in light-matter interactions to subtly affect a material's thermodynamic properties. This section also includes a brief discussion of conventional approaches to photon modulation and process control. Section 9.2 comprehensively describes the development and capabilities of our novel laser genotype pulse modulation technique that facilitates the controlled and precise delivery of photons to a host material during direct-write patterning. This section also reviews the experimental design setup and synchronized photon control scheme, along with performance tests and diagnostic results. Section 9.3 discusses selected applications of the new laser genotype processing technique, including optical property variations and silicate phase fractionation in a commercial photosensitive glass ceramic and pyroelectric phase transitions in a perovskite

F.E. Livingston (✉)
Micro/Nanotechnology Department, Space Materials Laboratory, The Aerospace Corporation, 2350 E. El Segundo Blvd., El Segundo, CA 90245-4691
e-mail: frank.e.livingston@aero.org

nanostructured thin-film. Finally, a chapter summary and future perspective are provided in Sect. 9.4.

9.1 Laser Machining and Materials Processing

9.1.1 Introduction

During the past 20 years there have been great strides concerning the development of new promising techniques for the laser-based processing of materials [1–15]. Many of these accomplishments have been facilitated by the equally significant developments in laser technology, where improvements in pulse stability and reliability represent the current hallmarks and the controlled delivery of a prescribed photon flux corresponds to a capability on the near horizon [16]. Sufficient evidence exists in the literature that suggests further advancements in the field of laser material processing will rely significantly on the development of new process control schemes. The process control system must enable the precise delivery of photons to a specific material with high spatial and temporal resolution; i.e., the laser control system parameters must be appropriately varied for the particular material under irradiation at the optimum time. Prior experiments have demonstrated that a diverse set of material transformations can be realized by a judicious choice of the common laser process parameters, such as the laser wavelength, pulse amplitude, temporal and spatial characteristics, polarization, and total photon exposure dose [17–28]. Consequently, traditional concepts such as "laser process window" must now be redefined to include these additional laser process parameters in a composite manner, and permit their synchronous alteration in real time during patterned exposure. These advancements and capabilities are essential to account for the continual evolution in a material's chemical and physical properties that occur during sequential pulse irradiation, and to help maintain efficient laser energy-material coupling during dynamic material transformations and phase state transitions. For example, time-dependent incubation effects and thermal loading processes can influence a material's optical and thermodynamic properties, and these effects must be addressed on a per-pulse and per-spot basis to ensure optimum laser material processing.

Precise real time modulation of the laser parameters and system controls permits the control of energy flow into the material system during processing and patterning. Consequently, the energy flux can be regulated to induce or "express" specific chemical and physical properties in the material on a highly localized scale. High-precision modulation can be used to influence both thermal and non-thermal processes and facilitate the desired type of materials processing and alteration, such as crystallization and phase transformation, welding and sintering, and micro- and nanostructure fabrication. This approach is ideal for a moving substrate under constant laser irradiation and essential for a variegated substrate that comprises heterogeneous interconnected materials or phases that require different processing

conditions. This approach also enables the co-fabrication of multiple functionalities and physical devices on a common substrate, and thereby facilitates next-generation systems integration and packaging. To realize these ambitious goals, high synergy must exist between the laser process architecture and the mutable (protean) material. This chapter focuses on the control system architecture and its implementation to precisely govern the laser source and deliver well defined photon exposures at the proper location and time.

Since processing dimensions are approaching nanometer length scales, future commodity manufacturing will place increased emphasis on fabrication processes that retain comparatively more precision than today's material processing techniques. Lasers provide an attractive, cost-effective processing tool that is physically non-intrusive and capable of delivering spatially focused and diffraction-limited action at a distance. Consequently, manufacturing technology will rely on lasers and laser-based material processing for the development of new material processing methodologies and multifunctional device integration solutions. The requirement for high fidelity modulation of the laser photon flux will become more urgent as the dimensional scale for processing decreases. Consequently, precision modulation techniques for laser exposure will be implemented not only to minimize unwanted thermal effects (e.g., heat affected zone formation), but more likely used to strategically confine the laser energy along a specific light-matter interaction channel. Traditional laser material processing approaches, such as ablative or percussive machining, utilize the laser as the principle directed energy source to drive the fundamental interaction. In this chapter, we examine the development and implementation of software and hardware control schemes that enable a complementary capability, where the laser energy is used to facilitate a specific chemical or physical reaction and achieve the desired processing effect.

In this idea, the bulk of the processing energy is supplied by the inherent energy that is stored in the nascent material - e.g., the Gibbs energy. The proposed approach could have immediate applications in the transformation of nanometer-scale molecular entities and chemical domains and thereby permit the in situ growth or fabrication of complex materials that comprise multiple stable phases. These laser engineered materials could display novel macro-scale properties by virtue of their nanoscale "ordering." To enable this level of laser material processing complexity, the optimum photon control scheme would have to mimic the optical modulation techniques that are now emerging for coherent molecular control applications [29]. This chapter presents a laser pulse modulation scheme and material processing architecture that is somewhat below the penultimate of the coherent spatial control technique. Nevertheless, the proposed approach has relevance to a diverse array of applications ranging from novel materials development, that requires precision photon delivery for facilitating reactions, to traditional laser fabrication where the primary driving force is the laser energy. Consequently, our novel laser processing architecture can be readily integrated into most current commercial and industrial laser material processing stations. As a conceptual framework, the proposed laser processing architecture applies insights from molecular biology and the genome and genotype concepts, and therefore carries the moniker "*laser genotype pulse modulation technique* [30]."

9.1.2 Materials, Thermodynamic Properties, and Light/Matter Interaction

Every closed system "seeks" to minimize its free energy. In mixed element materials a quantitative measure exists that describes how far a material system resides from an energy minimum or equilibrium state. If the thermodynamic properties of the material are known then the calculated change of the Gibbs energy ΔG can serve as a quantitative measure of this displacement from equilibrium. Alternatively, the Gibbs energy can be viewed as a measure of a system's capacity to perform work or used to predict the rate at which a closed chemical system can transition into specific equilibrium states. For a closed system at constant temperature and pressure the thermodynamic relationship of the Gibbs energy, G, can be written as:

$$G = H - TS, \tag{9.1}$$

where H is the enthalpy, T the absolute temperature, and S is the entropy.

Device manufacturers and systems developers would prefer to utilize materials that are near equilibrium (i.e., $\Delta G \approx 0$); in reality, however, many commercial materials are used in their metastable, non-equilibrium state (e.g., glass). These materials often appear "stable" because the reaction rates and material kinetics that govern the transition to equilibrium are inherently very slow (e.g., low diffusion rates). A Gibbs energy analysis of this type of material system would reveal a large negative ΔG value. The application of a laser pulse sequence with appropriately tailored amplitude and temporal profiles could be used to facilitate the transition to an equilibrium or low-energy state by activating or accessing this inherent potential energy. Particular interest relates to attaining specific *local* equilibrium states that retain novel material properties, rather than achieving the *global* minimum energy state. Our prior experimental studies concerning the laser processing of a commercial photosensitive glass ceramic have shown that careful articulation of key laser parameters can be used to establish reaction pathways for the formation of distinct equilibrium phase states [31, 32].

Re-examination of the laser material processing literature reveals that many results support the notion that lasers can selectively alter the thermodynamic quantities that comprise the Gibbs equation; namely a system's enthalpy (e.g., via formation of radicals), temperature (e.g., via absorption), and entropy (e.g., via formation of lattice defect sites, crystallization). We first consider the fundamental dynamic processes that can be manipulated in a *bulk solid lattice* by the application of a well controlled photon flux. In the simplest case, laser irradiation can be used to induce point defects in the lattice structure which may lead to the formation of new absorption bands in the optical or infrared wavelength regions, along with alterations in the frequencies of the local phonon modes. While the creation of new absorption bands in the host material could have practical consequences for the laser processing efficiency and material functionality, the utility of modifying the local phonon modes should not be casually dismissed.

Modification of the local phonon modes can influence the thermal conductivity of the material. The thermal conductivity can be modeled as the averaged value of the collective relaxation times associated with the phonon modes [33], where the relaxation times correspond to the decay rates of local perturbations. This relaxation not only controls the rate of thermal energy dissipation, but reflects the rate at which equilibrium is attained. Thus, a material transformation process – e.g., atom diffusion and charge dissipation – that follows a *laser induced* disturbance would evolve in a thermal environment that is appreciably different compared with a perturbation-free environment. In principle, the controlled delivery of an articulated laser pulse sequence could be employed to alter the initial defect state distribution in the lattice and synchronously modulate the thermal conductivity and diffusion rates. Diffusion represents the transport of matter and can be dramatically affected by temperature, pressure, and chemical potential gradients. Laser-controlled variations of the diffusion processes could lead to the aggregation of specific species and the concomitant precipitation of preferential complexes in the bulk. For example, laser-scripted photon modulation could facilitate the aggregation of M^{2+} complexes in alkali-metal halides which precipitate first and lead to the ultimate formation of new MX_2 phases, where M is a metal ion and X_2 is a superlattice structure [34, 35].

Prudent modulation of the incident laser energy may also assist in the controlled manipulation of the *surface and near-surface* chemistry of a material. Comprehensive experimental studies have demonstrated that the surface crystal structure of a material can be dramatically altered by the addition of particular adsorbates, and this structural rearrangement can subsequently facilitate specific chemical reactions via catalytic activation. For example, chemical induced surface modifications have been successively utilized on various metallic systems – including platinum, platinum/rhenium, and iridium/gold – to form aromatic hydrocarbons via dehydrocyclization reactions [36] which has enabled the commercial production of high-octane, low-lead fuels. We envision that precision laser modulation techniques could be employed to modulate the thermodynamic driving forces that enhance catalytic activation and thereby control adsorbate desorption and surface structural rearrangement on a patterned, site-selective basis.

9.1.3 Photolytic Control: Conventional Approaches and Future Trends

Conventional laser material processing techniques commonly fix the laser power and minimize laser power fluctuations during patterning, which forces the continual movement of a homogeneous single-phase substrate. These traditional material processing approaches rely on the determination and application of a *fixed* laser process window which often accounts only for basic repetitive or multiple laser pulse phenomena, such as rep-pulse and incubation effects [37]. However, this rudimentary system control does not compensate for variations in substrate velocity during regions of deceleration and acceleration. This limitation can lead to

various unwanted material processing characteristics, including inconsistent photo-exposure, thermal energy transfer outside the irradiated region, material removal from non-irradiated regions, and residual stress and fracture. Clearly, these effects will significantly reduce pattern complexity and adaptability and degrade component functionality and device performance. For direct-write applications, simple mitigation strategies include laser beam shuttering and "cut-in" and "cut-out" techniques to apply laser light only during motion sequences where the velocity is constant, and the implementation of digital fabrication via bitmap image patterns and 2D layering schemes. Although these alternative approaches have proved useful, several key limitations still exist including lack of laser pulse modulation to enable complex patterning, increased processing and manufacturing time with the consequent effects of increased production costs and reduced rapid prototyping capabilities.

Recent developments in laser technology could have a marked impact on the operational mode of future laser processing systems. Innovative industrial fiber laser systems are now emerging that retain remarkable power stability and mode quality and allow exquisite control of the output laser pulse train. The Pyroflex^{TM} fiber laser (Pyrophotonics, Inc., Canada) permits software-level modulation of the laser pulse intensity, pulse duration and shape, and repetition rate. The pulse parameters can be adjusted to produce well defined laser pulse trains with pulse durations that range from 1 to 250 ns at repetition rates of up to 500 kHz [16]. Next-generation laser processing methods will rely on the ability to customize or tailor the temporal profile of the laser pulse with high fidelity. Experimental studies [23] and industrial developments [16] have demonstrated that vast improvements in laser processing efficiency and quality may be possible via synchronous control and variation of the temporal pulse shape. The importance of tailoring pulse trains is particularly highlighted in the laser heating of a metal. Below the Debye temperature, the heat capacity of a metal is proportional to T^3, where T is the temperature in Kelvin. Because of the strong temperature dependence, it is possible to dynamically compensate for the variation in heat capacity and achieve efficient and well controlled laser processing of metallic systems. The Pyroflex and similar next-generation laser systems will certainly be implemented in a diverse array of industrial and commercial applications; however, as designed, these lasers are not amenable for use in coherent molecular control processes [38]. Molecular vibrations occur on the picosecond time scale and, consequently, coherent control in a chemical reaction is best achieved via the spectral shaping of high bandwidth femtosecond laser pulses [39]. As the development and utilization of coherent spatial control for heterogeneous materials processing is still in its infancy [40, 41], this chapter does not address the role of coherent control in materials processing applications.

9.1.4 Process Control

Traditional commercial and industrial laser processing stations employ standardized material processing procedures, where each procedure comprises a collection

of laser and machine tool parameters that are designed for a specific type of material processing – e.g., the laser machining of glass might include material processing protocols that correspond to cutting, bending, ablation and scribing, and welding and joining. Current laser machining stations are generally designed to execute the material processing procedures in a repetitive manner and produce results with a predefined tolerance. Both *material preparation* and the *nature of the photon flux delivery* are important for optimum laser material processing. Material preparation procedures may correspond to simple routines such as maintaining the substrate orientation and incident angle of laser irradiation during processing, or may involve more complex protocols that alter the material's processing environment (e.g., heating-cooling, high vacuum conditions) to enhance the laser-material interaction. These types of material preparation protocols are commonly implemented in industry for automated process control; unfortunately, the capability to include other critical processing protocols and integrate these protocols with the tool path machine code are not available on current commercial laser processing systems.

In this chapter, we focus on the development and application of a laser processing architecture that permits precision modulation of photon flux and the position-synchronized delivery of discrete laser pulse scripts to a substrate during patterning [23, 30–32, 42–44]. The laser processing platform is highly versatile and is able to seamlessly and dynamically merge a diverse array of other process scripts including material type (e.g., metal, semiconductor, and polymer), surface topography (e.g., rough, smooth, textured), prior photon dose history and the desired type of material processing (e.g., ablation, deposition, phase transformation), along with automated calibration routines and diagnostic tests. For this integrated system to operate with optimum fidelity and efficiency, the laser processing architecture must also permit transparent closed loop control – e.g., an integrated in situ spectroscopic detection scheme that provides real time feedback for improved process control and laser pulse script generation. This requirement invokes the question: Can a closed loop material processing architecture be developed that synchronously modulates the laser pulse train at real time processing speeds approaching 1 m per second? For a laser system operating at a repetition rate of 50 MHz and a motion control platform moving at an average velocity of 1 m/s while maintaining submicron accuracy (e.g., Aerotech Corp., ABL8000 air bearing translation stage), a laser direct-write processing tool can service 10^6 spot sizes per second for a nominal focal spot diameter of 1 μm. The average time duration that the laser processing tool spends over a single spot diameter is 1 μs at a motion control platform velocity of 1 m/s. The closed loop system would comprise numerous optical and electronic devices and software subsystems, including an optical sensor for spectroscopic detection and endpoint analysis, an evolutionary algorithm for pulse script generation and mutation, and electro- or acousto-optic devices for pulse modulation, along with various microprocessor units and analog-to-digital converters (ADCs). The required optical and electronic devices are commercially available and retain the following typical operational cycle times:

1. Optical sensor and photodiode response times <1 ns
2. Electrical signal transfer rates ~ 3 ns/m

3. Microprocessor speeds >37 GFLOPS (Intel Core 2 Extreme QX6800)
4. Acousto-optic modulator (AOM) bandwidths 20 GHz [45]
5. Analog-to-digital converter (ADC) sample rates 2 GS/s (Delphi Engineering ADC3244)

The technical data reveal that competent technology exists to assemble a closed loop laser processing system that can respond within a 1 μs time duration, while sequentially analyzing and systematically varying the laser pulse parameters for endpoint analysis and process optimization. This example retains several inherent but benign assumptions. First, the laser pulse-to-pulse amplitude variation represents a small percentage of the total energy required per spot size. This assumption is reasonable given the recent development of extremely stable solid state laser systems that are based on semiconductor saturable-absorber mirror (SESAM) technology [46] where power stabilities better than 0.3% have been reported at output powers exceeding 10 W. Second, the processing event or material transformation requires the administration of multiple (>10) laser pulses. This assumption is also valid given that multiple-pulse processing – i.e., *burst mode* processing – has been shown to yield significant improvement in processing fidelity and efficiency compared with single-pulse processing [47].

9.2 Laser Genotype Pulse Modulation Technique

9.2.1 Concept

To address the inherent limitations and expand the capability of conventional laser material processing techniques, we have developed a novel direct-write approach that facilitates the controlled and precise delivery of photons to the substrate during patterning [23, 30–32, 42–44]. Our experimental technique is aptly named *laser genotype pulse modulation processing* because its inspiration is derived from the concept of the genome and the function of the genotype. The genotype (Gr. Gen: to produce + tupos: impression) describes the "genetic constitution of an individual either with respect to a single trait or with respect to a larger set of traits," [48] and the genome represents a sequence of concatenated genotypes or genetic scripts. In our approach, a similar "genotype laser pulse process script" is first developed and is then synchronously matched with the laser tool path profile or tool path machine code. Figure 9.1 provides a conceptual overview of the laser genotype material processing technique.

First, the high repetition rate pulsed laser is allowed to operate at its optimum repetition rate where the pulse-to-pulse variation is minimized. The fundamental key to this technique corresponds to the scheme by which the laser photon flux is modulated to provide the "correct" genotype pulse script for each irradiated zone. As currently designed, the delivery of a precision photon flux and dose can be accomplished using intensity (amplitude) modulation, pulse selection and

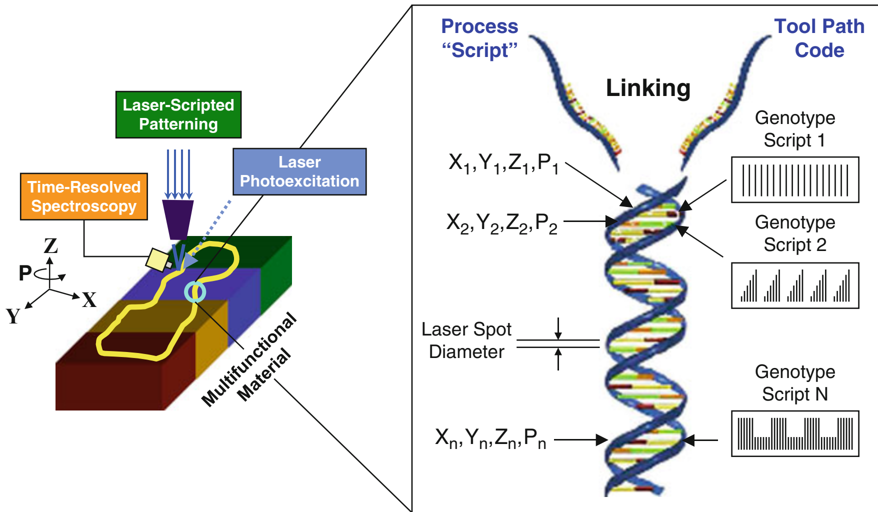

Fig. 9.1 Conceptual overview of the laser genotype material processing technique. The concept is inspired by the genome, where the analogy of the line-by-line base-pairings is used to merge the tool path code (i.e., a "Pattern Script") with the corresponding laser material processing parameters (i.e., a "Process Script)

extraction, temporal modulation, or a combination of these methods, along with concomitant variation in the incident polarization of the laser beam during patterning. A second key element is that the laser pulse sequence is determined by the travel distance (as opposed to discrete time intervals) and is related to the laser spot diameter. Consequently, the laser exposure dose is velocity-independent and each laser spot receives a user-defined and predetermined photon dose. Table 9.1 summarizes the advantages and capabilities of this new genotype-inspired laser material processing technique. These features cannot be achieved with traditional laser material processing approaches and do not currently exist on other laser processing instruments.

The genotype laser material processing method not only enables heterogeneous multimaterial processing and the *expression* of multiple functionalities on a single common substrate, but also allows the laser pulse scripts to be adapted in near real time to compensate for chemical and physical property changes in a material system that occur with each sequential laser pulse; e.g., incubation effects and time-dependent phenomena associated with the continuous evolution in the material's absorptivity and reflectivity, thermal conductivity and diffusivity, heat capacity, morphology, and composition and phase. Recently, we have demonstrated the capability and versatility of the laser direct-write genotype pulse modulation technique on several material systems, including:

1. The preferential and site-selective formation of distinct silicate phases in a photosensitive glass ceramic [31, 32],

Table 9.1 Genotype-inspired, digitally scripted laser processing technique

Advantages	Implications
Laser pulse control achieved by intensity modulation, pulse extraction, temporal and spatial modulation	Precision photon flux control and high-fidelity regulation of chemical/physical properties
Predefined laser pulse script can be delivered on a per spot basis	Photon flux is highly spatially localized
User-defined patterns with systems integration and CADCAM capability	Precision 2D and 3D laser processing of existing architectures
Genetic algorithm and intelligent feedback capability	Simultaneous laser patterning and end-point control for in situ optimization of processing conditions
Articulate and rapid prototype processing	Low-cost fabrication with high degree of pattern and component uniformity

2. The pyroelectric phase transformation in bio-inspired perovskite thin-films [49, 50],
3. The precision ablation of thin-film gold and tungsten substrates [23, 31, 32], and
4. The polarization-dependent crystallization in bulk amorphous metallic glasses [51].

9.2.2 Experimental Setup and Design

This novel material processing approach relies on three key subsystems that enable the synchronized delivery of complex laser pulse sequence profiles to a substrate during patterning and exposure. The first subsystem utilizes the inherent capabilities of computer-assisted design (CAD) and manufacturing (CAM) software that permit the design engineer to formulate critical decisions concerning how each section of a block material is to be processed. The second subsystem corresponds to the software that facilitates the intricate transfer of data and process information between the motion control system and the electronic, optical, and photonic devices. The third subsystem corresponds to the hardware and comprises a motion control platform with integrated position synchronized output (PSO) for event orchestration, an arbitrary waveform signal generator (AWSG) that creates the desired genotype laser pulse script on demand, the electro-optic devices that modulate the laser pulse amplitude and polarization, and the electronic circuits that coordinate the pulsed laser with the motion control platform and the AWSG. The intercommunication link between the laser modulation system and the motion control platform is based on a series of signal pulses generated from the motion stage encoders via a PSO card (i.e., an application specific integrated circuit, ASIC) that delineates the progression of a prescribed distance along a three dimensional (3D) tool path pattern.

Figure 9.2 highlights the *software control system* and outlines the data and process information flow that corresponds to the laser genotype material processing

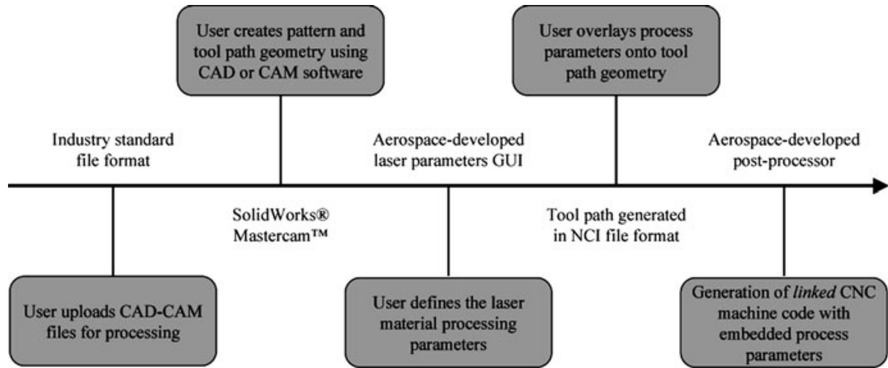

Fig. 9.2 Overview of the software control system that defines and controls the data and process information flow

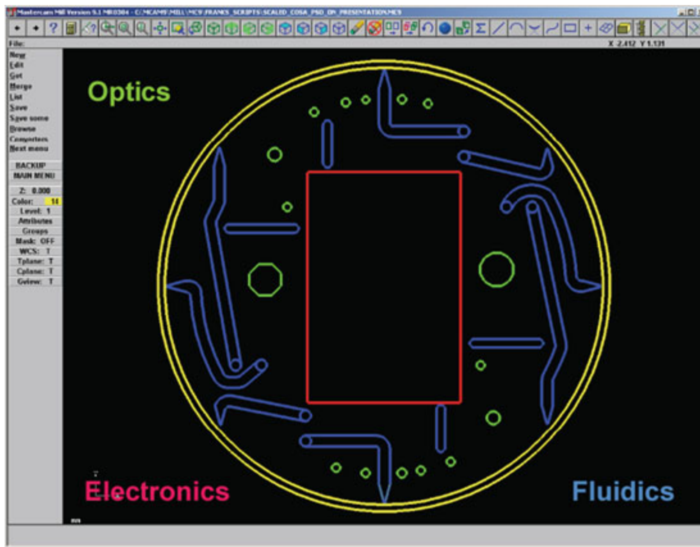

Fig. 9.3 Screen capture showing several representative device patterns and integrated tool path geometries that were created using Mastercam™ multiaxis associative CNC software. The multiple components and functionalities are represented by the separate colors and are individually assigned during tool path formulation

technique. Initially, the pattern and tool path geometry are created using CAD or CAM software; e.g., SolidWorks® 3D mechanical design software or Mastercam™ multiaxis, associative computer numerical controlled (CNC) programming software (Fig. 9.3). During the design phase, the user selects and defines the relevant laser processing parameters that are required for the specific type of material processing. The processing parameters are designated using a laser parameters graphical user

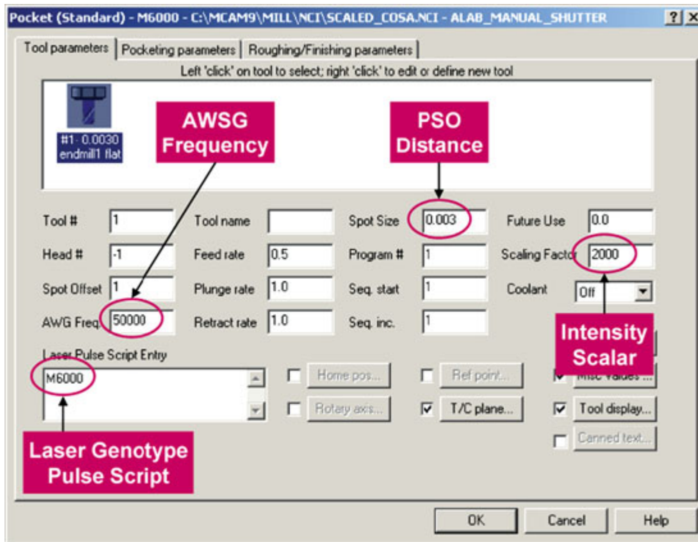

Fig. 9.4 Laser parameters graphical user interface that is used to define and select the material processing parameters that comprise a typical laser genotype pulse script. The laser pulse structure is defined by the laser genotype pulse script parameter and is selected via the appropriate *M-code*. The output frequency and temporal resolution of the laser genotype pulse script is defined by the arbitrary waveform signal generator clock frequency and is denoted as AWSG frequency. The PSO distance parameter defines the position synchronized output firing distance in Cartesian space and is typically equivalent to the laser spot diameter. The intensity scalar defines the laser pulse amplitude and per-pulse energy

interface (GUI) that has been adapted from a traditional tool parameters page in a milling machine CAM system as illustrated in Fig. 9.4.

In a conventional CNC machining system, the user identifies and selects specific tool properties that are needed to accomplish the desired type of machining, including the tool type and diameter, the flute length or effective cutting length, dynamic feed rate and spindle speed, and multiaxis work coordinate offset. In our analogous approach, the Aerospace Corporation (Aerospace)-developed laser processing parameter GUI permits the user to select and define the relevant *laser material processing* parameters down to the *per spot* level if desired. Table 9.2 summarizes the laser material processing parameters that can be designated in our current laser genotype software version; additional control parameters can be incorporated as needed.

As a visual aid to the user, the process information is visually overlain onto the tool path geometry, and the predefined laser processing parameters are correlated with discrete locations or segments along the pattern. The design engineer must then make decisions regarding laser tool sequencing and progression in Cartesian space, which ultimately defines the laser processing tool path. Following laser parameter designation and tool path generation, a numerical control intermediate (NCI) file is

Table 9.2 Laser material processing parameters that define a typical laser process script

Laser processing parameters	Purpose	G-code parameter
Laser genotype pulse script	Defines laser pulse structure within a single genotype (waveform) or series of genotypes (sequence)	*M*-code
Processing wavelength	Selects laser processing wavelength	*L*-code
Pulse intensity scalar	Defines laser pulse amplitude and per-pulse energy	*S*-code
AWSG clock frequency	Defines output frequency of genotype pulse script for pulse extraction, repetition rate control and pulse script concatenation	*H*-code
Incident laser polarization	Specifies incident angle of polarization with respect to the tangential along the tool path	*P*-code
Spectrometer delay time	Defines time delay between incident laser pulse and CCD gating for pulse-by-pulse spectroscopic detection	*D*-code

created that corresponds to hidden compiler code and comprises all the appropriate and prescribed laser material processing parameters (i.e., a *"Process Script"*) and tool path information (i.e., a *"Pattern Script"*). A postprocessor software module has been developed that enables the interleaving of these two key information segments: first, the intermediate file parameter information is converted or translated into CNC tool path machine code (i.e., RS274 G-code), and second, the laser processing parameters are inserted into specific locations in the G-code subroutines that define the tool path geometry in Cartesian space. The Aerospace-developed postprocessor facilitates line-by-line level insertion of the laser processing parameters into the tool path G-code, and ultimately enables the synchronization and merging of the laser process script with the pattern script on a per spot basis. This laser material processing and script-linking concept is analogous to the base-pairing protocol that regulates the linking of complementary DNA strands to form a unique composite genetic script. A simple example of the compiled and merged G-code is provided below, where a small set of execution lines have been extracted from a larger composite G-code file. The G-code shows the insertion of several key laser process parameters into the motion control code.

```
N2 M6015
N3 G71
N4 H52000
N5 S2000
N6 G0 G90 X-.012000 Y.000000
N7 G1 G76 G90 X-.012000 Y.000000 F.500
N8 PSOCFG.003 ; PSOCFG = laser spot diameter
N9 M6015
N1609 M6015
N1610 M6000
N1611 G1 X.994500 Y.002598
```

```
N1612 M6015
N1613 M6001
N1614 G1 X.993000 Y.005196
N1615 M6015
N1616 M6002
N1617 G1 X.991500 Y.007794
N1618 M6015
N1619 M6003
N1620 G1 X.990000 Y.010392
N1621 M6015
N1622 G0
N1623 H52000
N1624 S2000
N1625 M6015
```

The PSOCFG command (line N8) calls the position synchronized output subroutine and activates or enables PSO functionality. The PSO firing distance is designated in the command argument, and is typically defined to be equivalent to the laser spot diameter. In the example above, the PSO firing distance is set to 3 μm. The PSO firing distance can be dynamically varied along the tool path and assigned values down to the optical encoder resolution of 40 nm if required. Global values for the arbitrary waveform signal generator clock frequency (*H-code*) and pulse intensity scalar (*S-code*) have been inserted into the tool path machine code at program lines N4 and N5, and correspond to predefined values of 52.0 kS/s and 2.0 V, respectively. The laser pulse scripts are designated using *M-codes* and appear at numerous locations in the tool path machine code. A series of *M-code* commands appear in program lines N1610-1621, where each individual *M-code* represents a different pulse script profile that ultimately defines the specific laser pulse script to be delivered to each sequential irradiated spot. Note that between each sequential linear feed rate move (as defined by the *G1* command), a distinct pulse script profile (*M6000-M6003*) has been inserted into the subsequent program line and ensures the delivery of a predefined laser pulse script to each laser spot during patterning. The *M6105* code corresponds to a null genotype waveform, and prevents any additional laser pulses to be administered to the substrate following pulse script execution and during transition to an adjacent tool path location.

The Aerospace modifications and enhancements to the computer-assisted manufacturing software permit the end-user to select preprogrammed genotype pulse scripts that reside on the AWSG flash memory board. While there is an inclination to store all of the functional information on the controlling computer, synchronized high-speed generation of this functional information is problematic. The Aerospace approach corresponds to the distribution of functionality, where coded information is sent only to select control instruments (e.g., the arbitrary waveform signal generator) and the functionalization is administered locally. A distributed control architecture has the advantage that the local instruments retain a level of

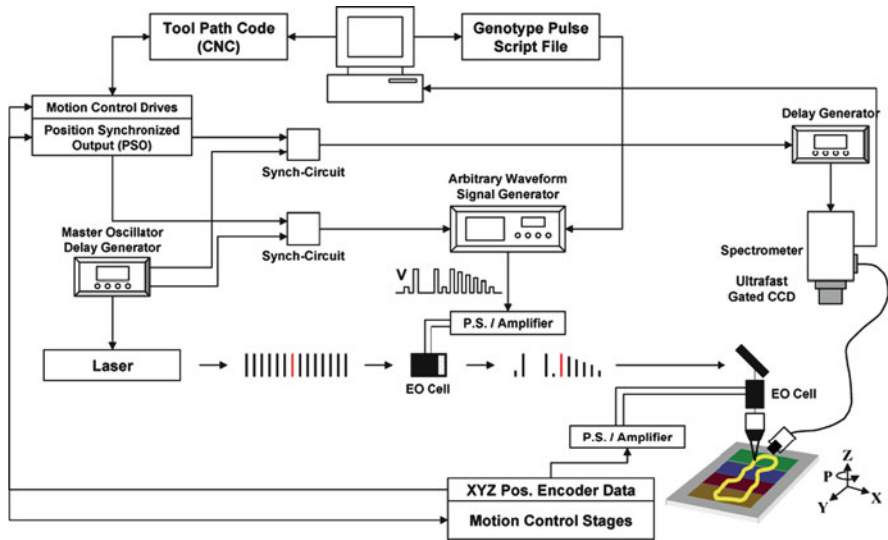

Fig. 9.5 Schematic representation of the hardware control system that encompasses the laser genotype experimental setup

autonomy. For the AWSG, the end-user can also utilize the onboard waveform editor application program to compose the desired genotype waveform patterns. The pre-programmed laser pulse scripts or waveforms correspond to voltage profiles that will be delivered to the electro-optic devices for amplitude and polarization modulation on a per spot basis. The individual pulse scripts and the user-composed waveforms can be further parceled and concatenated ad infinitum to form extremely complex sequences that comprise the overall laser genotype process script.

Figure 9.5 displays a schematic representation of the *hardware control system*. A significant technological enhancement corresponds to the manner in which the pre-defined laser pulse script or exposure dose is synchronously parceled and delivered to discrete substrate locations during 3D patterning. In our application, a position synchronized output trigger signal is generated each time the 3D-vectored travel distance in XYZ Cartesian coordinate space is equivalent to the laser spot size. As we mark the progress in units of distance rather than time, this technique is independent of the local velocity of the motion control stage. Consequently, each laser spot receives a user-defined, predetermined photon dose regardless of the stage velocity. Based on the tool path parameters and embedded laser parameter codes, subroutines are initiated that force the AWSG to synthesize a *voltage pulse script*, which is then amplified and delivered to the electro-optic modulator for the creation of a specific *laser pulse script*. The modulation of the electro-optic Pockels cell is synchronized with the arrival time of the Q-switched laser pulses. After the genotype laser pulse script has been delivered to the substrate at a single-spot location, the laser pulse train is shuttered off by the EO cell and no light is administered to the surface until another position synchronized output signal marks the transition to a new laser spot.

While the technique of marking distance in 3D Cartesian space facilitates the controlled deposition of a prescribed amount of light within a specific volume element, the idea can be generalized to incorporate higher dimensions and thus better define the chemical and physical state of the specific volume element. Chemical and physical transformations are commonly designated in units of time, but with detailed knowledge of the transformation kinetics, it is possible to transform the time dimension into artificial units of distance. Consequently, aspects of the material's physical state can be seamlessly integrated into this control architecture.

9.2.3 Performance Tests and Diagnostics

9.2.3.1 PSO Functionality

Several diagnostic tests were employed to assess the performance and capabilities of the laser genotype pulse synchronization system, including PSO firing characteristics and correlation to laser spot size, velocity compensation with PSO control, and variation of the laser pulse scripts on a per spot basis. The results presented in Fig. 9.6 summarize the real-time acquisition of position [Pos(x), Pos(y)] and velocity [Vel(x), Vel(y)] data during the execution of the coordinated sequential line fill patterning of a 1-μm-diameter regular octagon, where the nominal commanded stage velocity (feed rate) and PSO spot size were set to 1.0 μm/s and 4.0 μm, respectively. The position synchronized output firing event signals are also shown in Fig. 9.6 and are denoted in the bottom trace as PSO. The measured signals have been delineated into eight distinct regions that correspond to each of the eight pattern segments that comprise the polygon structure. As anticipated, the measured position, velocity, and PSO firing data are consistent with the octagon geometry (symmetry group: dihedral, D_8) and the designated velocity and PSO parameter values. For example, constant values for Pos(x) and zero values for Vel(x) were measured in regions 3 and 7, while constant values for Pos(y) and zero values for Vel(y) were measured in regions 1 and 5. Regions 2, 4, 6, and 8 corresponded to slanted line segments, and therefore retained continually variable position and velocity values. The measured PSO signals reveal consistent repetitive firing within each respective region or line segment; however, variable delays in PSO firing are observed at the transition points between each line segment which are associated with the acceleration, deceleration, and inertial changes that occur during motion maneuvers through the octagon vertices.

Figure 9.7a displays close-up views of the measured position, velocity, and PSO signals that corresponds to the transition between segment 6 and segment 7, and reveal several features of the PSO that are critical to the synchronized delivery of modulated laser pulses during patterning and motion sequences. During linear travel along line segments 6 and 7, the measured PSO firing interval is 4.0 ms and corresponds to a firing frequency of 250 Hz. The PSO firing interval is consistent with a 3D-vectored pattern velocity and travel distance of 1.0 μm/s and 4.0 μm,

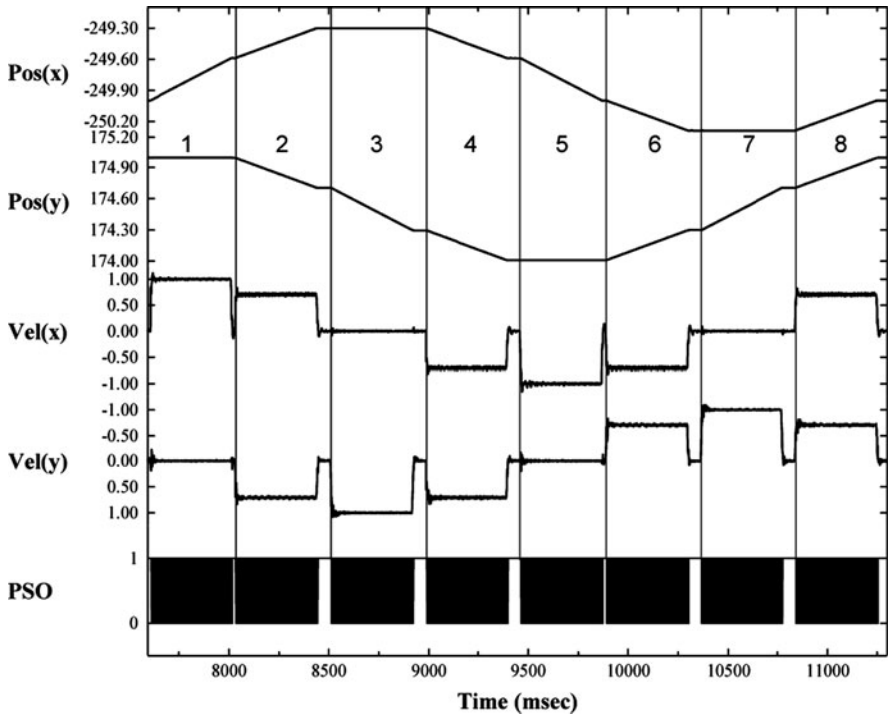

Fig. 9.6 Real-time position [Pos(x), Pos(y)], velocity [Vel(x), Vel(y)], and position synchronized output (PSO) signals that were measured during the patterning of a 1-μm-diameter octagon. The nominal commanded XY stage velocity and PSO firing distance were set to 1.0 μm/s and 4.0 μm, respectively. [Units: position (μm), velocity (μm/s)]

respectively. However, an appreciable delay between PSO firing events is observed during the transition through the vertex that adjoins segment 6 and segment 7.

The measured PSO firing interval has increased from the nominal value of 4.0 ms to a much larger value of 67.0 ms during the transition through the vertex region, and this delay is correlated with the velocity and inertial variations of the motion control platform stages that occur during directional changes along the tool path. The measured 3D-vectored *travel distance*, however, still corresponds to a value of 4.0 μm and reflects that the PSO firing interval is dependent on the predefined and preprogrammed PSO travel distance and is independent of the pattern velocity. Figure 9.7b shows expanded views of the measured Pos(x) and Pos(y) signals that were acquired at the vertex location highlighted by the circle in Fig. 9.7a. The position data in Fig. 9.7b more clearly reveal the 3D-vectored travel distance of 4 μm and also indicate that the primary component of the travel distance corresponds to the Δ[Pos(y)] value; this behavior is expected for the transition between segment 6 and segment 7 (cf., inset showing octagon geometry transition points).

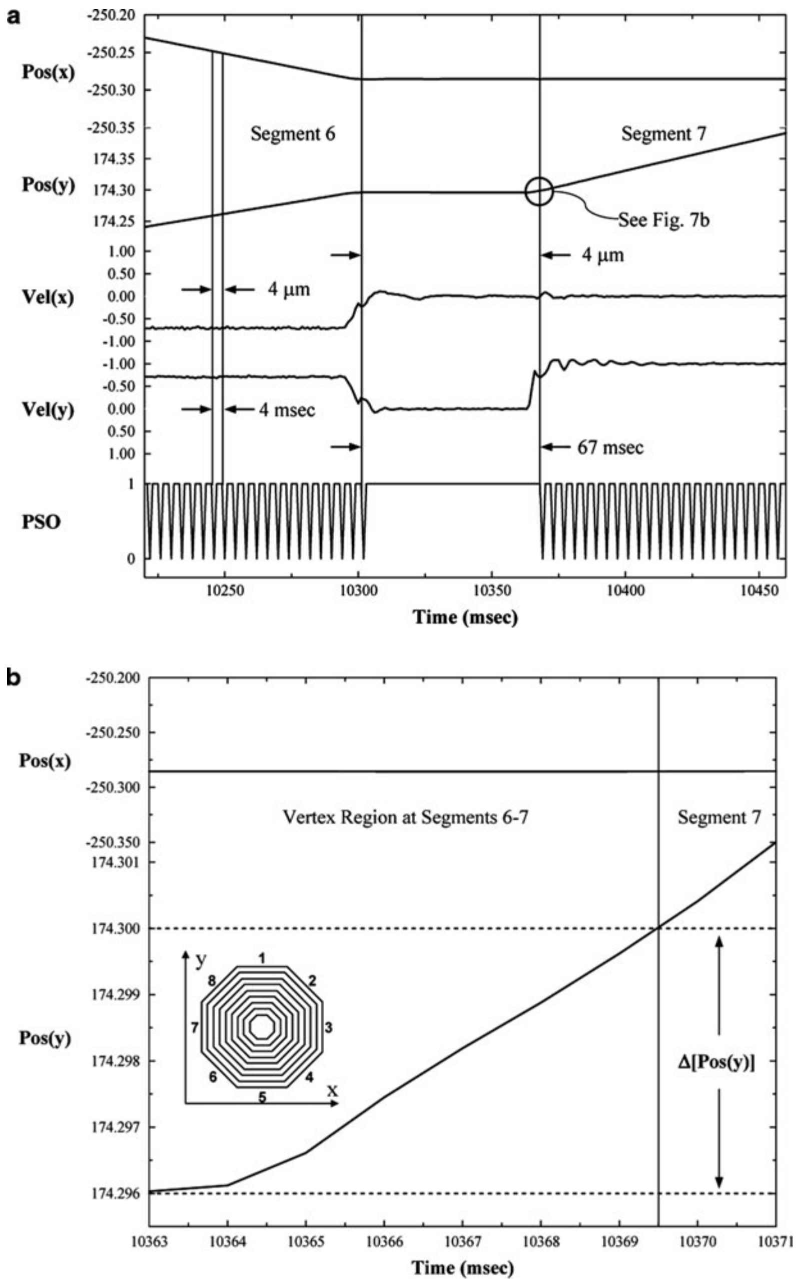

Fig. 9.7 (**a**) Close-up views of the position [Pos(x), Pos(y)], velocity [Vel(x), Vel(y)], and position synchronized output (PSO) signals that were measured during the transition from segment 6 to segment 7. Note that the firing of the PSO signals is suspended during the transition through the vertex region, and despite the significant increase in the delay between PSO signal events, the corresponding travel distance remains equivalent to the predefined PSO distance of 4.0 µm. (**b**) Expanded views of the measured position signals that were acquired at the vertex location highlighted by the *circle* in Fig. 9.7a. [Units: position (µm), velocity (µm/s)]

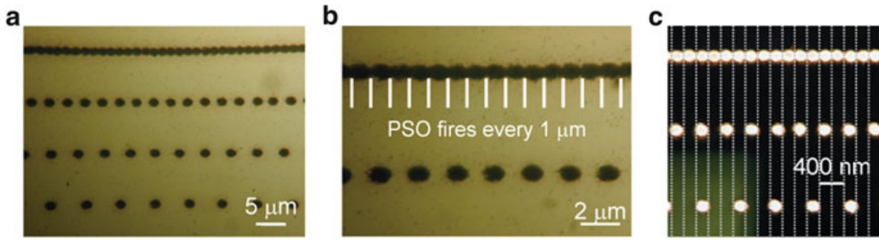

Fig. 9.8 Single-pulse ablation results showing the fidelity of the PSO control and the correlation with the experimental laser spot size. (**a**) Low magnification and (**b**) high magnification microscope images acquired following the ablation of a gold thin-film deposited on quartz. The PSO firing distances were predefined as: (**a**) from top row to bottom row: 1 μm, 2 μm, 3 μm, and 5 μm. (**b**) 1 μm (top) and 2 μm (bottom). (**c**) High magnification microscope image acquired following the ablation of a polyimide film, where the PSO firing distances were predefined as 200 nm (top), 400 nm (middle), and 600 nm (bottom)

The fidelity of the position synchronized output control and the correlation with laser spot size were empirically examined by performing ablation tests on metallic and polymer thin-films. Figure 9.8a shows the low magnification (20x) photomicrograph results that were acquired following the single-pulse ablation of a 1000 Å gold film deposited on a quartz substrate, where the predefined PSO firing distance was varied from 1.0 μm to 5.0 μm. Ablation was achieved using laser irradiation at $\lambda = 800$ nm and a pulse repetition rate of 5.0 kHz. The laser pulse length (fwhm) was 500 fs and the single per-pulse fluence was set to 5 J/cm^2 with an incident laser spot diameter of 1.0 μm. The microscope images in Fig. 9.8a show several sets of ablation patterns, where each pattern comprises a series of ablation holes and the period spacing is determined by the predefined PSO firing distance. Figure 9.8b displays a high magnification (50x) expanded view of the single-pulse ablation hole patterns that were obtained using PSO firing distances of 1.0 μm (top row) and 2.0 μm (bottom row). The results presented in Fig. 9.8b show that the outer edges of each distinct laser-irradiated and ablated spot are serially linked when the PSO distance is equivalent to 1.0 μm, and clearly demonstrate that the PSO firing distance can be selectively tuned to match the experimental laser spot diameter.

The PSO functionality is further illustrated in Fig. 9.8c, which displays the photomicrograph images acquired following the single-pulse ablation of a 100 μm-thick polyimide (Kapton$^{\text{TM}}$) film at $\lambda = 400$ nm. The pulse repetition rate was 5.0 kHz and the pulse length (fwhm) was 500 fs. The laser beam was focused to a spot diameter of ca. 200 nm and corresponds to a per-pulse fluence of 10 mJ/cm^2. The ablation hole patterns presented in Fig. 9.8c were prepared using predefined PSO firing distances of 200 nm (top), 400 nm (middle) and 600 nm (bottom). The polyimide ablation results reveal that the PSO firing distance can be defined and controlled to match the laser spot diameter at near diffraction-limited length scales. The ability to correlate the PSO firing distance and the laser spot size facilitates the delivery of preprogrammed genotype pulse scripts on a per spot basis, and ensures that the

application of a precision photon dose is determined solely by the travel distance and is independent of the local velocity of the motion control platform.

9.2.3.2 Velocity Compensation via PSO Control

Next we examine the capability to compensate for variations in motion control platform velocity during laser patterning and ensure that each laser spot receives an equivalent and prescribed photon exposure dose. Figure 9.9 displays the oscilloscope traces that correspond to several critical signals measured during the ablative patterning of gold deposited on quartz. The ablated pattern is a square wave geometry with overall dimensions of 1,650 μm × 400 μm and a 300 μm pitch. Ablation was achieved using laser irradiation at $\lambda = 800$ nm, a pulse repetition rate of 5.0 kHz and a pulse length of 520 fs. A nominally low programmed velocity of 0.50 μm/s was employed due to the low laser repetition rate. The PSO signals, which appear as negative voltages in the top trace in Fig. 9.9, mark the traverse of

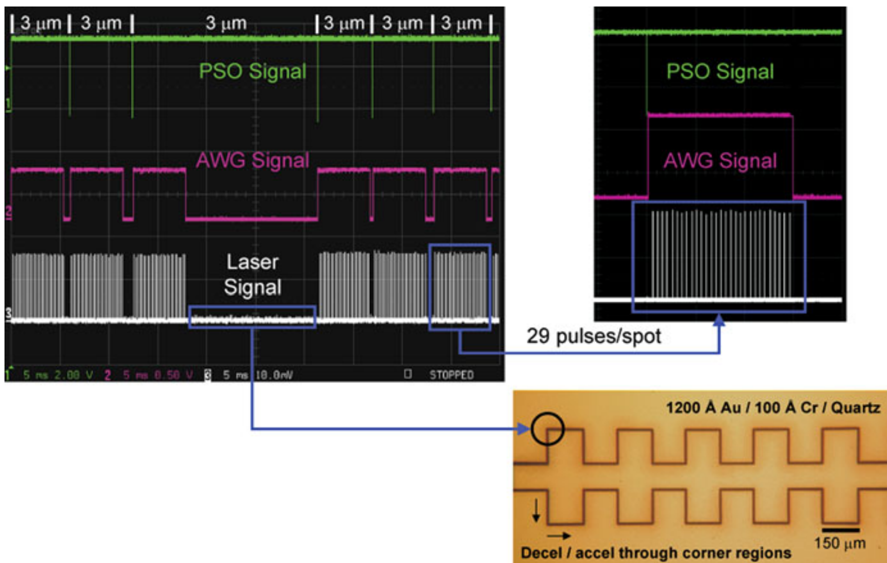

Fig. 9.9 Oscilloscope traces (left and expanded right) that were measured during the genotype-scripted ablative patterning of a gold thin-film deposited on quartz. The raster pattern corresponds to a square wave geometry (*lower right*) with a 300-μm pitch. The position synchronized output (PSO) signals are denoted by the top trace and mark the traverse of 2D-vectored distances of 3 μm in XY Cartesian space. The arbitrary waveform signal generator (AWSG) signals are represented by the *middle trace* and define the voltage pulse scripts that trigger the delivery of a prescribed 29 pulses to each spot during pattering. The *bottom trace* shows the laser pulses, as measured by a photodiode, that were measured during patterning and represent the composite laser ablation process script

2D-vectored distances of 3 μm in XY Cartesian space. The PSO firing distance was predefined to be equivalent to the laser spot size of 3 μm. Note that the PSO signals arrive at non-uniform time intervals. This variation in PSO firing frequency is related to the changes in local velocity of the motion control platform that occur while negotiating the square wave pattern. The middle trace in Fig. 9.9 represents the measured arbitrary waveform generator signals that define the individual voltage pulse scripts (waveforms) which are amplified and synchronously transmitted to the electro-optic modulator. The bottom trace in Fig. 9.9 represents the incident laser pulse signals that were measured by a photodiode. The expanded view shows the delivery of a prescribed 29-pulse exposure dose to each sequential laser spot.

For this demonstration, the arbitrary waveform signal generator was commanded to synthesize a simple square wave that comprised 29 pulses of equivalent amplitude. The results shown in Fig. 9.9 indicate that *each* PSO firing event triggers the generation of a *single* square wave, and the formation of this voltage pulse script is independent of the local velocity of the motion control stages and time duration between successive PSO trigger signals. In the center of the bottom oscilloscope trace we have highlighted a region in the motion tool path where a significant change in local velocity has occurred during the transition through a corner region of the saw tooth pattern. The measured PSO signals occur at 6 ms time intervals while traveling along straight line sections at the nominal velocity of 0.50 μm/s. However, the motion control platform velocity slows by a factor of nearly three while transitioning through the 90° corner over a spot size distance of 3 μm. Despite the significant reduction in the motion control platform velocity, precisely 29 laser pulses are delivered to the substrate as prescribed. This result highlights the synchronization of the software and hardware control systems, and illustrates that the composite system waits until the motion control platform has transitioned into a new "fresh" surface region before allowing the administration of additional laser pulses to the substrate. In our current configuration, up to 32 individual pulse script profiles can be dynamically selected and concatenated in real time ad infinitum, and can routinely be applied to the substrate surface in the form of laser pulse scripts at motion velocities exceeding 400 μm/s and laser spot sizes less than 500 nm.

9.2.3.3 Site-Selective Pulse Script Variation

The ability to alter the voltage pulse scripts at every laser spot location and consequently deliver different laser pulse scripts to adjacent spots is a powerful feature of this new technique and represents an unprecedented resource in the field of laser material processing. This capability has profound consequences for the development of novel materials that are the result of precise localized changes in adjacent functional units or chemical entities. Figure 9.10 shows the laser patterning results in which the voltage pulse scripts were altered "on the fly" as the motion control platform performed patterned maneuvers. Figure 9.10a shows the oscilloscope traces that were captured by a photodiode and correspond to four modulated laser

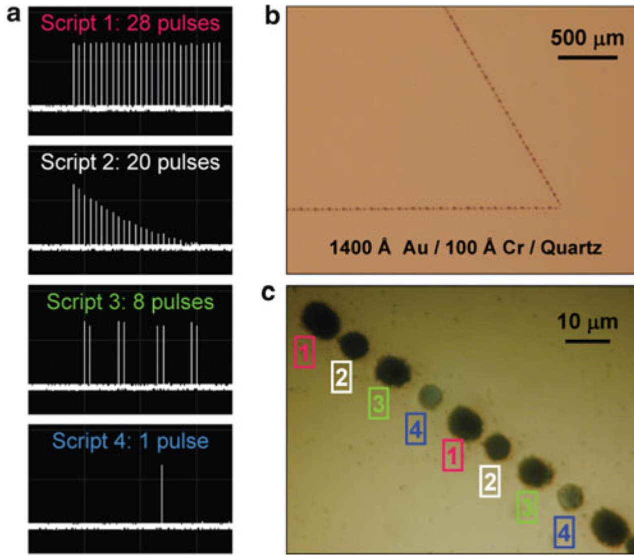

Fig. 9.10 Ablation results showing the capability to selectively and synchronously deliver different laser pulse scripts to each irradiated spot during patterning. (**a**) Oscilloscope traces that correspond to the four laser ablation pulse scripts as detected by a photodiode during patterning. Script 1: 28 laser pulses of equivalent amplitude; Script 2: 20 laser pulses with monotonically decreasing amplitude; Script 3: 8 laser pulses in a quartet of doublets; and Script 4: a single laser pulse. (**b**) Low magnification and (**c**) high magnification microscope images of the ablation patterns, where the ablation regions are identified by their respective laser pulse scripts

pulse scripts that were sequentially administered to a gold film deposited on a quartz substrate. Low-magnification and high-magnification microscope images of the ablation pattern are displayed in Figs. 9.10b and 9.10c, respectively. The ablation was performed using 500-fs pulses at a wavelength of 800 nm and a pulse repetition rate of 5.0 kHz. The number and amplitude of the pulses comprising the four laser pulse scripts were as follows: *script 1*: 28 laser pulses of equivalent amplitude, $E = 1$ J/cm^2; *script 2*: 20 laser pulses with sequentially descending amplitude, $E = 2.3$ J/cm^2 to $E = 0.17$ J/cm^2; *script 3*: 8 laser pulses in a quartet of doublets, $E = 3.3$ J/cm^2; and *script 4*: a single laser pulse, $E = 1.2$ J/cm^2. The results shown in Fig. 9.10c correspond to two sequential four-script applications. For ease of analysis and visual clarity, the laser pulse scripts have been applied at a PSO firing distance of 10 μm which is larger than the laser spot diameter of 3 μm. As anticipated, the results reveal a significant change in the ablated shape and morphology associated with the variegated laser pulse scripts. More reassuring, however, is the fact that the ablated surface for each laser pulse script is equivalent when comparing the corresponding spot within each of the two four-script sequences. This supports the proposed notion that the application of diverse laser pulse scripts can facilitate controlled material transformation on a highly localized scale with high fidelity.

9.3 Selected Applications

9.3.1 Photosensitive Glass Ceramics: A Candidate Protean Material Class

The laser genotype pulse modulation technique is highly versatile and can be utilized with virtually any laser system and applied to essentially any type of laser-material interaction process. A fundamental goal of our research is to develop laser pulse scripts that induce specific material transformation processes during coordinated direct-write patterning, and to acquire a detailed understanding of the underlying photophysics and chemistry that relates to these laser-induced conversion processes. Our prior studies have examined the laser-induced photophysical processes that occur in a commercial photostructurable glass ceramic known as Foturan^{TM} (MikroGlas, Germany). Specifically, we have investigated the efficiency and mechanisms of the photoexcitation process [52, 53], the sensitivity of the nascent chromophore to various exposure wavelengths [44, 54–56], the corresponding phase separation and chemical solubility of the laser-exposed material [52, 53], the applicability of the photoexposure and chemical etching for 3D volumetric patterning and structure fabrication [53, 56–59], and the selective material properties that can be influenced by the photon dose [43, 53, 56].

Foturan is an amorphous photostructurable glass ceramic of the alkali aluminosilicate family. A photosensitive agent (cerium, Ce^{3+}) is incorporated in the base glass which undergoes ionization ($Ce^{3+} + h\nu \rightarrow Ce^{4+} + e^{-}$) upon irradiation to release an electron that is nominally trapped in a defect site. Subsequent thermal treatment "fixes" the exposure process, where the trapped photoelectrons reduce the nascent silver ions ($Ag^{+} + e^{-} \rightarrow Ag^{0}$). At moderate thermal treatment temperatures of ≈500°C, the diffusion rate of Ag^{0} is sufficient to induce the agglomeration of silver nanoparticles, $(Ag^{0})_x$. When the silver nanoparticle size grows to a critical diameter of ≈8 nm, precipitation and growth of lithium metasilicate crystallites occur around the silver nanoparticles. Depending on the maximum thermal treatment temperature, the in situ phase segregation event can result in the eventual formation of two primary silicate phases: (1) a lithium metasilicate (Li_2SiO_3) crystalline phase which is soluble in dilute hydrofluoric (HF) acid, and in similar glass systems, is known to dissolve in the base glass at high temperatures (>800°C), and (2) a lithium disilicate ($Li_2Si_2O_5$) crystalline phase which is relatively insoluble in HF, but grows at higher bake temperatures and can survive to high temperatures near 900°C.

9.3.1.1 Modification of Optical Properties

The results of our comprehensive studies [23, 31, 32, 43, 44, 52, 53, 56] indicate that photostructurable glass ceramics represent strong protean material candidates, where laser excitation can be used to alter material properties with high fidelity and

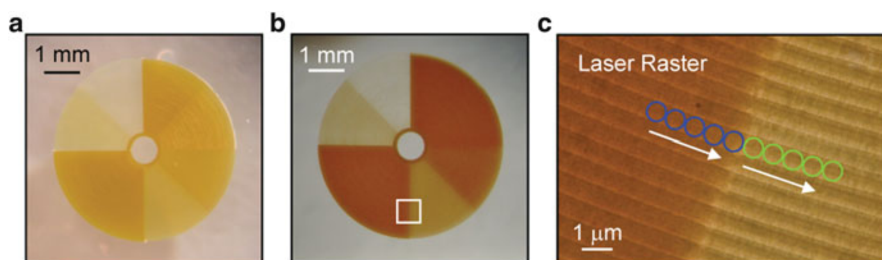

Fig. 9.11 (**a-b**) Microscope images of circular multistep attenuators that were created using laser-scripted processing to control the number and intensity of laser pulses delivered to each spot during continuous direct-write concentric patterning. (**c**) High-magnification microscope image showing the transition region between adjacent attenuation sectors depicted by the highlighted box in (**b**)

produce or "express" multiple functionalities in a single base material [23, 31, 32]. For example, the laser-scripted modulation technique can be implemented to control the density of lithium metasilicate crystallites that are formed in Foturan following laser excitation and thermal processing and tailor the optical transmission properties of the glass ceramic in the visible and infrared wavelength regions [23, 31]. These capabilities facilitate the fabrication of variable wavelength attenuators and embedded cutoff filters, and could stimulate the development of new 3D bit-data storage and RW-memory devices.

Figures 9.11a and 9.11b show the optical photomicrographs of two circular multistep attenuators that were prepared using laser-scripted direct-write processing. Sixteen distinct laser pulse scripts were designed to synchronously control the number of laser pulses that were administered to each section of the optical filter elements, and regulate the total exposure dose that was delivered to each spot during concentric patterning. The results in Figs. 9.11a and 9.11b reveal the formation of diverse hues related to each attenuation sector, where the color variations are associated with the respective lithium metasilicate crystallite densities formed in the glass ceramic. A transition region between adjacent attenuation sectors is depicted in the magnified microscope image in Fig. 9.11c, and corresponds to the real time selection and application of individual laser pulse scripts during photoexposure. The photomicrograph reveals that the transition between regions of different density occurs over lengths scales that are equivalent to the laser spot size; transition regions are limited to domain sizes of $\sim 1\,\mu$m due to the size of the lithium metasilicate crystallites that are formed during the thermal treatment steps required for nucleation and growth.

9.3.1.2 Silicate Phase Fractionation

The laser genotype processing approach was recently utilized to explore the effect of various amplitude modulated laser pulse scripts on the preferential growth and dissolution kinetics of the primary metasilicate and disilicate phases in Foturan [31,32]. Three discrete pulse scripts were designed to deliver equivalent total photon exposures (doses), but each script contained a different number of pulses: region *A*,

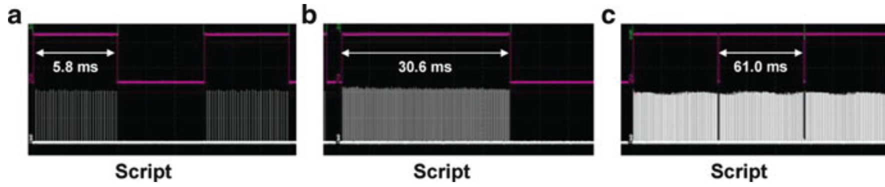

Fig. 9.12 Measured oscilloscope traces of the three laser pulse scripts that were utilized to explore the preferential growth and dissolution kinetics of the primary metasilicate and disilicate phases in a commercial photosensitive glass ceramic, Foturan. The laser pulse scripts were designed to deliver equivalent total photon exposures, but retained a different number of pulses: script (**a**) 29 pulses/spot, E = 1 J/cm^2; script (**b**) 153 pulses/spot, E = 211 mJ/cm^2; and script (**c**) 305 pulses/spot, E = 100 mJ/cm^2

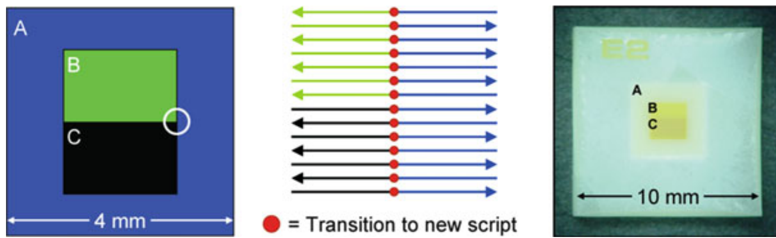

Fig. 9.13 *Left*: CAD illustration of the raster pattern comprising three juxtaposed regions (*A*, *B*, and *C*) that received the three preprogrammed laser pulse scripts shown in Fig. 9.12. *Middle*: Schematic showing the laser pulse script transition points for the three exposure patterns. *Right*: Microscope image of the three laser-exposed regions on a Foturan coupon following a two-step thermal treatment at 500°C (1 h) and 800°C (1 h)

29 pulses/spot, E = 1 J/cm^2; region *B*, 153 pulses/spot, E = 211 mJ/cm^2; and region *C*, 305 pulses/spot, E = 100 mJ/cm^2. Figure 9.12 shows the measured oscilloscope traces for the three square wave laser pulse scripts, along with the laser pulses detected by a photodiode during raster patterning. The peak height equivalence revealed in Fig. 9.12 is an artifact of the amplitude auto-ranging feature of the digital oscilloscope. The laser-scripted exposures were performed using 800-nm irradiation with a pulse length of 500 fs and a pulse repetition rate of 5.0 kHz.

The left panel in Fig. 9.13 displays a schematic illustration of the raster pattern that was used for the laser-scripted exposure of a 1 cm × 1 cm × 1 μm Foturan coupon. The raster pattern comprised three juxtaposed regions denoted as *A*, *B* and *C*, where each region received a different laser pulse script. The middle panel in Fig. 9.13 shows an expanded view of the transition points for the three laser exposure patterns and highlights a critical junction where transitions occur from region *B* to region *A* and from region *A* to region *C*. The composite raster pattern was created using a sequential line fill and a line scan step-over distance that was equivalent to the laser spot diameter of 3 μm.

The right panel in Fig. 9.13 shows an optical photomicrograph of the Foturan coupon following high temperature thermal processing at 800°C. The results reveal

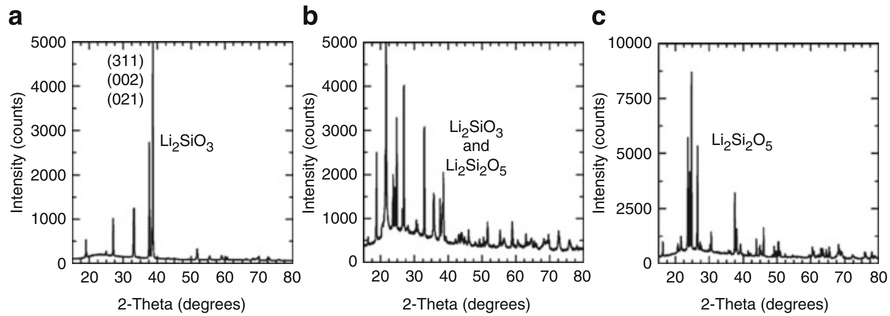

Fig. 9.14 X-ray diffraction results obtained for the three laser-exposed and thermally processed regions showing the simultaneous formation of various and distinct silicate phases for each respective laser pulse script. (**a**) Extreme preferred orientation for lithium metasilicate, Li_2SiO_3. (**b**) Mixed-phase system comprising lithium metasilicate-disilicate, Li_2SiO_3-$Li_2Si_2O_5$. (**c**) Predominant formation of lithium disilicate, $Li_2Si_2O_5$

that the three exposed regions display dramatically different colors: region *A* – milky white, region *B* – light yellow, and region *C* – mustard. Simple alterations in the laser pulse script have enabled the controlled variation of the optical properties; more importantly, however, are the profound changes that have occurred which relate to silicate phase fractionation in the glass ceramic. Figure 9.14 shows the X-ray diffraction (XRD) spectra measured for each of the three regions displayed in Fig. 9.14. The XRD results reveal the *simultaneous* formation of several distinct silicate phases in Foturan. The XRD spectrum measured for region *A* reveals the exclusive formation of Li_2SiO_3 crystals that retain an extreme preferred orientation and correspond to the chemically soluble lithium metasilicate phase. In contrast, the XRD spectrum measured for region *C* shows the predominant formation of $Li_2Si_2O_5$ crystals, which correspond to the lithium disilicate phase that is chemically insoluble and can withstand temperatures exceeding 800°C. Finally, the XRD spectrum measured for region *B* shows the growth of a mixed phase comprising both metasilicate and disilicate phases.

Using Foturan as a candidate protean material, these results demonstrate that it is possible to locally alter the phase state of the material and thus control various chemical and physical properties, including the chemical solubility, optical transmission and absorption, mechanical compliance and strength, and operational temperature. With the laser genotype processing architecture, one can envision the fabrication of a multifunctional device, where the individual material property changes are created or expressed by the delivery of discrete laser pulse scripts. For example, the development of miniature, fully integrated next-generation space satellites [60] will require the co-fabrication of a complex set of functionalities that could be realized with the application of the appropriate laser pulse scripts:

1. Regions that guide light – e.g., waveguides fabricated by laser compaction,
2. Regions where material must be removed – e.g., microfluidic channels fabricated by the laser induced precipitation of a chemically soluble crystalline phase,

3. Regions that are resistant to high temperature operation – e.g., combustion chambers and exhaust plume nozzles formed by the laser induced precipitation of a high temperature crystalline phase,
4. Regions where the optical absorption and transmission must be tuned for selective bands – e.g., optical filters fabricated by the laser induced formation of optical defects or nanoparticles, and
5. Regions where surface or embedded metallization is required – e.g., electronic interconnects fabricated by laser filamentation or laser-induced plasma assisted ablation (LIPAA).

9.3.2 Nanostructured Perovskite Thin-Films

Complex metal oxides have enjoyed success as low loss dielectric layers in thermal pyroelectric detectors [61] and as electroacoustic transducer elements in piezoelectric sensors [62]. Pyroelectric-based infrared sensors, in particular, retain a number of attractive attributes compared with traditional thermopiles and resistive bolometers, including uncooled room-temperature operation, broad wavelength response, and high stability and high sensitivity. Recent advances in the bio-inspired/biomimetic synthesis of nanostructured multimetallic perovskites have enabled the fabrication of high quality, stoichiometric and homogeneous perovskite thin-films via low cost and low energy processes [49, 63, 64]. The bio-inspired synthetic pathways are compatible with monolithic integration with commercially fabricated readout integrated circuits, and facilitate rapid prototype development and manufacture along with batch processing and quality control. Consequently, perovskite nanoparticle thin-films have received significant recent attention in a diverse array of military, homeland security and intelligence community sensing applications [65].

Nanostructured barium titanate ($BaTiO_3$) thin-films have stimulated noteworthy interest related to the development of novel uncooled passive IR capacitive sensors since $BaTiO_3$ possesses the high pyroelectric coefficients and low dielectric loss tangents that are requisites for high figure of merit values. We are now investigating the feasibility and facility of utilizing laser direct-write techniques to induce site-selective and patterned micro- and nanoscale transformation of $BaTiO_3$ nanoparticle aggregates from the nascent pyroelectrically inactive cubic phase to the pyroelectrically active tetragonal phase [49, 50]. Prior XRD and Raman studies on barium titanate system ranging from macroscopic powders to monodispersed fine particles have revealed that the cubic-to-tetragonal phase transformation occurs at temperatures of ca. 900–1100°C [66–72]. This phase conversion has typically been accomplished using conventional resistive and furnace heating [73]. Unfortunately, these traditional thermal processing techniques lead to global phase transformations, where the entire deposited $BaTiO_3$ film undergoes structural conversion. This limitation eliminates spatial control and pattern capability, and prevents the highly

selective and localized activation/deactivation of pyroelectric/non-pyroelectric domains in the thin-film $BaTiO_3$ substrates.

9.3.2.1 Conventional Laser Direct-Write Processing

Two distinct laser processing approaches were employed to examine laser-mediated pyroelectric phase conversion in bio-inspired $BaTiO_3$ nanoparticle thin-films: conventional laser direct-write processing and genotype-inspired, digitally scripted laser processing. The contrasting results from these two approaches clearly illustrate the importance of synchronized, high fidelity photon modulation during laser patterning. In the conventional laser direct-write processing scenario, the incident and repetitive laser pulse train remains unarticulated, and the only modulation employed corresponds to simple power control; i.e., the laser pulse intensities are uniformly attenuated to achieve the desired static power level and per-pulse fluence for material exposure and processing. Figure 9.15 provides a compilation of the Raman spectra that were measured for a set of 500-nm-thick $BaTiO_3$ thin-films following conventional laser direct-write processing at $\lambda = 355$ nm. Panel (*a*) in Fig. 9.15 shows the Raman spectrum acquired for the as-prepared cubic $BaTiO_3$ prior to exposure, as well as the comparison spectrum for tetragonal $BaTiO_3$.

The vertical lines denote the locations of the prominent Raman-active bands associated with the tetragonal phase of $BaTiO_3$, which occur at 305 cm^{-1}, 540 cm^{-1}, and 720 cm^{-1}. The cubic-to-tetragonal phase conversion was examined over a wide laser parameter space, including power and per pulse intensity, pulse repetition rate, pulse length, and total exposure dose. The variation in laser pulse repetition rate is used to elucidate the kinetics of energy transfer into the $BaTiO_3$ crystal lattice system. Additionally, the variation in pulse length provides information for determining whether partial or complete phase conversion can be accomplished during a single pulse event (intra-pulse) or by the administration of a succession of laser pulses (inter-pulse).

Panels (*b*)–(*e*) in Fig. 9.15 display the Raman results obtained under these various processing conditions, and reveal several important features. The lower power and higher pulse repetition rate exposures yielded little change in the Raman spectra, and indicate that the pulse energies and related thermal transients were insufficient to induce phase conversion. The higher power and lower pulse repetition rate exposures also show no evidence of structural phase conversion, but did reveal appreciable film fracture and material desorption due to excessive heat loading and thermal confinement. The laser excitation wavelength of $\lambda = 355$ nm was selected due to the relatively low absorptivity ($\approx$25%) of the nascent $BaTiO_3$ thin-films, thereby facilitating a large or extended laser processing window. With a large laser process window the determination of the appropriate laser pulse energetics and processing parameters required to achieve phase transformation becomes easier. However, the composite results shown in Fig. 9.15 strongly suggest that enhanced, high fidelity laser pulse and heating control are needed to promote phase conversion,

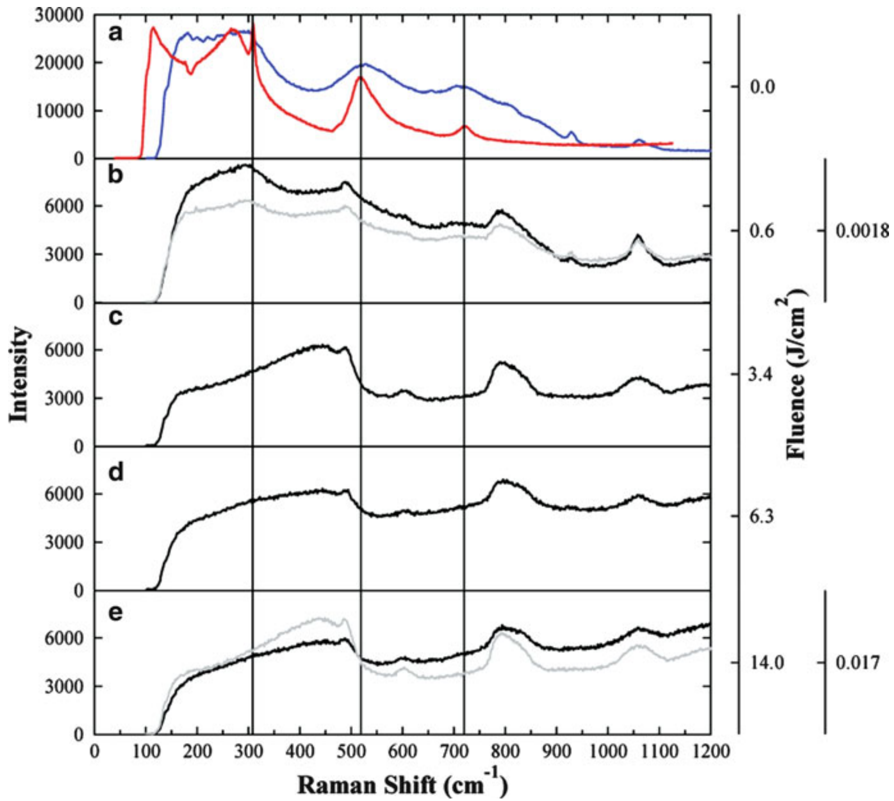

Fig. 9.15 Raman spectra measured for bio-inspired $BaTiO_3$ thin-films following conventional laser direct-write processing under various experimental conditions at $\lambda = 355$ nm. (**a**) Unexposed cubic phase spectrum (*blue*) and tetragonal phase reference spectrum (*red*). (**b**) 30 pulses at 10 kHz (*black*) and 8,000 pulses at 80 MHz (*grey*). (**c**) 120 pulses at 50 kHz. (**d**) 60 pulses at 20 kHz. (**e**) 30 pulses at 10 kHz (*black*) and 24,000 pulses at 80 MHz (*grey*). The inner right ordinate axis corresponds to the per-pulse fluence values for the lower repetition rate (10–50 kHz; 5 ns pulse width) exposures, while the extended ordinate axis corresponds to the per-pulse fluence values for the higher repetition rate (80 MHz; 10 ps pulse width) exposures

while maintaining the overall integrity and mechanical stability of the $BaTiO_3$ thin-films.

9.3.2.2 Genotype-Inspired, Digitally Scripted Laser Direct-Write Processing

Figure 9.16 displays a set of Raman spectra that were acquired following laser processing of 500-nm-thick $BaTiO_3$ thin-films using the genotype-inspired, digitally scripted laser direct-write technique. The tetragonal phase spectra measured following furnace heating at 1000°C for 30 min and 600 min are provided for

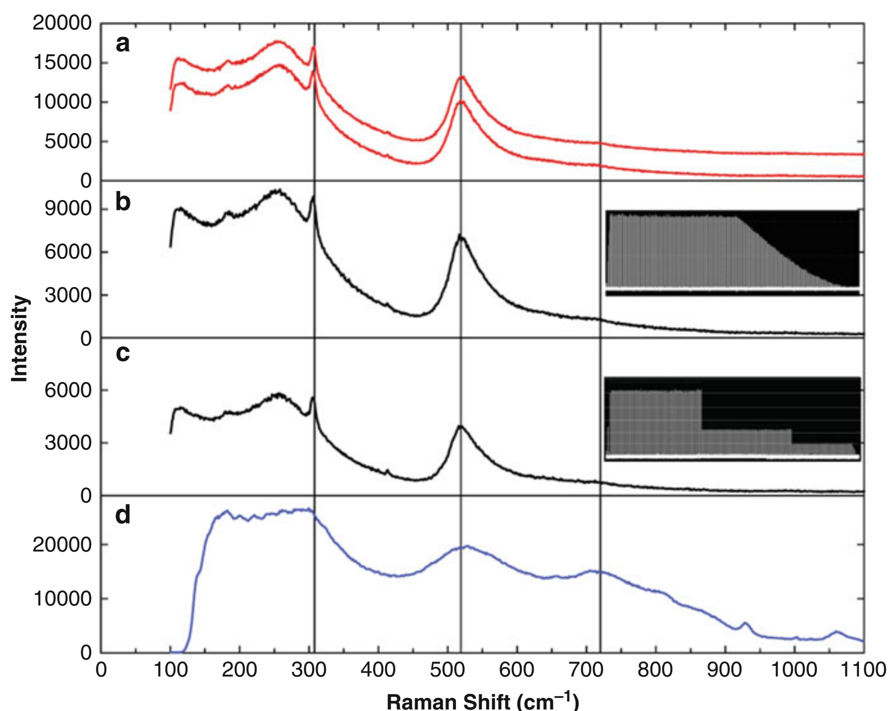

Fig. 9.16 (**a**) Tetragonal phase spectra acquired after furnace heating at 1,000°C for 30 min (*top*) and 600 min (*bottom*) with no laser exposure. (**b**)–(**c**) Raman spectra measured for bio-inspired $BaTiO_3$ thin-films following digitally scripted, laser genotype direct-write processing at $\lambda = 355$ nm. The respective laser pulse scripts are shown in the insets. (**d**) Unexposed cubic phase spectrum of the nascent $BaTiO_3$ thin-film prior to phase conversion

comparison and are represented by the top and bottom spectra in Fig. 9.16a, respectively. The Raman results shown in Fig. 9.16b, c correspond to $BaTiO_3$ thin-films that were exposed to incident laser irradiation at $\lambda = 355$ nm (80 MHz; 10 ps pulse width) using the composite laser pulse scripts shown in the insets. The composite laser pulse scripts were synchronously delivered to each laser-irradiated spot (1–3 μm diameter) during patterning, where the laser raster pattern corresponded to a 2 μm $\times$ 2 μm square with a sequential line fill, and a step-over between line scans that was equivalent to the laser spot size. For Fig. 9.16b, the composite pulse script contained a total of 300 pulses, and comprised two individual concatenated pulse scripts. The primary pulses (1–150) were of equivalent amplitude (per-pulse fluence = 0.6 J$\cdot$cm^{-2}), and were intended to rapidly increase the temperature of the $BaTiO_3$ nanoparticle thin-film above the phase transition temperature. The secondary pulses (151–300) were of monotonically decreasing amplitude, and were meant to maintain the temperature at or near the phase transition temperature and facilitate the controlled cooling of the $BaTiO_3$ nanoparticle thin-film. For Fig. 9.16c, the composite pulse script again contained a total of 300 pulses, but now comprised

three individual concatenated pulse scripts in a "stair-step" sequence. The laser pulses comprising each individual script were of equivalent amplitude, and retained the following per-pulse fluence values: pulse set 1 (1–100), $0.60\ \mathrm{J \cdot cm^{-2}}$; pulse set 2 (101–200), $0.25\ \mathrm{J \cdot cm^{-2}}$; and pulse set 3 (201–300), $0.11\ \mathrm{J \cdot cm^{-2}}$. In this composite pulse script, pulse set 1 was intended to increase the temperature of the $BaTiO_3$ nanoparticle crystal lattice above the phase transition temperature, and pulse sets 2 and 3 were designed for maintaining the phase transition temperature along with controlling the cooling rate of the $BaTiO_3$ nanoparticle thin-film.

The results presented in Fig. 9.16b, c reveal the presence of several new peaks not evident in the cubic phase spectrum of the as-prepared unexposed $BaTiO_3$ thin-film [spectrum (*d*)], and are correlated with the phase transformation to the tetragonal pyroelectric polymorph. By comparison with the tetragonal phase spectra in Fig. 9.16a, the extent of laser-induced pyroelectric conversion is qualitatively consistent with the phase conversion attained via bulk furnace heating. Of more importance are the results of the subsequent microscopic structural analysis, which revealed little or no damage to the $BaTiO_3$ thin-film. These results illuminate the importance of utilizing distinct laser pulse scripts to control heat (energy) flow into the phonon subsystem for improved distribution of temperature throughout the $BaTiO_3$ crystal lattice. The results also imply that the laser-induced phase conversion occurs over a period of several microseconds. Preliminary modeling studies of the interaction between picosecond laser pulses and single $BaTiO_3$ nanoparticles indicate that the electron thermalization and cooling rates are very rapid, and that the lattice temperature distributions can be adequately described using a "one-temperature" model [74, 75]. These initial modeling investigations further suggest that the $BaTiO_3$ cubic-to-tetragonal phase transformation temperature is attained within several hundred picoseconds. We are continuing to explore the digitally scripted laser-induced phase conversion in bio-inspired $BaTiO_3$ nanoparticle thin-films, along with examinations of the kinetics and mechanisms associated with the transformation process.

9.4 Summary and Perspective

9.4.1 Laser Genotype Process Integration

We have developed a new architecture for laser material processing that permits the controlled and precise delivery of laser photons to a substrate during direct-write patterning. The laser material processing approach derives inspiration from the genome concept and genotype functionality, where predetermined and prescribed sequences of concatenated laser pulse scripts (i.e., a "Process Script") are merged with the Cartesian tool path (i.e., a "Pattern Script"), and each laser pulse script is intended to express a specific material attribute. Since the laser pulse modulation is synchronously matched with the tool path geometry in a line-by-line fashion, each

laser-irradiated spot receives the appropriate photon exposure that is required for the desired photophysical outcome. The laser processing architecture is highly versatile and allows the integration of other powerful functionalities, including synchronized polarization control for optical poling applications and real time diagnostics for in situ end point control and process optimization. The laser genotype processing architecture can be readily applied to fundamental investigations of complex laser-material interaction phenomena, and is particularly well suited for protean or mutable materials that can be transformed with extreme sensitivity by the application of high-precision photon exposures. This new approach also facilitates the processing and alteration of heterogeneous materials comprising discrete and interconnected chemical entities that require a diverse array of processing conditions. We envision that multifunctional and adaptive materials can be altered on near diffraction-limited length scales to create fully integrated devices on a common substrate. The laser genotype technique can also be easily integrated into existing laser-material processing schemes and laser processing stations for commercial and industrial applications.

The continued development and refinement of the laser genotype processing architecture should have profound consequences for laser-based materials processing. The realization of significant future advances in laser material processing will rely particularly on the complementary development of new versatile micro- and nanomaterials and improved computer modeling of laser-material interaction phenomena. We envision the creation of new photosensitive metastable materials that will enhance systems integration and the viability and performance of next generation multifunctional devices. Attractive new materials should be photoactive and protean in nature, and thus capable of undergoing well controlled material transformation via selective and site-specific photolytic excitation. The compositional uniformity of these new materials will significantly affect the fidelity and efficiency of laser material processing approaches and influence device utility and performance. However, using the laser genotype processing approach, the compositional non-uniformities could be characterized prior to processing, and the laser pulse scripts could be appropriately designed and tailored to account for these material irregularities. Finally, as the fidelity of laser processing techniques improves and the development of new materials flourishes, there still exists a strong need for a detailed understanding of the underlying photophysics and photochemistry of laser-material interactions. For laser genotype-like processing architectures to be successful, the fundamental investigations (experimental and theoretical) must view the laser-material interaction phenomena from the perspective that there is a time-dependent evolution of a material's chemical and physical properties during laser irradiation. For example, computer simulations of electronic and lattice dynamics, phase transitions and heat transfer in solids will help to guide the formulation and tailoring of laser pulse scripts for optimum material processing.

Current and near-term improvements to the laser genotype processing approach include the implementation of synchronous polarization control and evolutionary algorithms and intelligent feedback loops. Polarization control permits the selective optical poling of materials for induced-dipole formation. Controlled variations in

the incident laser polarization can also affect the low-fluence surface texturing of metals and the fabrication of uniform width trenches via laser direct-write chemical etching. Genetic or evolutionary algorithms can be readily integrated into the laser genotype pulse modulation scheme to optimize the laser pulse scripts in real time for endpoint analysis and process control and to provide working pulse scripts for subsequent theoretical analysis. For example, in situ spectroscopic probes can be used to measure the photoluminescence characteristics and monitor the formation of transient metastable species or defect states in the irradiated material during patterning. Based on the measured spectral response of the substrate, the laser pulse script could be adjusted and optimized in real time to ensure the proper laser parameters are applied to achieve the desired phase transformation or other photophysical/chemical event.

9.4.2 Pulse Script Database: A Public Domain Catalog for Materials Processing

Sufficient evidence exists in the current literature to support the proposition that the sequential application of a series of tailored pulses is more efficient and effective for materials processing compared with the use of a single pulse or the global application of a pulse train. In this chapter, we have presented a laser-based materials processing approach that promotes the utilization of discrete laser pulse scripts to affect material transformations, in marked contrast to more traditional materials processing approaches where the laser power is fixed and fluctuations are minimized in order to define the optimum process window. The laser-scripted approach to materials processing could facilitate the generation of standardized laser pulse scripts that are designed for specific chemical and physical processes and tailored for particular material types. Fundamental photophysical measurements could be performed, for example, on individual samples under well controlled laser-scripted conditions, and the results could then be assembled to form a digest of laser pulse scripts for various types of material processing. The laser pulse script concept represents a workable context for theoretical and computer simulations of laser-material interaction phenomena, and modeling software could be adapted and designed to output the results in the form of an appropriate pulse script train.

These laser pulse scripts could then be promoted by material manufacturers, much like chemical recipes are provided with many material systems to describe the relevant processing and handling conditions. Conceivably, particular laser pulse scripts could have inherent commercial value and be treated as intellectual property. The authors would prefer an alternative approach where the laser pulse scripts remain in the open literature and public catalogs or script libraries could be developed where a user is able to download the specific laser pulse script for the desired material processing application. In this scenario, the laser pulses scripts would need to be standardized and formatted for consistency and be independent of how the laser pulse script was generated – e.g., theoretical model or experimental analysis.

In this regard, traditional quantitative descriptions of the laser exposure – e.g., average power, irradiance, and fluence – do not sufficiently convey the relevant parameters that are needed to define the photophysical interaction process. An alternate perspective is required: Perhaps the laser pulse scripts could be globally defined by an amplitude (intensity) function that describes the total photon exposure dose per spot. This amplitude function could be expanded using the appropriate Gaussian basis set, where the amplitude coefficients are derived via a Laplace or Fourier transform. Based on this mathematical formalism, a user would generate a Gaussian basis set function that is related to the Gaussian temporal shape of the user's individual laser pulse. The mathematical transformation would yield a series of coefficients and time delays that can be predefined and experimentally implemented. The combination of the amplitude coefficients and time delays, along with the Gaussian basis set, would then enable the reconstruction of a standardized laser pulse script function.

Acknowledgements The authors gratefully acknowledge support for this research from The Aerospace Corporation's Independent Research and Development Program (IR&D) and Product Development Program, and The Air Force Office of Scientific Research (Dr. H. Schlossberg, Program Manager). FEL also acknowledges financial support for the laser processing studies on perovskite thin-films from the U.S. Army Research Office through grant DAAD19-03-D-0004 to the Institute for Collaborative Biotechnologies and contract DAAD19-03-D-0004 Subagreement No. KK8132 from the Army Research Laboratory (ARL) to The Aerospace Corporation, Institute for Collaborative Biotechnologies and the ARL Sensors and Electron Devices Directorate (Dr. N. Fell, Jr., Program Manager). The authors recognize the efforts of W.W. Hansen (electronic systems design), L.F. Steffeney (CAD-CAM programming) and P.M. Adams (XRD and Raman analysis).
All trademarks, service marks, and trade names are the property of their respective owners.

References

1. D. Bäuerle, *Laser Processing and Chemistry*, 1st edn. (Springer, Heidelberg, 1986)
2. L.D. Laude, D. Bäuerle, M. Wautelet (eds.), *Interfaces Under Laser Irradiation, NATO ASI*, vol. 134 (Martinus Nijhoff, Boston, 1987)
3. M. von Allmen, A. Blatter (eds.), *Laser Beam Interactions with Materials*, 1st edn. (Springer, Heidelberg, 1987)
4. D.J. Ehrlich, J.Y. Tsao (eds.), *Laser Microfabrication: Thin Film Processes and Lithography* (Academic, London, 1989)
5. W.M. Steen, *Laser Material Processing*, vol. 1 (Springer, London, 1991)
6. D.B. Chrisey, G.K. Hubler (eds.), *Pulsed Laser Deposition of Thin Films* (Wiley, New York, 1994)
7. J.C. Miller (ed.), *Laser Ablation: Principles and Applications* (Springer, Heidelberg, 1994)
8. L. Migliore (ed.), *Laser Materials Processing* (Marcel Dekker, New York, 1996)
9. H.G. Rubahn, *Laser Applications in Surface Science and Technology* (Wiley, New York, 1999)
10. J.F. Ready, D.F. Farson (eds.), *LIA Handbook of Laser Materials Processing* (Magnolia Publications, Orlando, FL, 2001)
11. A. Pique, R.C.Y. Auyeung, H. Kim, K.M. Metkus, S.A. Mathews, in *Proceedings of LPM2008 - 9th International Symposium on Laser Precision Microfabrication*, vol. 34 (2008), p. 1
12. N. Itoh, A.M. Stoneham, *Materials Modification by Electronic Excitation* (Cambridge University Press, Cambridge, UK, 2001)

13. K.K. Seet, T. Kondo, V. Mizeikis, V. Jarutis, S. Juodkazis, H. Misawa, Proc. SPIE **6161**, 616103 (2005)
14. J.J. Dubowski, S. Tanev (eds.), *Photon-based Nanoscience and Nanobiotechnology NATO ASI*, vol. 239 (Springer, Heidelberg, 2006)
15. N. Dahotre, S. Harimkar, *Laser Fabrication and Machining of Materials* (Springer, Heidelberg, 2008)
16. R. Murison, B. Reid, R. Boula-Picard, R. Larose, T. Panarello, JLPS (2008)
17. A. Vogel, J. Noack, G. Huttermann, G. Paltauf, J. Phys. Conf. Ser. **59**, 249 (2007)
18. A. Vogel, J. Noack, G. Huttman, G. Paltauf, Appl. Phys. B **81**, 1015 (2005)
19. S.Y. Chou, Q. Xia, Nat. Nanotechnol. **3**(5), 295 (2008)
20. W. Hoving, Proc. SPIE **3097**, 248 (1997)
21. E. Louzon, Z. Henis, S. Pecker, Y. Ehrlich, D. Fisher, M. Fraenkel, App. Phys. Lett. **87**, 241903 (2005)
22. R.J. Levis, G.M. Menkir, H. Rabitz, Science **292**(5517), 709 (2001)
23. F.E. Livingston, L.F. Steffeney, H. Helvajian, Appl. Surface Sci. **253**, 8015 (2007)
24. S.M. Pimenov, G.A. Shafeev, A.A. Smolin, V.I. Konov, B.K. Vodolaga, Appl. Surface Sci. **86**(1–4), 208 (1995)
25. C. Ristoscu, G. Socol, C. Ghica, I.N. Mihailescu, D. Gray, A. Klini, A. Manousaki, D. Anglos, C. Fotakis, Appl. Surface Sci. **252**(13), 4857 (2006)
26. J. Solis, C.N. Afonso, J.F. Trull, M.C. Morilla, J. Appl. Phys. **75**(12), 7788 (1994)
27. B. Tan, K. Venkatakrishnan, K.G. Tok, Appl. Surface Sci. **207**(1–4), 365 (2003)
28. V.P. Veiko, G.K. Kostyuk, N.V. Nikonorov, A.N. Rachinskaya, E.B. Yakovlev, D.V. Orlov, Proc. SPIE **6606**, 66060Q (2007)
29. T. Feurer, J.C. Vaughan, R.M. Koehl, K.A. Nelson, Optics Lett. **27**(8), 652 (2002)
30. F.E. Livingston, H. Helvajian, Genotype Pulse Modulation Laser Writing System, U.S. Patent No. 7,526,357, issued April 28, 2009
31. F.E. Livingston, H. Helvajian, Special Issue MRS Bull. Direct Write Technol. **32**, 40 (2007)
32. F.E. Livingston, L.F. Steffeney, H. Helvajian, Appl. Phys. A **93**(1), 75 (2008)
33. A.M. Stoneham, *Theory of Defects in Solids: Electronic Structure of Defects in Insulators and Semiconductors* (Clarendon, Oxford, 1975)
34. E. Lilley, in *Proceedings of the 6th International Symposium on Reactivity of Solids*, ed. by J.W. Mitchell, R.C.D. Vries, R.W. Roberts, P. Cannon (Wiley-Interscience, 1969), p. 631
35. J. Corish, P.M. Jacobs, in *Surface and Defect Properties of Solids* (The Chemical Society, London, 1973), pp. 160–228
36. R.W. Joyner, B.A. Somorjai, in *Surface and Defect Properties of Solids, A Specialist Periodical Report*, vol. 2 (The Chemical Society, London, 1973), pp. 1–33
37. S. Preuss, H.C. Langowski, T. Damm, M. Stuke, Appl. Phys. A **65**(4), 360 (1992)
38. T. Brixner, T. Pfeifer, G. Gerber, M. Wollenhaupt, T. Baumert, in *Femtosecond Laser Spectroscopy, vol. Progress in Lasers*, ed. by P. Hannaford (Kluwer, Dordecht, 2004), pp. 229–271
39. A. Prakelt, M. Wollenhaupt, A. Assion, C. Horn, C. Sarpe-Tudoran, M. Winter, T. Baumert, Rev. Sci. Inst. **74**(11), 4950 (2003)
40. M. Wollenhaupt, V. Engel, T. Baumert, Annu. Rev. Phys. Chem. **56**, 25 (2005)
41. R. Bayer, M. Wollenhaupt, C. Sarpe-Tudoran, T. Baumert, Phys. Rev. Lett. **102**, 023004 (2009)
42. F.E. Livingston, H. Helvajian, SPIE Proc., 6th Int. Symp. Laser Precision Microfabric. **1**, 329 (2005)
43. F.E. Livingston, H. Helvajian, J. Photochem. Photobiol. A **182**, 310 (2006)
44. F.E. Livingston, H. Helvajian, Proc. NATO Adv. Sci. Inst. Photon Based Nanosci. Nanobiotechnol. **239**, 225 (2006)
45. R.L. Jungerman, C. Johnsen, D.J. Mcquate, K. Salomaa, M.P. Zurakowski, R.C. Bray, G. Conrad, D. Cropper, P. Hernday, J. Lightwave Technol. **8**(9), 1363 (1990)
46. R. Fluck, B. Braun, E. Gini, H. Melchior, U. Keller, Optics Lett. **22**(13), 991 (1997)
47. P.R. Herman, A. Oettle, K.P. Chen, R.S. Marjoribanks, Proc. SPIE **3616**, 148 (1999)
48. E. Wilson, T. Eisner, W. Briggs, R. Dickerson, R. Metzenberg, R. O'Brien, M. Susman, W. Boggs, *Life on Earth* (Sinauer Association, Stamford, 1973)

49. F.E Livingston, W.L. Sarney, K. Niesz, T. Ould-Ely, A.R. Tao, D.E. Morse, Proc. SPIE Bio-Inspired/Biomimetic Sensor Technol. Appl. **7321**, 732101 (2009)
50. W.L. Sarney, J.W. Little, A.R Tao, D.E. Morse, F.E. Livingston, Proc. 26th Army Science Conf. **MP-16**, 1 (2009)
51. F.E. Livingston, unpublished results (2009)
52. F.E Livingston, P.M. Adams, H. Helvajian, Appl. Phys. A **89**, 97 (2007)
53. F.E. Livingston, H. Helvajian, Appl. Phys. A **81**, 1569 (2005)
54. F.E. Livingston, P. Adams, H. Helvajian, SPIE Proc. Laser Precision Microfabrication **5662**, 44 (2004)
55. F.E. Livingston, P. Adams, H. Helvajian, Appl. Surf. Sci. **247**, 526 (2005)
56. F.E. Livingston, H. Helvajian, in *Three-Dimensional Laser Microfabrication: Principles and Applications*, ed. by H. Misawa, S. Juodkazis (Wiley, Weinheim, Germany, 2006), pp. 287–339
57. P.D. Fuqua, D.P. Taylor, H. Helvajian, W.W. Hansen, M.H. Abraham, Mat. Res. Soc. Symp. Proc. **624**, 79 (2000)
58. W.W. Hansen, S.W. Janson, H. Helvajian, in Laser Applications in Microelectronic and Optoelectronic Manufacturing II, vol. 2991 (SPIE, Bellingham, WA, 1997), vol. 2991, pp. 104–112
59. F.E. Livingston, H. Helvajian, SPIE Proc. Laser Adv. Mater. Proces. **4830**, 189 (2003)
60. S.W. Janson, A. Huang, W.W. Hansen, H. Helvajian, AIAA **6701**, 1 (2004)
61. J.F. Belcher, C.M. Hasnon, H.R. Beratan, K.R. Udayakumar, K.L. Soch, SPIE Proc. Infrared Technol. Appl. **3436**, 611 (1998)
62. J.F. Tressler, S. Alkoy, R.E. Newnham, J. Electroceram. **2**(4), 257 (1998)
63. R.L. Brutchey, D.E. Morse, Agnew. Chem. Int. Ed. **6564**, 45 (2006)
64. R.L. Brutchey, E. Yoo, D. Morse, J. Am. Chem. Soc. **128**, 10288 (2006)
65. R.W. Whatmore, J. Electroceram. **13**, 139 (2004)
66. B.D. Begg, K.S. Finnie, E.R. Vance, J. Am. Ceram. Soc. **79**, 2666 (1996)
67. T. Hoshina, H. Kakemoto, T. Tsurumi, M. Yashima, Y. Kuroiwa, S. Wada, Key Engineer. Mater. **320**, 131 (2006)
68. U.Y. Hwang, H.S. Park, K.K. Koo, J. Am. Ceram. Soc. **87**, 2168 (2004)
69. H. Ikawa, T. Nakai, S. Higuchi, K. Saitoh, M. Takemoto, Trans. Mater. Res. Soc. Jpn. **13**, 101 (2006)
70. S.W. Lu, B.I. Lee, Z.L. Wang, W.D. Samuels, J. Cryst. Growth **219**, 269 (2000)
71. M.B. Smith, K. Page, T. Siegrist, P.L. Redmond, E.C. Walter, R. Seshadri, L.E. Brus, M.L. Steigerwald, J. Am. Chem. Soc. **130**, 6955 (2008)
72. M.-S. Zhang, Z. Yin, Q. Chen, W. Zhang, W. Chen, Solid St. Commun. **119**, 659 (2001)
73. M.E. Lines, A.M. Glass, *Principles and Applications of Ferroelectrics and Related Materials* (Clarendon, Oxford, 1977)
74. R.R. Letfullin, T.F. George, G.C. Duree, B.M. Bollinger, Adv. Opt. Technol. **ID 251718** (2008)
75. F.E. Livingston, Laser-$BaTiO_3$ nanoparticle interactions: One-temperature model approach, unpublished results (2009)

Index

Ablation debris, 182
Ablation rate, 94, 169, 171, 172
Absorbing defects, 173
Absorption coefficient, 29, 53
Absorption length, 59
Absorption wave life-time, 63
Absorption wave propagation velocity, 65
Adiabatic coefficient, 39
Aerosols, 73
Aforementioned depolymerization, 106
Algorithm for pulse script generation, 195
Ammosov–Delone–Krainov (ADK) model, 53
Amplified spontaneous emission (ASE), 80
Angular broadening, 96
Angular distribution of the propagation, 94
Anti-chirped laser pulse, 72
Application specific integrated circuit, ASIC), 198
Arbitrary waveform signal generator (AWSG), 198
Aspheric lenses, 15
Atmospheric analyses, 73
Atomization, 149, 150
Attosecond pulses, 83
Attosecond radiation pulses, 80
AWSG flash memory board, 202

Background gas, 93
Background oxygen, 94
Backside wet etching, 176
Barium titanate ($BaTiO_3$), 215
Basic physical processes, 21
Beam path, 14
Beam profile, 92
Beamshaper, 15
Beam splitter, 181
Bifurcations, 44
Bio-inspired synthetic pathways, 215
Blackbody spectrum, 148
Blast wave model, 95
Bragg reflectors, 182
Breakdown criterion, 56
Breakdown in hydrogen, 64
Breakdown modeling, 55
Breakdown threshold, 55
Breakdown threshold of gas, 68
Breakdown time, 67
Breakdown wave, 65
BreakdownWaveVelocity, 65
Bremsstrahlung, 77
Bulk solid lattice, 192
Bunch, 11
Bunch frequency, 11
Burst mode, 196

CA film, 145
CA materials, 140, 141
(CAM) software, 198
CAM system, 200
Carbonization, 104
Catalytic activation, 193
Cavity lengths, 11
Cavity Q, 8
Centre of mass velocity, 94
Centrosymmetric atomic structure, 79
Ceramic materials, 173
Characteristic times, 66
Chemical equilibrium, 98
Chirped pulse amplifier (CPA), 71
Clausius-Clapeyron equation, 31, 37
Cleaning, 80, 81
Cluster energy, 135
Cluster formation, 154
Cluster nucleation, 135
Cluster-assembled (CA), 132, 158
Clusters, 98

Coalescence, 140, 144, 146, 148
Co-fabrication, 214
Coherence parameters, 180
Coherent molecular control process, 194
Coherent wake emission, 83
CO_2 laser, 152
Colliding pulse amplification (CPA), 9
Collimating lens, 70
Collision, 96
Collisional and non-collisional processes, 52
Collisional heating, 132
Collisional sticking, 149, 150
Collision frequency, 52
Complete thermal equilibrium, 54
Complex stoichiometry, 154
Conductivity, 102
Conical emission, 72
Continuous wave (cw) mode, 22
Controlled cooling, 218
Controlled material transformation, 210
Controlled variation of the optical properties, 214
Convection, 42
Conventional laser direct-write processing, 216
Coulomb explosion, 93
Crack formation, 100
Cracking, 173
Critical density, 51, 64
Critical layer thickness, 104
Critical power, 71
Cr-masks, 179
Cumulative ablation, 162
Cut-off, 78

Damage, 17
2D-conducting interface layers, 103
Debye frequency, 25
Debye shielding length, 50
Debye sphere, 51
Debye temperature, 194
Defect-induced conductivity, 104
Defocusing, 79
Defocusing lens, 71
Delay generator, 69
Demultiplexers, 182
Deposition parameters, 102
Depth modulation, 180
Depth of focus (DOF), 170
Detonation wave, 65
Detrimental effects, 98
2D growth, 99
Diagnostic test, 204
Dielectric mask, 179
Dielectric mirrors, 179
Diffraction, 15
Diffractive optical elements (DOE), 15, 180
Diffractive phase elements, 180
Diffusion length, 57
Diffusion losses, 68
Diffusion model, 136
DiffusionLossCriterion, 57
Digitally scripted laser-induced phase conversion, 219
Digitally scripted laser processing, 198
Direct ablation of polymers, 106
Direct patterning, 105
Direct writing, 107, 152
Direct-write application, 194
Direct-write patterning, 211
Direct-write processing tool, 195
Dissolution kinetics, 212
Disturbance, 193
Divergence, 13
2D layering scheme, 194
Donor, 107
Drag model, 136
Drilling, 178
Droplets, 149
Drude model, 24
Drude's model, 60
3D-vectored travel distance, 205
Dynamic release layer (DRL), 107
Dynamical restocking, 72

Edge curling, 175
Edge definition, 180
Effective collision frequency, 52
Effective temperature, 97
Ejection of droplets, 93
Electrical conductivity, 29
Electric field plane wave, 28
Electroacoustic transducer elements, 215
Electron avalanche process, 17
Electron bunch, 11
Electron diffusion, 57
Electron-electron, 23
Electron-electron scattering time, 25
Electron-electron thermalization, 24
Electron gas, 25
Electron-hole pair, 23
Electronic reconstruction, 103
Electronic relaxation, 93
Electronic temperature, 24, 25
Electronic thermalization, 24
Electron-lattice scattering, 24
Electron-phonon coupling, 25, 93

Electron-phonon interactions, 23
Electron scattering, 24
Electrostatic energy analyzer, 97
Electron's trajectory, 11
Emission intensity profiles, 96
Energy growth rate, 55
Energy losses, 56
EO cell, 203
Epitaxial growth, 99
Erbium doped fiber amplifers (EDFA), 7
Evaporation, 31
Evaporation of nanoparticles, 63
Excimer lasers, 152
Excitation, 97
Excitation of electrons, 27
Expanding vapor plume, 36
Expansion, 35
Extinction coefficient, 28

Fast photography, 139, 143
Femtosecond laser, 152
Fermi energy, 24
Fermi liquid theory, 24
Fiber laser, 194
Fiber optics, 14
Filamentation, 50
Film growth, 90, 98
Fluence, 147, 148, 150
Fluorescent molecules, 184
Flux velocity, 136
Focal plane, 13
Focal volume, 63
Focussability, 22
Foturan, 211
Fragmentation, 150
Free-electron laser (FEL), 10, 76
Free energy, 192
Free energy of the film surface, 99
Free expansion, 134
Front side ablation, 175, 180
Fs ablation, 93, 132, 146
Fundamental physical processes, 44

Gain, 6
Galilean telescope, 15
Gaussian profile, 30
G-code, 201
Genotype-inspired, digitally scripted laser direct-write technique, 217
Genotype pulse script, 196
Geometrical optics, 13
Giant pulsing, 8
Gibbs energy, 191, 192
Glasses, 173
Global minimum energy state, 192
Grating, 181
Griem, 54
Group dispersion parameter, 72
Group velocity dispersion parameter, 70
Growth kinetic, 90
Growth modes, 99
Growth rate of electron energy, 52

Hagen-Rubens-equation, 29
Hardware control system, 203
Harmonic generation, 10, 80
H-code, 202
Heat-affected zone (HAZ), 151
Heat conduction, 29
Heat diffusion length, 59
Heat source, 21
Hemispherical shock wave, 95
Heterostructure, 103
HHG by plasma mirrors, 83
High angle annular dark field (HAADF), 103
High-energy particle accelerator, 76
High fidelity photon modulation, 216
High-order harmonic generation (HHG), 77
High-order harmonic generation efficiency, 79
High-order harmonics, 82
High-power pulsed laser, 159
Hole arrays, 179
Hole drilling, 178
Holographic optical elements (HOE), 15, 16
Hydrodynamic motion, 35
Hydrodynamic speed, 35

IB effect, 55
Images distances, 13
Imaging, 76, 95
Impact velocity, 142
Impurities, 61
Incubation effects, 193
Indirect ablation, 176
Indium-tin-oxide (ITO), 108
Inherent limitations, 196
Injection nozzles, 179
Integrated position synchronized output (PSO), 198
Intense laser, 39
Intra-pulse, 216
Inverse bremsstrahlung (IB), 52, 55, 93
Inversion, 22
Ion-damage, 103

Ionic compensation mechanism, 104
Ionization, 140
Ionization avalanche, 61
Ionization channel, 75
Irradiance, 30
Island growth, 99
ITO patterning, 179

Keldysh parameter, 53
Kerr effect, 70, 81
Kerr lens mode-locking (KLM), 9
Kinetic energy, 97
Knudsen layer, 35, 94, 136

$LaAlO_3$, 103
Laser, 22
Laser ablation, 151
Laser ablation systems, 91
Laser assisted chemical vapor deposition, 161
Laser assisted etching (LAE), 153
Laser beam filamentation, 69, 72
Laser damage, 17
Laser etching, 153
Laser fluence, 32
Laser-generated plasma, 132, 139, 150
Laser genotype pulse modulation processing, 196
Laser genotype pulse modulation technique, 191
Laser-induced breakdown, 63
Laser-induced breakdown spectroscopy (LIBS), 54
Laser-induced damage thresholds (LIDT), 18
Laser-induced forward transfer (LIFT), 105, 107
Laser-induced plasma, 92
Laser-induced X-ray plasma, 77
Laser LIGA, 152
Laser pulse script, 203, 209
Laser spot size, 30
Laser-supported absorption wave (LSAW), 38, 63
Laser-supported combustion wave (LSCW), 38
Laser-supported detonation wave (LSDW), 38
Laser supported radiation (LSR), 40
Laser-triggered lightning, 74
Latent heat, 30
Lattice dynamics, 23
Lattice temperature, 24, 26
Layer thickness, 100
Layer-by layer growth, 99
LIBDE, 177
LIBWE, 177
Light channelling, 170
Light detection and ranging (LIDAR), 73
Liquid-vapor interface, 35
Liquid-vapor phase transition, 31
Local phonon modes, 193
Local thermal equilibrium (LTE), 26, 54
Long duration contrasts, 80
Lorentz model, 28
Low background pressure, 95
Luminous ablation plume, 89

Machining of glass, 195
Mach number, 36
Marangoni convection, 43
Material preparation, 195
Material transport phenomena, 42
Matrix, 156
Matrix-assisted pulsed laser evaporation (MAPLE), 106, 160
Maxwell-Boltzmann distribution, 94
Maxwell's equations, 70
M-code, 200, 202
Mechanical fragmentation, 132
MEH-PPV, 106
Melt ejection, 42
Melting depth, 33
MEMS, 163
Metallic nanoclusters, 156
Metals, 174
Metastable, non-equilibrium state, 192
Microcrater, 179
Microelectronic fabrication, 75
Micro fluidic devices, 183
Micro lenses, 182
Micromachining, 151, 169
Micro optical structures, 181
Mie absorption, 63
Misfit-dislocations, 100
Mixed model, 105
Mixed-propagation, 138
Mixed-propagation model, 141, 143, 145
Mn-plume species, 95
Mode-locking, 9
Model of mixed-propagation, 133
Model the laser ablation, 105
Modified diffusion model, 136
Modified drag model, 138
Modulation, 190
Modulation of photon flux, 195
Molecular collision time, 69
Molecular dynamics (MD) simulations, 147, 148

Moving focus, 71
Multihole pattern, 178
Multilayer stacks, 179
Multiphoton absorption, 53, 171
Multiphoton ionization, 55, 57, 71
Multiphoton ionization rate, 58
Multi-photon processes, 27
Multiple scattering, 94
Multistep attenuators, 212

N-photon transition probability, 27
Nano-particle formation, 93
Nanoparticles, 156, 211
Nanopearls, 160
Nano-structuring, 158
Nanotubes, 162
Nanowires, 159
National Ignition Facility (NIF), 7
Nature of the photon flux delivery, 195
Nd:YAG laser, 152
Neutral species, 98
Nitrification, 44
Noncollisional interaction, 78
Non-equilibrium velocity, 35
Nonlinear optics, 70
Nonlinear processes, 29
Nonlinear refractive index, 81
Non-thermal evaporation process, 99
Nozzle plates, 178
NP asymptotic size, 133, 141
NP formation, 133
NPs, 140
Nucleation, 98
Numerical aperture (NA), 170
Numerical control intermediate (NCI), 200

Optical absorption length, 29
Optical breakdown, 55, 68
Optical fiber, 183
Optical frequency doubling, 92
Optical penetration depth, 59
Optical reflectivity, 33
Optical resolution, 170
Optical transport system, 13
Organic light emitting diode (OLED), 108
Oscillating mirror model, 82
Oscilloscope traces, 208
Outcoupler, 6
Outcoupler mirror, 12
Outcoupling mirror, 6
Oxygen background, 96
Oxygen defects, 102

Partially ionized, 39
Partial pressure, 90
Particle cooling, 142
Pattern script, 201
Patterned maneuvers, 209
PEDOT:PSS, 106
Penning effect, 57
Percolated structure, 145
Perovskite thin-films, 215
Phase explosion, 150, 151
Phase transformations, 30, 216
Photochemical degradation, 104
Photochemical models, 105
Photoexposure, 211
Photoionization, 93, 132
Photoionization cross section, 53
Photomechanical spallation, 150
Photon absorption, 92
Photon bath, 71
Photon modulation, 193
Photophysical models, 105
Photophysical processes, 211
Photostructurable glass ceramic, 211
Photothermal models, 105
Photovoltaic cells, 179
Physical optics, 14
Piston effect, 39, 43
Pixel by pixel irradiation, 180
Planar waveguides, 181
Plasma, 37
Plasma-assisted ablation, 176
Plasma breakdown, 52
Plasma formation, 60
Plasma frequency, 28, 51
Plasma heating efficiency, 53
Plasma luminosity, 142
Plasma mirror, 81
Plasma oscillations, 51, 134
Plasma parameter, 50
Plasma shielding, 59
Plasma shutter, 68
Plasma's optical thickness, 59
Plasma surface pressure, 41
Plasma temperature, 65
Plasmatron, 39
Plume dynamics, 95
Plume expansion, 94
Plume imaging, 67
Plume mass, 95
Plume sharpening, 134
Plume species, 97
Plume splitting, 134
PMMA, 156
Pockels cells, 80, 203

Polarization-dependent crystallization, 198
Polyimide ablation, 207
Polymers, 104, 171
Polysilicon, 153
Ponderomotive potential, 52
Ponderomotive wave, 11
Postpulses, 80
Precision laser modulation techniques, 193
Preionization, 57
Prepulse, 80
Prepulse contrast, 81
Process Script, 201
Processing limits, 169
Propagation factor, 70
Propagation mechanism, 66
Protocols, 195
PSOCFG command, 202
PSO control, 204
PSO firing, 204
Pulse chirp, 70
Pulsed laser deposition (PLD), 89, 154
Pulsed mode, 22
Pulsed reactive crossed beam laser ablation (PRCLA), 90
Pulse modulation, 194
Pulse train, 194
Pyroelectric phase transformation, 198

Q - Switching, 8
Quasi-adiabatic initial expansion, 54
Quasi-transparent plasma, 71
Quiver energy, 52, 79

Radiofrequency, 158
Raman-active bands, 216
Rarefaction, 41
Raster patterning, 213
Reactive atmosphere, 37
Reactive pulsed laser deposition, 156
Rear side ablation, 175
Rear surface absorption, 173
Recoil pressure, 42
Recombination, 97
Recondensation, 36
Redeposition, 172
Reduce the kinetic energy, 94
Re-excitations, 97
Reflection and absorption, 28
Reflectivity, 29
Refraction, 10
Refractive index, 28, 70
Relativistic electrons, 75
Relaxation, 25
Relaxation mechanism, 100
Resistive bolometers, 215
Resonant cavities, 8
Resonator, 9
Retrodiffused emission, 72
Ripples, 35

Saha equation, 37
S-code, 202
“scratch-dig” values, 18
Screw dislocation, 100
Self-amplified stimulated emission (SASE), 7, 11
Self-focusing, 71
Self-guiding, 72
Self-phase modulation, 72
Semiconductor saturable-absorber mirror (SESAM), 196
Separation of the plume, 96
Shadowing, 144
Sharpening, 96
Shock wave, 41, 59, 63, 95, 134, 141
Shock wave model, 136
Silicon technology, 163
Silver islands, 144
SimpleBreakdownCriterion, 61
Single photon processes, 27
Single-walled nanohorns, 162
Single-walled nanotubes, 161
Site-selective and patterned micro- and nanoscale transformation, 215
Site-selective formation, 197
Slicing, 75
Software, 19
Software control system, 198
Soft X-ray lasers, 8
Solar cells, 178
Solidification, 32
Solid state laser, 22
Spectroscopic detection scheme, 195
Spherical lenses, 182
Spontaneous emission, 6
Square wave, 209
Stable shock wave front, 138
Stimulated emission, 22
Stopping distance, 95
Strain, 100
Structural conversion, 215
Structure resolution, 170
Sub-micron patterning, 182
Subtractive diffraction geometry, 72
Superconducting linear accelerator, 10

Superconducting radiofrequency (SRF) linac, 11
Supercritical density, 81
Supercritical plasma, 81
Supersaturation, 37, 99, 100
Surface debris, 172
Surface defects, 61
Surface plasmon resonance (SPR), 145
Surface reflectivity, 60
Surface relief, 180
Surface temperature profiles, 33
Surface tension, 42
Surface topography, 34
Synchronized-image-scanning (SIS), 183
Synchrotron radiation, 75

Tabletop, 76
Target surface, 35
Temperature profiles, 31
Temporal broadening, 72
Temporal dephasing, 72
Temporal profile, 194
Terrace width, 100
Thermal conductivity, 33
Thermal decomposition, 107
Thermal diffusion length, 29
Thermal pyroelectric detectors, 215
Thermal radiation, 38
Thermocapillary effect, 42
Thermodynamical critical temperature, 150
Thermodynamical equilibrium, 35
Thermoioniс effect, 60
Thermopiles, 215
Thin film growth, 93
Thin film patterning, 179
Three-dimensional concentration mapping, 73
Three-step model, 79
Threshold condition, 6
Threshold fluence, 105
Threshold irradiance, 27
Threshold voltage, 104
THz radiation, 75
Time-bandwidth product, 9
Time dependence of laser, 8
Time of flight analysis, 106
Time-resolved photoemission experiments, 24
Titania, 160
Top hat, 43
Transfer precise patterns, 107
Transmitted fraction, 68
Tungsten oxide, 157
Tunneling ionization, 53, 79
Turbulence, 44, 135
Twinning, 100
Two-temperature model (TTM), 25

Ultrafast optical switches, 69
Ultrashort laser damage, 18

Vacuum conditions, 94
Vapor pressure, 31
Vaporization, 35, 93
Vaporization threshold, 59
Vaporization threshold of defect, 62
Vaporization threshold reduction, 62
Vaporization time, 67
Velocity compensation, 208
Viscosity, 137
Vlasov equation, 53
Voltage pulse, 209
Voltage pulse script, 203

Wavelength, 22
4ω criterion, 14
White light LIDAR, 73
Wiggler, 11

X-ray emission, 81
X-ray emission spectrum, 78
X-ray imaging, 76
X-ray laser, 76
XUV-lithography, 75
XUV radiation, 75
XUV source, 76

Z-pinch, 76
Z-positioning, 170